

2009

## Multi-mode coherent ladar imaging via diverse periodic pseudo noise waveforms and code division multiple access apertures

Matthew Paul Dierking  
*University of Dayton*

Follow this and additional works at: [https://ecommons.udayton.edu/graduate\\_theses](https://ecommons.udayton.edu/graduate_theses)

---

### Recommended Citation

Dierking, Matthew Paul, "Multi-mode coherent ladar imaging via diverse periodic pseudo noise waveforms and code division multiple access apertures" (2009). *Graduate Theses and Dissertations*. 2341.  
[https://ecommons.udayton.edu/graduate\\_theses/2341](https://ecommons.udayton.edu/graduate_theses/2341)

This Dissertation is brought to you for free and open access by the Theses and Dissertations at eCommons. It has been accepted for inclusion in Graduate Theses and Dissertations by an authorized administrator of eCommons. For more information, please contact [mschlange1@udayton.edu](mailto:mschlange1@udayton.edu), [ecommons@udayton.edu](mailto:ecommons@udayton.edu).

**MULTI-MODE COHERENT LADAR IMAGING VIA DIVERSE PERIODIC  
PSEUDO NOISE WAVEFORMS AND CODE DIVISION  
MULTIPLE ACCESS APERTURES**

**Dissertation**

**Submitted to**

**The School of Engineering**

**UNIVERSITY OF DAYTON**

**In Partial Fulfillment of the Requirements for**

**The Degree**

**Doctor of Philosophy in Electrical Engineering**

**Matthew Paul Dierking**

**THE UNIVERSITY OF DAYTON**

**DAYTON, OHIO**

**December 2009**

**MULTI-MODE COHERENT LADAR IMAGING VIA DIVERSE PERIODIC  
PSEUDO NOISE WAVEFORMS AND CODE DIVISION MULTIPLE ACCESS  
APERTURES**

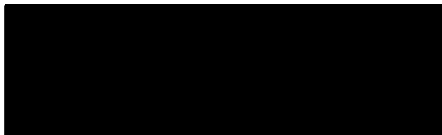
APPROVED BY:



Bradley D. Duncan, Ph.D.  
Professor  
Electro-Optics Program  
Committee Chairman



Peter E. Powers, Ph.D.  
Professor  
Department of Physics  
Committee Member



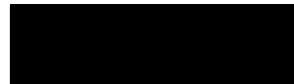
Russell C. Hardie, Ph.D.  
Professor  
Department of Electrical and  
Computer Engineering  
Committee Member



Paul F. McManamon, Ph.D.  
Technical Director  
Ladar and Optical  
Communications Institute  
Committee Member



Malcolm Daniels, Ph.D.  
Graduate Engineering Programs  
& Research  
School of Engineering



Tony E. Saliba, Ph.D.  
Dean  
School of Engineering

## **ABSTRACT**

### **MULTI-MODE COHERENT LADAR IMAGING VIA DIVERSE PERIODIC PSEUDO NOISE WAVEFORMS AND CODE DIVISION MULTIPLE ACCESS APERTURES**

Matthew Paul Dierking, Ph.D.  
University of Dayton, 2009

Advisor: Bradley Duncan, Ph.D

Since the invention of the laser, laser radars (ladars) have been investigated following the extensive development path of radio frequency radar systems. Ladar systems have progressed from simple rangefinders to ladar systems demonstrating 2-D and 3-D geometric imaging, vibrometry, polarization diverse imaging and recently synthetic aperture ladar imaging. This research focuses on ladar techniques which provide sensing capability beyond the diffraction limit of the primary aperture. Periodic, pseudo noise (PPN) waveforms and code division multiple access (CDMA) multiplexing are utilized to provide simultaneous multimode ladar imaging including range, range-Doppler, synthetic aperture and micro-Doppler imaging.

A theoretical foundation is developed for each imaging mode. A generic signal model is used to derive the measurement requirements independent of pulse format or implementation constraints. Multifunction waveforms are developed based on genetically selected, diverse PPN waveform sets and implemented in a code division multiple access architecture. An analytic model is developed describing the transmitted PPN waveform,

targets, target-beam interactions, receiver, data acquisition and signal processing. The performance of the PPN waveform is characterized for each measurement mode. Composite code and diverse sub-code processing demonstrate adaptable Doppler tolerance and energy usage. A scaled experimental system is developed and demonstrates PPN pulse compression, agile phase recovery and imaging in each of the four modes. Finally, PPN waveforms and CDMA multiplexing are utilized to demonstrate multiple aperture operation including waveform compression and phase recovery.

## **DEDICATION**

To my wife, Lynn Mishler – This dissertation is just one more thing we share in our life together. I would not be here without you.

To my sons, Justin and Kelby, It's not the destination, but the journey that matters. If you love the puzzle, it does not seem like work.

To my parents, Arthur and Dora Dierking – for all the steadfast faith and support.

## ACKNOWLEDGEMENTS

I would like to thank Larry Barnes, not only for his support in this research, but for more than a decade of cooperative laser radar research, discussions and friendship. I would like to recognize John Schmoll and Timothy Meade from Optimetrics, for their technical discussions and support during the development of the experimental system. I would like to thank Gregory Rubertus, Col Brian Ford, and especially Robert Feldman for providing the opportunity to complete my PhD.

My thanks to my committee members Dr. Peter Powers, Dr. Russell Hardie and Dr. Paul McManamon for their service and many contributions to this dissertation.

Finally, I am especially grateful to Dr. Bradley Duncan who directed my dissertation. Dr. Duncan provided guidance, many challenges, and a passion for understanding. His dedication to me, and all of his students, has truly taught me the meaning of "teacher".

This research was supported in part by the U.S. Air Force Research Laboratory and the Ladar and Optical Communications Institute (LOCI) at the University of Dayton. The views expressed in this dissertation are those of the author and does not reflect on the official policy of the Air Force, Department of Defense or the U.S. Government.

## TABLE OF CONTENTS

ABSTRACT.....	iii
Chapter I Introduction.....	1
A. Historical Background .....	1
B. Dissertation Overview.....	3
Chapter II Ladar Background.....	5
A. Ladar Applications.....	5
B. Ladar Diffraction Limited Beamwidth.....	6
C. Ladar Imaging Modes and Requirements.....	7
D. General Signal Model .....	8
E. Range Imaging.....	12
F. Range-Doppler Imaging.....	14
G. Synthetic Aperture Ladar Imaging .....	16
H. Micro-Doppler Imaging .....	21
I. Waveform Requirement Summary .....	24
Chapter III Coherent Ladar Techniques.....	27
A. Elements of a Monostatic, Coherent Ladar.....	27
B. Master Oscillator .....	29
C. Waveform Generation .....	29
D. Polarization Sensitive Transmit/Receive Switch .....	30

E. Quadrature Detection.....	32
1) Free Space IQ Detection .....	32
2) Common Path Interferometer for IQ Detection .....	37
F. Coherent Detection .....	40
1) Noise Sources .....	43
2) Laser Radar Equation .....	48
Chapter IV Waveform Constraints and Figures of Merit.....	50
A. General Waveform Constraints.....	50
1) High Time Bandwidth Product form Multimode Imaging .....	51
2) Support Phase Recovery from Multiple Apertures.....	51
3) Detect and Mitigate Residual Doppler .....	51
4) Minimize Energy .....	51
5) Minimize Peak Power.....	52
6) Minimize Hardware Complexity .....	52
B. Figures of Merit.....	53
1) Ideal Point Response (IPR) Mainlobe Width .....	53
2) Compression Factor .....	54
3) Integrated Sidelobe Ratio (ISLR) .....	54
4) Peak Sidelobe Ratio (PSLR).....	55
5) Noise Equivalent Vibration Velocity (NEVV).....	57
6) Ambiguity Velocity .....	57
7) Range Ambiguity.....	57
8) Velocity Resolution .....	58

9) Frequency Resolution .....	58
Chapter V PPN Waveforms in Coherent Ladar .....	59
A. Periodic Pseudo Noise Waveform .....	59
B. PPN Taxonomy .....	60
C. Multi-Code Periodic Pseudo Noise Waveforms .....	64
D. Discrete PPN Signal Model .....	65
E. Discrete PPN Matched Filter .....	67
F. PPN Waveform Doppler Sensitivity.....	69
G. PPN Multiple TDM Sub-Code Processing .....	75
H. PPN Multiple CDMA Sub-Code Processing .....	79
Chapter VI PPN Experimental System .....	82
A. Laboratory Ladar System Description.....	83
B. Experimental PPN Waveform Generation and Pulse Compression.....	86
C. Preliminary Phase Measurements .....	88
D. PPN Waveform Combination.....	90
Chapter VII Genetically Optimized PPN IPR.....	93
A. Genetic Optimization of the IPR.....	94
B. Genetic Algorithm Convergence with Code Length .....	97
C. Genetic Algorithm Experimental Demonstration .....	98
D. CNR Impact on the Genetic Algorithm IPR .....	101
E. Genetic Algorithm Composite IPR.....	102
F. Multi-Notch IPR .....	104
Chapter VIII PPN Range Imaging.....	108

A. Simulated PPN Ladar Range Imaging.....	108
B. Range Imaging Experimental PPN System.....	110
C. PPN Range Image Experimental IPR.....	112
Chapter IX Range-Doppler Imaging .....	114
A. Range-Doppler Experimental System.....	116
B. Range Doppler Experimental Targets .....	118
C. Composite Code Matched Filter .....	120
D. Sub-Code Processing .....	122
E. Filter bank Processing .....	124
Chapter X Synthetic Aperture LADAR Imaging .....	129
A. Stripmap SAL Phase Variation .....	129
B. .Simulated PPN Synthetic Aperture Ladar Imaging.....	131
C. Experimental Block Diagram.....	135
D. PPN SAL Imaging Experimental Targets .....	136
E. Experimental Results.....	137
Chapter XI Micro-Doppler Imaging .....	145
A. Simulated PPN Micro-Doppler Imaging.....	147
B. Experimental Block Diagram.....	149
C. Micro-Doppler Target Description.....	149
D. Experimental Results .....	151
Chapter XII Multi-Aperture Interferometric Imaging.....	159
A. CDMA Multi-Aperture Ladar .....	160
B. Optical Delay CDMA/MIMO .....	161

C. Cross-Track Interferometric SAL.....	164
D. Along Track Differential SAL .....	169
E. MIMO Experimental Ladar System .....	173
F. Optically Delayed CDMA Multi-Aperture Waveforms and Pulse Compression...	175
G. MIMO Phase Recovery .....	176
H. Conclusions .....	179
Chapter XIII System Level Modeling .....	180
1) Laser Radar Equation .....	180
Chapter XIV Summary and RecommendationS .....	194
A. Summary and Contributions .....	194
B. Directions for Future Research.....	196
C. Summary of Original Contributions.....	198

## TABLE OF FIGURES

Figure 1: Electromagnetic spectrum from laser radar to radio frequency radar.....	6
Figure 2: Three point targets encompassed within the beam footprint.....	7
Figure 3: Range (a), range-Doppler (b), synthetic aperture (c) and micro-Doppler images for the three point target array. ....	9
Figure 4: Stripmap SAL imaging geometry for three point target array.....	19
Figure 5: Summary of phase histories for range-Doppler (dash-dot), synthetic aperture (dashed), and micro-Doppler (solid) ladar imaging modes. ....	25
Figure 6: Block diagram of a typical monostatic, coherent ladar system. ....	27
Figure 7: Polarization sensitive transmit/receive switch diagram .....	30
Figure 8: Laboratory IQ Detection Diagram.....	33
Figure 9: Tapered Sinusoidal signal: real component (solid line) and imaginary component (dashed line).....	35
Figure 10: Signals in the complex plane of tapered sinusoid for positive frequency (a) and negative frequency (b).....	35
Figure 11: IQ signals due to a 10% channel bias (a) and a 2:1 channel imbalance (b).....	36
Figure 12: IQ signal with common phase rotation on both legs (a) and inter-leg rotation (b). ....	37
Figure 13: IQ Demodulator based on polarization sensitive common-path interferometer has better stability and alignment properties.....	38
Figure 14: Small signal, shot noise, and combined signal gain impact on the local oscillator and coherent mixing.....	47
Figure 15: Optimal MO Power based on the performance of the PicoSecond Pulse Laboratory amplifier. ....	48
Figure 16: IPR for a 20,000 point PPN waveform (a) and the 3 db (i.e., full-width half-maximum) resolution metric definition (b).....	53

Figure 17: Integrated sidelobe ratio (ISLR) metric definition (a) and close up about the mainlobe showing regions of summations (b). .....	55
Figure 18: Peak sidelobe ratio (PSLR) metric definition.....	56
Figure 19: Single binary phase, pseudo random noise code segment with $N_c$ phase chips of length $T_c$ . .....	60
Figure 20: PPN Waveform and CDMA Taxonomies .....	62
Figure 21: Conceptual diagram of PPN waveform with $N_{code}$ sub-codes.....	65
Figure 22: The effects of residual Doppler phase modulation on PPN waveforms: (a) three identical non-contiguous transmit codes, (b) the real component of the residual Doppler phase modulation for an assumed line-of-sight velocity of 3.75 m/s, (c) the transmitted waveforms after modulation, and (d) the ideal matched filter output.....	71
Figure 23: The peak matched filter output for a binary phase coded waveform is shown as a function of code length for line-of-sight velocities of 1 m/s (dotted line), 0.1 m/s (dash line) and .0375 m/s (solid line). Calculated locations of the matched filter output nulls for these velocities are indicated by the diamond, triangle and square markers, respectively.....	72
Figure 24: The theoretical peak matched filter output for a binary phase coded waveform is shown as a function of code length for line-of-sight velocities of 1 m/s (dotted line), 0.1 m/s (dash line) and .0375 m/s (solid line). Calculated locations of the matched filter output.....	76
Figure 25: Single matched filter for a multi-code PPN waveform (a), and the composite output for multiple single sub-code matched filters (b). .....	77
Figure 26: IPR for a single matched filter processed waveform (a) and for the composite of 20 TDM matched filtered processed sub-codes (b). .....	78
Figure 27: Composite sidelobe level as a function of the number of TDM sub-codes processed.....	78
Figure 28: CDMA matched filter structures for (a) a single matched filters, and (b) for a bank of sub-code matched filters. ....	80
Figure 29: Preliminary PPN ladar experimental setup.....	83
Figure 30: (a) A segment of the Ideal PPN waveform (solid line) has been temporally registered with corresponding chips of the detected signal (dashed line) from the vibrating target. (b) The ideal (solid line) and measured (dashed line) IPRs are in excellent agreement with one another.....	87

Figure 31: The experimental micro-Doppler phase history for a 2 kHz vibrating target (a) and the corresponding normalized amplitude spectrum (b) demonstrate excellent phase recovery when using PPN waveforms and matched filter processing. ....	89
Figure 32: The ideal (solid curve), range compressed IR for a 1000 chip PPN waveform with $T_c = 2$ ns. The dashed and dotted curves represent, respectively, the coherent addition of 10 and 100 sequentially measured, range compressed IPR's. In (a) the experimental CNR is $\sim 0$ dB, while in (b) the CNR is approximately -20 dB. ....	91
Figure 33: PPN IPR optimization for finite range depth allows increased sidelobes outside of the region and suppresses the sidelobes within the desired range window. ....	94
Figure 34: Block diagram of the genetic algorithm used to optimize pseudo noise sequences. ....	95
Figure 35: The genetic ISL/PSL algorithm path of convergence (a) and corresponding genetically optimized IPR for a 20,000 chip waveform within a range window of 600 ns, or 90 m, around the IPR mainlobe. ....	97
Figure 36: Genetic algorithm convergence as a function of code length. ....	98
Figure 37: Simplified, experimental PPN radar Block diagram. ....	99
Figure 38: Ideal (a) and measured (b) IPRs of a genetically optimized PPN sequence and the randomly selected PPN waveform ISL (dashed line). ....	100
Figure 39 PPN Waveform and genetically optimized PSLR as a function of transmit attenuation. ....	102
Figure 40: The GA-IPR for a single sub-code (a) and the superposition of 20 sub-codes (b). ....	103
Figure 41: Comparison of the composite IPR (circles) and complete code IPR as a function of the number of 1000 chip sub-codes processed. ....	104
Figure 42: Optimization regions for multiple notch GA-IPR (a) and expanded view of the mainlobe and adjacent IPR notches. ....	105
Figure 43: Genetic algorithm ISL/PSL convergence for 20 notch IPR. ....	106
Figure 44: Range IPR for the: PPN (solid line), LFM (dashed line), and unmodulated Gaussian (dashed line) waveforms. ....	109
Figure 45: Range imaging experimental radar block diagram. ....	111
Figure 46: Range imaging collimator and target placement diagram. ....	111
Figure 47: Range image IPR for two range separated point targets. ....	112

Figure 48: Range IPR variation as a function of single waveform CNR.....	113
Figure 49. (a) The real component of the range compressed Macro-Doppler phase history for three targets illuminated with a $T_c=1\text{ns}$ PPN waveform. (b) The fully compressed range-Doppler image correctly identifies each target's range and velocity. ....	115
Figure 50: Range-Doppler experimental ladar block diagram.....	117
Figure 51: Range-Doppler target placement within expanded beam.....	117
Figure 52: Cross section view of Range-Doppler targets with respect to the expanded beam footprint.....	120
Figure 53: Range-Doppler phase history for SAL target (lower) and large amplitude oscillating Doppler target (upper) for a single composite code $N_c=20000$ . ....	121
Figure 54: Cross section of the phase history at the oscillating Doppler target range (a) and expanded view (b) illustrating the attenuation and nulls due to Doppler sensitivity. ....	122
Figure 55: Range-Doppler phase history for SAL target (lower) and large amplitude oscillating Doppler target (upper) with sub-code processing $N_c=1000$ and $N_{codes}=20$ . ....	123
Figure 56: Range slice of the phase history for the oscillating Doppler target (a) and expanded view (b) showing the phase wraps associated with the recovered motion using sub-code processing with $N_c=1000$ and $N_{codes}=20$ . ....	124
Figure 57: Illustration of Doppler Tolerance nulls within translating target phase history (a), and measured output showing Doppler suppression (b). ....	126
Figure 58: Doppler filter bank processing block diagram with $n$ offset frequencies.....	127
Figure 59: Ten element Doppler filter bank output showing phase histories for velocities ranging from $+5.52\text{ cm/s}$ (a) to $-11.25\text{ cm/s}$ (j).....	128
Figure 60: SAL Phase migration for three targets is illustrated by the phase factor (top), quadratic phase (center) and frequency (bottom).....	130
Figure 61(a) A synthetic aperture phase history for the PPN waveform demonstrating the range dependent phase migration for each of three point targets. (b) The DBS fully compressed image demonstrating effective cross-range localization of each of the three targets. ....	132
Figure 62: Cross-range IPRs for the LFM, (solid line), PNN (dashed line) and $1\text{ ns}$ FWHM Gaussian pulse (dotted line) waveforms. The cross-range phase modulation is the same for each waveform, producing nearly identical results in cross-range compression. ....	133

Figure 63: Simulated PPN waveform synthetic aperture image of complex array of point targets, (University of Dayton Logo), demonstrating PPN synthetic aperture image quality. ....	134
Figure 64: SAL experiment target layout within 12 inch collimator. ....	136
Figure 65: IPR for SAL and vibration targets at 0 m and -1 m respectively. The returns at -6 m and -8 m are due to back reflections in the telescope. ....	138
Figure 66: SAL phase history for a SAL target and vibrating target (a). The expanded phase history (b) clearly show the difference between the phase of the two targets. ....	139
Figure 67: Spectrogram of the phase of the SAL target (a) and vibration target (b). ....	140
Figure 68: In-phase and quadrature components of the cross-range matched filter kernel demonstrate quadrature phase offset and beam amplitude profile. ....	141
Figure 69: Central portion of the fully focused SAL image of the SAL and vibration targets. ....	142
Figure 70: Cross-range IPR for the SAL target and Vibe Target. ....	142
Figure 71: Comparison of the cross-range IPR (a) and the range IPR (b). ....	143
Figure 72: Measured (solid) and theoretical (dashed) cross-range IPR. ....	144
Figure 73: Micro-Doppler phase signature. ....	146
Figure 74: The real component of the range compressed micro-Doppler phase history for three point targets illuminated by a $T_c=1$ ns PPN waveform. (b) The micro-Doppler image of the point target array. ....	148
Figure 75: Micro-Doppler Experimental block diagram. ....	150
Figure 76: Micro-Doppler target diagram with 12 inch collimator. ....	150
Figure 77: Phase history of 30 Hz micro-Doppler Target. ....	151
Figure 78: Micro-Doppler phase history (a) and spectra (b). ....	152
Figure 79: Phase of 30 Hz micro-Doppler target (a) and the phase difference for a 5 PPN waveform (i.e., 100 $\mu$ s) coherent processing interval. ....	153
Figure 80: Vibration velocity spectra (a) and an expanded view (b) showing the noise system noise floor. ....	154
Figure 81: Matched filter complex output for a vibrating target as a function of transmit power attenuation. ....	156

Figure 82: Recovered phase as a function of transmit power attenuation. ....	157
Figure 83: Normalized output as a function of transmit power attenuation. ....	158
Figure 84: Two aperture MIMO fiber implementation block diagram. ....	162
Figure 85: Interferometric SAL measurement geometry with two apertures offset in the cross-track (i.e., vertical) direction. ....	165
Figure 86: Interferometric SAL phase variation as a function of platform location, $u$ . ..	166
Figure 87: Interferometric SAL phase (a) and phase difference (b). ....	167
Figure 88: Differential SAL Geometry with two apertures offset in the along-track (i.e., horizontal) direction. ....	170
Figure 89: Along track Differential SAL phase variation with aperture location. ....	171
Figure 90: DSAL phase for a stationary target (solid lines) and a target with translational and vibrational motion components (dashed lines). ....	172
Figure 91: DSAL phase for moving target (solid line) and stationary target (circles). ...	173
Figure 92: MIMO/CDMA Experimental ladar block diagram. ....	174
Figure 93: Measured IPRs for the TDM/CDMA MIMO LADAR. ....	176
Figure 94: Two aperture MIMO wrapped phase for UU, DD, and DU paths. ....	177
Figure 95: Theoretical phase (a) and measured phase (b) for the two aperture MIMO configuration. ....	178
Figure 96: Synthetic aperture fraction relating required baseline to the atmospheric coherence diameter. ....	184
Figure 97: Hufnagel-Valley HV 5/7 Index structure function altitude profiles. ....	187
Figure 98: Calculated coherence diameter isocontours for all platform range and altitude combinations with the target at the origin. ....	188
Figure 99: Aperture fraction iso-contours for the standard HV 5/7 atmosphere (top) and the 5xHV 5/7 atmosphere (bottom). ....	189
Figure 100: Two way atmospheric transmission iso-contours calculated with FASCODE for a target at the origin to a platform at any range altitude combination. ....	191
Figure 101: CNR isocontours for a PPN coherent laser radar transmitting 10W of Average Power. ....	192

## **CHAPTER I**

### **INTRODUCTION**

The performance of a multi-dimensional ladar system measuring the spatial and temporal characteristics of a target is governed by competing requirements. Three dimensional (3-D) spatial imaging is governed in angular resolution by the diffraction limit imposed by the pupil diameter and in range resolution by the bandwidth of the transmitted signal. The temporal characteristics, primarily velocity and vibration, are induced by translation or rotation and small surface motions. The resolution of the velocity and vibration spectra is limited by the observation time of the target where longer observation times provide better resolution. The primary goal of multifunction range-Doppler imaging is to provide simultaneous, high resolution imaging in both spatial and frequency domains, completely describing the target through range imaging, range-Doppler imaging, synthetic aperture imaging and range resolved vibrometry or micro-Doppler imaging. High time-bandwidth product waveforms and agile processing techniques are used to provide this capability and can also be used to detect and mitigate degrading factors such as residual platform motion and atmospheric turbulence.

#### **A. Historical Background**

Since the invention of the laser, laser radars (ladars) were investigated following the extensive development path of radio frequency radar systems. Ladar systems have progressed

from simple rangefinders to ladar systems demonstrating 2-D and 3-D geometric imaging, micro-Doppler imaging or vibrometry, and recently synthetic aperture laser imaging. The greatest maturity resides with direct detection ladars performing ranging or geometric imaging. A variety of coherent systems have been developed including range finders, wind sensors, vibrometers and synthetic aperture imaging systems. Vibrometers have been developed ranging from mature commercial instruments based on continuous wave (CW) transceivers and spectral processing, pulsed architectures based on poly-pulse phase processing, and chirp processing as well as a variety of laboratory research vibrometers exploring new approaches[1,2,3,4]. Moreover, synthetic aperture ladar was first demonstrated in the laboratory in the late 1980's with subsequent laboratory experiments through 2005 [5,6]. These early efforts used variations of radar-heritage pulse formats including linear frequency modulation and short pulses. A Defense Advanced Research Projects Agency/Air Force Research Laboratory (DARPA/AFRL) program demonstrated the first synthetic aperture ladar transceivers in flight in 2006 [7].

Single purpose ladar systems were developed which optimize individual functions based on component, target and measurement constraints. This research describes the use of periodic, pseudo-noise (PPN) waveforms to enable agile multi-function ladar systems capable of simultaneous range, range-Doppler, synthetic aperture and micro-Doppler imaging. The PPN class of waveform allows the conflicting requirements of diverse imaging modes to be satisfied by utilizing a single transmitted waveform combined with flexible, mode specific signal processing.

## **B. Dissertation Overview**

This research investigated ladar architectures, waveforms and processing techniques which simultaneously support range imaging, range-Doppler imaging, synthetic aperture imaging and vibrometry with enhanced performance in each measurement domain. Chapter II presents a summary of the ladar modes and applications. Waveform independent signal models are developed describing the measurement and processing requirements independent of pulse format or implementation constraints. A theoretical foundation is developed for each laser radar mode. A summary of the modes, detection techniques, modulation approaches, and analytic descriptions are presented. Chapter III summarizes the salient elements of a coherent ladar including the transmitter, waveform generation approaches, and detection methods. The electro-optic components and techniques used for modulation and detection are presented with their capabilities as well as their limitations to bound realizable waveform formats. The system requirements are derived with respect to the constraints are presented including performance requirements, waveform generation techniques and limitations, as well as signal acquisition and processing. Noise sources and the laser radar equation are also introduced. Chapter IV summarizes the waveform constraints and figures of merit including both performance requirements such as resolution and sidelobe performance as well as implementation issues such as measurement energy and peak power.

Chapter V develops the expressions describing the application of PPN waveforms in multimode coherent ladar. The waveform and its various taxonomies are introduced. PPN specific discrete signal and matched filter models are developed including descriptions of the Doppler sensitivity and multiple sub-code processing. Application of the PPN waveforms for multiple input, multiple output apertures is also presented. Chapter VI describes the PPN

ladar system which provides the experimental underpinning for this research. The system is used to illustrate salient properties of the PPN ladar including the performance of the waveform at low signal levels, the benefits of diverse sub-codes, and the Doppler sensitivity of the waveform. Mode specific processing is used to selectively optimize phase sensitivity and recovery for each imaging mode. The same basic system is used in all experiments; however, variations in the output coupling and targets are described which support specific measurements. In Chapter VII, the genetic algorithm used to optimize the PPN waveform IPR is described. The algorithm convergence is and waveform performance is presented for both single and multiple aperture applications.

Chapters VIII through XI describe the simulation, experimental validation and important performance characteristics of PPN waveform in range, range-Doppler, synthetic aperture and micro-Doppler imaging, respectively. Chapter XII describes the application of PPN waveforms to multi-aperture interferometric imaging. Multiple sub-code PPN waveforms are used with code division multiple access multiplexing to enable multiple apertures. In addition, an implementation based on an optically delay is described. Applications of the approach to interferometric and differential synthetic aperture ladar are introduced, and the required multi-aperture phase recovery was experimentally demonstrated.

In Chapter XIII, a system analysis is performed based on the waveforms and established requirements and predicted performance curves are presented. The system level modeling was conducted over a range of operational conditions including system configurations, measurement geometries, and atmospheric conditions. Finally, Chapter XIV summarizes the research, presents conclusions, and makes recommendations for future research directions.

## **CHAPTER II**

### **LADAR BACKGROUND**

#### **A. Ladar Applications**

Ladar based remote sensing of objects has broad application throughout the military and civilian sectors. Every object has a finite number of observable features which can be exploited by a remote, electro-optic sensing system. These features are broadly categorized into the following five types: geometry, surface character, plant noise, effluents, and gross motion. Geometric sensing characterizes the shape of the object in one, two or three dimensions including the fully geometrically resolved intensity distributions of the object. Surface character includes roughness, the spectral and directional distribution of scattered energy, and polarization properties. Plant noises include a variety of vibrations and cyclical motions attributed to the operation of the target and can range from signatures associated with piston or turbine engines, transmissions or other moving components. Effluents include exhaust air, gases, and waste heat. The gross motions are movements of the system including system translation, rotation or articulation.

A variety of laser radar modes exploiting these characteristics were developed following the long history of RF radar. Many of the same techniques are utilized but the large decrease in operating ladar wavelength, as shown in Figure 1, enables sensitivities and resolutions not possible at radio frequencies. The decrease in wavelength also introduces

stringent operating requirements. This research investigates operation at 1.5  $\mu\text{m}$  in the short wave infrared (SWIR). Compared to an x-band synthetic aperture ladar (SAR) with a 3 cm wavelength, the SWIR system will have more than 4 orders of magnitude greater phase sensitivity and spatial resolution.

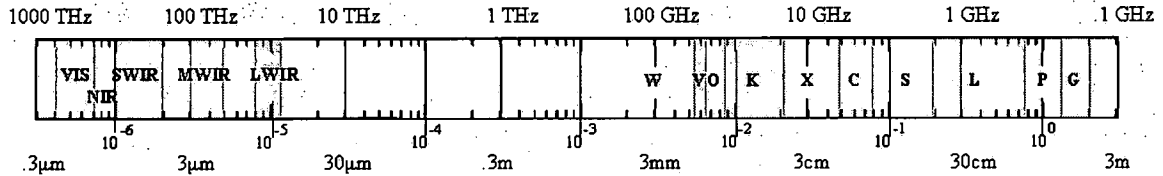


**Figure 1: Electromagnetic spectrum from laser radar to radio frequency radar**

This focus of this research is on methods to provide range, range-Doppler, synthetic aperture, and micro-Doppler imaging using a single a waveform. This includes investigation of flexible waveforms which adapt to provide the required resolutions, minimize required power, and mitigate sources of degradation.

## B. Ladar Diffraction Limited Beamwidth

Just as in radar, the transmitted ladar angular beam width  $\theta_D$  is governed by the physical aperture. For a circular optical aperture the approximate full-width, half-maximum (FWHM) beam width is given as

$$\theta = \frac{\lambda}{D}, \quad (1)$$

where  $\lambda$  is the operating wavelength and  $D$  is the diameter of the aperture [8]. Note that this definition is consistent with RF apertures where the exact beam width again depends on the details of the physical aperture [9]. The cross-range spatial resolution of a real aperture

system is limited in turn by this beam width. Even with ladar's decrease in wavelength from RF systems, the diffraction limit of the aperture is still the factor limiting the cross-range resolution at long ranges, or for small aperture systems, as shown in Figure 1.

### C. Ladar Imaging Modes and Requirements

Figure 2 shows a constellation of three point targets, encompassed by a diffraction limited beam at range  $R$ , which is unresolvable by conventional ladars. The  $n$  targets are assumed to have cross section  $\sigma_n$  and velocity  $v_n(t)$ .

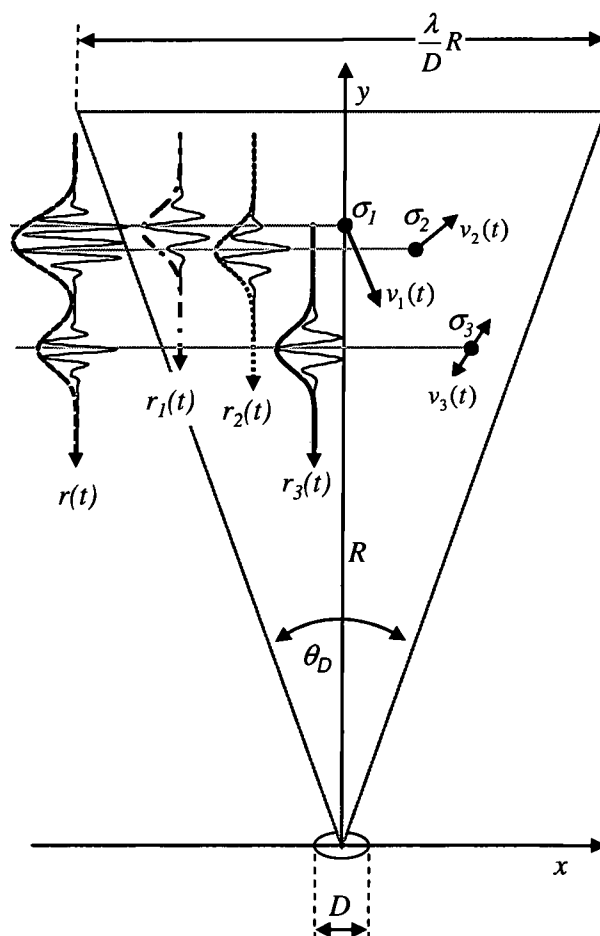


Figure 2: Three point targets encompassed within the beam footprint.

As an example, a typical ladar system with a 15 cm aperture, operating at a wavelength of  $\lambda=1.5 \mu\text{m}$ , produces a 50 cm FWHM spot on the target at a range of 50 km.

The required spatial resolution is strongly dependent on the size and nature of the object to be imaged. The Johnson Criteria for vehicle identification, for example, requires a minimum of 12 pixels across the smallest dimension of the target [10]. As the minimum target dimension for vehicles will likely be less than 3-m, a resolution of only 50 cm will thus be insufficient for effective spatial imaging of a wide variety of objects of interest.

To overcome the real aperture resolution limitation, we focus on four ladar imaging techniques. Three of the techniques do not affect cross-range resolution and include range imaging, range-Doppler imaging, and micro-Doppler imaging. The fourth, synthetic aperture imaging, allows cross-range resolution to surpass the real aperture limit.

Typical images for the target array of Figure 2 are shown in Figure 3. The range-Doppler, synthetic aperture and micro-Doppler images exploit motion induced phase variations to provide the macro velocity, cross-range distribution and surface vibrations of each target. The use of multiple phased apertures provides additional spatial information to resolve height or motion ambiguities of the target.

#### **D. General Signal Model**

A general model of the observable signal is used to analyze each of the ladar imaging modes. Referring to Figure 2, each of the three point targets within the beam is interrogated by a transmitted waveform  $\tilde{w}_0(t)$  denoted in complex notation as

$$\tilde{w}(t) = w_0(t) \exp(j\theta(t)) \exp(j2\pi f_c t), \quad (2)$$

where  $w_0(t)$  is the temporal amplitude profile,  $\theta(t)$  is the phase modulation applied to the waveform and  $f_c$  is the optical carrier frequency. The first two factors of Equation (2) represent the baseband complex envelope  $w(t)$  of the signal, while the last exponential factor represents the carrier.

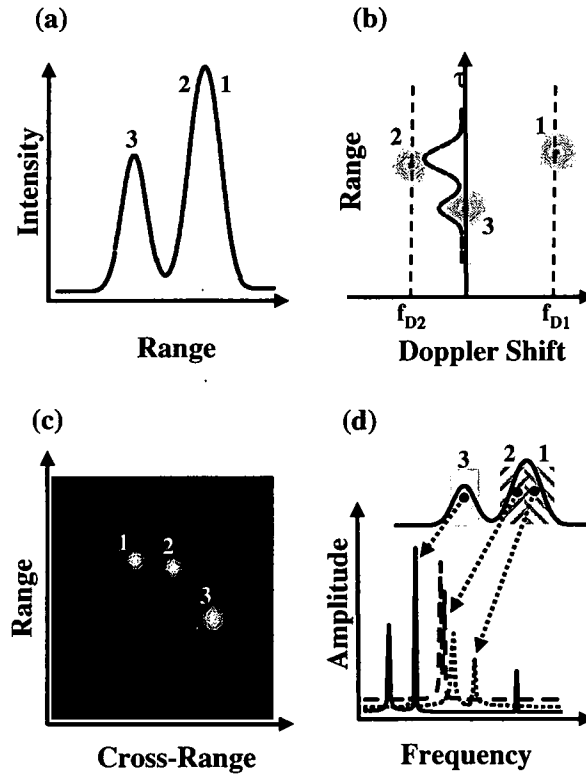


**Figure 3: Range (a), range-Doppler (b), synthetic aperture (c) and micro-Doppler images for the three point target array.**

A waveform with duration  $T_w$  is normalized so that

$$\frac{1}{T_w} \int_0^{T_w} |w(t)|^2 dt = 1, \quad (3)$$

allowing the waveform to be represented as the product of the normalized waveform  $s(t)$  and average transmit power  $P_T$ .

The return phasor  $s_n(t)$  reflected from the  $n^{\text{th}}$  target is a scaled and shifted replica of the transmitted signal, and is encoded with information about the target. When mixed to baseband  $s_n(t)$  is given by

$$\begin{aligned} s_n(t) &= A(x_n, y_n, z_n) \sigma_n w(t - \gamma_n) \exp(j2\pi f_{Dn} \times (t - \gamma_n)) \\ &= A(x_n, y_n, z_n) \sigma_n w(t - \gamma_n) \exp(j\phi_{Dn}(t - \gamma_n)) \end{aligned} \quad (4)$$

where  $\gamma_n = 2R_n/c$  is the propagation delay,  $R_n = (x_n^2 + y_n^2 + z_n^2)^{1/2}$  is the range to the  $n^{\text{th}}$  target,  $c$  is the speed of light,  $w(t - \gamma_n)$  is the baseband complex envelope of the transmitted waveform shifted by the propagation delay, and  $\sigma_n$  and  $A(x_n, y_n, z_n)$  are, respectively, the effective cross section of the  $n^{\text{th}}$  target and the spatial amplitude profile of the transmitted beam at the  $n^{\text{th}}$  target's location. The Doppler frequency shift  $f_{Dn}$ , is due to the relative motion between the ladar and the object being imaged. This is proportional to the  $n^{\text{th}}$  target velocity  $v_n$  projected along the line-of-sight (LOS) to the ladar according to the relationship  $f_{Dn} = 2v_{n-LOS}/\lambda$ , where  $v_{n-LOS}$  is the line of sight velocity [11]. Also note that as shown in Eq. 3, the final exponential factor can be written in terms of the time delayed Doppler phase,  $\phi_{Dn}(t - \gamma_n)$ .

Now let the line-of-sight target velocity be a function of time, defined as

$$v_{n-LOS}(t) = v_{no} - \mu_n \sin(\omega_n t) \quad (5)$$

where  $v_{no}$  is a constant translational velocity and  $\mu_n \sin(\omega_n t)$  is a time varying velocity component attributed to surface vibrations (i.e., micro-motions) of extended targets. Note that we will always assume the line-of-sight vibration velocity  $\mu_n$  to be much smaller than the mean line-of-sight velocity  $v_{no}$ . If the transmitter and receiver are collocated (i.e., monostatic conditions), the corresponding instantaneous Doppler frequency shift components are then found according to the relation

$$f_{Dn} = \frac{2v_{n-LOS}(t)}{\lambda} = \frac{2v_{no}}{\lambda} - \frac{2\mu_n \sin(\omega_n t)}{\lambda}. \quad (6)$$

Since the Doppler frequency shift of Eq. (4) now has a time dependent term, the time dependent Doppler phase  $\phi_D(t)$  is found by integrating over time

$$\begin{aligned} \phi_D(t) &= 2\pi \int \frac{2v_{n-LOS}(t)}{\lambda} dt = 2\frac{2\pi}{\lambda} \int v_{no} - \mu_n \sin(\omega_n t) dt \\ &= 2\frac{2\pi}{\lambda} v_{no} t + 2\frac{2\pi}{\lambda} \frac{\mu_n}{\omega_n} \cos(\omega_n t), \end{aligned} \quad (7)$$

where the first term is the Doppler phase associated with the mean line-of-sight translational velocity component and the second term is the micro-Doppler phase associated with scatterer vibrations. Inserting the Doppler phase terms from Eq. (7) in Eq. (4) and coherently summing the returns from all targets within the beam, the composite return  $s(t)$  can be written as

$$\begin{aligned} s(t) &= \sum_n \left\{ A(x_n, y_n, z_n) \sigma_n w\left(t - \frac{2R_n}{c}\right) \right. \\ &\quad \times \exp\left[j2\pi \frac{2v_{no}}{\lambda} \left(t - \frac{2R_n}{c}\right)\right] \exp\left[j\frac{2\pi}{\lambda} \frac{2\mu_n}{\omega_n} \cos\left(\omega_n \left(t - \frac{2R_n}{c}\right)\right)\right] \left. \right\}. \end{aligned} \quad (8)$$

Note that while we have described target vibrations with the single sinusoid  $\mu_n \sin(\omega_n t)$ , this could be written more generally as  $\mu_n(t)$ , which could in turn be represented as a finite summation of scaled and shifted sinusoids through Fourier decomposition.

Equation (8) contains all of the information to be exploited for each target including the spatial distribution of each target within the beam, the ladar cross section  $\sigma_n$ , the range to target  $R_n$ , as well as the line-of-sight translational and vibration motion components  $v_{no}(t)$  and  $\mu_n$ , respectively. Equation (8) is sufficient to describe the basic signal in each of the four imaging modes described herein, where the envelope of  $s(t)$  contains information about

location of the targets and the phase of  $s(t)$  contains information about both the location and the relative motion of the target. The methods and salient requirements to exploit the returns to provide range imaging, range-Doppler imaging, synthetic aperture imaging and micro-Doppler imaging are discussed in the following sub-sections.

### E. Range Imaging

A range image, or range profile, localizes individual scattering centers within a beam is a function of range, resulting in a range-intensity image. For each target, the return is a copy of the transmitted pulse, delayed by the round trip time and scaled by both the reflectivity of the target and the amplitude profile of the transmitted beam at the target [12]. For multiple, spatially distributed targets as shown in Figure 2, the return is simply the superposition of the individual returns. Each return contains its own delay and scaling. Figure 3(a) illustrates a possible range image for the targets of Figure 2.

Range resolution is the primary metric in range imaging and is inversely proportional to the effective bandwidth of the transmitted signal  $w(t)$  when using matched filter detection. In Figure 2 and Figure 3(a), the bandwidth of the transmitted pulse is assumed to be insufficient to resolve the farthest two targets and so the two individual returns merge into a single large intensity feature. To extract the range profile from the return of Eq. (4), the matched filter  $w^*(-t)$  is simply convolved with the return signal  $s(t)$ . The output of the matched filter is then

$$q(t) = \int_{-\infty}^{\infty} s(\tau) w^*(\tau - t) d\tau = \mathcal{F}^{-1} \left\{ \sum_n S_n(\omega) \cdot W^*(\omega) \right\}, \quad (9)$$

where  $S(\omega)$  and  $W(\omega)$  are the Fourier transforms of the received and transmitted signals, respectively and where  $\mathcal{F}^{-1}\{\}$  indicates the inverse Fourier transform operation.

To illustrate range image matched filtering, assume for now that the targets are stationary with both the translational and micro-velocity components,  $v_{no}$  and  $\mu_n$ , equal to zero for all  $n$ . Substituting the Fourier transform of Eq. (8) into the right hand side of Eq. (9) and then simplifying yields

$$q_R(t) = \mathcal{F}^{-1} \left\{ \sum_n A(x_n, y_n, z_n) \sigma_n \exp \left( -j\omega \frac{2R_n}{c} \right) |W(\omega)|^2 \right\}. \quad (10)$$

After performing the inverse Fourier transform operation, the matched filter output is then

$$q_R(t) = \sum_n A(x_n, y_n, z_n) \sigma_n \mathcal{R}_w \left( t - 2 \frac{R_n}{c} \right). \quad (11)$$

The result is simply a summation of scaled and delayed copies of the autocorrelation  $\mathcal{R}_w$  of the transmitted waveform  $w(t)$ .

The detailed behavior (e.g., width and sidelobes) of the autocorrelation depends on the shape of the pulse spectrum  $W(\omega)$ , but in general the range resolution  $\Delta R$  is inversely proportional to the signal bandwidth according to the relationship

$$\Delta R = \frac{c}{2B}, \quad (12)$$

where  $B$  is the bandwidth of  $w(t)$  [9]. For an un-modulated, transform limited pulse the bandwidth is inversely proportional to the temporal pulse width (*i.e.*,  $B \propto 1/T_w$ ) [13]. Note that in Figure 2 and 3(a), the bandwidth of the transmitted pulse is assumed to be insufficient to resolve the farthest two targets, causing the two individual returns merge into a single large intensity feature.

## F. Range-Doppler Imaging

Range-Doppler imaging assumes that the targets within the beam have a finite average translational line-of-sight velocity component and localizes the individual scattering centers in two dimensions. This results in an intensity image as a function of range and target velocity (or induced Doppler frequency shift). Like range imaging, the intensity is localized as a function of range; however, range-Doppler imaging exploits the phase due to the mean translational velocity expressed in the first exponential factor in Eq. (8).

An example range-Doppler image for the targets of Figure 2 is shown in Figure 3(b). On average, targets 1 and 2, respectively, are assumed to be moving towards and away from the ladar at different rates where positive velocities are defined to be toward the ladar. Both are also assumed to have relatively large mean velocities that are constant on the time scale of a single range-Doppler measurement. Unity beam amplitude and target cross sections are assumed (i.e.,  $A(x_n, y_n, z_n) = \sigma_n = 1$  for all  $n$ ). Target 3 is assumed to be at rest (i.e.,  $v_3 = 0$ ), and all targets are assumed to have no vibrational motion (i.e.,  $\mu_n = 0$ , for all  $n$ ). The Doppler shifts are then proportional to the mean velocity  $v_{no}$  projected along the line-of sight to the ladar. Figure 3(b) shows the range profile along the range axis, and also demonstrates that targets 1 and 2 are now separable due to their positive and negative Doppler frequency shifts, respectively.

As with range imaging, the range-Doppler image is extracted from the return of Eq. (8) via matched filtering. By inserting Eq. (8) into (9), and setting  $\mu_n = 0$  for all  $n$ , the matched filter output  $q_{RD}(t)$  is then given as

$$q_{RD}(t) = \sum_n A(x_n, y_n, z_n) \sigma_n \int_{-\infty}^{\infty} \exp\left(-j2\pi \frac{2v_{no}}{\lambda} \left(\tau - \frac{2R_n}{c}\right)\right) w\left(\tau - \frac{2R_n}{c}\right) w^*(\tau - t) d\tau, \quad (13)$$

where the exponential phase factor is due to the Doppler shift. For the general waveform  $w(t)$ , it is assumed that the Doppler phase is constant over the waveform duration  $T_w$ . The matched filter output then reduces to

$$q_{RD}(t) \approx \sum_n A(x_n, y_n, z_n) \sigma_n \times \exp\left(-j2\pi \frac{2v_{no}}{\lambda} T_w \left\lfloor \frac{t + \frac{T_w}{2} - \frac{2R_n}{c}}{T_w} \right\rfloor\right) \int_{-T_w}^{T_w} w\left(\tau - \frac{2R_n}{c}\right) w^*(\tau - t) d\tau, \quad (14)$$

where last factor of the exponential is the floored division of  $t$  (i.e., remainder is discarded after division). This insures that the constant velocity assumption is valid allowing the phase term to be removed from the integral. The final matched filter output is then

$$q_{RD}(t) = \sum_n A(x_n, y_n, z_n) \sigma_n \exp\left(j2\pi \frac{2v_{no}}{\lambda} T_w \left\lfloor \frac{t + \frac{T_w}{2} - \frac{2R_n}{c}}{T_w} \right\rfloor\right) \mathcal{R}_w\left(t - 2\frac{R_n}{c}\right), \quad (15)$$

which is the summation of scaled and delayed copies of the autocorrelation  $\mathcal{R}_w$ , similar to range imaging, but also contains the Doppler phase rotation for each target. Note that the assumption that the phase is constant over the duration of the waveform is stringent but reasonable since large common Doppler offsets are mitigated by applying Doppler corrections [14]. Moreover, the differential velocities of interest are relatively small due to the finite size of the beam, and may be accommodated for by using Doppler filter banks or processing shorter sections of the waveform as necessary [14].

The range resolution of a range Doppler image remains unchanged and is governed by Eq. (12). The velocity or Doppler resolution  $\Delta v$  is also governed by the bandwidth  $B$  of the waveform spectrum  $W(\omega)$ . However, for fine velocity resolution a narrow bandwidth, or an equivalently long pulse duration  $T_w$  is required as demonstrated in the following relationship

$$\Delta v = \frac{\lambda}{2T_w} \propto \frac{\lambda B}{2}, \quad (16)$$

where a transform limited waveform is assumed [14].

Equations (12) and (16) highlight one of the conflicting requirements in multi-mode imaging. High bandwidth waveforms are required for high range resolution, but long time duration waveforms are required for high Doppler resolution or phase sensitivity. Measuring both requires high time-bandwidth product waveforms; therefore, a single transform limited pulse, with a time bandwidth product of unity, cannot be employed. Modulated or repetitive waveforms which have time bandwidth products much greater than unity are required for simultaneous imaging in both domains. For example, a 100 microsecond pulse with a 1 GHz linear frequency modulation results in a time-bandwidth product  $T_w B = 100,000$  which provides simultaneous range resolution  $\Delta R$  of 15 cm and velocity resolution  $\Delta v$  of 7.5 mm per second, assuming a wavelength of 1.5  $\mu\text{m}$ .

### **G. Synthetic Aperture Ladar Imaging**

Range-Doppler imaging clearly shows that additional information about an array of targets can be obtained by exploiting the target motion induced phase within the return. Synthetic aperture radar (SAR), initially developed in the 1950's and 1960's, again exploits

the relative phase differences between targets to overcome the resolution limitations imposed by the diffraction limit of finite aperture sizes. Unlike range-Doppler imaging, SAR assumes the targets are fixed. The motion of the aperture is used to carefully induce and control the geometry dependent phase which is used to resolve the spatially distributed targets. The resolution of a real aperture imaging system was given by Equation (1)

$$\theta_D = k \frac{\lambda}{D} \quad (17)$$

where  $\lambda$  is the operating wavelength,  $D$  is the aperture of the system, and the factor  $k$  is determined by the details of the aperture. From this equation it is clear that there are two methods to increase the resolution of a diffraction limited imaging system. One is to reduce the wavelength of the system and the other is to increase the effective aperture size. As shown in Figure 1, imaging at optical wavelengths provides a 3 to 4 order of magnitude decrease in wavelength over x-band SAR. This greatly reduces the length of the aperture required to produce comparable resolution at optical wavelengths and also moves the operation into a more favorable scattering regime. Most man made surfaces are rough on the order of optical wavelengths with diffuse scattering generally associated with the enhanced interpretability in optical images when compared to RF images.

The second method is to increase the size of the optical aperture. However, in the majority of cases, even at optical wavelengths, increasing the physical aperture size to achieve high resolution at extended range is not practical. For example, an aperture of at least 1.5 meters would be required to produce a system operational at a wavelength of  $1.5 \mu\text{m}$  with 5-cm FWHM resolution at a range of 50 km. The larger size, weight and cost of the

optical and pointing systems for such a ladar are prohibitive for most applications. In addition, atmospheric turbulence may also limit the maximum useful diameter.

Synthetic aperture ladar (SAL) imaging is a geometric imaging approach which localizes targets as a function of range and cross-range. Figure 3(c) illustrates a possible SAL image for the targets of Figure 2. In its simpler forms, targets are localized in range utilizing high bandwidth waveforms for good range resolution. Cross-range localization is then achieved by exploiting phase variation in the signal due to a controlled relative motion between the aperture phase center and the targets.

To form a SAL image, multiple target observations are required. In particular, a sequence of temporal waveforms (i.e., fast-time records) is collected as a function of the aperture location  $u$  along the slow-time axis, as shown in Figure 4. (Note that in this figure we assume the slow-time platform motion to be along the x-axis.) The fast-time records are assembled into a two dimensional phase history. Each fast-time record encodes the range to each target from the slow-time measurement location. The range, or equivalently the return phase, to each target then varies as function of slow-time aperture location.

While a wide variety of collection geometries and image formation algorithms are in the literature, the primary goal here is to illustrate the nature of the synthetic aperture phase migration, its relative magnitude to the other imaging modes, and its implications for a ladar system. For simplicity then we will confine our SAL discussions here to the strip map geometry and Doppler beam sharpening (DBS) image formation algorithms [9]. Doppler beam sharpening is a commonly used SA algorithm whose cross-range processing is simplified by constraining the length of the synthetic aperture baseline. Never the less, the full range-Doppler algorithm will be used in the experimental demonstrations.

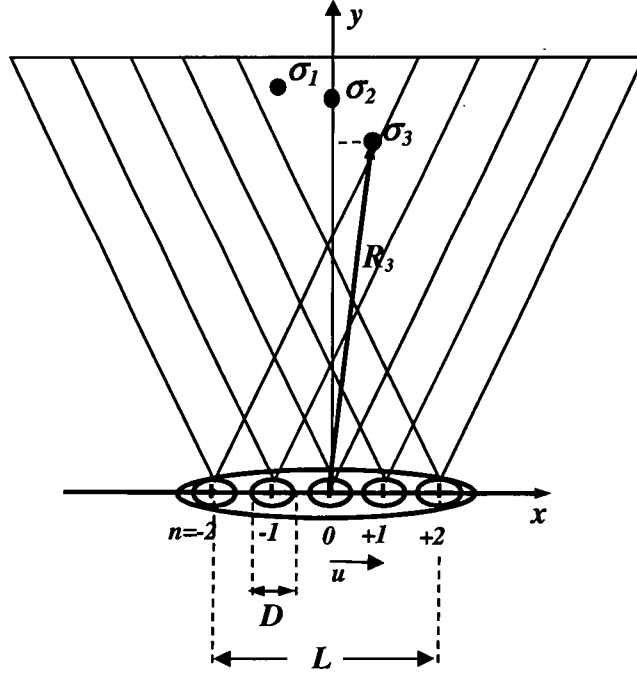


**Figure 4: Stripmap SAL imaging geometry for three point target array.**

As shown in Figure 4, for the stripmap SAL case the aperture moves in a straight line perpendicular to the targets so that the range to each target point varies approximately quadratically across the slow-time aperture samples. If at time  $t$  a waveform  $w(t)$  is transmitted to the  $n^{\text{th}}$  target from location  $u$ , the range to the target  $R_n(t, u)$  is then given by

$$R_n(t, u) \approx \left[ y_n + \frac{u^2}{2y_n} - \frac{ux_n}{y_n} + \frac{x_n^2}{2y_n} \right], \quad (18)$$

where  $u$  is an implicit function of time and describes the aperture location on the x-axis and  $x_n$  and  $y_n$  are the cross-range and range coordinates of the  $n^{\text{th}}$  target, respectively [9]. Notice that the range is minimum at the closest point of approach for each target. Assuming stationary targets (i.e.,  $v_{no} = \mu_{no} = 0$ , for all  $n$ ), inserting Eq. (18) into the return  $s(t)$  of Eq. (8) then produces a function of two variables. In particular, the two dimensional return  $s(t, u)$ , or phase history, for multiple targets is

$$s(t, u) = \sum_n A(x_n, y_n, z_n) \sigma_n w\left(t - \frac{2R_n(u)}{c}\right) \quad (19)$$

where the parabolic phase due to the aperture location is embedded within the propagation delay.

The range-compressed image is then found by using a one dimensional fast-time matched filter  $w^*(-t)$ . Inserting Equation (18) into Equation (8), the matched filter output  $q_{SA}(t, u)$ , written in the Fourier domain, is then

$$q_{SA}(t, u) = \mathcal{F}^{-1} \left\{ \sum_n A(x_n, y_n, z_n) \sigma_n \exp\left(-j\omega \frac{2R_n(t, u)}{c}\right) |W(\omega)|^2 \right\}, \quad (20)$$

where the exponential term represents a phase shift dependent upon the aperture location  $u$ .

After performing the inverse Fourier transform operation, the matched filter output is

$$q_{SA}(t, u) = \sum_n A(x_n, y_n, z_n) \sigma_n \mathcal{R}_w\left(t - 2\frac{R_n(u)}{c}\right). \quad (21)$$

Again, the result is the summation of scaled and delayed copies of the autocorrelation  $\mathcal{R}_w$  of the transmitted waveform  $w(t)$ .

In general, to form a SAL image, a two dimensional matched filter is constructed based on this phase variation for a target at the center of the field. For Doppler beam sharpening, a relatively short synthetic aperture limits the phase variation resulting in an approximately sinusoidal variation with positive and negative frequencies increasing with increasing distance from the range center  $R_c$ . The two dimensional matched filter output is then the Fourier transform of the range compressed image of Equation (19) with respect to the slow time dimension [9].

The quadratic phase associated with the range  $R(u)$  of Equation (18) corresponds to a linear frequency modulation across the slow-time measurement. The spatial frequency modulation is obtained by calculating the instantaneous frequency as the derivative of the phase

$$\begin{aligned} K_u = \frac{d\phi(u)}{du} &= \frac{d}{du} \left[ \frac{4\pi}{\lambda} \left[ y_n + \frac{u^2}{2y_n} - \frac{ux_n}{y_n} + \frac{x_n^2}{2y_n} \right] \right] \\ &= \frac{4\pi}{\lambda} \left[ \frac{2u}{2y_n} - \frac{x_n}{y_n} \right] = \frac{4\pi}{\lambda y_n} [u - y_n] \end{aligned} \quad (22)$$

where the term outside the brackets in the final equation is the frequency slope as a function of the relative range between the aperture and the scatterer location  $x_n$ . The spatial frequency bandwidth  $\beta_u$  swept out by the range variation is

$$\beta_u = \frac{2L_{SA}}{\lambda y_n} \frac{\text{cycles}}{m}, \quad (23)$$

where  $u=L_{SA}$  is the length of the synthetic aperture. Analogous to the time bandwidth product, the bandwidth-space product of the frequency modulation is

$$\beta_u u = \frac{2L_{SA}^2}{\lambda y_n} \frac{\text{cycles}}{m}. \quad (24)$$

The space-bandwidth product is a measure of the achievable resolution.

Equation (24) indicates that the synthetic aperture must be increased to maintain a constant space bandwidth product as the range to the target point  $y_n$  grows.

## H. Micro-Doppler Imaging

Remote vibrometry provides insight to the nature and state of the plants which power, cool, control or move a system. A variety of rich spectra are associated with various plants. These

can be interpreted by a human operator, or analyzed with autonomous recognition algorithms, depending on the application. Micro-Doppler imaging assumes that the targets within the beam have small surface oscillatory motions with a component along the ladar line-of-sight. Micro-Doppler images then localize the individual scattering centers in two dimensions resulting in images of intensity or vibration amplitude, as a function of range and surface oscillation frequency. As in the previous imaging modes, the intensity due to the target distribution is localized as a function of range. Similar to range-Doppler imaging, micro-Doppler imaging also exploits an additional phase term due to the motion of the target; however, here the motions are the minute oscillatory motions due to surface vibrations.

The micro-Doppler return signal  $s(t)$  is modeled with Eq. (8) where the translational velocity  $v_{no}$  is set zero for all  $n$ . Notice that the remaining exponential factor describes only the micro-Doppler phase. Using Eq. (9), the micro-Doppler matched filter output  $q_{\mu D}(t)$  using is then

$$q_{\mu D}(t) = \sum_n A(x_n, y_n, z_n) \sigma_n \int_{-\infty}^{\infty} \exp \left[ j \frac{2\pi}{\lambda} \frac{2\mu_n}{\omega_n} \cos \left( \omega_n \left( \tau - \frac{2R_n}{c} \right) \right) \right] w \left( \tau - \frac{2R_n}{c} \right) w^*(\tau - t) d\tau. \quad (25)$$

The oscillation frequencies for mechanical vibration are typically quite low and fall within the acoustic region, ranging from a few Hertz to a few kilohertz. As a result, in many applications the micro-Doppler phase variation over the waveform duration are approximately constant. The phase factor of Eq. (25) can therefore be written using a stepwise approximation with respect to the waveform period, thereby insuring it is constant over the region of integration.

Similar to Eq.(14), the phase term can then removed from the integral of Eq. (25) yielding

$$q_{\mu D}(t) \approx \sum_n A(x_n, y_n, z_n) \sigma_n \times \exp \left[ j \frac{2\pi}{\lambda} \frac{2\mu_n}{\omega_n} \cos \left( \omega_n T_w \left[ \frac{t + \frac{T_w}{2} - \frac{2R_n}{c}}{T_w} \right] \right) \right] \times \int_{-T_{wc}}^{T_w} w \left( \tau - \frac{2R_n}{c} \right) w^* (\tau - t) d\tau. \quad (26)$$

As in previous discussions, the integral in Eq. (26) is the autocorrelation of the original signal  $w(t)$ , shifted by the propagation delay. The matched filter output can then be written as

$$q_{\mu D}(t) = \sum_n A(x_n, y_n, z_n) \sigma_n \times \exp \left[ j \frac{2\pi}{\lambda} \frac{2\mu_n}{\omega_n} \cos \left( \omega_n T_w \left[ \frac{t + \frac{T_w}{2} - \frac{2R_n}{c}}{T_w} \right] \right) \right] \mathcal{R}_w \left( t - 2 \frac{R_n}{c} \right), \quad (27)$$

which is the summation of the autocorrelations for all targets, each scaled by the corresponding cross section, delayed by the range propagation delay, and rotated by the micro-Doppler phase of the  $n^{th}$  target.

Figure 3(d) illustrates a possible micro-Doppler image for the targets of Figure 2 where the return from each target is localized in range as indicated by the range profile. Each range has an associated vibration spectra describing the amplitude, frequency and phase of each of target's surface oscillations. We note that in order to detect these relatively slow phase variations, long temporal records must be acquired, after which temporally resolved Fourier analysis can be used to generate the range-resolved vibration spectra [15].

## I. Waveform Requirement Summary

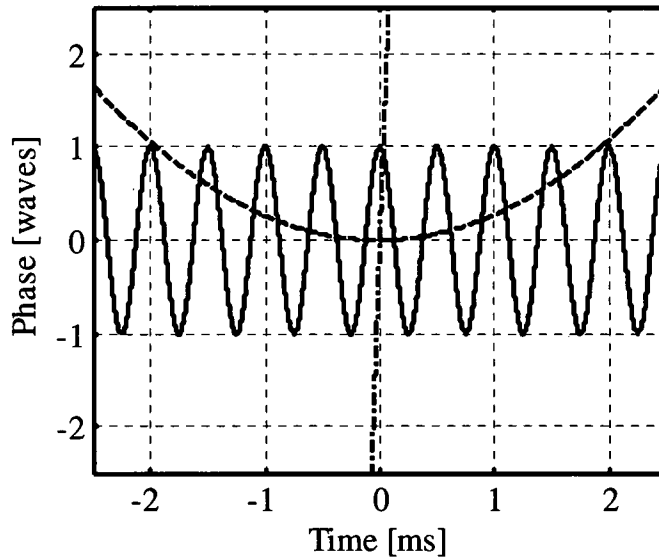
The matched filter response models for range, range-Doppler, synthetic aperture and micro-Doppler imaging demonstrates both common and conflicting requirements. All modes localize target distributions as a function of range, therefore requiring short pulses or high bandwidth. The phase requirements vary significantly from no requirement for range imaging, to the high phase tolerance, or insensitivity, to accommodate the relatively large velocities in range-Doppler imaging, to the relatively high phase sensitivity required for synthetic aperture and micro-Doppler imaging.

Figure 5 illustrates the phase variations for range-Doppler (dash-dot line), synthetic aperture (dashed line) and micro-Doppler (solid line) imaging, all based on a operating wavelength of  $1.5 \mu\text{m}$ , a single on axis target at a range  $R_n$  of 50 km, a waveform period  $T_w$  of  $10 \mu\text{s}$  and 2000 consecutively transmitted waveforms, at a pulse repetition frequency of 400 kHz.. As the range center of interest was assumed to be 50 km for all imaging modes, the phase axis in Figure 5 was re-centered to zero waves for clarity.

The range-Doppler phase history was calculated using the phase factor of Eq. (14) and assumed a stationary ladar and a line of sight target velocity  $v_{no}$  of 5 cm/s. Notice the expected linear phase variation and that the relatively steep slope of this macro-Doppler phase indicates that it must be sampled at a high rate to minimize wrapping. The synthetic aperture phase was calculated by dividing the synthetic aperture range  $R_n(t,u)$ , given in Eq. (20), by the wavelength  $\lambda$ . For the SAL case, the platform velocity is assumed to be 200 m/s with the closest point of approach being at the center of the measurement. The 2000 transmitted waveforms correspond to a SAL baseline of 1 m, but here the SAL phase is plotted as a function of the waveform sample time (slow-time) in conventional SAL

discussions) for comparison with the range-Doppler and micro-Doppler phase histories. Finally, the sinusoidal micro-Doppler phase history was similarly calculated using the phase factor of Eq. (26) and again assumes a stationary platform. In this case, the vibration frequency  $\omega_h$  and maximum displacement  $\mu_r/\omega_h\lambda$  were assumed to be  $4000\pi$  rad/s and one wave, respectively.

The synthetic aperture and micro-Doppler phase variations have significantly different shapes, but the maximum rates of phase change are comparable, at least in comparison to the range-Doppler case. In both cases, the faithful reproduction of the phase history shape is extremely important to the quality of the resulting image. Although the gross translation induced Doppler phase variation can be steeper even for relatively low velocities, it can often be mitigated by assuming it to have a fixed slope over short measurement times.



**Figure 5: Summary of phase histories for range-Doppler (dash-dot), synthetic aperture (dashed), and micro-Doppler (solid) ladar imaging modes.**

The detection of targets with large velocity induced Doppler phase variations will require the use of Doppler tolerant waveforms or Doppler tuned processing. Simultaneous multimode imaging therefore requires high time-bandwidth product waveforms which can selectively provide high bandwidths for fine range resolution, Doppler tolerance for range-Doppler imaging and efficient detection, and the fine phase measurements necessary for synthetic aperture and micro-Doppler imaging. The multi-function ladar problem is then to select waveforms (i.e., amplitude, frequency and/or phase modulations) which provide the best estimates of the target characteristics, maximize the tolerance of the system to degradations, and minimize the complexity of the optical system and signal processing.

Ladar based remote sensing exploits observable target characteristics including geometry, surface, plant noise, effluents, and translational/rotational motion. Signal models describing these observables were developed. Signal phase was shown to be of prime importance to most imaging modes and will be investigated further in subsequent chapters.

### CHAPTER III

## COHERENT LADAR TECHNIQUES

Laser radar is an extremely broad topical area with virtually unlimited variations in purpose, approach, technology, and implementation. This chapter presents selected ladar techniques which are salient to the theoretical development, experimental implementation and system analysis.

#### A. Elements of a Monostatic, Coherent Ladar

Although many variations are possible, Figure 6 shows a block diagram of a typical monostatic, coherent ladar system [16,17].

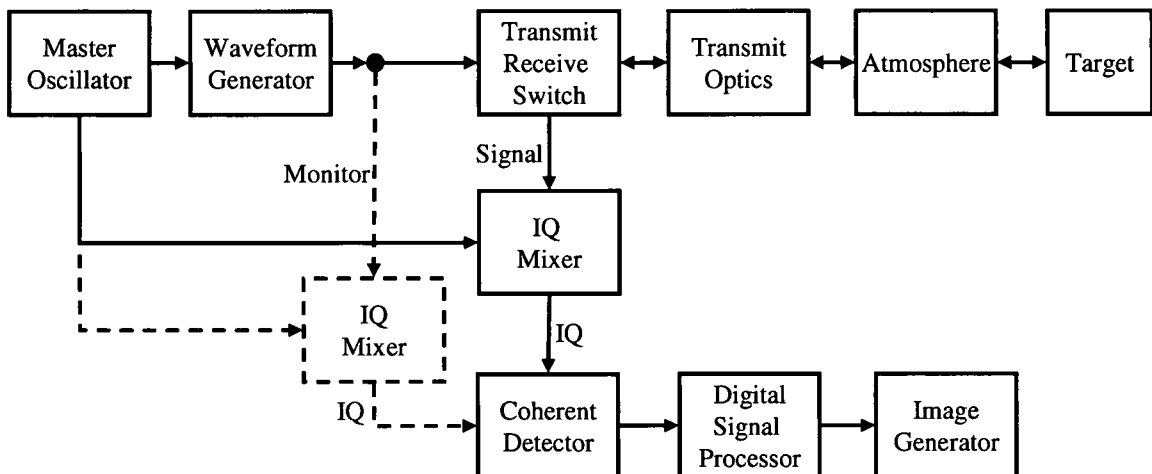


Figure 6: Block diagram of a typical monostatic, coherent ladar system.

The master oscillator (MO) is the system reference clock which provides a phase reference for the system with accuracy to a fraction of transmit wavelength. The waveform generator modulates the amplitude, phase, and/or frequency of the master oscillator to provide the desired measurement waveform. The waveform generator may also include amplification stages to increase the output power of the waveform to satisfy performance requirements. The output signal waveform then passes through the transmit/receive switch (T/R). The transmit/receive switch is a bidirectional device which allows the outgoing transmit waveform to pass through to the primary optics, and then out through the atmospheric channel to the target. After reflecting off the target, a reflected, or return copy, of the waveform passes back through the atmosphere and the primary optics. However on return, the transmit/receive switch directs the return energy into the receiver train. The IQ mixer coherently combines the return with both in-phase and quadrature shifted fractions of the MO to provide in-phase and quadrature return signals. In the Coherent Detector, the returns are coherently detected and digitized. The Monitor is a small fraction of the transmit waveform which is picked off before transmit to the target. It provides a record of the waveform modulation and system noise without channel or target signature contributions. The digital signal processor combines the signal and monitor complex returns to provide a corrected phase history. Finally, the image processor utilizes the phase history data to generate images in each of the desired modes. This basic system architecture with slight variations has been used in a variety of ladar imaging applications from range imaging, Doppler-wind sensing to synthetic aperture imaging.

## B. Master Oscillator

The master oscillator (MO) serves as the precision spatio-temporal reference for the system. Ideally, the MO would be an infinitely coherent, constant amplitude laser source; however, physical issues limit its frequency, phase and amplitude stability [18,19]. The allowable noise levels within the MO depends on the desired measurement, the required measurement quality (sensitivity, precision, accuracy, resolution, etc), and the distance between the ladar and the target. Since stable lasers are required in fields as diverse as gravity wave sensors, ring-laser gyros, and laser spectroscopy, significant advancements in laser stabilization have been made. A variety of stable sources have been developed which employed as a master oscillator form the basis for seeding a cavity or amplifier [20,21,22].

## C. Waveform Generation

In this research, only binary phase modulation is required. This reduces hardware complexity and increases the reliability while enabling multi-mode operation. The electro-optic modulator utilizes a crystal (lithium niobate,  $\text{LiNbO}_3$ ). The index of refraction within the crystal is controlled by the strength of an applied electric field and is linearly related to the field where the Pockel's effect dominates. An increase in voltage leads to an increased index of refraction causing the light to travel slower through the crystal. This leads to a phase change at the output of the crystal proportional to the index and the path length. For a transverse electrode electro optic modulator (EOM), the phase change is given as

$$\Delta\phi = \eta \frac{\pi}{\lambda} n^3 r \frac{V}{d} L, \quad (28)$$

where  $\eta$  is a modulator efficiency factor,  $n$  and  $r$  are the index of refraction and the electro-optic coefficient of the crystal,  $V$  is the applied voltage,  $d$  is the separation of the electrodes, and  $L$  is the length of the crystal [23]. For a binary phase code, only 0 V and  $V_\pi$  are used to produce 0 phase and  $\pi$  phase states, respectively.

#### D. Polarization Sensitive Transmit/Receive Switch

As discussed earlier, Monostatic ladar systems provide several advantages including reduced size through use of a single aperture, ease and maintenance of alignment, common focusing, and common path phase perturbations. To realize these advantages, a transmit/receive (T/R) switch must be implemented that directs energy from the transmitter to the output optics, and then directs the return energy reflected from the target into the receive train. A variety of T/R methods have been used including spatial methods and circulators based on faraday rotators. Here, a free space, polarization based switch as shown in Figure 7 is used.

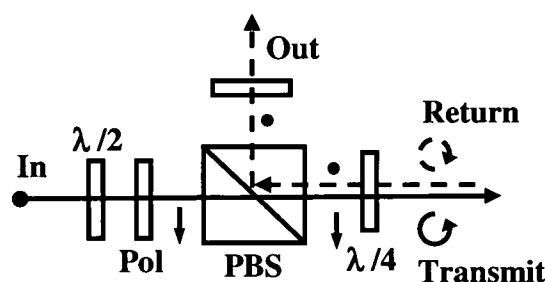


**Figure 7: Polarization sensitive transmit/receive switch diagram**

This three port switch takes advantage of the fact that the transmitted energy is linearly polarized to provide the desired directivity and isolation between the inputs and outputs. The approach is common and fiber based versions are available; however, their power handling is

relatively low. More importantly, the isolation achieved between the input and receive ports is relatively low ranging from -40 dB to -55 dB. Just the range loss for a resolved target (i.e.,  $1/R^2$ ) at 50 km is nearly 94 dB indicating significantly better isolation is required. The Jones calculus for the polarization based T/R switch is shown in Figure 7 can be written

$$\begin{aligned}
 OUT &= PBS_V \cdot QWP \cdot TGT \cdot QWP \cdot PBS_H \cdot POL_H \cdot HWP \cdot IN \\
 &= \begin{pmatrix} 1 & 0 \\ 0 & 0 \end{pmatrix} \frac{1}{\sqrt{2}} \begin{pmatrix} 1 & e^{-i\pi/2} \\ e^{i\pi/2} & 1 \end{pmatrix} \\
 &\quad TGT \frac{1}{\sqrt{2}} \begin{pmatrix} 1 & e^{-i\pi/2} \\ e^{i\pi/2} & 1 \end{pmatrix} \begin{pmatrix} 0 & 0 \\ 0 & 1 \end{pmatrix} \begin{pmatrix} 0 & 0 \\ 0 & 1 \end{pmatrix} \frac{1}{\sqrt{2}} \begin{pmatrix} -1 & 1 \\ 1 & 1 \end{pmatrix} \frac{1}{\sqrt{2}} \begin{pmatrix} 1 \\ 1 \end{pmatrix} \quad (29) \\
 &= \begin{pmatrix} 0 \\ 1 \end{pmatrix}
 \end{aligned}$$

where  $IN$  is the input,  $HWP$  is a half wave plate,  $POL$  is a linear polarizer,  $PBS$  is the polarizing beam splitter,  $QWP$  is quarter wave plate and  $TGT$  is the target [23]. The input polarization is assumed to be linear, but oriented at 45 degrees for this example. The half wave plate is rotated to produce linear, horizontal polarization at the input to the polarizer  $POL_H$ . In practice, the half wave plate is used to optimize coupling and would generally make smaller rotations. The polarizer is used to insure that any residual vertical components are removed. The polarizing beam splitter is the heart of the switch, and the horizontally polarized light from the input enters and is transmitted through. The light passes through the quarter wave plate and produces a right circularly polarized beam which propagates to the target. Upon reflection from the target, the propagation direction is reversed, and the return light has left circular polarization. The return light passes through the quarter wave plate again and the left circular polarization is changed to vertical polarization. The light re-enters the polarizing beam splitter, but now the vertically polarized return is reflected to the output port. The free space T/R switch fabricated for this research used this configuration had

excellent performance with a measured insertion loss (i.e., signal lost at device input) of 1.2 dB and input to output port isolation greater than 70 dB.

### **E. Quadrature Detection**

Quadrature detection has been applied across a wide range of disciplines including radar, sonar, magnetic resonance imaging, general detection and ladar [24, 25, 26]. In phase and Quadrature (IQ) detection in ladar is important for many reasons. Two of the most important are avoiding the signal fades associated with interferometric detection and discerning the direction of the phase rotation associated with Doppler, SAL and micro-Doppler signatures. In addition, IQ detection effectively doubles the sampling rate providing either enhanced sampling or conversely lowering the system's overall sample rate requirement.

#### ***1) Free Space IQ Detection***

As shown in Figure 8, it is common practice to use two detector channels separated by 90 degrees to optically generate the IQ signals within the laboratory. In this implementation, polarization independent, 50/50 beam splitters divide both the master oscillator *MO* and the signal *S*. The copies of the MO and signal fields are combined with polarization independent beam splitters, but the path length of the master oscillator in the quadrature (Q) channel is physically adjusted to provide a  $\pi/2$  delay with respect to the in-phase path length.

The electric field  $E_I$  at the in-phase output *I* is the combination of the signal and master oscillator fields and is written as

$$E_I = \sqrt{\frac{P_S}{4}} \text{Re}\{\exp(j\omega_s t + \theta)\} + \sqrt{\frac{P_{MO}}{4}} \text{Re}\{\exp(j\omega_M t)\}. \quad (30)$$

where  $P_S$  and  $P_{MO}$  are the signal and master oscillator power, respectively, and  $\omega_s$  and  $\omega_{MO}$  are their frequencies. After mixing on a square law detector, the in-phase current is written

$$i_I = \frac{1}{4} [P_S + P_{MO} + 2\sqrt{P_S P_{MO}} \cos((\omega_s - \omega_M)t + \theta)]. \quad (31)$$

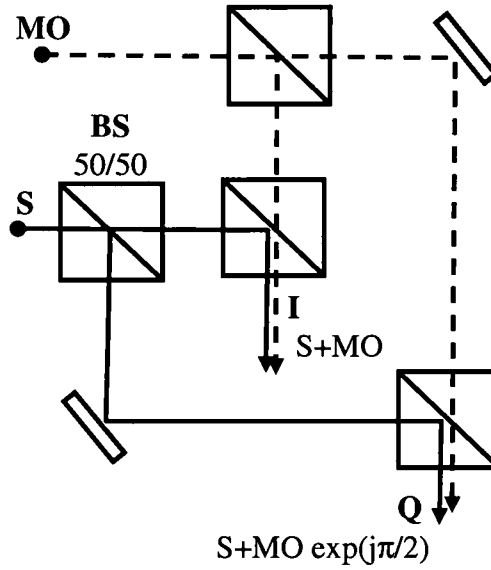


**Figure 8: Laboratory IQ Detection Diagram.**

Similarly, the electric field  $E_Q$  at the out-of-phase, or quadrature, output is

$$E_Q = \sqrt{\frac{P_S}{4}} \text{Re}\{\exp(j\omega_s t + \theta)\} + \sqrt{\frac{P_{MO}}{4}} \text{Re}\{\exp(j\omega_M t) \exp(j\pi/2)\} \quad (32)$$

where the  $MO$  leg has been delayed by the exponential phase factor [23]. After detection, the current at the quadrature output  $i_Q$  is

$$i_Q = \frac{1}{4} [P_S + P_{MO} + 2\sqrt{P_S P_{MO}} \sin((\omega_s - \omega_M)t + \theta)]. \quad (33)$$

where sine function is due to the  $\pi/2$  phase shift in the master oscillator leg.

The amplitude and phase of the signal are both utilized in ladar imaging. The magnitude  $M$  of the signal is the root mean square of the quadrature signal components and is written

$$M = \sqrt{i_I^2 + i_Q^2}. \quad (34)$$

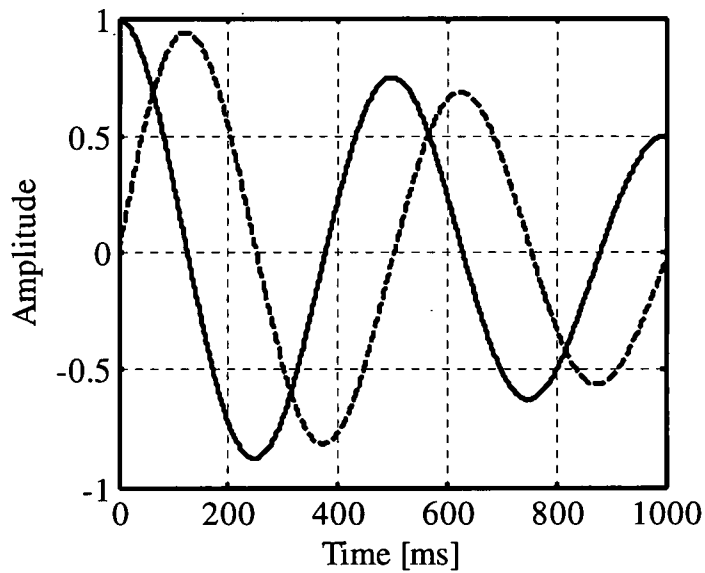
The phase between the master oscillator MO and signal leg is found using the ratio of the quadrature components and is written

$$\theta = \tan^{-1} \left( \frac{i_Q}{i_I} \right). \quad (35)$$

As will be discussed later, the in-phase and quadrature signals will generally be used to form a complex phase history relating in which the magnitude and phase to range (i.e., fast-time) and pulse number (i.e., slow-time). The phase history is similar for all modes, but the information within it are exploited differently in each of the imaging modes [27].

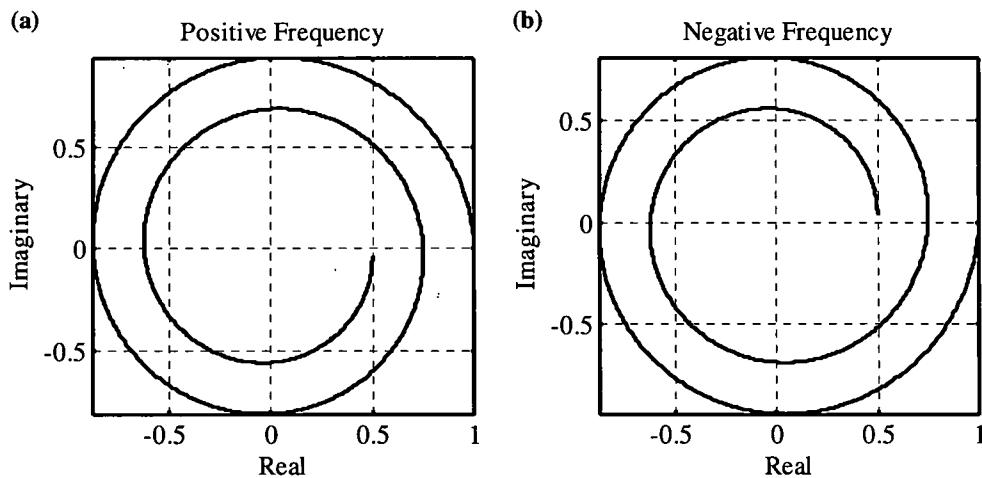
In practice, the alignment, splitting ratios, and especially the required delay are hard to establish and maintain. To illustrate the relationships between the IQ signals and the effects of non-ideal configurations, consider a tapered sinusoidal signal  $f(t) = (1-0.4t) \exp(j\alpha t)$  as shown in Figure 9. If only the real or imaginary component is measured in isolation, it is impossible to discern if the frequency associated with the oscillation is positive or negative. By considering both quadrature signals together, the sense of the signal can be detected.

This is more clearly illustrated by examining the signal in the complex plane as shown in Figure 10. Here the direction of rotation is clearly evident with the positive and negative frequency signals demonstrating a counter clockwise and clockwise rotation, respectively.



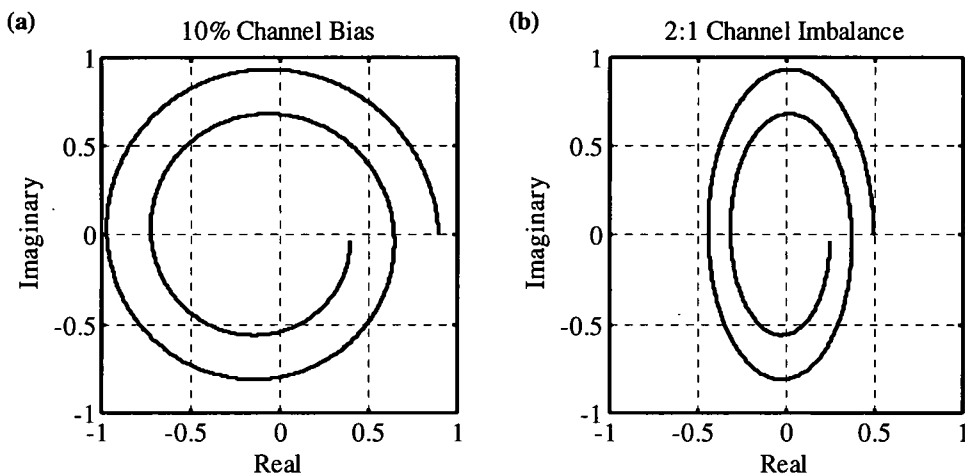
**Figure 9: Tapered Sinusoidal signal: real component (solid line) and imaginary component (dashed line).**

Figure 10 shows that IQ detection measures the signal amplitude as the signal radius from the origin, its frequency or phase variation in the length of the arc, and the sign of the frequency phase through the direction of rotation.



**Figure 10: Signals in the complex plane of tapered sinusoid for positive frequency (a) and negative frequency (b).**

If, as indicated above, the system is imperfect, several degradations may be manifest due to bias offsets on the channels, amplitude imbalances between the channels, and phase rotations. Channel bias (i.e., unequal DC offset) and imbalance (i.e., unequal channel gains) are both common in real systems, and can be mitigated with alignment and calibration. Channel bias shifts the center of the IQ circle in the complex plane as shown in Figure 11(a). This causes incorrect estimates of both amplitude and phase of the detected signal. Figure 11(b) shows the elliptical pattern in the complex plane resulting from a 2:1 channel imbalance.



**Figure 11: IQ signals due to a 10% channel bias (a) and a 2:1 channel imbalance (b).**

The required phase relationships are the most difficult to control and quickly produce significant errors within the signals. Variations in the path length on the order of a fraction of wavelength are sufficient to produce detectable degradations. Figure 12(a) shows an overall phase rotation associated with a common phase change to both legs such as master oscillator drift. The impact of this common rotation is small as long as the change is small within a measurement time. Figure 12(b) shows the impact of a  $\pi/6$  variation on the relative

delay between the in-phase and quadrature arms. This is the most severe impact including both a rotation and flattening of the signal in the complex plane. This results in a temporal amplitude estimate variation as well as erroneous phase estimates.

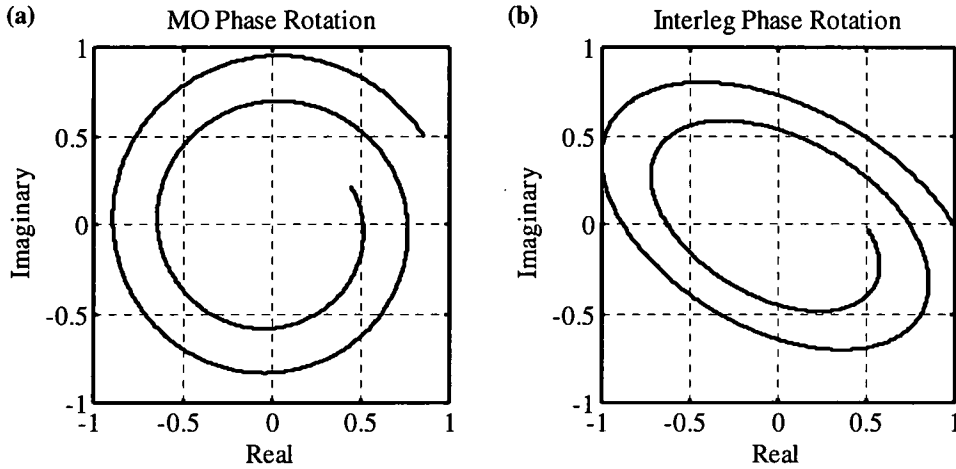


**Figure 12: IQ signal with common phase rotation on both legs (a) and inter-leg rotation (b).**

## **2) Common Path Interferometer for IQ Detection**

In order to avoid the stability and alignment issues associated with the free space IQ detection, the polarization based, common path interferometer (CPI) architecture shown in Figure 13 was adopted [25, 28, 29, 30]. This architecture minimizes the sensitivity to path length changes since both the MO and signal legs are generally common path, the overall path lengths are reduced, and the optical delay is generated by a fixed optical element. The CPI has four paths which are combined to create the in-phase and quadrature signals. The first two paths are from the signal to the in-phase and quadrature outputs.

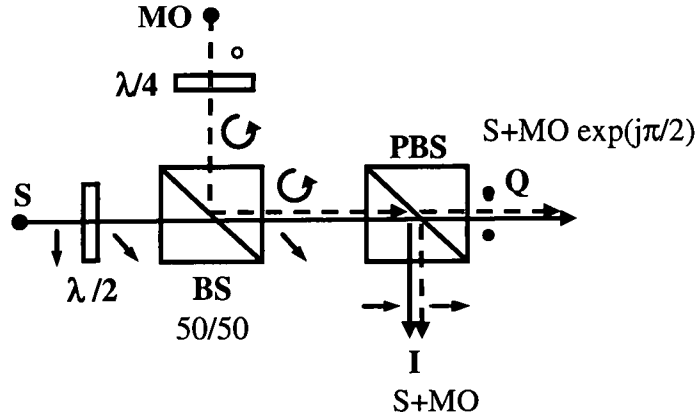


**Figure 13: IQ Demodulator based on polarization sensitive common-path interferometer has better stability and alignment properties.**

The signal  $S$  is injected with horizontal, linear polarization and then rotated to a 45 degree linear polarization by the half wave plate. The non-polarizing, 50/50 beam splitter transmits 50% of the input signal to the polarizing beam splitter where the horizontal is reflected to the in-phase output and the vertical polarization is directed to the quadrature output. The Jones matrix representation for the signal fields propagating to the in-phase output  $S_I$  is

$$\begin{aligned}
 S_I &= PBS_H \cdot HWP \cdot BS \cdot S = \begin{pmatrix} 1 & 0 \\ 0 & 0 \end{pmatrix} \frac{1}{\sqrt{2}} \begin{pmatrix} 1 & 1 \\ 1 & -1 \end{pmatrix} \frac{1}{\sqrt{2}} \begin{pmatrix} 1 \\ 0 \end{pmatrix} \\
 &= \frac{1}{2} \begin{pmatrix} 1 \\ 0 \end{pmatrix}
 \end{aligned} \tag{36}$$

where  $S$  is the signal,  $BS$  is the non polarizing beam splitter,  $HWP$  is the half waveplate oriented at 22.5 degrees to provide 45 degree polarization, and  $PBS_H$  is the polarizing beam splitter horizontal reflection. Similarly, the signal at the quadrature output  $S_Q$  is

$$\begin{aligned}
 S_Q &= PBS_V \cdot HWP \cdot BS \cdot S = \begin{pmatrix} 0 & 0 \\ 0 & 1 \end{pmatrix} \frac{1}{\sqrt{2}} \begin{pmatrix} 1 & 1 \\ 1 & -1 \end{pmatrix} \frac{1}{\sqrt{2}} \begin{pmatrix} 1 \\ 0 \end{pmatrix} \\
 &= \frac{1}{2} \begin{pmatrix} 0 \\ 1 \end{pmatrix}
 \end{aligned} \tag{37}$$

where  $PBS_V$  is the polarizing beam splitter with vertical transmission. From these two equations, it is clear that the undelayed copies of the signal appear at both outputs.

In the paths from the master oscillator to the in-phase and quadrature outputs, the MO is also injected with linear polarization, but a quarter wave plate is set to produce a circularly polarized beam with a  $\pi/2$  delay in the vertical polarization component. The non-polarizing, 50/50 beam splitter then reflects 50% of the circularly polarized MO beam along the same path as the signal. At the polarizing beam splitter, the horizontal component of the circularly polarized beam is reflected to the in-phase output. The delayed vertical polarization is transmitted through to the quadrature output.

The Jones matrix result for the master oscillator propagating to the in-phase output  $MO_I$  is

$$\begin{aligned} MO_I &= PBS_H \cdot BS \cdot QWP \cdot MO = \begin{pmatrix} 1 & 0 \\ 0 & 0 \end{pmatrix} \frac{1}{\sqrt{2}} \frac{1}{\sqrt{2}} \begin{pmatrix} 1 & e^{i\pi/2} \\ e^{i\pi/2} & 1 \end{pmatrix} \begin{pmatrix} 1 \\ 0 \end{pmatrix} \\ &= \frac{1}{2} \begin{pmatrix} 1 \\ 0 \end{pmatrix} \end{aligned} \quad (38)$$

where  $MO$  is the master oscillator input and  $QWP$  is the quarter waveplate. This confirms the horizontal component of the  $MO$  beam is undelayed.

Finally, the path from the master oscillator to the quadrature output  $MO_Q$  is

$$\begin{aligned} MO_Q &= PBS_V \cdot BS \cdot QWP \cdot M = \begin{pmatrix} 0 & 0 \\ 0 & 1 \end{pmatrix} \frac{1}{\sqrt{2}} \frac{1}{\sqrt{2}} \begin{pmatrix} 1 & e^{i\pi/2} \\ e^{i\pi/2} & 1 \end{pmatrix} \begin{pmatrix} 1 \\ 0 \end{pmatrix} \\ &= \frac{1}{2} \begin{pmatrix} 0 \\ e^{i\pi/2} \end{pmatrix} \end{aligned} \quad (39)$$

In this case the transmitted vertical component is delayed by  $\pi/2$ . Now combining the signal and master oscillator, the output of a square law detector at the in-phase output is

$$\begin{aligned}
I_I &= |S_I + MO_I|^2 = \left| \frac{1}{2} \begin{pmatrix} 1 \\ 0 \end{pmatrix} S + \frac{1}{2} \begin{pmatrix} 1 \\ 0 \end{pmatrix} MO \right|^2 \\
&= \frac{1}{4} [P_S + P_{MO} + 2\sqrt{P_S P_{MO}} \cos((\omega_S - \omega_M)t + \theta)],
\end{aligned} \tag{40}$$

and the quadrature output is

$$\begin{aligned}
I_Q &= |S_Q + MO_Q|^2 = \left| \frac{1}{2} \begin{pmatrix} 1 \\ 0 \end{pmatrix} S + \frac{1}{2} \begin{pmatrix} 0 \\ e^{i\pi/2} \end{pmatrix} MO \right|^2 \\
&= \frac{1}{4} [P_S + P_{MO} + 2\sqrt{P_S P_{MO}} \sin((\omega_S - \omega_M)t + \theta)],
\end{aligned} \tag{41}$$

where  $P_S$  and  $P_{MO}$  are the signal and master oscillator power, respectively, and  $\omega_S$  and  $\omega_{MO}$  are their frequencies. These expressions are in agreement with the expressions for free space quadrature detection, but the result is achieved without mechanically adjusting the path lengths.

## F. Coherent Detection

Coherent detection is an interferometric process which coherently combines two beams allowing the fields to constructively and destructively interfere before the nonlinear square law detection process. Typically, a relatively strong reference, or local oscillator (LO) beam is combined with a much weaker signal beam. The phase differences between the two interfering beams generate signal changes that are manifest as intensity changes after detection. The coherent detection process provides significant advantages over direct detection including noiseless amplification of the signal, near-quantum limited detection, and most importantly, the ability to measure the phase of the optical signal [31]. To examine the details of coherent detection, recall the signal complex envelope  $\tilde{w}_0(t)$  of Eq. 2

$$w(t) = w_0(t) \exp(j\theta(t)) \exp(j2\pi f_c t). \quad (2)$$

The phase modulation  $\theta(t)$  does not affect the transmitted power and is assumed to be 0 for this discussion. The field of the transmitted waveform is then written in phasor form as

$$E_T(t) = \sqrt{\frac{2P_T}{c\epsilon_0}} \operatorname{Re}[w_0(t) \exp(ikz)], \quad (42)$$

where  $P_T$  is the power of the transmitted waveform,  $c$  is the speed of light, and  $\epsilon_0$  is the permittivity of free space. Similarly, the received field  $E_R$  is a copy of the transmit waveform combined with the background noise field  $E_n(t)$  and is written as

$$\begin{aligned} E_R(t) &= E_T(t) + E_n(t) \\ &= \sqrt{\frac{2P_T}{c\epsilon_0}} \operatorname{Re} \left[ w_0 \left( t - \frac{2R}{c} \right) \exp(j2\pi f_c t) \exp(j2\pi f_D t) \exp \left( j \frac{4\pi R}{\lambda} \right) \right] + \sqrt{\frac{2P_n}{c\epsilon_0}}, \end{aligned} \quad (43)$$

where  $2R/c$  is the round trip propagation delay,  $f_D$  is the motion induced Doppler frequency shift, and  $E_n$  and  $P_n$  are the background noise field and power, respectively. Although not included in this discussion, in practice the return of Eq. 39 is reduced by factors including system losses, propagation losses, and the size and reflectivity of the target.

The field of the LO beam  $E_{LO}$  is

$$E_{LO}(t) = \sqrt{\frac{2P_{LO}}{c\epsilon_0}} \operatorname{Re} [s_{LO}(t) \exp(j2\pi(f_c + f_{IF} + \hat{f}_D)t) \exp(jkz)], \quad (44)$$

where  $f_{IF}$  is the carrier offset frequency and  $\hat{f}_D$  is an estimate of the return Doppler frequency shift. The delay factor in Eq. (44) can be assumed to be unity for a perfectly coherent master oscillator or short range operation. Otherwise, the MO can be delayed to match the delay associated with the range of the target. The field at the detector is the superposition of the return signal and the local oscillator

$$E_D(t) = E_R(t) + E_{LO}(t). \quad (45)$$

For a square law detector the output photocurrent  $i(t)$  is

$$\begin{aligned} i(t) &= \eta_q \frac{q_e}{hf_c} \frac{c\epsilon_0}{2} [E_r(t) + E_{LO}(t)][E_r(t) + E_{LO}(t)]^* A_R \\ &= \eta_q \frac{q_e}{hf_c} \frac{c\epsilon_0}{2} \left[ |E_r(t)|^2 + |E_{LO}(t)|^2 + 2|E_r(t)E_{LO}(t)| \right] A_R \end{aligned} \quad (46)$$

where  $\eta_q$  is the detector quantum efficiency,  $A_R$  is the area of the aperture and  $c\epsilon_0/2$  is a constant of proportionality relating the fields to current. Again writing in terms of the average waveform power yields

$$i(t) = \eta_q \frac{q_e}{hf_c} \left[ P_r + P_{LO} + 2\sqrt{\eta_h P_r P_{LO}} \right], \quad (47)$$

where  $P_r$  is the received power and  $\eta_h$  is the heterodyne efficiency which accounts for non-ideal beam matching, alignment, and detectors. Recognizing the detector responsivity  $\mathfrak{R}$  is

$$\mathfrak{R} = \frac{\eta_q q_e}{hf_c} \left[ \frac{A}{W} \right], \quad (48)$$

and inserting the responsivity into Equation (47), the measured output voltage  $v(t)$  is written

$$v(t) = \eta_h \mathfrak{R} \left[ P_r + P_{LO} + 2\sqrt{\eta_h P_r P_{LO}} \right] G_{Eff} R_L, \quad (49)$$

where  $G_{Eff}$  and  $R_L$  are the effective gain of the detector amplifier and the measurement load resistance, respectively. The first two terms are due to the signal and local oscillator if each had been measured independently. The last term is the interference signal of interest and shows that the power of the received signal  $P_r$  is multiplied by the local oscillator power  $P_r$ , providing greatly enhanced performance. This will be important in discussion of the noise sources.

## 1) Noise Sources

Noise in coherent detection systems is contributed from a variety of sources including the background radiation, the non-ideal nature of the detector and amplifier, and from the master oscillator.

### (i) Background Noise

The background noise is due to the optical background power from solar, thermal or other sources within the target field [32]. The mean-squared background noise current  $i_{Bkgd}$  is written as

$$\langle i_{Bkgd}^2 \rangle = 2q_e B P_{Bkgd} \mathfrak{R}, \quad (50)$$

where the background power is  $P_{Bkgd}$ ,  $B$  is the bandwidth, and  $\mathfrak{R}$  is the detector responsivity.

Background noise can be significant, but is not dominant in most scenarios due to both the spectral and spatial selectivity of the coherent detection process. Coherent detection and electronic filtering of the signal effectively limit the spectral bandwidth. The spectral bandwidth accepted is

$$\Delta\lambda = \lambda \left( 1 - \frac{c}{c - B\lambda} \right) \approx \frac{B\lambda^2}{c}, \quad (51)$$

where  $B$  is the bandwidth of the received signal  $B$  and  $\lambda$  the transmit wavelength [33, 34, 35]. Since  $c$  is large with respect to  $B\lambda$ , then  $\Delta\lambda$  can be approximated as shown in Eq. (51) which shows the spectral width has a strong dependence on both  $B$  and  $\lambda$ . For a bandwidth of 2-GHz and an transmit wavelength of 1.55 microns, the effective spectral bandwidth is still very narrow at 0.016 nanometers.

The heterodyne efficiency also falls off rapidly with off axis targets providing high angular selectivity. The angular acceptance limit  $\theta_{max}$  is given as

$$\theta_{max} = \frac{\lambda}{D_{pupil}} \quad (52)$$

where  $D$  is the diameter of the pupil [33]. For a 10 centimeter pupil and a wavelength of 1.55 microns, the maximum angular limit is approximated 15 micro-radians. With the relatively low background power contained within the spectral and angular extents, background noise is of minimal impact.

#### (ii) *Dark Current Noise*

Dark current noise is due to the leakage currents within the detector present without illumination. Dark currents are typically quite small and not dominant noise sources. The mean-squared dark noise current  $\langle i_{Dark}^2 \rangle$  is given as

$$\langle i_{Dark}^2 \rangle = 2q_e B i_{Dark} , \quad (53)$$

where  $i_{Dark}$  is the detector dark current,  $q_e$  is the charge of an electron, and  $B$  is the detector bandwidth. The dark current depends on the device structure, the bias condition, and the operating temperature of the device.

#### (iii) *Thermal Noise*

Thermal noise stems from the random thermal disturbances within the electronic components. Although not as dominant as in radio frequency systems, thermal noise can be significant in optical detection. The mean-squared thermal noise current  $\langle i_{TH}^2 \rangle$  is

$$\langle i_{TH}^2 \rangle = 4k_B TB / R_{Load} , \quad (54)$$

where  $k_B$  is Boltzmann's constant in Joules per degree Kelvin,  $T$  is the Temperature in degrees Kelvin,  $B$  is the bandwidth and  $R_{Load}$  is the effect load resistance. Thermal noise is based on the random motion of electrons within the electronics or detectors and produces an approximately white noise spectrum. The noise current increases with system bandwidth and can be come dominant with wide bandwidth systems. Increasing the load resistance  $R_{Load}$  decreases the thermal noise contribution, but also effects the bandwidth. Generally, decreasing  $R_{Load}$  will decrease the effective detector circuit bandwidth. With the Bandwidth and load resistance fixed by operational requirements, the thermal noise may only be reduced by cooling or mitigated by techniques such as coherent detection.

(iv) *Shot Noise and Total Noise*

From Equation (49) it would appear that the local oscillator should be as large as possible to provide the best coherent detection performance. In practice, the detector's and amplifier's linear range of operation and the detector's ability to dissipate the LO power will all limit the useful LO power. This relatively high local oscillator power will produce shot noise due to the random arrival and detection of the local oscillator photons. The mean-squared shot noise current  $\langle i_{shot}^2 \rangle$  is effectively

$$\langle i_{shot}^2 \rangle = 2q_e P_{LO} \Re B , \quad (55)$$

where  $\Re$  is the responsivity of the detector in amps/watt [23]. The shot noise is caused by the random arrival of photons and produces a nearly white noise spectrum. Although the shot noise is impacted by the signal and background power as well, in practice  $P_{LO}$  will be

chosen such that its contribution to the shot noise is at least ten times greater than the other contributions. Shot noise increases with increasing bandwidth, local oscillator power  $P_{LO}$ , or responsivity. To realize the full benefit of coherent detection, the shot noise must dominate the other noise sources.

The relationship between the shot noise and total noise is described by the shot noise efficiency  $\eta_{Shot}$

$$\eta_{Shot} = \frac{\langle i_{Shot}^2 \rangle}{\langle i_{Total}^2 \rangle} = \frac{\langle i_{Shot}^2 \rangle}{\langle i_{Shot}^2 \rangle + \langle i_{Bkgd}^2 \rangle + \langle i_{Dark}^2 \rangle + \langle i_{TH}^2 \rangle}, \quad (56)$$

which is the ratio of the mean-squared shot noise current squared to the sum of all noise sources squared. The shot noise efficiency increases to near unity with increasing  $P_{LO}$  where the shot noise current  $i_{Shot}$  dominates all other sources.

Non-ideal detector and amplifier performance introduce an additional limitation on the useful amount of LO power. As the LO power is increased, the overall small signal gain decreases. In practice, both the detector and amplifier contribute to the compression. Here, the compression is dominated by the amplifier and is modeled as an effective gain  $G_{Eff}$

$$G_{Eff} = \frac{S_{21} G_{TIA} P_{LO}}{\left[ 1 + \left( \frac{S_{21} G_{TIA} P_{LO}}{V_{Sat}} \right)^4 \right]^{-1/4}}, \quad (57)$$

where  $S_{21} = 19.25$  dB is the amplifier voltage gain factor used to fit the 1 dB compression point,  $G_{TIA} = 26$  dB is the effective trans-impedance gain of the detector and amplifier, and  $V_{Sat} = 3$  V is the saturation voltage [36]. Using these parameters for the detector/amplifier pair used in this research, the gain compression is shown in Figure 14. The small signal efficiency  $\eta_{SS}$  is defined as

$$\eta_{ss} = \frac{G_{Eff}}{S_{21}P_{LO}G_{TIA}} \quad (58)$$

which is the ratio of the effective gain to the ideal unsaturated gain. The small signal efficiency decreases with increasing LO power, but the shot noise efficiency  $\eta_{Shot}$  increases. Both efficiencies and their combination are shown in Figure 15.

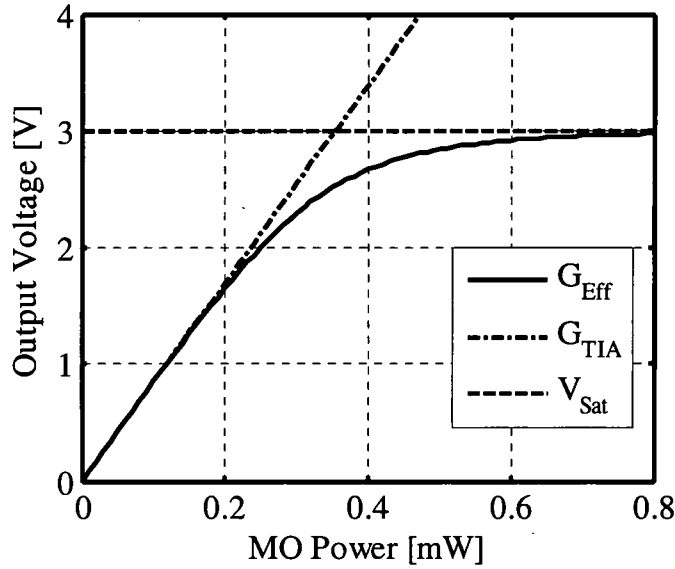


**Figure 14: Small signal, shot noise, and combined signal gain impact on the local oscillator and coherent mixing.**

Low shot noise efficiency dominates at low LO powers and the low small signal efficiency dominates at high LO powers resulting in an optimum efficiency LO power at the peak of the combined curve. For this detector amplifier-combination, the optimum LO power is just over 200  $\mu$ W and should provide near quantum limited operation.

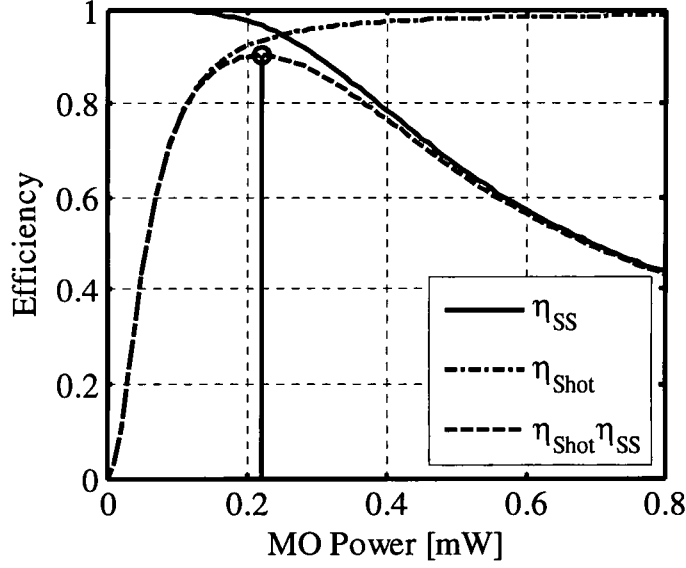


**Figure 15: Optimal MO Power based on the performance of the PicoSecond Pulse Laboratory amplifier.**

## 2) Laser Radar Equation

Coherent detection is an extremely sensitive detection method relatively immune to a variety of noise sources. The performance of the laser radar systems depends on the system characteristics, the channel the laser light propagates through, and the nature of the target being imaged. The power received by the laser radar detector  $P_R$  is described by the laser radar equation

$$P_R = P_T T_{ATM}^2 \frac{A_{TGT}}{A_B} \rho_{TGT} \frac{A_{RCVR}}{A_R}, \quad (59)$$

where  $P_T$  is the transmitted power,  $T_{ATM}$  is the one way atmospheric transmission,  $A_{TGT}$  is the target area,  $A_B$  is the area of the beam at the target,  $\rho_{TGT}$  is the target reflectivity,  $A_{RCVR}$  is the area of the receiver, and  $A_R$  is the area of the returned beam at the ladar aperture [37,38]. The atmospheric transmission depends on the atmospheric conditions and the altitude and

locations of the target and ladar system. For a given target, the area of the target is fixed. The area of the beam at the target varies with range, turbulence and focus range. The range equation is often defined in two ways for resolved and unresolved targets. For resolved targets, the diameter of the beam is smaller than the target and for unresolved targets where the diameter of the beam is greater than the target. A more general approach is taken during the discussions of the system level modeling that will smoothly transition between cases.

## **CHAPTER IV**

### **WAVEFORM CONSTRAINTS AND FIGURES OF MERIT**

A variety of waveforms were developed over the years ranging from simple transform limited pulses to complex waveforms with amplitude, phase and/or frequency modulation. These waveforms were used in a variety of application including conventional range finding, range-Doppler imaging for moving target indicator radar, weather radar and many versions of synthetic aperture radar. Each waveform was optimized under a set of constraints specific to each application [14]. Multifunction laser radar provides additional capability as well as additional constraints on the modes, expected geometry, and signals. This chapter will outline the waveform constraints and figures of merit that govern or characterize the waveform's ability to make the necessary measurements, to be efficiently implemented in hardware, and the resulting performance in each mode.

#### **A. General Waveform Constraints**

The general waveform constraints are common to all imaging modes addressed including range, range-Doppler, synthetic aperture, and micro-Doppler imaging. These constraints govern both the performance of the ladar as well as its implementation.

### ***1) High Time Bandwidth Product form Multimode Imaging***

The waveform should have a high time-bandwidth product to provide both high temporal and frequency resolution [14]. This dictates that the waveform must either be modulated, repetitive, or both.

### ***2) Support Phase Recovery from Multiple Apertures***

The waveforms should support transmission, reception, and phase recovery from both single and multiple apertures. The use of a single aperture will allow ladar imaging in each of the modes described. The use of multiple apertures can be used to increase cross-track resolution (i.e., height estimation), to mitigate undesired platform motions or to decrease SAL measurement times.

### ***3) Detect and Mitigate Residual Doppler***

The waveform should be able to detect and mitigate unknown Doppler. Delay-Doppler coupling should be avoided so that unique spatial localizations are possible. The waveform should provide continuous monitoring of the phase evolution as well as methods to recover the phase, increase or exploit the Doppler tolerance, and mitigate ambiguities. Complete phase sampling will also allow non-linear platform motions to be detected and mitigated.

### ***4) Minimize Energy***

The waveform energy should be minimized to provide the required imaging performance in each mode at the required range. The energy usage should be adapted as

range changes providing high area rate imaging at short range and maintaining minimum waveform carrier to noise ratio (CNR) for processing at long range.

#### ***5) Minimize Peak Power***

The peak to average power ratio of the system should be near unity. It is assumed that modulated/repetitive waveforms must be used to satisfy the wide range of requirements, so a master oscillator power amplifier architecture is utilized. High peak powers can drive the architecture, efficiency and noise performance of the amplifier. Low peak power with respect to the average power will allow the use of highly efficient continuous amplifiers and reduce the risk of damage. The use of continuous waveforms will also mitigate the amplified spontaneous emission noise in the amplifier.

#### ***6) Minimize Hardware Complexity***

The waveform design should be realizable with reliable, stable components. Although high bandwidths and high stabilities are required to provide high performance, the modulation format and techniques realizing them should be repeatable and reliable. The telecommunications industry has greatly advanced the state of the art for modulators, but the requirements for simultaneous high bandwidth and frequency stability still present significant challenges. For example, using an LFM pulse for SAL or micro-Doppler imaging requires extremely linear frequency sweeps. Non linearity is manifested as resolution decreases or as noise floor increases.

## B. Figures of Merit

Each imaging mode has multiple figures of merit which describe the performance on the laser radar and specifically the laser waveform employed. Common figures of merit are employed for all waveforms although the details of implementation may differ.

### 1) Ideal Point Response (IPR) Mainlobe Width

One of the most fundamental measures of the performance of an imaging system is the resolution of the system. The resolution, or the minimum resolvable target separation, is defined in either in range or cross-range as the width of the ideal point response (IPR). A typical IPR is shown for a 20,000 chip bi-phase code in Figure 16(a).

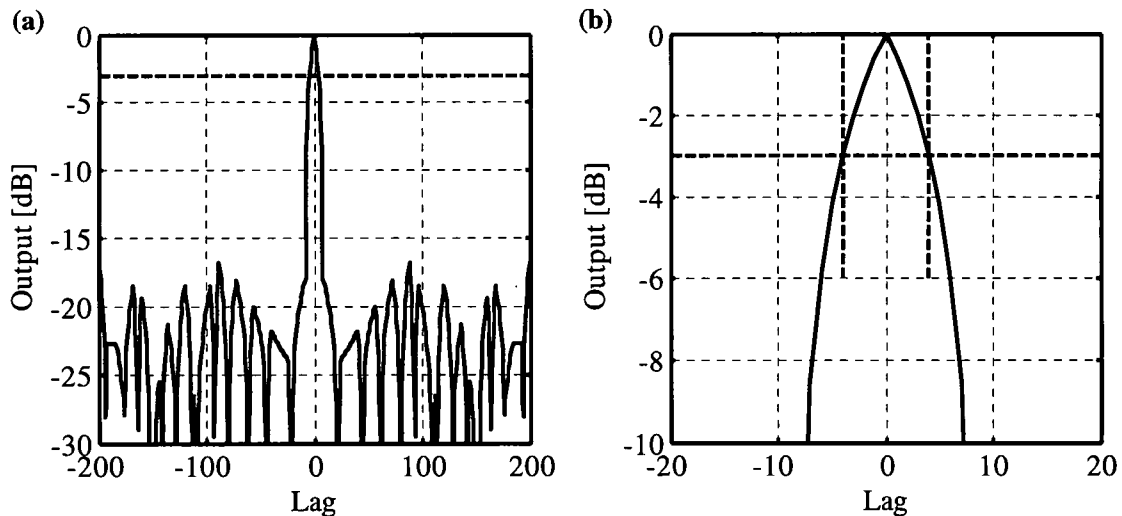


**Figure 16: IPR for a 20,000 point PPN waveform (a) and the 3 db (i.e., full-width half-maximum) resolution metric definition (b)**

The IPR width is defined as the distance between the full-width, half-maximum (FWHM) points of the one dimensional cross section of the IPR intensity. This is equivalent

to the points 3 dB below the peak power of the IPR which is shown in the expanded version of the central portion of the IPR as shown in Figure 16(b). The vertical dashed lines indicate the points where the IPR crosses the FWHM point.

## ***2) Compression Factor***

The compression factor describes the effective compression in either range or cross-range. For the temporal, or fast-time, compression the factor is on the order of the time-bandwidth product. For typical systems, the temporal compression factors can be quite large. In synthetic aperture radar, the cross-range (i.e. slow-time) compression factor is the gain associated with the increase in effective aperture length. Although much smaller than the temporal compression, a cross-range compression factor between 5 and 10 is of great consequence when compared to the physical aperture requirements.

## ***3) Integrated Sidelobe Ratio (ISLR)***

Although resolution is usually the first metric considered in imaging system, the integrated sidelobe ratio (ISLR) is nearly as important. The ISLR quantifies the fraction of the waveform energy compressed into the mainlobe relative to that present in the sidelobes. Energy within the sidelobes contributes to image clutter and reduces contrast within the image. Ideally, all of the signal energy would be in the mainlobe; however, sidelobes are always present. A low ISLR image may indicate an image with extremely low quality even though it may have excellent IPR resolution. The ISLR is calculated as the ratio of energy within the mainlobe out to the first theoretic null to the energy outside the mainlobe as

$$ISLR = 10 \log \left( \frac{|IPR_0|^2}{\sum_{k \neq 0} |IPR_k|^2} \right), \quad (60)$$

where  $IPR_0$  and  $IPR_k$  are the values of the IPR inside and outside of the IPR 3 dB points, respectively [39, 40, 41]. Figure 17(a) shows a notional IPR and the regions of summation for the ISLR. A close up of the mainlobe shown in Figure 17(b) more clearly illustrates the region of summation. Notice that the summation in the denominator of Eq. (60) has the form of the variance of a zero mean signal.

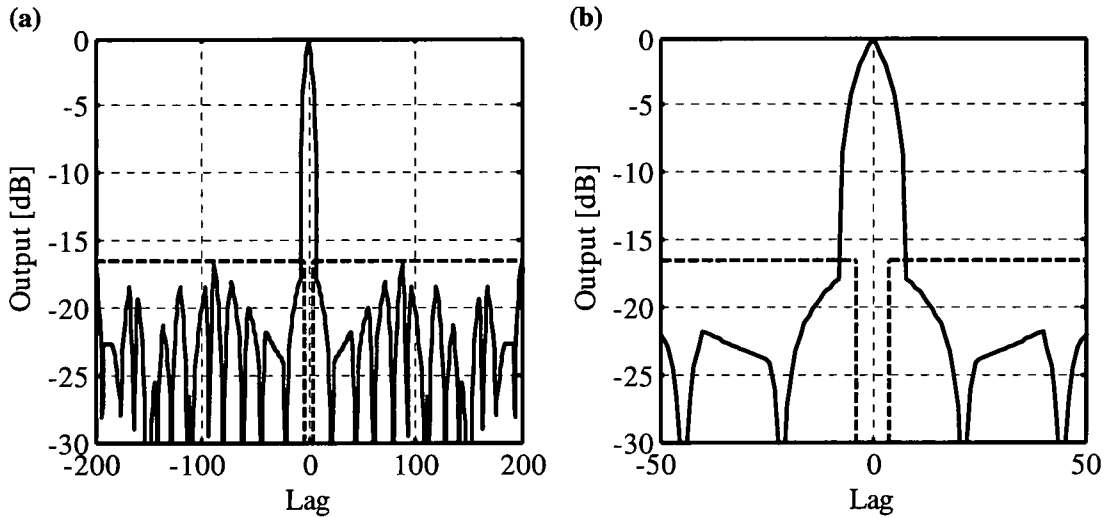


**Figure 17: Integrated sidelobe ratio (ISLR) metric definition (a) and close up about the mainlobe showing regions of summations (b).**

#### **4) Peak Sidelobe Ratio (PSLR)**

The peak sidelobe ratio (PSLR) is also an important metric, but unlike the ISLR which focuses on the average sidelobe level, the peak sidelobe ratio specifically identifies the strongest sidelobes [39, 42]. As shown in Figure 18, the peak sidelobes may be significantly greater than the average sidelobe level. High peak sidelobes may not significantly decrease

the overall contrast, but their appearance can generate secondary targets or “ghost” images leading to degradations that range from loss of interpretability to resolution loss. The PSLR is calculated as the ratio of the peak IPR intensity within the mainlobe to the largest exterior peak as

$$PSLR = 10 \log \left( \frac{|IPR_o|^2}{\max_{k \neq 0} |IPR_k|^2} \right). \quad (61)$$

where  $IPR_o$  and  $IPR_k$  are the values of the IPR inside and outside of the IPR mainlobe, respectively.

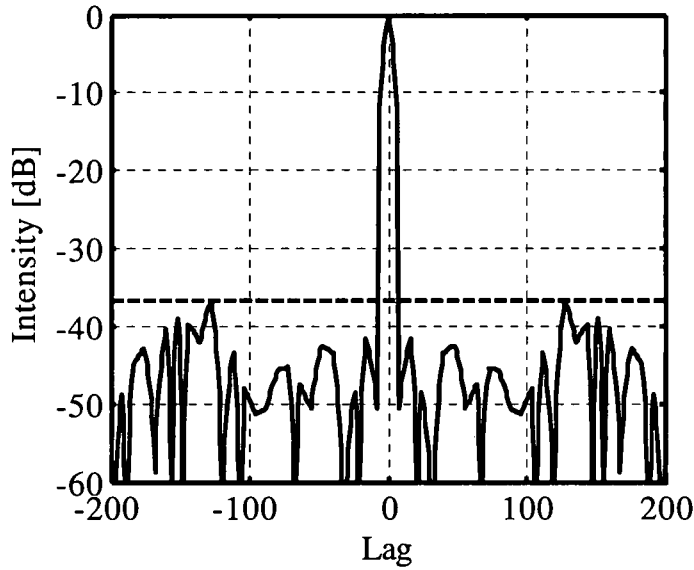


**Figure 18: Peak sidelobe ratio (PSLR) metric definition.**

Ideally, the PSLR would be very large with all energy in the mainlobe. In addition, the PSLR can also be calculated over a finite range record if the range region of interest is limited which is usually the case.

### **5) Noise Equivalent Vibration Velocity (NEVV)**

The noise equivalent vibration velocity is the square root of the signal spectral amplitude equal to the measurement noise floor [18]. The noise floor is determined by system parameters such as measurement carrier to noise ratio (CNR), master oscillator linewidth, and shot noise level and external parameters such as atmospheric turbulence environment, platform residual motion, and pointing system angular jitter. NEVV is measured in units of  $\mu\text{m}/(\text{sec}\sqrt{\text{Hz}})$ .

### **6) Ambiguity Velocity**

The ambiguity velocity  $V_{\text{amb}}$  is the maximum velocity that can be sensed uniquely and is referenced to the wavelength of the source. It is the maximum velocity that will produce a wavelength equivalent displacement over the shortest measurement time, usually  $1/\text{PRF}$ . For macro-Doppler imaging, large  $V_{\text{amb}}$  are required since targets may be moving at speeds of many meters per second. High PRFs make  $V_{\text{amb}}$  larger, but make micro-Doppler measurements less sensitive [18].

### **7) Range Ambiguity**

The ambiguity range  $R_{\text{amb}}$  is the maximum range interval that can be measured uniquely and depends on the PRF and the range to target [9]. At long ranges and high PRF's, multiple pulses may be in transit to the target and back creating ambiguity in the range estimate. For laser based sensing, range gates are typically fixed at the nominal target range. Due to the narrow beamwidth, relatively short range extents are required for imaging.

### ***8) Velocity Resolution***

The velocity resolution is defined as the minimum change in velocity between two targets that can be resolved. Large translational Doppler phase in ladar can be detected, but may be limited by beam crossing time. Ladar may be best suited to the detection of small differential velocities such as those due to rotating targets [9].

### ***9) Frequency Resolution***

The frequency resolution is defined as the resolution required to isolate the significant spectral content for acoustic/surface vibrations of interest. The signal resolution is determined by the coherence time of the target of interest and ranges from less than a second for vehicular targets to tens of seconds for generators and turbines [9].

## CHAPTER V

### PPN WAVEFORMS IN COHERENT LADAR

The use of periodic, pseudo-noise waveforms in coherent laser radar allows the conflicting requirements of the various imaging modes to be satisfied with a single waveform, assuming post detection processing tailored to each mode. This chapter introduces the basic periodic pseudo noise (PPN) waveform, the taxonomies in which it is applied, and develops expressions for its salient performance parameters.

#### A. Periodic Pseudo Noise Waveform

The periodic pseudo noise waveform consists of a fixed length binary phase code repeated at fixed intervals. Figure 19 shows a single waveform segment. The fundamental unit energy PPN waveform  $w(t)$  is defined as

$$w(t) = \frac{1}{\sqrt{N_c T_c}} \sum_{m=1}^{N_c} \exp(-j\pi\phi_m) \text{rect}\left(\frac{t - (m-1)T_c}{T_c}\right), \quad (62)$$

where  $N_c$  is the number of code chips in the sequence,  $T_c$  is the width of each phase chip, and  $\phi_m$  are the elements of a binary (i.e., 0 or 1) pseudo-noise sequence that define the phase of the  $m^{\text{th}}$  chip [11]. The range resolution of the PPN waveform is governed by the chip width. Doppler sensitivity then depends on the length of the code and is adapted by processing variable length or variable separation code segments.

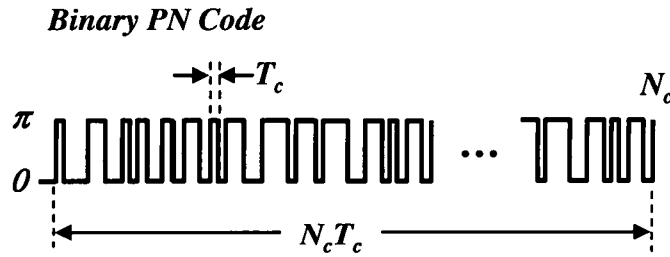


**Figure 19: Single binary phase, pseudo random noise code segment with  $N_c$  phase chips of length  $T_c$ .**

In order to optimize imaging in each mode, adaptive processing can also be used to identify and mitigate any residual Doppler phase due to the relative motion between the sensor and the target. Finally, longer code segments or code repetition can be used to achieve the phase resolution required for synthetic aperture and micro-Doppler imaging.

## **B. PPN Taxonomy**

This basic PPN waveform is implemented in several ways depending upon the requirements of the imaging mode. A single PN code is shown in Figure 20(a) and the three salient PPN and CDMA taxonomies are shown in Figure 20(b)-(d). The PPN waveform is generated reliably with relatively simple hardware and uses stable and efficient continuous wave sources and amplifiers. The single code PN waveform shown in Figure 20(a) has many desirable properties. The code has  $N_c$  binary phase chips of length  $T_c$ . The chip length determines the temporal bandwidth (range resolution) and is independent of code length. A single code, or even sub-code segments, can be processed in applications where high sample rates are required and relatively high sidelobe levels can be tolerated. An example would be wide area mapping where ranges are usually relatively short and first surface returns are usually of interest. The short sequence PN waveform segments are also more Doppler

tolerant and can be used without additional processing for spatial measurements. As the range increases, additional energy is required to produce a useful measurement.

The single code, denoted as  $C_1$ , is transmitted repetitively to produce the periodic pseudo noise (PNN) waveform shown in Figure 20(b) which allows integration of multiple waveforms for long range detection. Then measurement energy is increased in increments of the code length until the desired, single waveform carrier to noise ratio (CNR) is reached. Here, the CNR is defined after detection and digitization as

$$\text{CNR} = \frac{\sum_{m=1}^{N_c} s_m^2}{\sum_{m=1}^{N_c} n_m^2}, \quad (63)$$

which is the ratio of the power in the return signal waveform  $s_m$  to the noise power  $n_m$ . A specified CNR level can be maintained over a wide range extent by exploiting differing lengths of a single waveform. The number of combined waveforms is increased at longer ranges without change in waveform, only the processing is adapted to the requirements. The combined processing of multiple copies the single code  $C_1$  mitigates the contributions of additive noise to the theoretical limits of the single PN code IPR, but the PSLR and ISLR are limited by the single code PNN since the sidelobes of the repetitive code are correlated.

In many imaging applications, further reduction of the sidelobe energy is desired. The third configuration of Figure 20(c) shows a multiple diverse (i.e., orthogonal) code time division multiplexed (TDM) PPN waveform. Here each of the  $N_c$  sub-codes, denoted as  $C_n$ , are transmitted sequentially. The multiple sub-codes are random and orthogonal; therefore, their sidelobes are generally uncorrelated resulting in decreased sidelobe levels for the combination of codes. In practice, many diverse codes can be utilized, but the TDM

structure means the overall waveform will grow long. Long PNN waveforms are significantly less Doppler tolerant requiring Doppler compensation to maintain detection efficiency and the desired sidelobe suppression.

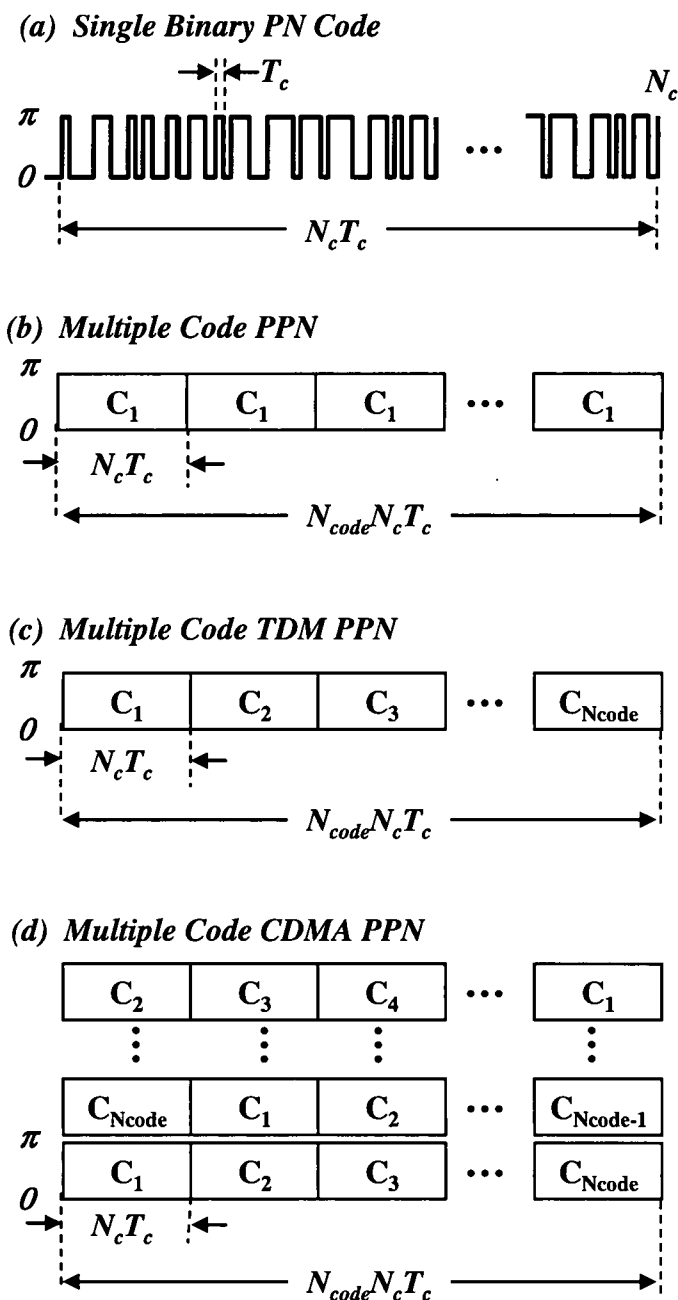


Figure 20: PPN Waveform and CDMA Taxonomies

The fourth taxonomy, shown in Figure 20(c), uses code division multiple access (CDMA) multiplexing to transmit multiple orthogonal codes simultaneously [43,44]. Since the codes are transmitted during the same times, multiple independent codes can be processed to reduce the IPR sidelobes without significantly impacting the Doppler sensitivity.

A single transmit/receive aperture can be used to detect all of the CDMA signals, but post detection processing is used to coherently combine the diverse codes to provide the waveform enhancements. The number of codes are limited in practice by two factors. First, a CDMA code results in a peak to average power ratio (PAPR) on the order of the square root of the number of codes. This limits the number of codes which can efficiently exploit continuous wave amplifiers. Second, although the waveforms are orthogonal by design, the superposition of the waveforms results in an increased noise floor after matched filter processing tailored to any one of the codes analogous to inter-symbol interference and multipath effects in communications. For the ladar application, the return from the target includes a distribution of range returns requiring each code to be detected asynchronously, and the waveforms to be circularly orthogonal over the range swath. Leakage between codes increases as the number of codes is increased decreasing the sidelobe reduction by  $1/\sqrt{N_{code}}$  [45].

An important variation of the CDMA taxonomy is its use in multiple aperture ladar where multiple signals are transmitted and received from multiple apertures. Each aperture still requires a single transmitter and receiver, but each aperture transmits unique code sequences or a time delayed copy of the same code. The orthogonal, simultaneous measurements from each of the apertures can be exploited to provide relative aperture phase

and differential phase of the target for enhanced aperture synthesis. Much of the CDMA discussion and experimental demonstrations focuses on this important application.

In summary, all of these configurations use reliable, simply generated CW waveforms with high average transmit powers and are well suited for use with saturated amplifiers. The bandwidth of the waveform is fixed by the chip length, but the time-bandwidth product is selectable based on processing providing flexible use of energy and Doppler sensitivity. Finally, the continuous nature of the waveform allows continuous phase monitoring for metrology, detection and rejection of a wide range of gross Doppler offsets. The application and performance of each configuration is discussed in the following sections.

### C. Multi-Code Periodic Pseudo Noise Waveforms

The use of periodic, pseudo-noise waveforms in coherent laser radar allows the conflicting requirements of the various imaging modes to be satisfied with a single waveform and mode specific processing [46, 47, 48, 17]. The PPN waveform consists of a fixed length binary phase code repeated at fixed intervals. The fundamental code defined in Eq. (62) is where  $N_c$  is the number of chips in the code,  $T_c$  is the width of each code chip, and the  $m^{\text{th}}$  phase chip is written as  $u_m = \exp(j\pi\phi_m)$  [11]. If  $N_{\text{code}}$  mutually orthogonal sub-codes are transmitted sequentially, the composite waveform is

$$w(t) = \frac{1}{\sqrt{N_{\text{code}} N_c T_c}} \sum_{p=1}^{N_{\text{code}}} \sum_{m=1}^{N_c} u_{(p-1)N_{\text{code}}+m} \text{rect}\left(\frac{t - (p-1)N_{\text{code}}T_c - (m-1)T_c}{T_c}\right), \quad (64)$$

where matched filters are applied to each sub-code or to the composite code depending on the application. The multiple sub-code PPN wave form is illustrated in Figure 21. Each sub-

code  $C_n$  is transmitted sequentially resulting in a composite code of length  $N_c N_{code}$ . Multiple Sub-code processing is addressed in detail in subsequent sections.

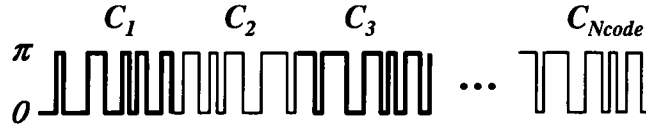


**Figure 21: Conceptual diagram of PPN waveform with  $N_{code}$  sub-codes.**

Since the basic properties of the PPN waveform can be deduced from a single code, the focus here is on the complete composite code, written in the same form as for a single code (i.e., Eq.(62))

$$w(t) = \frac{1}{\sqrt{N_c T_c}} \sum_{m=1}^{N_c} u_m \text{rect}\left(\frac{t - (m-1)T_c}{T_c}\right), \quad (65)$$

where  $N_c$  is the total number of chips in the composite waveform and  $u_m = \exp(j\pi\phi_m)$ . The range resolution of the PPN waveform is governed by the chip length  $T_c$  of the code which is defined to satisfy the required resolution. The sidelobe levels and Doppler sensitivity depend on the effective length of the code and are adapted by processing variable lengths or variable separations of code segments. Although range and frequency resolution depend primarily on the width of the transmitted spectrum, the shape of the IPR also depends on the spectrum shape and the distribution of energy within the spectrum.

#### **D. Discrete PPN Signal Model**

In a digital receiver, the continuous time transmit waveform  $w(t)$  is sampled at times  $kT_s$  resulting in the sampled transmit signal  $w[kT_s]$

$$w(kT_s) = \frac{1}{\sqrt{N_c T_c}} \sum_{m=1}^{N_c} u_m \text{rect} \left[ \frac{kT_s - (m-1)T_c}{T_c} \right], \quad (66)$$

where ( $k=0,1,2,3\dots$ ). It is assumed that the chip time  $T_c$  is a positive integer multiple of the sampling period and the discrete sequence  $w[k]$  is

$$w[k] = \frac{1}{\sqrt{N_s T_c}} \sum_{m=1}^{N_c} u_m \text{rect} \left[ \frac{kT_s}{T_c} - (m-1) \right], \quad (67)$$

where there are  $T_s/T_c$  samples within each chip. In practice, there may be many samples per chip, but for this analysis the sample time is set equal to the chip time,  $T_s=T_c$ . In this case, there is a single sample per chip and the waveform is written

$$\begin{aligned} w[k] &= \frac{1}{\sqrt{N_c T_c}} \sum_{m=1}^{N_c} u_m \text{rect} [k - (m-1)] \\ &= \frac{1}{\sqrt{N_c T_c}} \sum_{m=1}^{N_c} u_m \text{rect} [k+1-m] = \frac{1}{\sqrt{N_c T_c}} \phi_{k+1}, \end{aligned} \quad (68)$$

where the sampled transmit waveform  $w[k]$  is simply the  $k+1$  phase chip.

The return signal can also be sampled with one sample per chip. The continuous time return signal  $s(t)$  is generated by inserting the PPN code, Eq. (65), into the signal model, Eq. (8), to yield

$$\begin{aligned} s(t) &= \sum_{n=1}^{N_{gt}} A(x_n, y_n, z_n) \sigma_n \\ &\times \frac{1}{\sqrt{N_c T_c}} \sum_{m=1}^{N_c} u_m \exp \left( -j \frac{4\pi R_n}{\lambda} \right) \text{rect} \left( \frac{t - \frac{2R_n}{c} - (m-1)T_c}{T_c} \right) \\ &\times \exp \left[ j 2\pi \frac{2v_{no}}{\lambda} \left( t - \frac{2R_n}{c} \right) \right] \exp \left[ j \frac{2\pi}{\lambda} \frac{2\mu_n}{\omega_n} \cos \left( \omega_n \left( t - \frac{2R_n}{c} \right) \right) \right] \end{aligned} \quad (69)$$

where the delay within the *rect* functions shifts the envelope of the chip and the exponential phase factor inside the summation is included to account for the propagation induced phase rotation between the propagating signal and the reference waveform. Now the continuous return signal  $s(t)$  is sampled at  $kT_s$  to produce the sampled return  $s[k]$  as

$$s[k] = \sum_{n=1}^{N_{gt}} \left\{ A(x_n, y_n, z_n) \sigma_n \exp\left(-j \frac{4\pi R_n}{\lambda}\right) \times \exp\left[j 2\pi \frac{2v_{no}}{\lambda} \left(kT_s - \frac{2R_n}{c}\right)\right] \exp\left[j \frac{2\pi}{\lambda} \frac{2\mu_n}{\omega_n} \cos\left(\omega_n \left(kT_s - \frac{2R_n}{c}\right)\right)\right] \right. \\ \left. \times \frac{1}{\sqrt{N_c T_c}} \sum_{m=1}^{N_c} u_m \text{rect}\left[k \frac{T_s}{T_c} - (m-1) - \frac{2R_n}{T_c c}\right] \right\}. \quad (70)$$

Again letting  $T_s = T_c$  so there is one sample per chip, the return signal is written as

$$s[k] = \sum_{n=1}^{N_{gt}} \left\{ A(x_n, y_n, z_n) \sigma_n \exp\left(-j \frac{4\pi R_n}{\lambda}\right) \times \exp\left[j 2\pi \frac{2v_{no}}{\lambda} \left(kT_s - \frac{2R_n}{c}\right)\right] \exp\left[j \frac{2\pi}{\lambda} \frac{2\mu_n}{\omega_n} \cos\left(\omega_n \left(kT_s - \frac{2R_n}{c}\right)\right)\right] \right. \\ \left. \times \frac{1}{\sqrt{N_c T_c}} \sum_{m=1}^{N_c} u_m \text{rect}\left[k - (m-1) - \frac{2R_n}{T_c c}\right] \right\}, \quad (71)$$

where the sampling within the *rect* function is shifted by a non-integer factor due to the range to the  $n^{\text{th}}$  target which prevents further simplification.

## E. Discrete PPN Matched Filter

The information within the discrete return of Eq. (71) is extracted using matched filter processing. The matched filter output  $q[l]$  is the convolution of the matched filter and is written as

$$q[l] = \sum_{k=-\infty}^{\infty} s[k] w^*[k-l], \quad (72)$$

where  $s[k]$  is the return signal and  $w^*[-k]$  is the complex conjugate of the transmit waveform.

Inserting the waveform of Eq. (68) and the discrete return in Eq. (71) into Eq. (72) and sampling yields the PPN matched filter output  $q[l]$  as

$$\begin{aligned} q[l] = \sum_{k=-\infty}^{\infty} \left\{ \sum_{n=1}^{N_{tgt}} A(x_n, y_n, z_n) \sigma_n \exp\left(-j \frac{4\pi R_n}{\lambda}\right) \right. \\ \times \exp\left[j 2\pi \frac{2v_{no}}{\lambda} \left(kT_s - \frac{2R_n}{c}\right)\right] \exp\left[j \frac{2\pi}{\lambda} \frac{2\mu_n}{\omega_n} \cos\left(\omega_n \left(kT_s - \frac{2R_n}{c}\right)\right)\right] \\ \left. \times \sum_{p=1}^{N_t} \phi_p \operatorname{rect}\left(\frac{kT_s}{T_c} - (p-1) - \frac{2R_n}{T_c c}\right) \left( \frac{1}{N_c T_c} \sum_{m=1}^{N_t} \phi_m^* \operatorname{rect}\left(\frac{kT_s}{T_c} - (m-1) - l\right) \right) \right\}. \end{aligned} \quad (73)$$

Since the convolution of the sum of the targets is equal to the sum of the convolutions, the outer summation are reordered yielding

$$\begin{aligned} q[l] = \sum_{n=1}^{N_{tgt}} \left[ A(x_n, y_n, z_n) \sigma_n \exp\left(-j \frac{4\pi R_n}{\lambda}\right) \right. \\ \times \sum_{k=-\infty}^{\infty} \left\{ \exp\left[j 2\pi \frac{2v_{no}}{\lambda} \left(kT_s - \frac{2R_n}{c}\right)\right] \exp\left[j \frac{2\pi}{\lambda} \frac{2\mu_n}{\omega_n} \cos\left(\omega_n \left(kT_s - \frac{2R_n}{c}\right)\right)\right] \right\} \\ \left. \times \frac{1}{N_c T_c} \sum_{p=1}^{N_t} \phi_p \operatorname{rect}\left(\frac{kT_s}{T_c} - (p-1) - \frac{2R_n}{T_c c}\right) \sum_{m=1}^{N_t} \phi_m^* \operatorname{rect}\left(\frac{kT_s}{T_c} - (m-1) - l\right) \right] \end{aligned} \quad (74)$$

Equation (74) describes the composite discrete matched filter output specifically for the PPN waveform rather than the general waveform  $w(t)$ . The convolution contains the time varying phase terms which can affect the amplitude, shape and phase of the matched filter output if the velocities are large enough to produce phase variations during a code period.

To examine the impact the effect of Doppler mis-match, the matched filter output is simplified by assuming a single, translating target with unity beam amplitude and target

cross-section. In addition, the single target is assumed to have a finite translational velocity,  $v_{no}$ . The matched filter output is then reduced to

$$q[l] = \sum_{k=0}^{N_c-1} \exp \left[ j2\pi \frac{2v_{no}}{\lambda} kT_c \right] w[k] w^*[k-l], \quad (75)$$

where there is a single sample per chip (i.e.,  $T_s = T_c$ ) and the range and vibration velocity is assumed to be zero (i.e.,  $R_n=0$  and  $\mu_n=0$ ). Breaking summation into the mainlobe and sidelobe components produces

$$q[l] = \begin{cases} \sum_{k=0}^{N_c-1} \exp \left[ j2\pi \frac{2v_{no}}{\lambda} kT_c \right] w[k] w^*[k-l] & l = 0 \\ \sum_{k=0}^{N_c-1} \exp \left[ j2\pi \frac{2v_{no}T_c}{\lambda} kT_c \right] w[k] w^*[k-l] & l \neq 0 \end{cases} \quad (76)$$

With the lag index  $l=0$ , the waveform factor within the summation is simply  $w[k]w^*[k]$  which allows the expression for the autocorrelation mainlobe to be reduced to

$$q[0] = \frac{1}{N_c T_c} \sum_{k=0}^{N_c-1} \exp \left[ j2\pi \frac{2v_{no}T_c}{\lambda} k \right]. \quad (77)$$

Equation (77) indicates that the mainlobe of the matched filter output is therefore modulated by the average of the phase of each chip over the length of the waveform. If the phase varies over the duration of the waveform, the amplitude of the mainlobe will be reduced. If the phase is constant over the waveform period, which is typical for SAL and micro-Doppler motions, the mainlobe output is a measure of the signal phase.

## F. PPN Waveform Doppler Sensitivity

The phase, or Doppler sensitivity of the PPN waveform is exploited in different ways for each imaging mode, but the effects of waveform Doppler sensitivity will impact all

imaging modes. The sensitivity results from mismatches in the matched filter due to ladar/target relative motion induced phase rotations impressed upon returns which in turn result in attenuation of the matched filter peak output. The filter mismatch grows with both increasing line-of-sight velocity and code length, and reaches a minimum each time the Doppler shift induces a  $2\pi$ -radian phase rotation across the full code length.

Figure 22 illustrates this sensitivity using three identical non-contiguous codes, each consisting of  $N_c=20$  phase chips with chip widths  $T_c=1$  ns. The three copies of the code are assumed to have been transmitted, as shown in Figure 22(a), beginning at 0 ns, 50 ns and 100 ns, respectively. Figure 22(b) shows the real component of a representative residual Doppler phase factor (i.e.,  $\cos(4\pi v_o(t-N_c T_c/2)/\lambda)$ ) due to a line-of-site velocity of 3.75 m/s, for a wavelength of  $\lambda=1.5\mu\text{m}$ . The three return signals, modulated by the Doppler phase, were calculated using Eq. (71) are shown in Figure 22(c).

Notice that the first code is relatively unchanged, but that the third has undergone a  $\pi$  phase rotation producing a complete code sign flip. The second code is, however, symmetric about the  $\pi/2$  rotation point causing the two halves of second code to be of opposite sign. The ideal (i.e., zero Doppler compensation) matched filter output, calculated using Eq. (76), is then shown in Figure 22(d) where the time axis is  $kT_c$ . Also, notice that the first and last codes have high amplitude anti-correlated responses due to the Doppler induced phase inversion in the third code. The second return, however, is completely suppressed due to the Doppler induced phase reversal across the code.

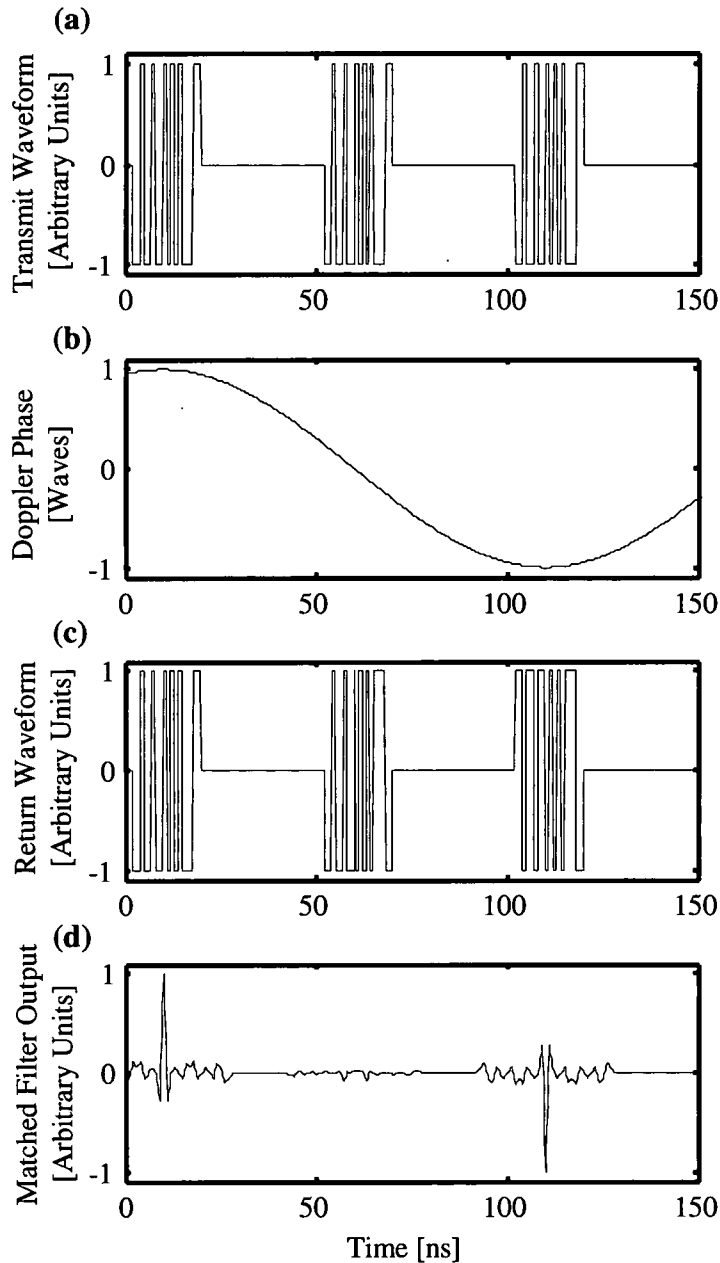


**Figure 22: The effects of residual Doppler phase modulation on PPN waveforms: (a) three identical non-contiguous transmit codes, (b) the real component of the residual Doppler phase modulation for an assumed line-of-sight velocity of 3.75 m/s, (c) the transmitted waveforms after modulation, and (d) the ideal matched filter output.**

Nulls in the matched filter output will therefore occur whenever the Doppler frequency is an integer multiple of the code length  $N_{code}T_c$  according to the relation

$$N_{code}T_c = m \frac{1}{f_d} = m \frac{\lambda}{2v_o}, \quad (78)$$

where  $f_d$  is the Doppler frequency shift,  $\lambda$  is the wavelength and  $v_o$  is the line-of-sight velocity between the ladar and target.

Figure 23 demonstrates the reduction in the absolute peak matched filter output due to Doppler mismatch for PPN waveforms with up to 20,000 phase chips where each chip is of 1 ns duration. To create this figure, the peak of the range-Doppler matched filter output  $q_{RD}(t)$  was calculated using Eq. (77) for three target velocities,  $v_{no} = 1.0$ -m/s, 0.1 m/s and 0.0375 m/s, the results for which are shown by the dotted, dashed and solid lines, respectively.

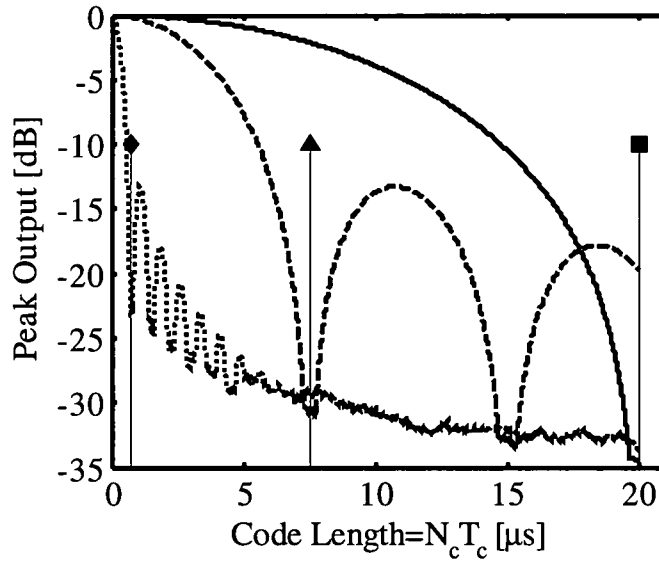


**Figure 23: The peak matched filter output for a binary phase coded waveform is shown as a function of code length for line-of-sight velocities of 1 m/s (dotted line), 0.1 m/s (dash line) and .0375 m/s (solid line). Calculated locations of the matched filter output nulls for these velocities are indicated by the diamond, triangle and square markers, respectively.**

The location of the first nulls corresponding to these three velocities were also calculated using Eq. (78) and are indicated in Figure 23 by the diamond, square and triangle markers, respectively. They are in excellent agreement with the matched filter outputs. Notice that although these curves were specifically calculated for the range-Doppler case, these results are common to all imaging modes where finite residual line-of-sight velocities exist in the signal  $s(t)$  as described by Eq. (8). Figure 23 again indicates that the PPN waveform has significant Doppler sensitivity that increases with increasing code lengths; however, this sensitivity occurs after detection and can be compensated, or exploited, in digital signal processing as required.

To examine the Doppler sensitivity of the PPN waveform in more detail, recall with Eq. (77) which describes the matched filter mainlobe with 1 sample per phase chip. Here, no assumptions are made regarding the magnitude of the line-of-sight velocity  $v_{no}$ . The phase may vary over the waveform duration; therefore, the exponential phase for each chip must be summed for each delay. The waveform phase term times its complex conjugate is unity, but the Doppler factor remains within the summation and impacts the IPR.

To find a closed form for Eq.(77), the summation  $S(N_0, N_1)$  is written as

$$S(N_0, N_1) = \sum_{k=0}^{N_1-1} a^k, \quad (79)$$

where  $N_0$  and  $N_1$  define the extent of the waveform, and the Doppler exponential phase factor is written in terms of  $a^k$  where  $a$  is

$$a = \exp\left(j2\pi \frac{2T_c}{\lambda} v_{no}\right). \quad (80)$$

Multiplying  $S(N_0, N_1)$  by  $a$  results in

$$aS(N_0, N_1) = \sum_{k=N_0}^{N_1} a^{k+1} = \sum_{k=N_0+1}^{N_1+1} a^k. \quad (81)$$

Subtracting Eq. (81) from Eq. (79) yields

$$(1-a)S(N_0, N_1) = \sum_{k=N_0}^{N_1} a^k - \sum_{k=N_0+1}^{N_1+1} a^k = a^{N_0} - a^{N_1+1}. \quad (82)$$

Dividing by  $(1-a)$  yields the summation in closed form as

$$S(N_0, N_1) = \frac{a^{N_0} - a^{N_1+1}}{(1-a)}. \quad (83)$$

If the summation is over the code duration (i.e.,  $N_0=0$  and  $N_1=N_c-1$ ), then the summation may be written

$$S(N_c) = \frac{1 - a^{N_c}}{(1-a)}. \quad (84)$$

Now replacing  $a$  with the original exponential factor yields

$$S(N_c) = \frac{1 - \exp\left(j2\pi \frac{2T_c}{\lambda} N_c v_{no}\right)}{1 - \exp\left(-j2\pi \frac{2T_c}{\lambda} v_{no}\right)}, \quad (85)$$

Bringing half of the exponential factor from the denominator outside the parenthesis, the summation is written

$$S(N) = \frac{\exp\left(-j2\pi \frac{2T_c}{\lambda} \left(\frac{1}{2}\right) v_{no}\right)}{\exp\left(-j\pi \frac{2T_c}{\lambda} v_{no}\right)} \times \left( \frac{\exp\left(j2\pi \frac{2T_c}{\lambda} v_{no} N_c\right) - \exp\left(j2\pi \frac{2T_c}{\lambda} v_{no} N_c\right)}{\exp\left(j\pi \frac{2T_c}{\lambda} v_{no}\right) - \exp\left(-j\pi \frac{2T_c}{\lambda} v_{no}\right)} \right). \quad (86)$$

Finally, the exponential factors may be simplified and written in terms of sine functions as

$$S(N) = \exp\left(j2\pi \frac{2T_c}{\lambda} v_{no} (N_c + 1)\right) \frac{\text{SIN}\left(\pi \frac{2T_c}{\lambda} v_{no} N_c\right)}{\text{SIN}\left(\pi \frac{2T_c}{\lambda} v_{no}\right)}. \quad (87)$$

Using this result the matched filter mainlobe output  $q[0]$  is written

$$q[0] = \frac{1}{N_c T_c} \exp\left(j2\pi \frac{2T_c}{\lambda} v_{no} (N_c + 1)\right) \frac{\text{SIN}\left(\pi \frac{2T_c}{\lambda} N_c v_{no}\right)}{\text{SIN}\left(\pi \frac{2T_c}{\lambda} v_{no}\right)}, \quad (88)$$

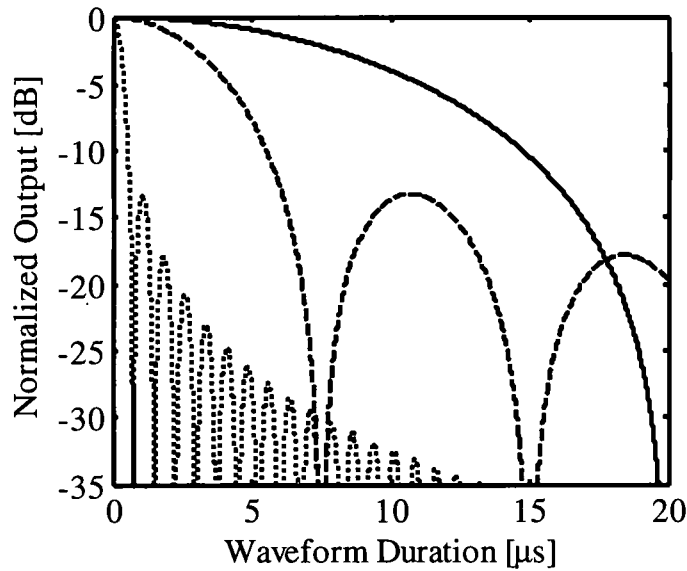
where the exponential factor is the Doppler phase as before, and the sine factor is the modulation of the mainlobe peak output due to phase rotations within a code time. For small  $v_{no}$ , this reduces to the same result using the constant velocity approximation.

Figure 24 shows the reduction in the peak matched filter output due to Doppler mismatch calculated using the theoretic expression of Eq. (88). A 20,000 chip PPN waveform with  $T_c=1$  ns was assumed for targets with 1.0-m/s, 10.0 cm/s and 0.0375 cm/s relative velocities. This theoretical result is in excellent agreement with the simulated results shown in Figure 23. The length of the code imposes stringent requirements on the compensation of the translational Doppler component for efficient compression; however, the compensation is applied post detection in digital processing which allows for adaptive estimation and mitigation before subsequent processing.

### G. PPN Multiple TDM Sub-Code Processing

Figure 24 highlights a conflict between image quality and Doppler tolerance. Sidelobe suppression demands large numbers of code chips in the PPN waveforms, but the

Doppler tolerance decreases with increasing code length. The matched filter for a time division multiplexed (TDM) PPN waveform with  $N_{code}$  sub-codes is shown in Figure 25(a). Here the matched filter consists of the entire composite code. The output has excellent sidelobe suppression for fixed or low velocity targets, but targets with significant radial relative motion have degraded responses.



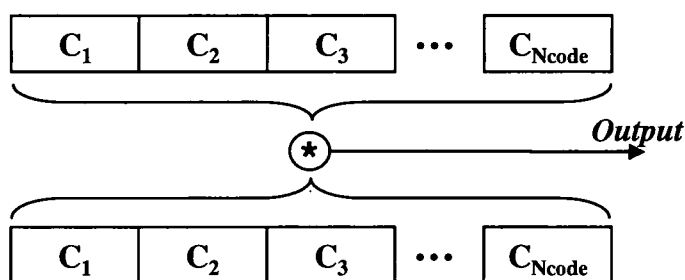
**Figure 24: The theoretical peak matched filter output for a binary phase coded waveform is shown as a function of code length for line-of-sight velocities of 1 m/s (dotted line), 0.1 m/s (dash line) and .0375 m/s (solid line). Calculated locations of the matched filter output.**

Processing the PPN waveform as a composite of sub-codes as shown in Figure 20(b)-(d) mitigates this conflict [49,50,51]. As discussed previously, a single PPN sub-code provides the requisite resolution defined by the chip length,  $T_c$ . The multi-sub-code matched filter structure is shown in Figure 25(b). Now, the overall matched filter convolution is broken up and computed on a sub-code basis, and the Doppler tolerance is increased  $N_{code}$  times. The individual sub-code matched filter outputs have sidelobe suppression inversely

proportional to the sub-code length  $N_c$ , but coherent summation of the individual sub-code matched filter complex outputs will provide suppression corresponding to the full length waveform.

For large velocities, the phase from each sub-code is measured and used to correct the sequence further before the composite IPR is formed.

(a) *Multiple code matched filter*



(b) *Composite combination of multiple single sub-code matched filters*

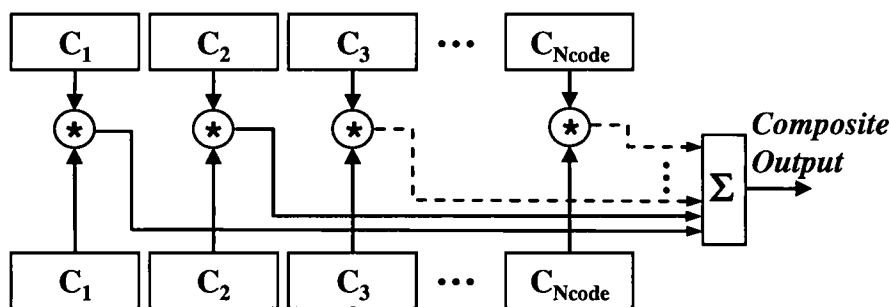


**Figure 25: Single matched filter for a multi-code PPN waveform (a), and the composite output for multiple single sub-code matched filters (b).**

The behavior of the composite IPR was simulated for a waveform with  $N_{code}=20$  sub-codes with  $N_c=1000$  phase chips in each sub-code. The left plot of Figure 26 shows the IPR for a single PPN sub-code. The sidelobes are relatively large, but in good agreement with

the theoretical values. The right plot of is Figure 26 shows the composite IPR formed by the coherent combination of the IPRs of 20 sub-codes as described in Figure 25. As expected, the sidelobes are significantly reduced and are in good agreement with the theoretical values. Figure 27 shows the variation of the sidelobe levels (circles) as a function of the number of processed sub-codes ranging from 1 to 20 sub-codes.

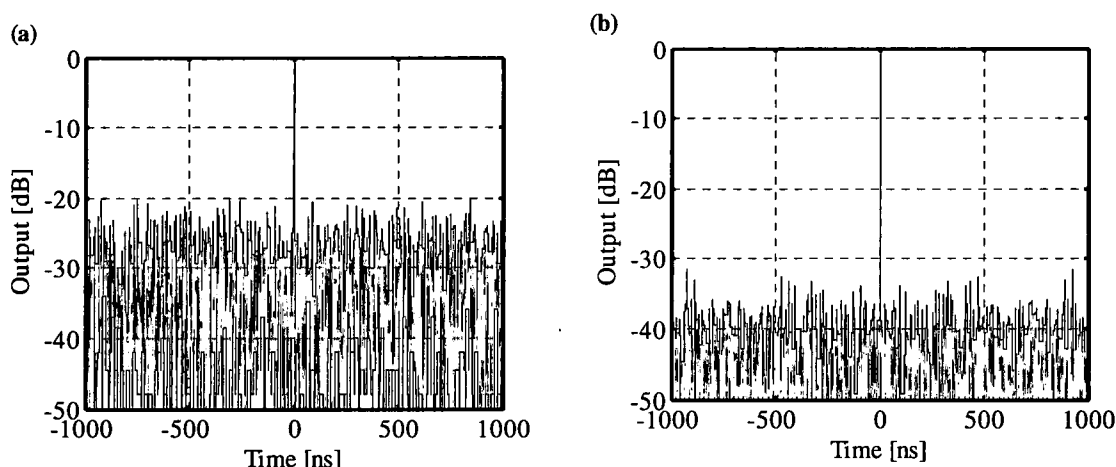


**Figure 26: IPR for a single matched filter processed waveform (a) and for the composite of 20 TDM matched filtered processed sub-codes (b).**

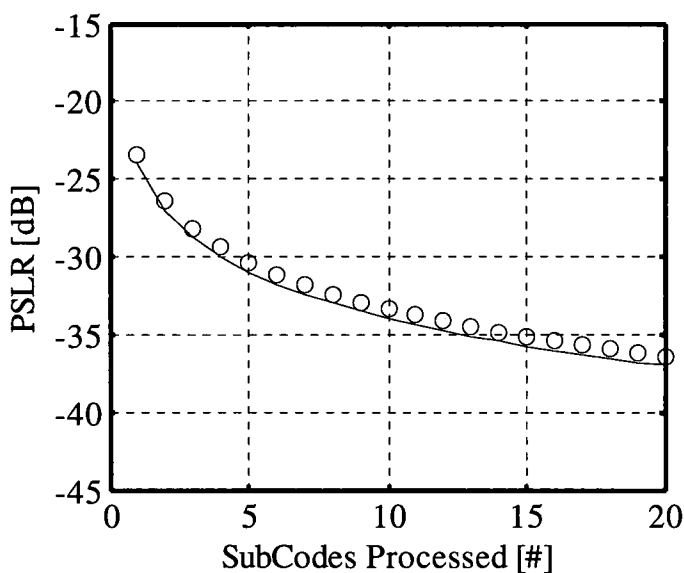


**Figure 27: Composite sidelobe level as a function of the number of TDM sub-codes processed.**

The expected peak sidelobes, assumed to be two times the sidelobe standard deviation, is also plotted (solid line) is in excellent agreement with the simulated results.

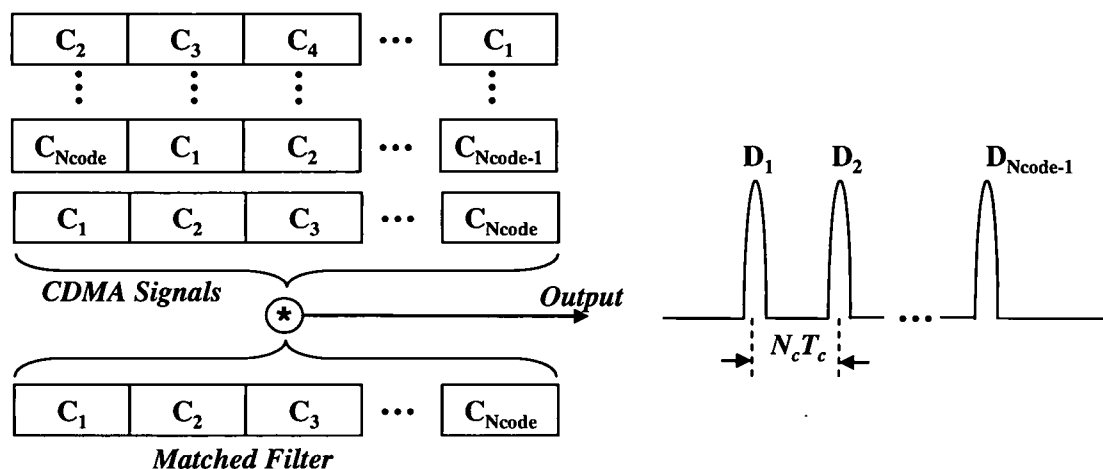
## **H. PPN Multiple CDMA Sub-Code Processing**

The use of CDMA has two significant benefits. First, since the multiple codes are transmitted within the same time period, the Doppler offset is greatly reduced and the Doppler tolerance is increased. Second, CDMA enables the use of multiple coherent apertures. Processing the TDM composite waveform provides better Doppler tolerance without sacrificing sidelobe suppression. Applying the PPN waveform with code division multiple access multiplexing also increases the Doppler tolerance, but more importantly enables multiple aperture radar. The matched filter structure for CDMA processing of  $N_{code}$  signals each with  $N_{code}$  TDM sub-codes is shown conceptually in Figure 28. In Figure 28(a), all of the delayed codes are transmitted simultaneously. The received signal is processed with a single matched filter containing all 20 sub-codes. The output consists of  $N_{code}$  time separated IPRs each delayed by a sub-code length. Each of the outputs  $D_1$ - $D_{N_{code}}$  has the identical properties of a single PPN waveform of the same length with the exception of an increased noise floor due to the superposition of the uncorrelated sidelobes of the other codes.

Figure 28(a), shows CDMA processing by sub-code matched filter. The composite return is again the super position of all the transmitted waveforms, but now each of the  $N_{code}$  sub-code matched filters shown in dashed boxes are applied to each time interval of the return. The result is  $N_{code}$  independent IPR's in each time interval. Since all of the codes are transmitted and received at the same time, the Doppler tolerance is much greater, and the

complex IPRs may be summed either in TDM as described previously or within each time slot.

(a) Multiple code CDMA with a single matched filter



(b) Composite CDMA combination of multiple single sub-code matched filters

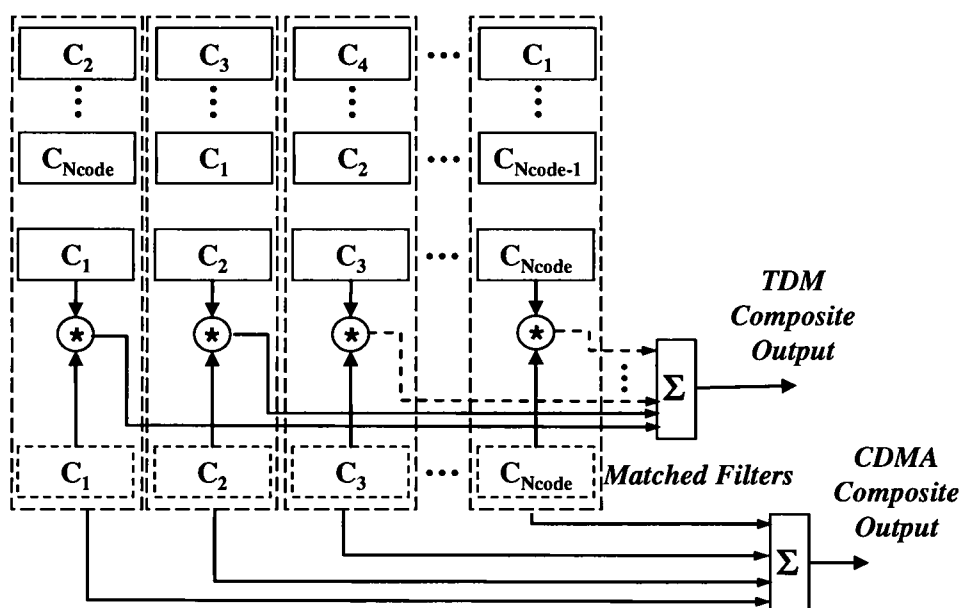


Figure 28: CDMA matched filter structures for (a) a single matched filters, and (b) for a bank of sub-code matched filters.

The CDMA approach provides variable Doppler tolerance, but more importantly, it can enable multiple aperture operation with minimal increases in hardware and processing. Application to multiple apertures is discussed further in Chapter XII.

## **CHAPTER VI**

### **PPN EXPERIMENTAL SYSTEM**

In this chapter, an experimental system is presented which was designed to demonstrate the key aspects of the generation, detection and utilization of PPN waveforms in ladar systems. The system demonstrates pulse compression which is common to all imaging modes, as well as the phase measurements required for each imaging mode. Finally, the system supports the demonstration of multiple aperture operation.

This chapter presents a description of the essential elements of the PPN ladar system. The majority of the system is common to all of the imaging modes, but slight variations of the system are used as necessary to demonstrate each mode. These variations are primarily confined to the transceiver output optics, the targets, and the post processing. A detailed description of the basic system is presented in the following sections as well as the points where modifications are introduced. The details of the modifications are described in the chapters where they are required.

The ladar experimentally demonstrates four key functions. First, the generation, transmission and reception of the PPN waveform is demonstrated. The waveforms must be sufficiently long that the measurements requiring the greatest phase sensitivity, micro-Doppler and synthetic aperture imaging, are supported. Second, range compression which is common to all of the imaging modes is demonstrated. Third, phase recovery from the compressed data is demonstrated. The sampling of the phase is sufficient to support all

imaging modes. Finally, the efficacy of the code division multiple access (CDMA) in multiple aperture ladar is demonstrated where the focus is on multiple aperture compression and phase recovery. The system also demonstrates secondary properties such as the ladar performance as a function of CNR and code length.

### A. Laboratory Ladar System Description

The laboratory ladar system shown in Figure 29 was designed to generate, transmit, detect and record long sequence PPN waveforms.

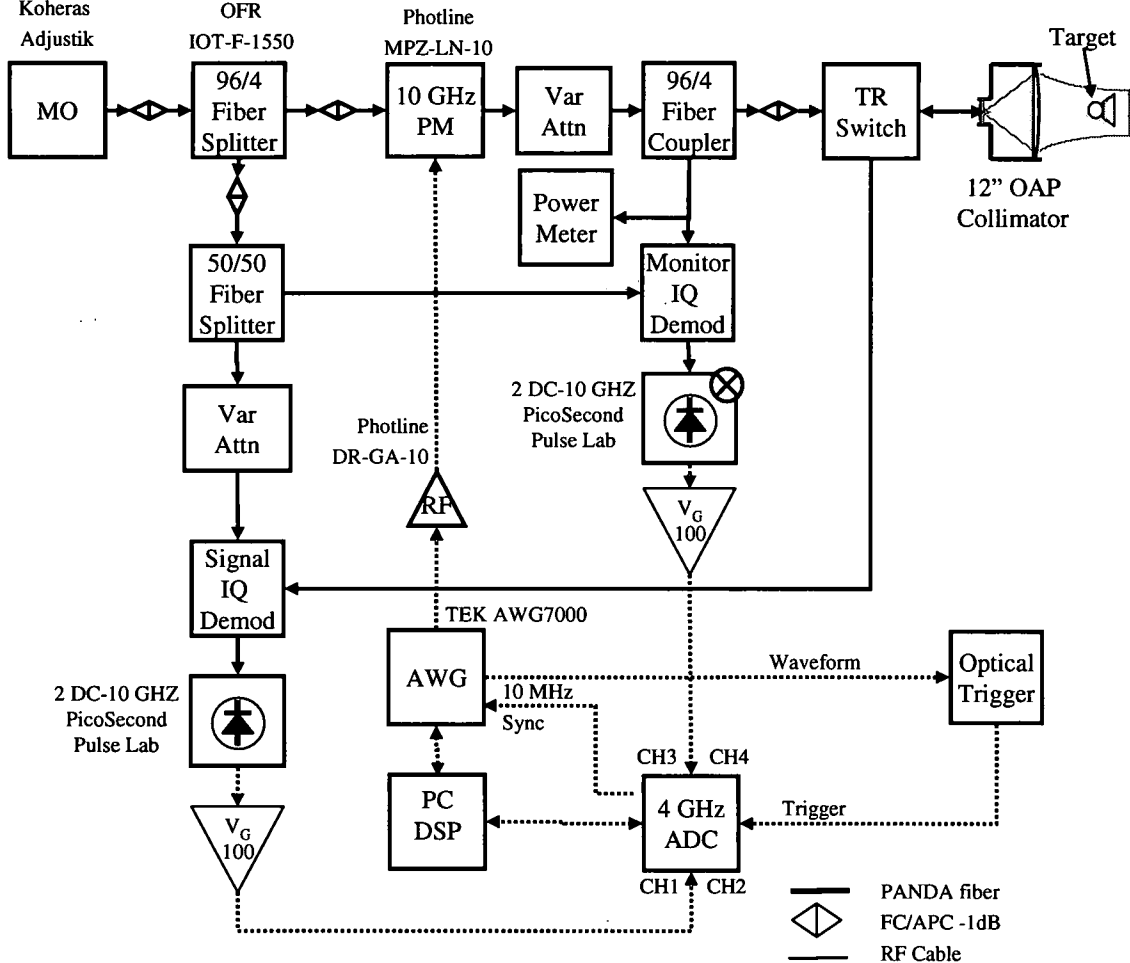


Figure 29: Preliminary PPN ladar experimental setup.

The PNN ladar system is an optical fiber based system and operates at a wavelength 1.5 micrometers. The stable master oscillator (MO) is a continuous wave (CW) Koheras Adjustik laser with a nominal spectral linewidth less than 1 kHz and a maximum CW output power of 135 mW. The MO provides the optical phase reference for the system. The MO output is split into two legs with a 96:4 fiber splitter.

The high energy MO leg serves as the foundation of the transmitted waveform and is injected into a 10 GHz phase modulator (PhotLine MPZ-LN-10) where the binary phase modulation is applied. The phase modulator electrical input signal is supplied by a Tektroniks 7200 arbitrary waveform generator (AWG). The AWG waveform was created in MATLAB and loaded into the AWG memory. Once activated, the waveform is transmitted continuously. PNN waveforms with phase chips as short as 0.25 nanoseconds were demonstrated, but 1.0 nanosecond phase chips were used throughout this research. The 1-volt binary signal produced by the AWG is amplified and offset (Photline DR-GA-10 RF Amplifier) to produce the 0 and  $V_\pi$  voltages required to produce, respectively, 0 and  $\pi$  phase shifts in the optical modulator.

The output of the phase modulator was then inserted into a fiber coupled variable attenuator. Although not required in an operational system, the attenuator is used here to adjust the transmit power without changing the operating conditions for the remainder of the system. The signal is split again using a second 96/4 fiber splitter. The high energy leg is input into a fiber coupled, free space transmit and receive switch. The T/R switch output is fiber coupled to the transmission optics. Three fiber coupled transmission optics configurations are used depending on the requirements of the experiment. A large aperture configuration is used in the majority of imaging demonstrations. A small output aperture is

used to support measurements where large excursions in CNR are required. Finally, a multi aperture configuration is used to demonstrate the CDMA based multi-aperture operation. The large aperture configuration is described below. The other two are described in conjunction with the experiments where they are used.

In the large aperture output configuration, the energy exiting the T/R switch is fiber coupled to a mode matching lens coupled to a 12 inch circular off axis parabolic (OAP) collimating mirror. The collimated beam illuminates a variety of fixed and moving targets. The discussion of the target details is deferred and presented in conjunction with the experiments in which they are used.

The light returning from the target is collected from the transmission optics, passes through the return path of the T/R switch, and is mixed with the un-modulated (reference) fraction of the MO in a quadrature demodulator, as described in Chapter 3. The resulting in-phase and quadrature (IQ) signals are detected at baseband on a fiber coupled 10 GHz photo detector (PicoSecondPulse Labs).

A portion of the transmitted waveform is split off using the 96/4 fiber splitter prior to the transmit receive switch. This monitor waveform is demodulated using a quadrature demodulator and detectors identical to the signal path. This monitor signal measures the exact state of the waveform on transmission so system variations can be mitigated. The monitor channel picks off a small portion of the transmit energy using the fiber splitter just prior to the transmit/receive switch. This monitor contains the majority of the phase noise introduced by the system, but none of the target signal and transmit path induced noise. In practice, this monitor can be used to correct the system phase variations; however, for the

short path within the laboratory, the monitor path is not required since the phase noise is low over these short ranges.

The in-phase and quadrature components of the signal and monitor are digitized and stored on four channels of an Aqiris 582 digitizer at 4 GS/second; however, at the short range within the laboratory, only the signal channel is recorded. The resulting waveform records are transferred to a personal computer (PC) for post processing and analysis.

### **B. Experimental PPN Waveform Generation and Pulse Compression**

Detailed results are presented for each imaging mode in subsequent chapters. Selected early results are presented here as an introductory demonstration of the operation of the PPN ladar and to illustrate some of the salient properties of the PPN system. For this preliminary demonstration, a PPN code was generated with  $N_c=1000$  bi-phase code chips, each  $T_c$  2 ns in length. Figure 30(a) shows a short sequence of the ideal code as well as the return from the corner cube target vibrating at 2 kHz. The ideal transmitted PPN waveform (solid line) is collected from the monitor channel and represents the voltage applied to the phase modulator driver. The monitor channel was then thresholded to recover the matched filter kernel. Comparison of representative segments of the nominal transmitted waveform and the received waveforms verifies the transmitted waveform corresponds to the matched filter kernel from the AWG. A short sequence of the matched filter kernel was temporally registered with the optical signal (dashed line) returned from the vibrating target. Although the return power is relatively low with a carrier to noise ratio only slightly greater than unity, inspection shows good agreement between the kernel and the returned signal.

Ideal and experimental range compressed IPRs were then computed by applying, respectively, the matched filter kernel to itself and the returned optical signal and are shown in Figure 30(b).

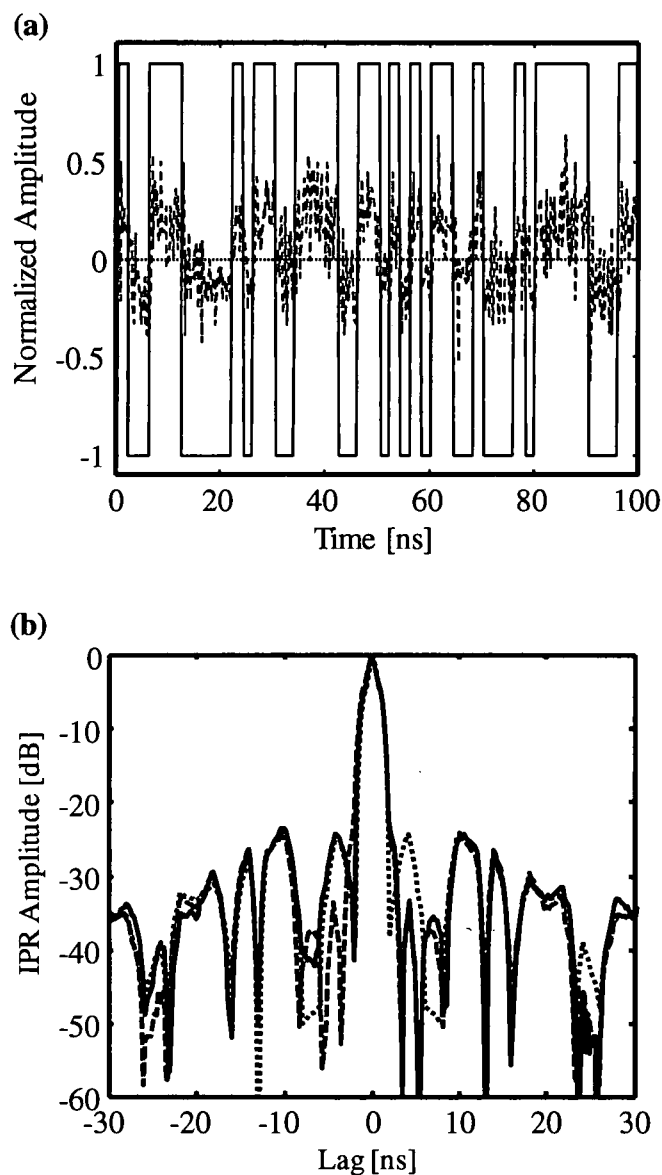


**Figure 30: (a) A segment of the Ideal PNN waveform (solid line) has been temporally registered with corresponding chips of the detected signal (dashed line) from the vibrating target. (b) The ideal (solid line) and measured (dashed line) IPRs are in excellent agreement with one another.**

The measured IPR (dashed line) is in close agreement with the theoretical IPR (solid line) demonstrating excellent IPR performance of the PPN waveform for ladar applications. This not only demonstrates the expected compression of the waveform, but highlights the fact that a nearly 0 dB waveform CNR is sufficient to produce an IPR with nearly ideal sidelobe structures.

### **C. Preliminary Phase Measurements**

Long record matched filter processing was then applied to detected waveforms using the recovered PPN kernel. In particular, as shown in Figure 31 (a), normalized peak values of the zero-lag, matched filter output for a series of 2500 sequentially transmitted code segments was recorded and plotted along a slow-time axis. This is equivalent to examining peak values of sequential range slices from the complete phase history and is proportional to instantaneous target displacement. Figure 31(b) then shows the normalized spectral amplitude obtained by taking the Fourier Transform of Figure 31(a) with respect to the slow-time axis. The low frequency broadening is attributed to non-ideal drift and other imperfections of the 2 kHz shaker, seen also in Fig. Figure 31(a), yet the results demonstrate excellent phase recovery and correct localization of the target's vibration spectrum using PPN waveforms. This important result, although for a vibrating target, demonstrates phase detection which is common to each of the modes.

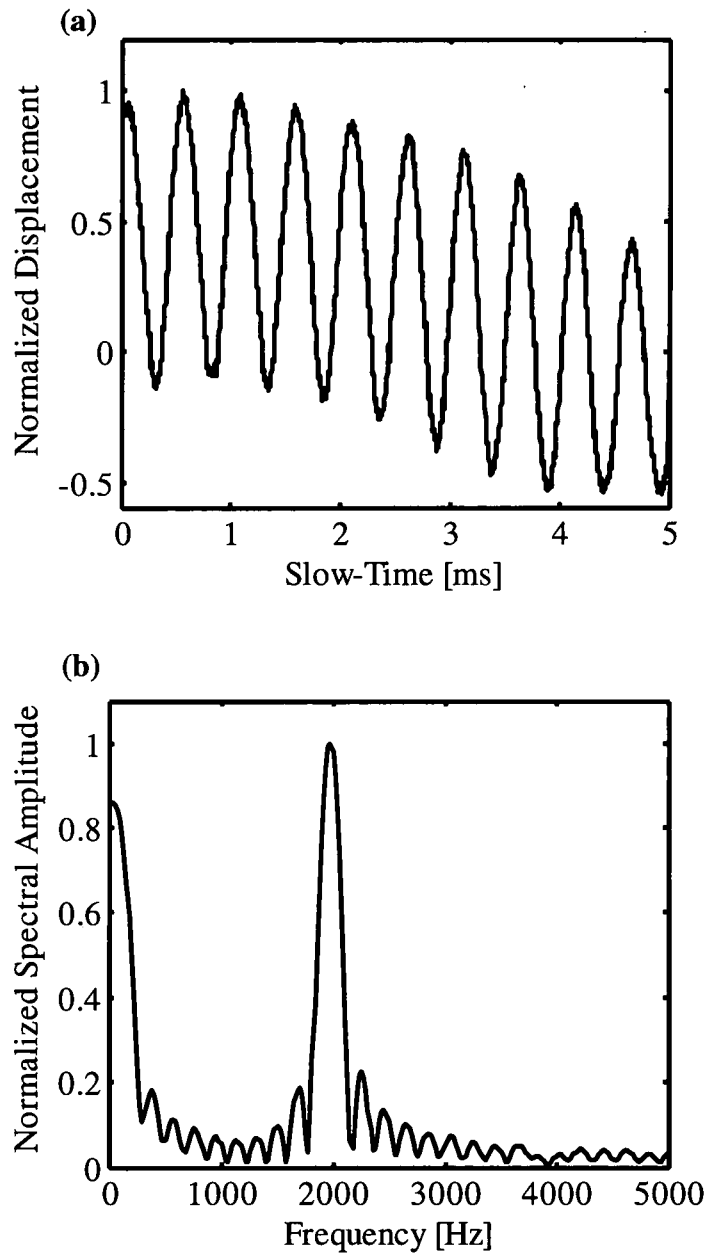


**Figure 31: The experimental micro-Doppler phase history for a 2 kHz vibrating target (a) and the corresponding normalized amplitude spectrum (b) demonstrate excellent phase recovery when using PPN waveforms and matched filter processing.**

#### D. PNN Waveform Combination

Either the coherent or incoherent addition of multiple matched filter outputs will allow enhanced performance in the presence of noise when using PPN waveforms in any of the various imaging modes. This will in turn allow the energy used per measurement to be adapted to varying measurement conditions, such as target range and atmospheric transmission. To illustrate, we will examine range compression performance in the presence of additive noise.

First consider Figure 32(a). The solid in this figure curve represents the ideal, range compressed IPR for a 1000 chip PPN waveform with  $T_c = 2\text{ns}$ . The dashed and dotted curves represent, respectively, the coherent addition of 10 and 100 sequentially measured, range and cross-range IPRs. The shaker in our experimental apparatus was turned off when making these measurements, and only the central autocorrelation peak and the nearby sidelobes are shown in each case. Note that in Figure 32(a) the CNR of the detected signal prior to any post detection processing was approximately unity (i.e.,  $\text{CNR}=0\text{ dB}$ ). We see in this case that there is little benefit in sidelobe suppression performance obtained by processing multiple waveforms. With CNRs approaching unity, nearly ideal sidelobe performance is possible after examining only a single PPN waveform return.

Now consider Fig. Figure 32(b). Again, the solid curve in this figure represents the ideal, range compressed IPR for a 1000 chip PPN waveform with  $T_c = 2\text{ns}$ . The dashed and dotted curves also represent, respectively, the coherent addition of 10 and 100 sequentially measured and range compressed IPR's. In this case, though, prior to range compression electronic white noise was added to the detected waveforms, creating pre-processing CNRs of approximately  $-20\text{ dB}$ .

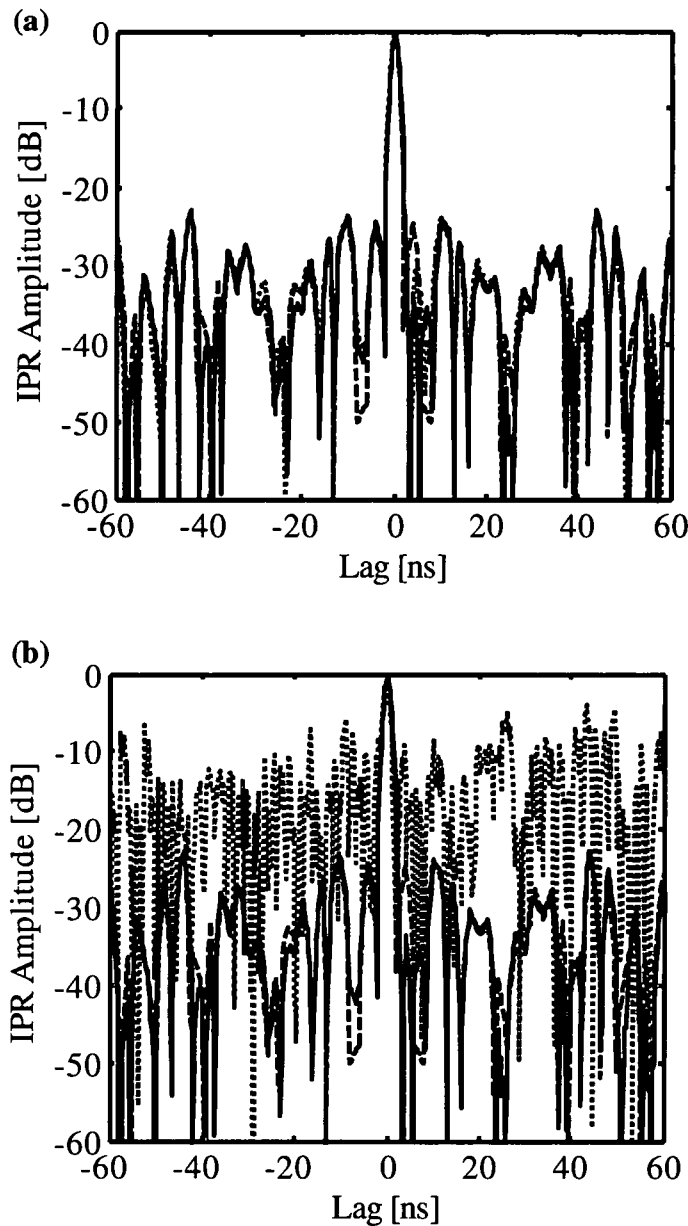


**Figure 32: The ideal (solid curve), range compressed IR for a 1000 chip PPN waveform with  $T_c = 2$  ns. The dashed and dotted curves represent, respectively, the coherent addition of 10 and 100 sequentially measured, range compressed IPR's. In (a) the experimental CNR is  $\sim 0$  dB, while in (b) the CNR is approximately -20 dB.**

After coherently processing only 10 waveforms we see that the peak sidelobes are suppressed on the order of -10dB, while after processing 100 waveforms the sidelobe suppression is

approaching ideal performance. Note that continued integration of additional waveforms will not reduce sidelobes significantly once they become dominated by the correlated sidelobe structure of the transmitted codes as in Figure 32(a). In fact, in practice only enough codes should be processed to yield the desired peak-to-sidelobe ratio. Notice that in all cases, the 3 dB resolution is approximately the same; however, the single waveform output would produce relatively low quality images even though the resolution metric was satisfied.

These preliminary demonstrations show that this PPN ladar system satisfies the four experimental requirements including PPN waveform generation, temporal compression, and phase recovery as well as operation over a wide CNR range. The waveforms are constructed as a single long pseudo-random sequence and is therefore orthogonal by design, CDMA operation is also possible; however, demonstration of CDMA will be deferred until Chapter XII.

## CHAPTER VII

### GENETICALLY OPTIMIZED PPN IPR

The periodic pseudo noise waveform allows the conflicting requirements of diverse imaging modes to be satisfied utilizing a single transmitted waveform combined with flexible, adaptive signal processing. Short optimized codes such as the Barker codes have been previously developed, but were only defined for relatively short code lengths [13]. Selection of longer pseudo noise codes is often accomplished by exhaustive search, but is impractical for long codes or if specific properties are desired within the resulting IPR.

The PPN waveform  $w(t)$  was first presented in Eq. (64) and is rewritten here for convenience as

$$w(t) = \frac{1}{\sqrt{N_{code} N_c T_c}} \sum_{p=1}^{N_{code}} \sum_{m=1}^{N_c} u_{(p-1)N_{code}+m} \text{rect}\left(\frac{t - (p-1)N_{code}T_c - (m-1)T_c}{T_c}\right). \quad (64)$$

where  $N_{code}$  is the number of mutually orthogonal sub-codes each of length  $N_c$  chips and the phase of the  $m^{\text{th}}$  chip is  $u_m = \exp(j\phi_m)$ . The non-optimized PPN waveform has randomly distributed sidelobes across all range values outside of the mainlobe where the sidelobe level variance is inversely proportional to the effective number of processed chips [11]. However, the range window of interest for a laser radar is relatively small due to the small beam footprint at the target. This fact is exploited to produce a waveform whose IPR behavior is significantly enhanced within the range window.

## A. Genetic Optimization of the IPR

A genetic algorithm (GA) is utilized to both optimize the IPR performance within a selected range window as well as reduce the number of code possibilities which must be searched. The PPN waveform has an effectively white spectrum which leads to an IPR with relatively large, random sidelobes. For imaging applications, it is important to reduce the sidelobes as much as possible since high peak and average sidelobes result in ghost images and contrast loss, respectively. Increasing the length of the code decreases the amplitude of the sidelobes, but also increases the Doppler sensitivity of the waveform.

The IPR sidelobes are significantly reduced by exploiting the relatively small range window of interest in ladar. Figure 33 shows an example IPR of a random binary code obtained by matched filter processing.

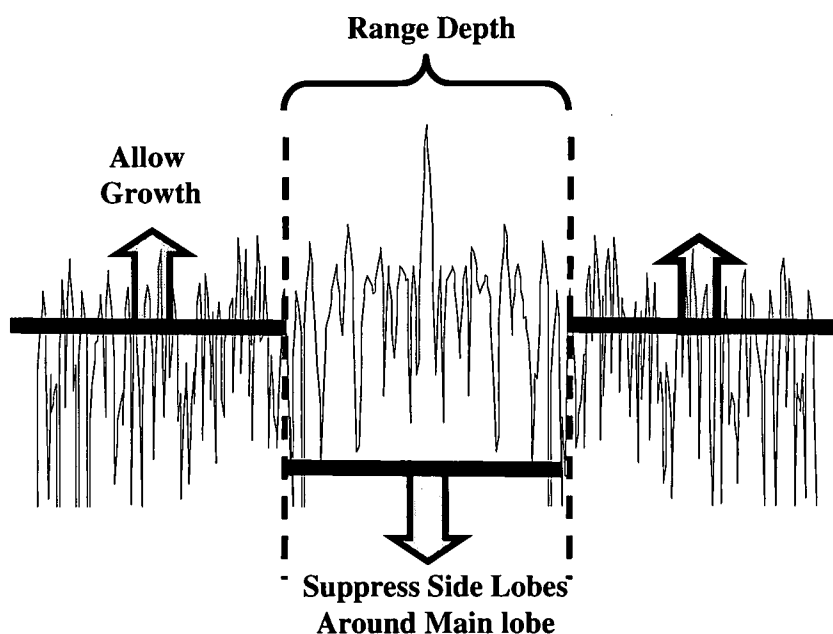


**Figure 33: PPN IPR optimization for finite a range depth allows increased sidelobes outside of the region and suppresses the sidelobes within the desired range window.**

A genetic algorithm is used to select a PNN sequence which suppresses the sidelobes of the IPR in the region of interest near the mainlobe at the expense of slight sidelobe level growth outside this region. The block diagram of the genetic algorithm is shown in Figure 34. The algorithm creates an initial random binary code, and then breaks the code into  $N_g$  equal length sequences, or genes [52].

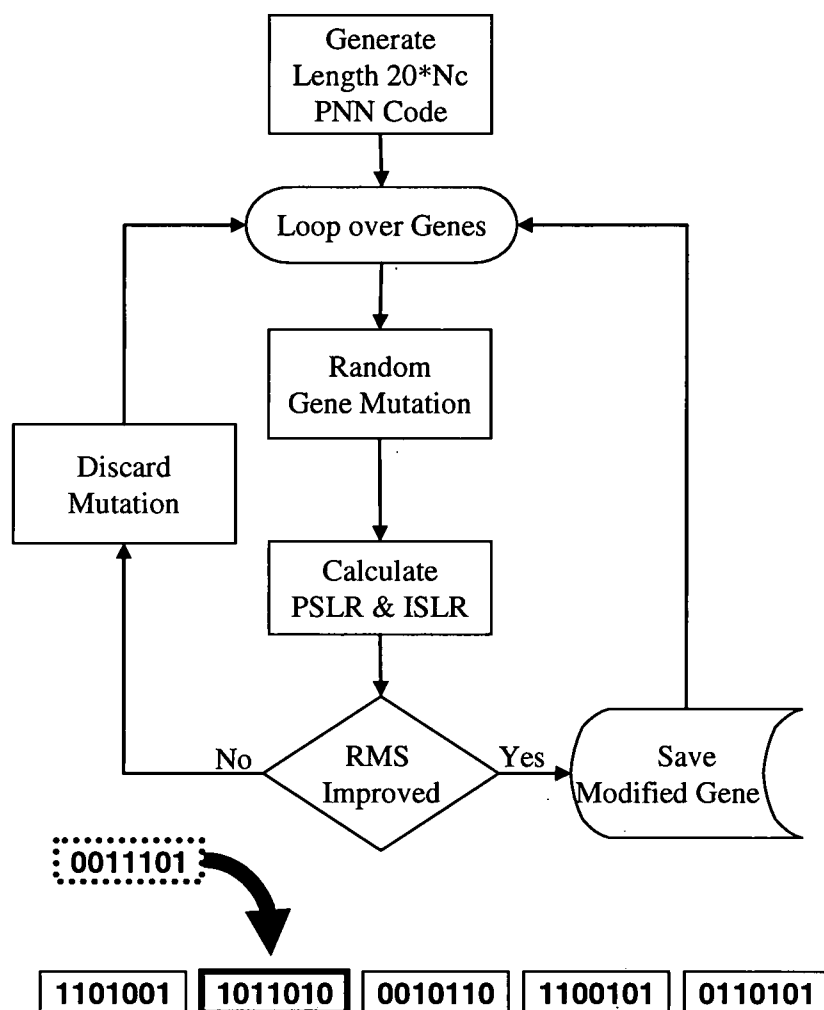


**Figure 34: Block diagram of the genetic algorithm used to optimize pseudo noise sequences.**

Each gene is then sequentially mutated by replacing the entire gene with a new random binary sequence. The peak sidelobe ratio (PSLR) and integrated sidelobe ratio (ISLR) of the composite code are then calculated within the desired range window. A cost function  $C$  was defined as the RMS sum of the PSL and ISL as

$$C = \sqrt{PSL_{\Delta R}^2 + ISL_{\Delta R}^2}, \quad (89)$$

where the subscript  $\Delta R$  denotes calculation of the range window of interest. If the mutation fails to reduce the cost function, then the new gene is discarded in favor of the previous gene.

If the new gene does yield an improvement, the mutation replaces the old gene and becomes part of the new composite sequence. The process is then repeated with the next gene.

Using the RMS sum of the PSL and ISL as the cost function ensures that both ratios are reduced equally, producing similar improvements in both image contrast and image ghosting.

Variations of this cost function are implemented to provide different emphasis to these or other image metrics.

The convergence of the genetic algorithm for a 20,000 chip code (i.e.,  $N_c=1000$ ,  $N_{code}=20$ ) and a 200 chip gene length is shown in Figure 35(a). A range window of 600 ns (i.e., ~90 m) was assumed which is sufficient to fully image a wide variety of targets. The path begins with relatively high normalized PSL and ISL in the upper right to the final lower values in the lower left. The resulting genetically optimized IPR is shown in Figure 35(b) and demonstrates the desired sidelobe notch over the range window surrounding the mainlobe. The ISLR and PSLR were improved by approximately 8 dB and 10 dB, respectively. These results were achieved after 84 successful mutations out of approximately 100,000 trials. The convergence path varies with each trial, but the overall character of the

convergence is similar. The rate of improvement slows with the number of successful mutations, but this still represents a vast improvement over exhaustive search of the  $2^{N_{code}N_c}$  possibilities in the composite code.

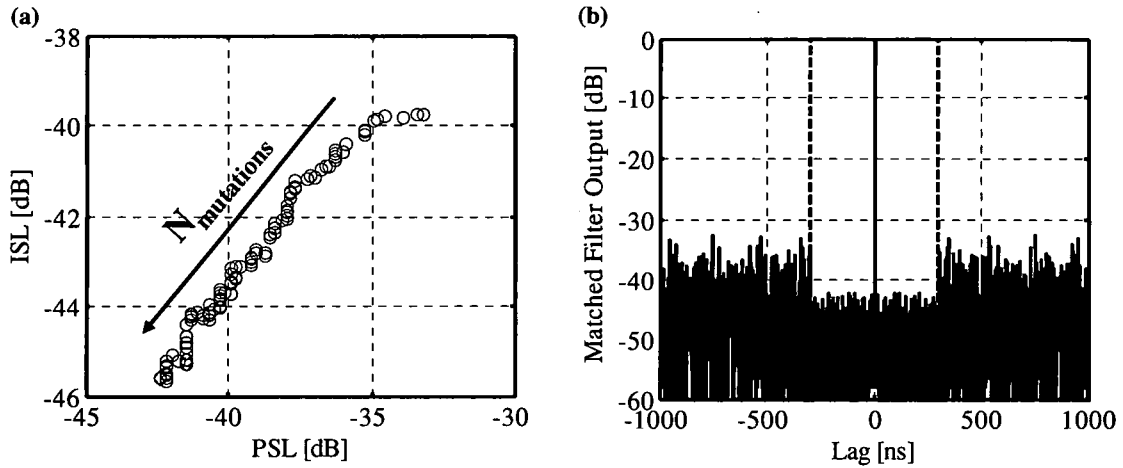


**Figure 35: The genetic ISL/PSL algorithm path of convergence (a) and corresponding genetically optimized IPR for a 20,000 chip waveform within a range window of 600 ns, or 90 m, around the IPR mainlobe.**

## B. Genetic Algorithm Convergence with Code Length

Both the PSLR and the ISLR of a binary pseudo random waveform depend inversely on the length of the code. The impact of the code length on the GA IPR is examined by characterizing the sidelobe performance as a function of code length. Randomly selected codes and genetically optimized codes were created for a single PNN waveform (i.e.,  $N_{code}=1$ ) and waveform lengths  $N_c$  from 1,000 to 20,000 chips. Figure 36(a) compares the PSLR and ISLR for randomly chosen PNN codes (open squares and circles) and genetically optimized codes (solid squares and circles) as a function of code length. The bold solid line shows the predicted  $1/N_c$  ISLR for a randomly selected PNN waveform. Both the randomly selected and genetic waveforms follow the  $1/N_c$  trend line, but the GA produces a nearly 6 dB improvement for both the PSLR and ILSR. Figure 36(b) shows a 20,000 chip GA IPR

and illustrates the relative enhancements within the range window. Since the range window is short compared to the waveform, the PSL (circle) and ISL (dashed line) of the GA IPR outside of the notch are similar to that of the randomly selected code.

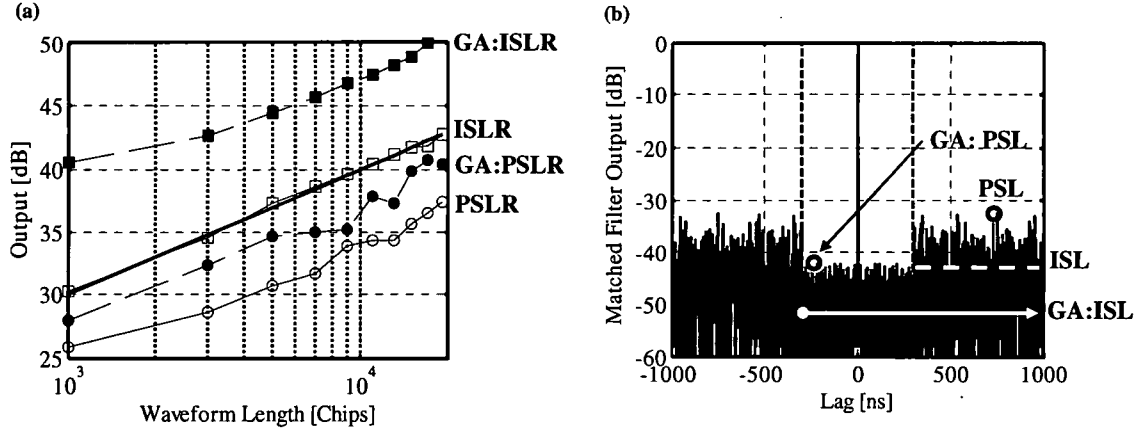


**Figure 36: Genetic algorithm convergence as a function of code length.**

### C. Genetic Algorithm Experimental Demonstration

The simulated GA-IPR results were experimentally validated with the ladar system shown in Figure 37. The system is a continuous wave, fiber based system operating at a wavelength 1.5 micrometers and is designed to generate, transmit, detect and record long sequence PPN waveforms. The master oscillator (MO) was a Koheras Adjustik laser with nominal spectral bandwidth less than 1 kHz. The MO was split with a 96/4 fiber splitter. The high energy leg was injected into a PhotLine MPZ-LN-10 10 GHz phase modulator used to produce the  $\pi$  phase shifts on the 1 nanosecond code chips. The GA-PPN code was loaded into a Tektronix 7052 arbitrary waveform generator (AWG) and then conditioned using a Photline DR-GA-10 radio frequency amplifier to produce the  $V_\pi$  voltages by the modulator.



of an Aqiris 582 digitizer at 4 GS/second. The resulting waveform was transferred to a PC for post processing and analysis.

The ideal IPR of the genetically optimized, composite code is shown in Figure 38(a). The IPR was generated via matched filtering the noiseless code with itself. The 600 ns central notch in the range window is clearly visible providing more than a 6 dB improvement in ISLR. Again, the sidelobes of a normal PNN pulse are similar to those outside of the GA-PNN notch region. The measured IPR is shown in Figure 38(b) is centered at the target location and is in excellent agreement with the simulated result. It clearly demonstrates the IPR improvement over the range extent. The dashed line shows the calculated ILSR level for a randomly selected PNN waveform.

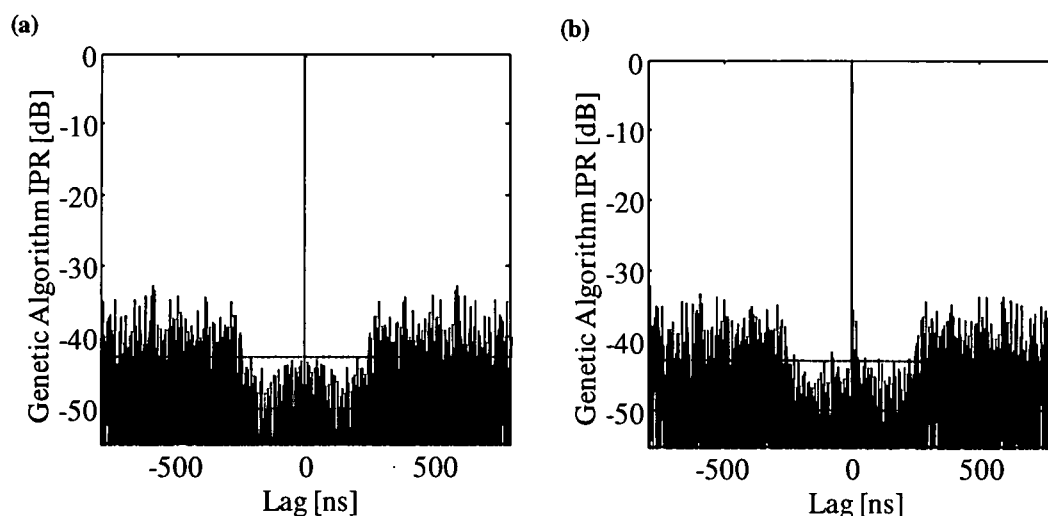


**Figure 38: Ideal (a) and measured (b) IPRs of a genetically optimized PNN sequence and the randomly selected PNN waveform ISL (dashed line).**

#### **D. CNR Impact on the Genetic Algorithm IPR**

Using the GA-PNN, the peak sidelobes are reduced below the ISLR of a random PNN waveform. Both the simulated and measured IPRs shown in Figure 40 are for high CNR signals (i.e.,  $\text{CNR} \approx 0$  dB). To investigate the performance with decreasing CNR, the measurements are repeated while systematically reducing the transmit power. The transmit power is reduced using the variable attenuator prior to the T/R switch as shown in Figure 39, and was monitored with the power meter as shown. The remainder of the receiver operating conditions remained unchanged for all measurements. The power was initially set to a level just sufficient to fully realize the GA-IPR notch (i.e., single waveform  $\text{CNR} \approx 0$  dB). The transmit power attenuation was then varied from 0 dB to -35 dB in approximately 5 dB increments. The PSLRs were calculated and are shown in Figure 39. For each attenuation level, the PSLRs were calculated from the same return for the entire IPR (All) and for the genetic algorithm notch region (GA). The CNR of the waveform at 0 dB attenuation was approximately one. As the attenuation is increased, the sidelobes are dominated by noise and the theory line represents the ideal waveform PSLR minus the attenuation level.

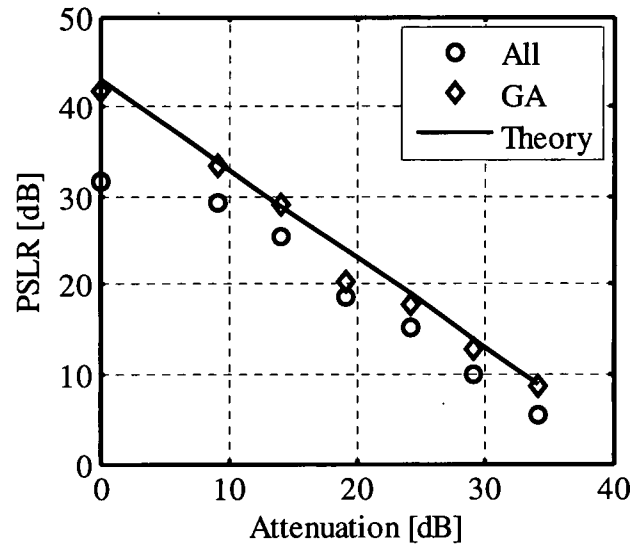


**Figure 39 PNN Waveform and genetically optimized PSLR as a function of transmit attenuation.**

The high CNR GA-PSLR exhibits nearly a 10 dB performance increase over a randomly selected PNN waveform at high CNR. As the attenuation increases and the CNR decreases, both PSLRs decrease; however, the PSLR for the genetically optimized waveform provides more than a 3 dB enhancement even at the highest attenuations levels.

### **E. Genetic Algorithm Composite IPR**

As discussed earlier, processing the waveform as  $N_{code}$  individual sub-codes provides flexibility to tailor the Doppler sensitivity and energy usage to changing imaging requirements. Here, the composite GA-IPR is examined as a function of number of sub-codes processed. Each sub-code is matched filtered independently, and the composite IPR is formed by the coherent superposition of each of the  $N_{code}$  complex IPRs. Figure 40 shows the GA-IPR from measured data for a single sub-code (a) and the superposition of 20 sub-

codes (b). The single code CNR is insufficient to fully realize the GA-IPR notch, but the notch is clearly shown in the composite IPR.

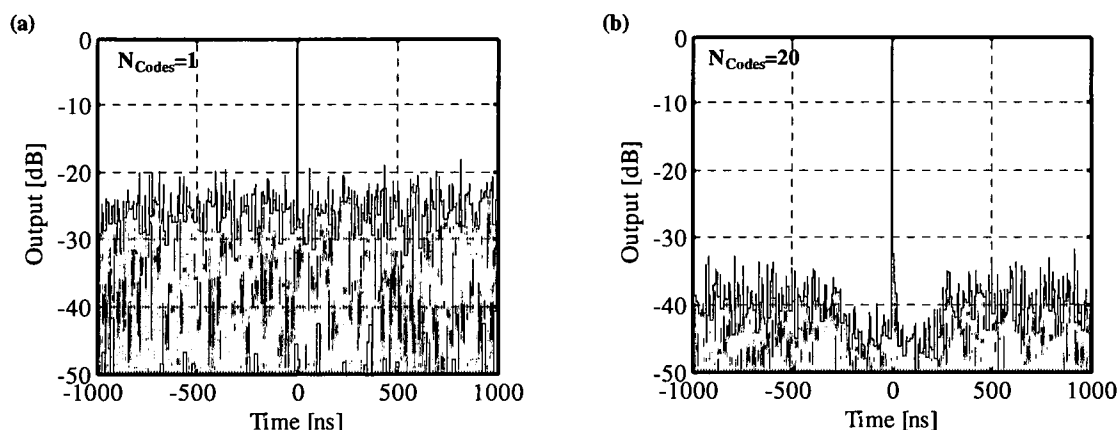


**Figure 40: The GA-IPR for a single sub-code (a) and the superposition of 20 sub-codes (b).**

Figure 41 shows the predicted  $4/N_c$  PSLR (line) and the measured PSLR (circles) as a function of the number of sidelobes included in the composite IPR. The PSLR generally follows the predicted line. The GA-IPR performs worse than expected at low code numbers. This may be do to the fact that the cost function constrained only the composite waveform performance not the individual sub-codes.

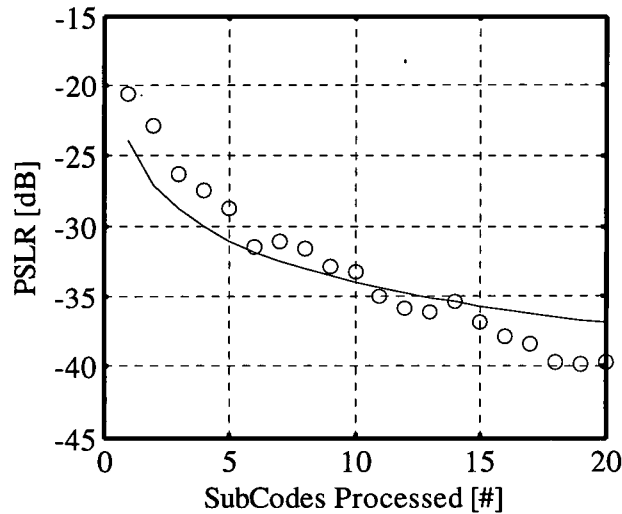


**Figure 41: Comparison of the composite IPR (circles) and complete code IPR as a function of the number of 1000 chip sub-codes processed.**

Without specific constraint, the individual codes may perform worse than the composite. The GA-IPR notch develops as the composite waveform CNR increases as the number of codes is increased. The single code PLSR varies over the 20 sub-codes and indicates that additional cost function constraints could possibly provide more uniform performance.

## **F. Multi-Notch IPR**

Section VII, A noted that the GA cost function used to optimize the IPR could be adapted to provide more complicated structures within the IPR. Here, the cost function is modified to support multiple aperture operations via PPN waveforms and code division multiple access (CDMA) processing. The details of multi-aperture CDMA are discussed in Chapter XXI, but the genetically optimized waveform is developed and presented here, as well as its resulting IPR.

The multiple aperture configuration used is based on code division multiple access where the transmitted codes are also time delay multiplexed by one code length. This requires a composite waveform IPR with sidelobe notches at integral multiples of the sub code length  $N_c$ . The cost function  $C$  is again based on the RMS sum of the PSL and ISL within the desired notch region. In this case,  $C$  is computed for multiple notches across the duration of the composite IPR and is written as

$$C = \frac{1}{N_{code}} \left[ \sum_{n=1}^{N_{code}} PSL_{\Delta R;n}^2 + ISL_{\Delta R;n}^2 \right]^{1/2}, \quad (90)$$

where  $PSL_{\Delta R;n}$  and  $ISL_{\Delta R;n}$  are computed within the range window  $\Delta R/T_c$  centered at the  $n^{\text{th}}$  code location. Figure 42(a) shows a genetically optimized IPR for a 20,000 chip composite code consisting of  $N_{code}=20$  sub-codes. For this example, each of the  $N_{code}$  range regions of interest is 500 chips in duration. Figure 42(b) shows the central region of the composite IPR where the sidelobe suppressed notches are more clearly visible.

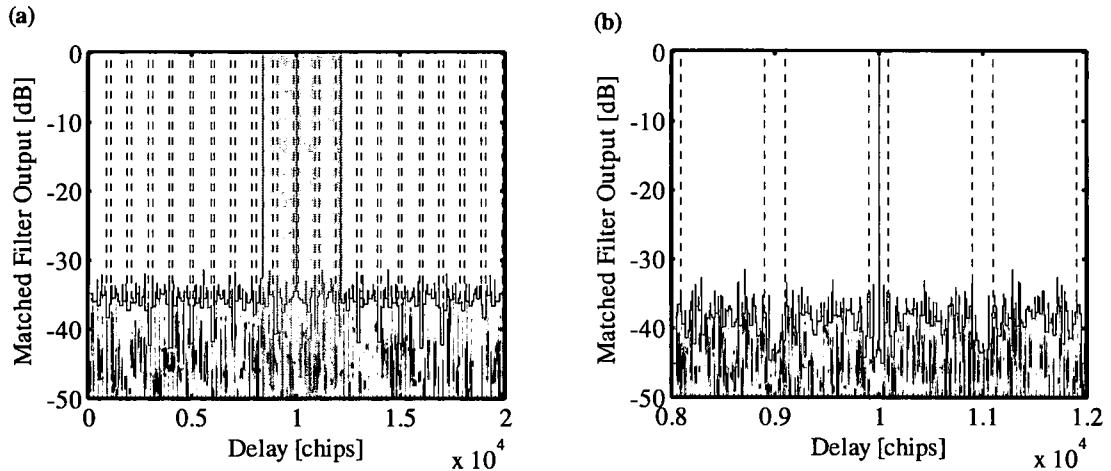


**Figure 42: Optimization regions for multiple notch GA-IPR (a) and expanded view of the mainlobe and adjacent IPR notches.**

A typical convergence for a 20 notch IPR is shown Figure 43. Note that the multiple notch regions  $N_{code}\Delta_R/T_c$  are a much greater fraction of the total number of code chips  $N_{code}N_c$ ; therefore, the genetic algorithm convergence is much slower than the single notch IPR case.

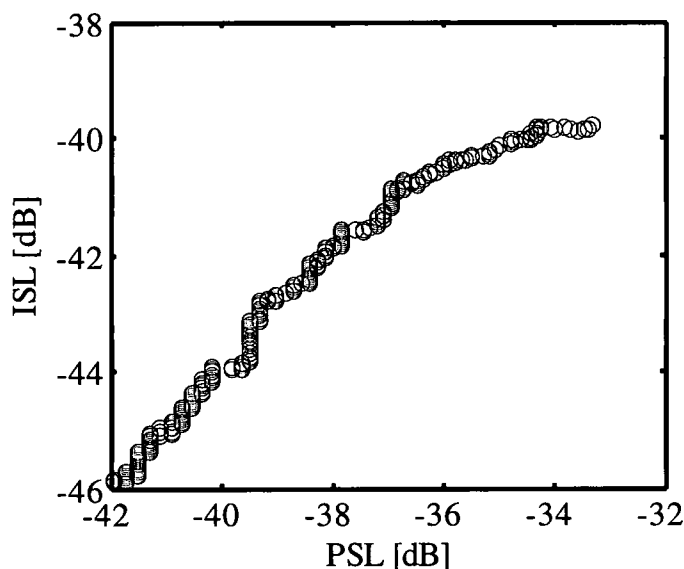


**Figure 43: Genetic algorithm ISL/PSL convergence for 20 notch IPR.**

Although the IPR notches are developed and do provide significant performance gain, the final PSLR and ILSR in the multiple notch IPR are elevated with respect to the single notch IPR. It may be possible to modify the algorithm to recover the full performance by reducing the gene size or allowing flexible gene sizes and locations, but these variations are beyond the scope of this research.

Periodic, pseudo noise sequences were shown to provide the capability to make simultaneous high range resolution and high phase resolution measurements in a multifunction imaging radar. Genetically optimized waveforms provide an additional performance enhancement by simply guiding the selection of the transmitted code to optimize the IPR with selected regions. The GA-PPN waveform is demonstrated in

simulation and laboratory experiment and is applied to multiple imaging modes in the subsequent chapters.

## CHAPTER VIII

### PPN RANGE IMAGING

A range image, or range profile, localizes the individual scattering centers within a beam width as a function of range resulting in range-intensity image. The most important factors governing the performance of range imaging are range resolution and sidelobe levels. In this chapter, simulations are presented for the PPN waveform as well as the two commonly used waveforms. The performance of the PPN waveform for range imaging was also experimentally verified.

#### A. Simulated PPN Ladar Range Imaging

A PPN range image is simulated using the range matched filter output  $q_R(t)$  of Eq. (10). Here a single on axis target is assumed at a range of 20 km (i.e.,  $(x_n, y_n, z_n) = (0 \text{ km}, 20 \text{ km}, 0 \text{ km})$ ) with both unity beam amplitude and target cross section (i.e.,  $A=\sigma_1=1$ ). Figure 44 shows the PPN temporal matched filter output (solid line) for a point target which is the ideal point-target response (IPR). The PPN IPR is calculated for a 1000 chip code and is compared to the IPR for a linear frequency modulated (LFM) waveform  $w_{LFM}(t)$  (solid line) and an un-modulated temporal Gaussian pulse  $w_G(t)$  (long dashed) which are defined as

$$w_{LFM}(t) = \frac{1}{\sqrt{T_w}} \text{rect}\left(\frac{t}{T_w}\right) \exp\left(\pm j\pi \frac{B}{T_w} t^2\right) \quad (91)$$

and

$$w_G(t) = \exp(-\ln(2)t^2 B^2), \quad (92)$$

respectively [11].

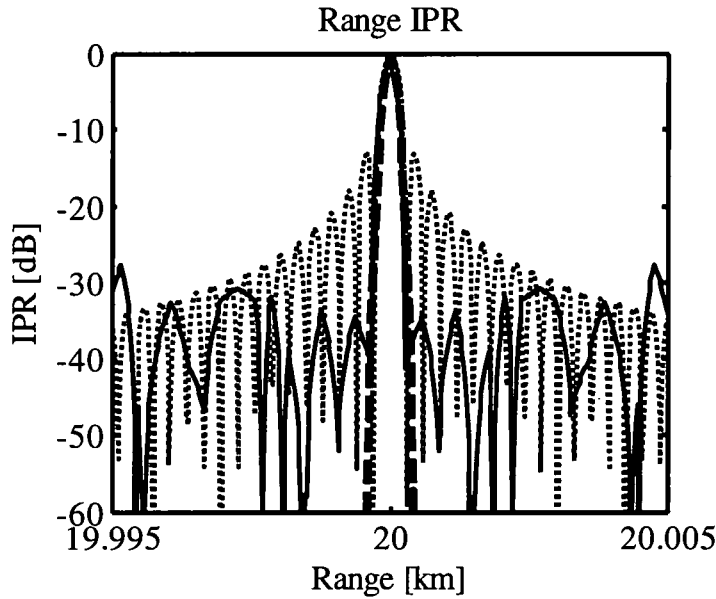


**Figure 44: Range IPR for the: PPN (solid line), LFM (dashed line), and unmodulated Gaussian (dashed line) waveforms.**

The temporal bandwidth  $B$  was assumed to be 1-GHz for each of the three waveforms resulting in a PPN waveform chip duration  $T_c$  of 1 ns, and a 1 ns full width, half maximum (FWHM) Gaussian pulse width.

The temporal IPR mainlobe resolution is nearly identical for each of the waveforms, but significant differences are apparent in the sidelobes. The Gaussian pulse is transform limited and produces the smallest sidelobes (<60 dB), but is a relatively low average power waveform. In practice, long range high resolution imaging may require peak transmit powers that are prohibitively high. The LFM compressed waveform, however, produces IPR sidelobe levels (-13 dB) which peak near the mainlobe and decay with distance from it. The LFM is also a high duty cycle Doppler tolerant waveform, but experiences range-Doppler coupling

resulting in an ambiguity between a target's velocity and spatial location [11]. Finally, the PPN waveform produces sidelobe levels of generally less than -30 dB which are randomly distributed with distance from the mainlobe. The PPN waveform is also a high duty cycle waveform with adaptively selectable Doppler tolerance, or sensitivity. Smaller codes, or code segments, are processed to provide the required Doppler tolerance.

### **B. Range Imaging Experimental PPN System**

The range imaging experiments are designed to demonstrate PPN operation with multiple targets, demonstrate the expected IPR width and sidelobe performance, and to characterize the IPR radar performance as a function of CNR. Multiple targets will appear as the superposition of targets within the return as described by Eq. (74).

The configuration of the laboratory radar used is shown in Figure 45. Since the operation is at short range, it uses only the signal channel omitting the monitor channel of the complete system as described in Chapter VI. Each transmitted waveform has 20 sub-codes with 1000 bi-phase code chips each 1-ns in duration. The composite 20  $\mu$ s waveform is generated and transmitted continuously. The transmitted power is monitored using the low energy leg of the 96/4 splitter and the power meter preceding the transmit/receive switch. The variable attenuator in the transmit leg is used to vary the transmitted power without changing the operating conditions of the receiver.

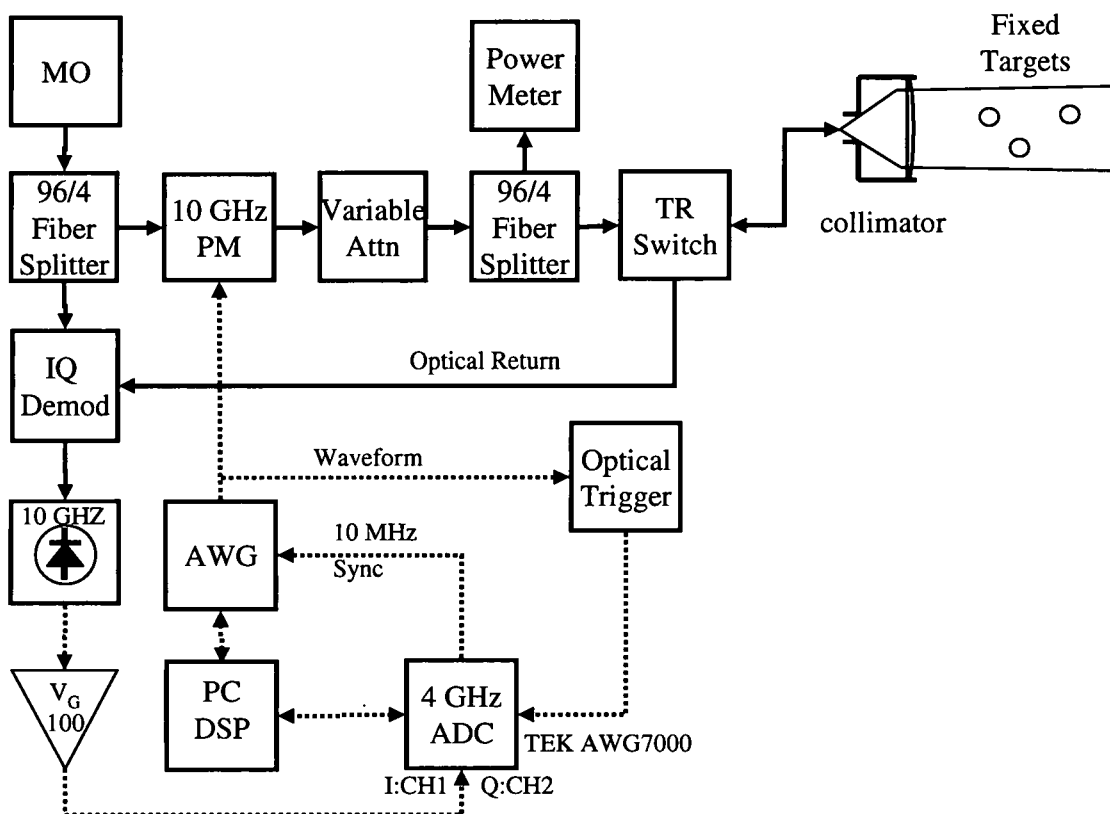


**Figure 45: Range imaging experimental ladar block diagram.**

After the T/R switch, the energy is collimated using the off axis parabolic (OAP) mirror as shown in Figure 46 to allow for spatially distributed targets. The OAP focal length and diameter are 280 cm and is 30 cm, respectively.

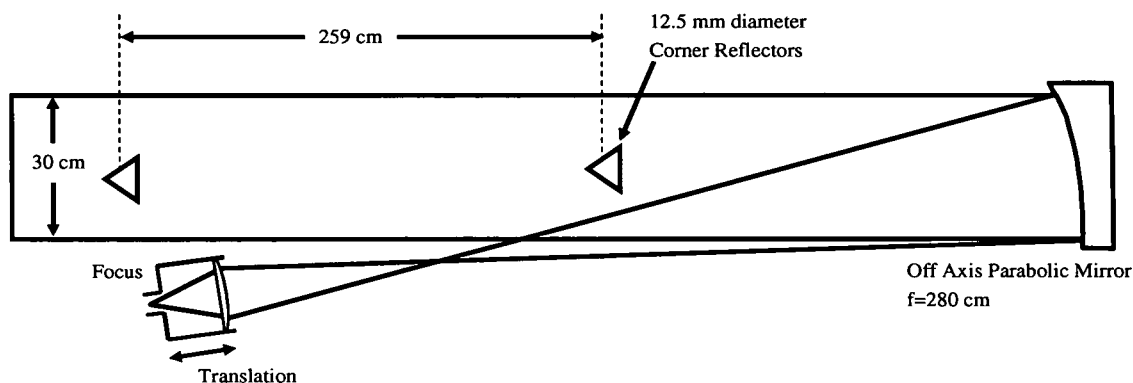
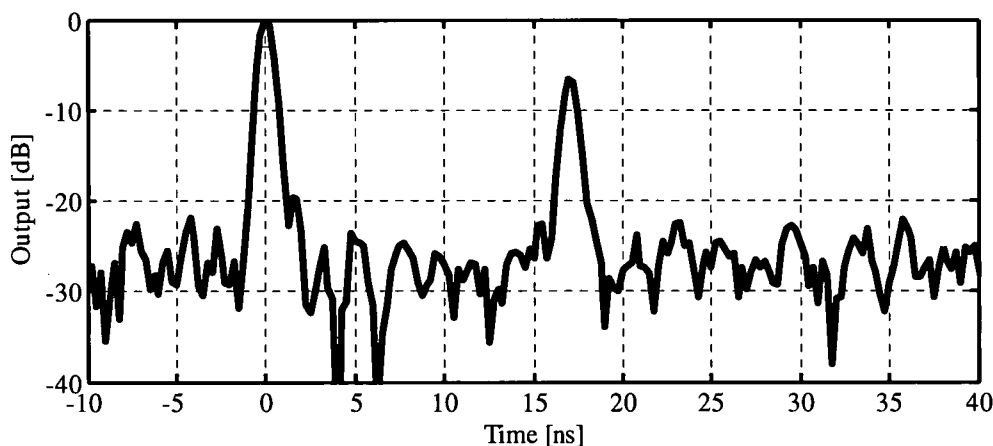


**Figure 46: Range imaging collimator and target placement diagram.**

The fiber coupled transmit energy is mode matched to the OAP by adjusting the focus of the mode matching optics to provide the desired beam divergence. The output beam is then collimated by translating the mode matching optics with respect to the OAP. Note that with the transmit beam expanded to the diameter of the OAP, the combination of the system optical efficiency, target coupling losses, and the limited input power (i.e., 135 mW), unity waveform CNRs cannot be achieved. The target, also shown in Figure 46, consists of two 12.5 mm diameter corner cubes separated in range by 259 cm which corresponds to a time delay of 17.28 ns.

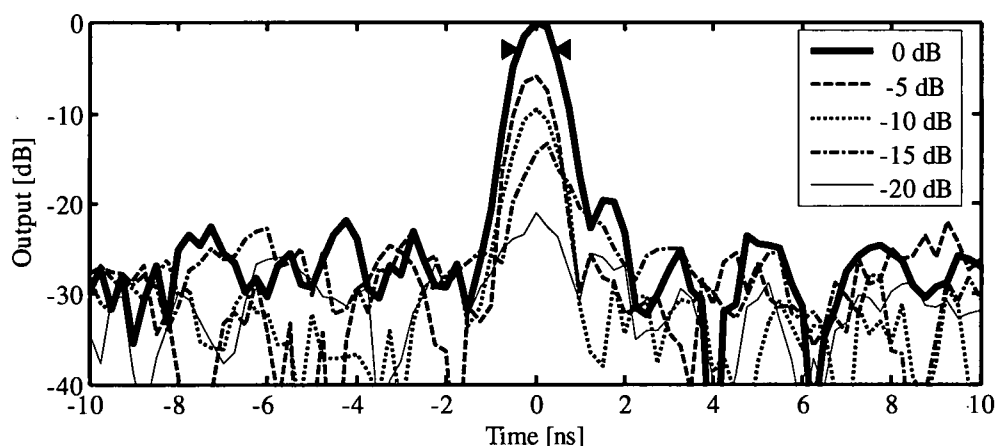
### C. PPN Range Image Experimental IPR

Figure 47 shows the range IPR after matched filter processing for the two targets where the matched filter center is defined at the center of the first target. The range delay between the targets is in excellent agreement with the measured separation. The PSL is -23 db which is degraded by approximately 20 dB from the theoretical limit for a 20,000 chip waveform,



**Figure 47: Range image IPR for two range separated point targets.**

but is consistent considering the reduced single waveform CNR produced in this configuration. Figure 48 shows the variation of the IPR as the single waveform CNR is attenuated. An additional 20 db of attenuation produced an IPR mainlobe peak on the order of the sidelobes which is consistent with an initial single waveform CNR of -20 dB.



**Figure 48: Range IPR variation as a function of single waveform CNR.**

The triangular markers in Figure 48 indicate the FWHM width for 0 dB attenuation. The measured width is in agreement with the theoretical value of 0.5 ns for a waveform with a 1 ns chip duration. As expected, the fidelity of the mainlobe decreases as the peak height becomes comparable to the waveform noise floor.

## CHAPTER IX

### RANGE-DOPPLER IMAGING

The PPN waveform was used to simulate range-Doppler imaging for three point targets similar to those shown notionally in Figure 2. Unity beam amplitudes and target cross sections (i.e.,  $A=\sigma_n=1$  for all  $n$ ) are assumed. Targets 1, 2 and 3 will be assumed to be located at  $(x_1, y_1, z_1) = (-0.25 \text{ m}, 20000.25 \text{ m}, 0.0 \text{ m})$ ,  $(x_2, y_2, z_2) = (0.0 \text{ m}, 20,000.0 \text{ m}, 0.0 \text{ m})$  and  $(x_3, y_3, z_3) = (0.5 \text{ m}, 19999.5 \text{ m}, 0 \text{ m})$ , respectively. Target 1 had an assumed line-of-sight velocity  $v_{1o} = 0.5 \text{ m/s}$  toward the ladar, while target 2 was assumed to be moving away from the ladar at  $v_{2o} = 0.25 \text{ m/s}$ . Target 3 was assumed to be stationary with  $v_{3o} = 0 \text{ m/s}$ , and the wavelength was assumed to be  $1.5 \mu\text{m}$ . Figure 49(a) then shows the real component of the range compressed phase history for a series of 300, 1000 chip PPN waveforms with 1-ns chip widths, (i.e.,  $T_w = N_c T_c = 1 \mu\text{s}$ ). Note that the real component is shown since it can illustrate both the amplitude of the target return as well as the phase variation.

Figure 49(a) was created by first calculating the range-Doppler matched filter output of Eq. (74) for each transmitted waveform (fast-time dimension) and then constructing the slow-time history by “vertically” aligning the matched filter output of each code sequence. This effectively samples the slow-time dimension every  $N_c T_c$  seconds (i.e., in this case the PRF was  $1/N_c T_c$ ). Note that in range-Doppler imaging, sinusoidal variations in phase are due to constant target velocities. As a result, target 3, with zero velocity, exhibits constant amplitude along the slow-time axis. The range-Doppler image, shown in Figure 49(b), was

then calculated by performing a Fourier transform operation with respect to the slow-time dimension.

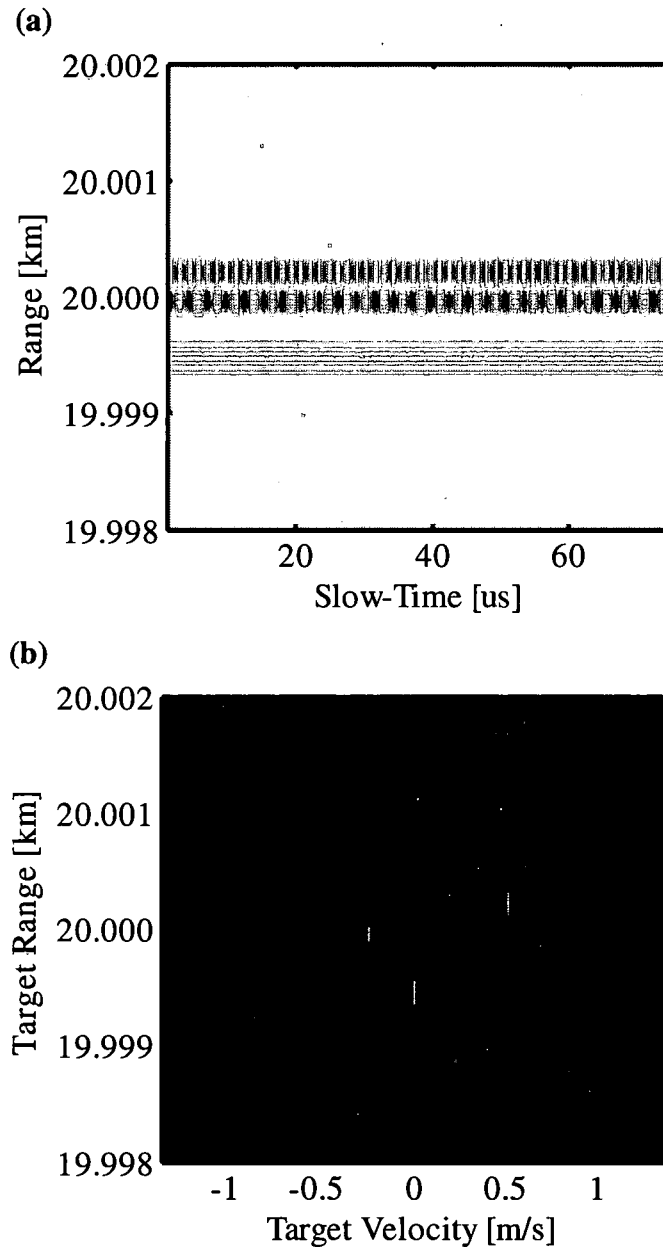


**Figure 49. (a) The real component of the range compressed Macro-Doppler phase history for three targets illuminated with a  $T_c=1\text{ns}$  PPN waveform. (b) The fully compressed range-Doppler image correctly identifies each target's range and velocity.**

Note that the image correctly localizes both the range and velocity for all targets. Also recall that the range resolution is governed by the PPN fast-time matched filter IPR, while the Doppler resolution is limited by the observation time or maximum code separation.

### **A. Range-Doppler Experimental System**

The experimental system shown in Figure 50 is used to demonstrate the capture of the phase associated with translating (or rotating) targets, the effects of Doppler sensitivity, and sub-code and filter bank processing of the signals. In addition, the use of Doppler compensation will be discussed.

The configuration of the laboratory ladar used is shown in Figure 50. Since the operation is at short range, it uses only the signal channel omitting the monitor channel of the complete system as described in Chapter VI. Each transmitted waveform has 20 sub-codes with 1000 bi-phase code chips each 1-ns in duration. The longer chip length is used here to better illustrate the Doppler sensitivity by increasing the Doppler sensitivity of the waveform. The composite 20  $\mu$ s waveform is generated and transmitted continuously. The transmitted power is monitored using the low energy leg of the 96/4 splitter and the power meter preceding the transmit/receive switch. The variable attenuator in the transmit leg is set for maximum transmission.

After the T/R switch, the energy is collimated using the off axis parabolic (OAP) mirror as shown in Figure 51 to allow for spatially distributed targets. The OAP focal length and diameter are 280 cm and diameter is 30 cm, respectively. The fiber coupled transmit energy is mode matched to the OAP by adjusting the focus of the mode matching optics to

provide the desired beam divergence. The output beam is collimated by translating the mode matching optics with respect to the OAP.

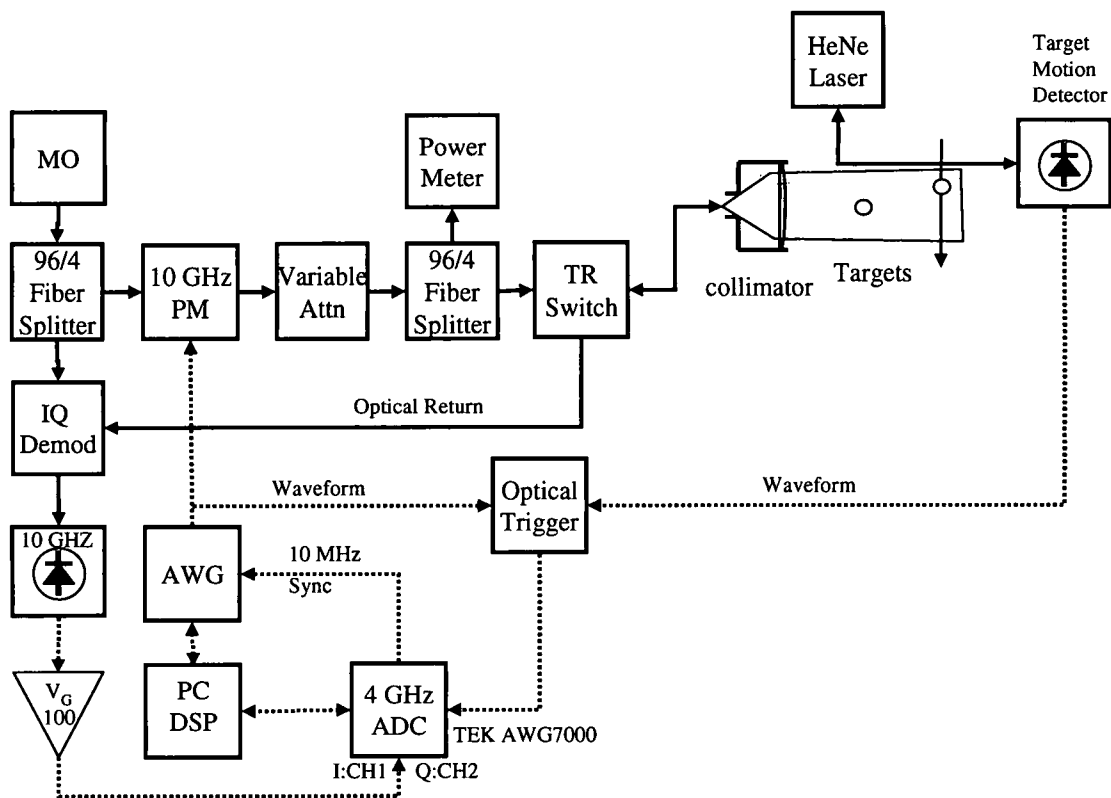


**Figure 50: Range-Doppler experimental ladar block diagram.**

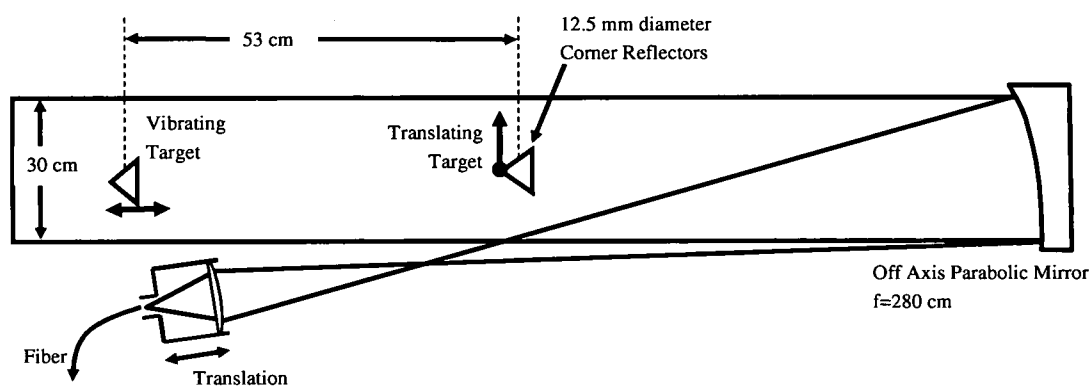


**Figure 51: Range-Doppler target placement within expanded beam.**

## B. Range Doppler Experimental Targets

Two moving corner cube targets are used in this experiment as shown in Figure 51. The targets are separated by 53 cm in range which corresponds to a time delay of 3.5 ns. The first target is designed to illustrate target translation with a large line-of-sight velocity components. For experimental simplicity, it was implemented using a Hardy vibration test instrument as a vibrating corner cube with a low oscillation frequency and large calibrated accelerations. The velocity of the vibrating target is calculated as

$$v(t) = \frac{C_1 g}{\omega_1} \cos \omega_1 t, \quad (93)$$

where  $g$  is the acceleration due to gravity,  $C_1$  is the acceleration setting from the vibration test stand, and  $\omega_1$  is the oscillation frequency. With an acceleration of  $C_1 g = 3g$  and an oscillation frequency  $\omega_1 = 2\pi 16$  Hz, target 1 has a sinusoidal motion with a peak velocity of 29 cm/s. This peak velocity is many times greater than the velocity corresponding to the first Doppler null of the 40  $\mu$ s waveform. The oscillation frequency produces 1.5 periods of oscillation during the measurement time of 100 ms so the full range of velocities between  $\pm 29$  cm/s are produced.

The second target in Figure 51 approximates a stripmap SAL target's relative motion with respect to the ladar. The target must cross the projected beam footprint during the synthetic aperture measurement time which for these experiments is typically 100 ms. This requires that the target velocity is 3 m/s. In addition, the cross-range velocity perpendicular to the target should be constant over the beam footprint. Finally, the target must traverse a linear path through the beam. It is difficult to generate this motion within the laboratory, but

here it is approximated using a pendulum as shown in Figure 52. From conservation of energy, the target velocity  $v_c$  at the bottom of the pendulum is

$$v_c = (2gh)^{\frac{1}{2}}, \quad (94)$$

where  $h$  is the starting height and  $g$  is the gravitational constant. The velocity at the edge of the beam  $v_e$  is then written

$$v_e = \left( 2g \left[ h - P + \left( P^2 - \left( \frac{D_b}{2} \right)^2 \right) \right] \right)^{\frac{1}{4}}, \quad (95)$$

where  $D_b$  is the beam diameter. For a pendulum arm  $P=1.0$  m, an initial height  $h$  of 0.5 m, and beam diameter  $D_b=30$  cm, the velocities at the center  $v_c$  and beam edge are 3.13 m/s and 3.09 m/s, respectively. The pendulum target provides the necessary velocity; however, the target will be accelerating everywhere but at the center resulting in velocity variations over the beam width of a few percent which will adversely affect the resulting phase history. The acceleration of the target is also non-linear for large values of  $\alpha$ , but can be approximated as linear over most of the beam footprint. The pendulum also has line of sight oscillations due to its structure as well as bearing friction losses which induce additional non-ideal behaviors. The pendulum is therefore sufficient to demonstrate stripmap SAL for a single target, but the non-ideal behavior makes it problematic for multiple targets without additional stabilization or compensation algorithms.

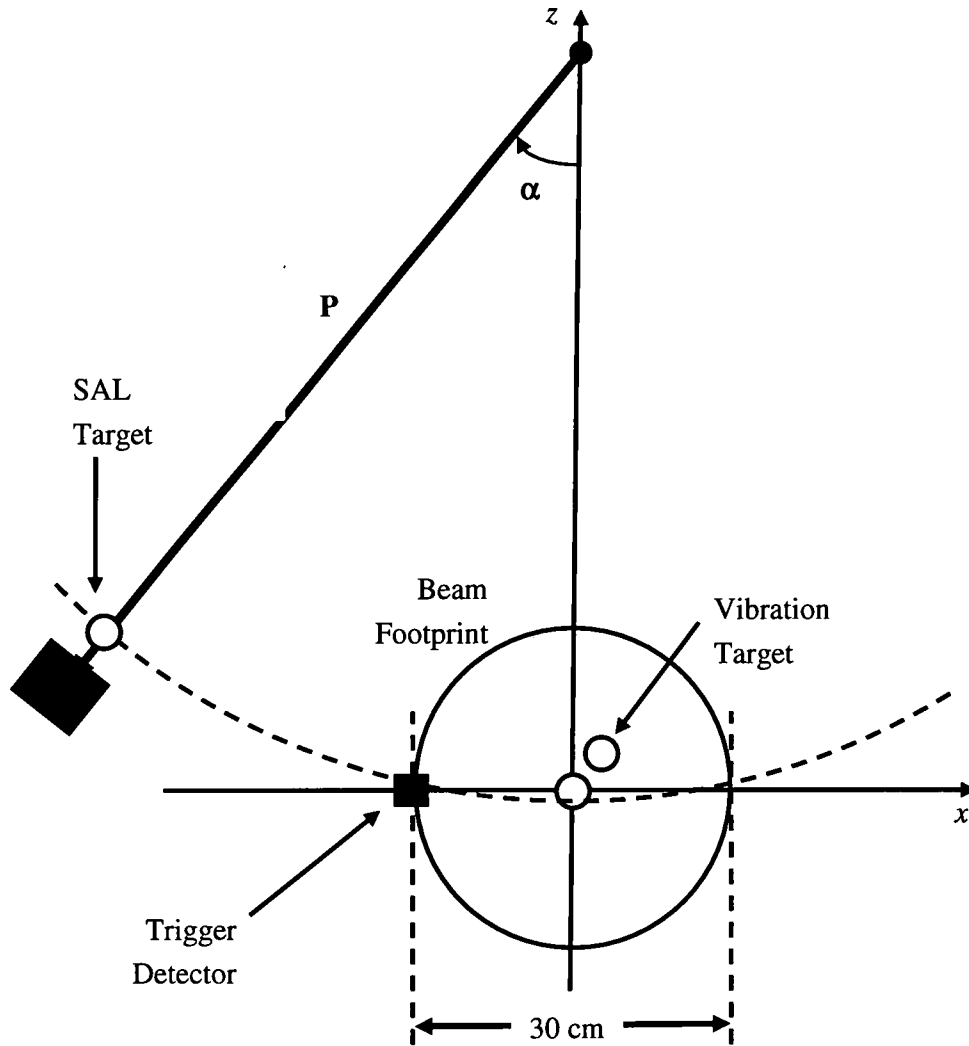


**Figure 52: Cross section view of Range-Doppler targets with respect to the expanded beam footprint.**

### **C. Composite Code Matched Filter**

The phase history shown in Figure 53 is developed by applying the range-Doppler matched filter of Eq. (15) for each transmitted composite waveform (fast-time dimension) and then constructing the slow-time history by aligning the matched filter output of each code sequence. This effectively samples the slow-time dimension every  $N_c T_c$  seconds.

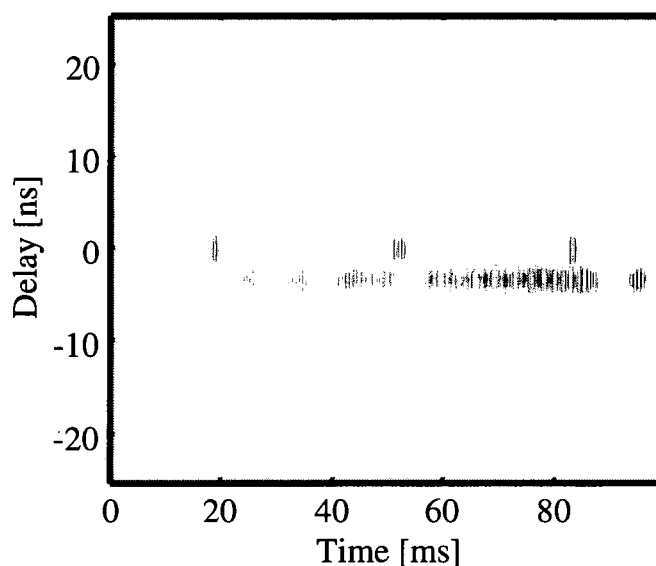


**Figure 53: Range-Doppler phase history for SAL target (lower) and large amplitude oscillating Doppler target (upper) for a single composite code  $N_c=20000$ .**

The two targets are correctly localized in delay (i.e., range), where the range center of the matched filter is defined at the location of the vibrating target. The Doppler induced modulation of Eq. (88) is apparent for each target where the SAL target produces a chirp as expected, but amplitude of the translation targets is attenuated. Figure 54 shows a slice through the phase history at the translation target. The attenuation of the range-Doppler matched filter output as a function of velocity is clearly illustrated in Figure 54(a) where the peaks of the output corresponds to velocity minimums of the oscillating Doppler target.

Figure 54(a) shows the normalized matched filter output near one of the target velocity minimums which occurs at approximately 52 ns within the 100 ns measured record. Here the amplitude modulation due to the Doppler sensitivity is clearly visible including the multiple nulls produced when the motion induced Doppler period is an integer multiple of the composite code length as described by Eq. (78).

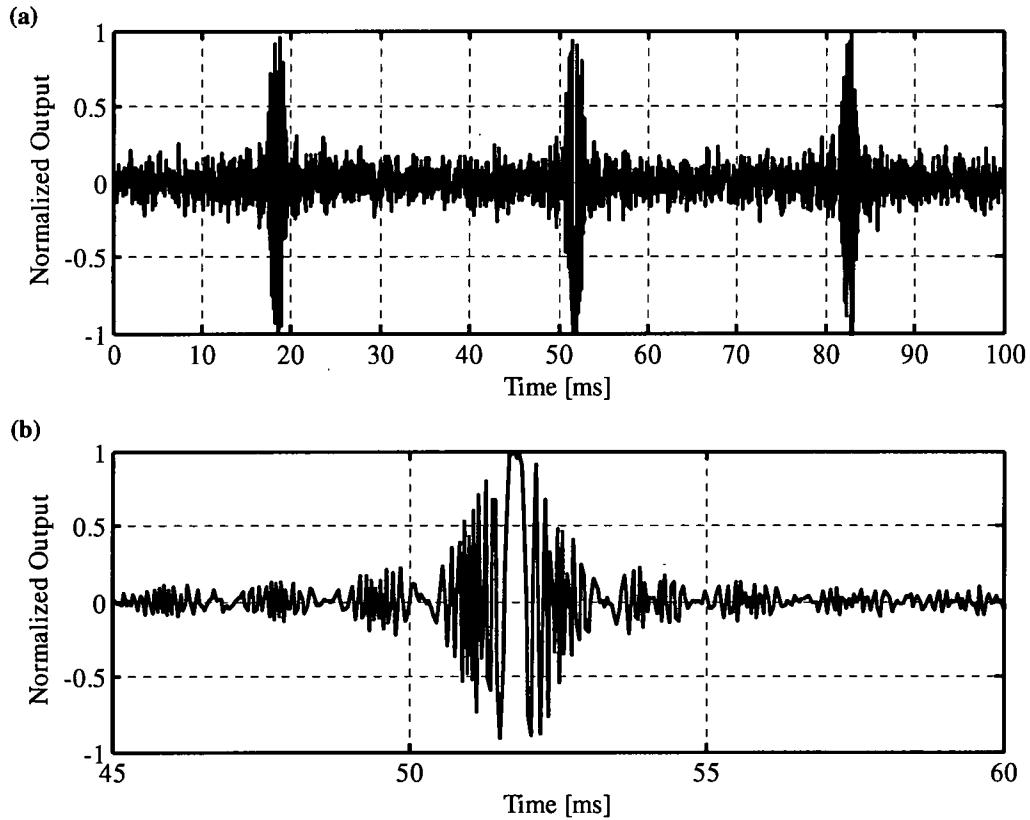


**Figure 54: Cross section of the phase history at the oscillating Doppler target range (a) and expanded view (b) illustrating the attenuation and nulls due to Doppler sensitivity.**

The matched filter response is attenuated for the composite waveform. This effect is mitigated using sub-code processing or exploited using Doppler filter banks.

#### **D. Sub-Code Processing**

The waveform Doppler sensitivity is mitigated by sub-code processing as described in Figure 25. Figure 55 shows the phase history resulting from processing one of the 20 sub-codes within the waveform. The SAL target remains essentially unchanged. The response of the Doppler oscillating target is recovered since processing a single sub-code corresponds to a factor of 20 increase in Doppler tolerance.

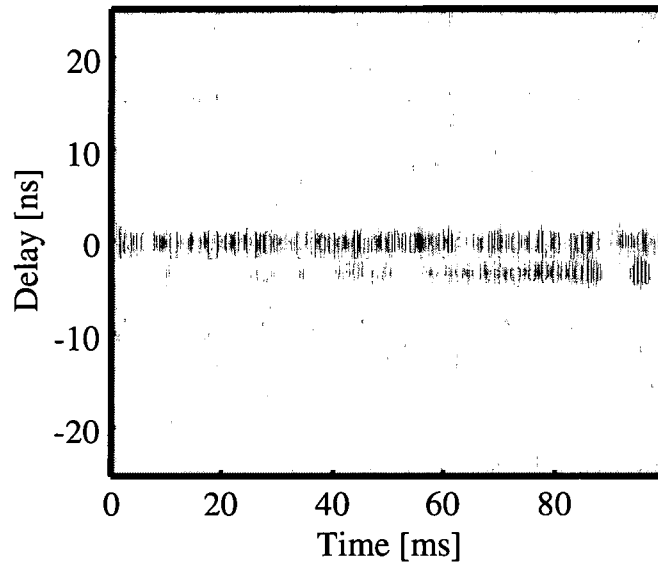


**Figure 55: Range-Doppler phase history for SAL target (lower) and large amplitude oscillating Doppler target (upper) with sub-code processing  $N_c=1000$  and  $N_{codes}=20$ .**

Figure 56(a) shows a slice of the sub-code phase history where only slight modulation of the output is visible. Figure 56(b) shows the variation in the real component of the matched filter output corresponding to the motion of the Doppler target. Processing shorter sub-codes can further reduce the Doppler sensitivity. In practice, the minimum length of is limited by the energy required to make a measurement.

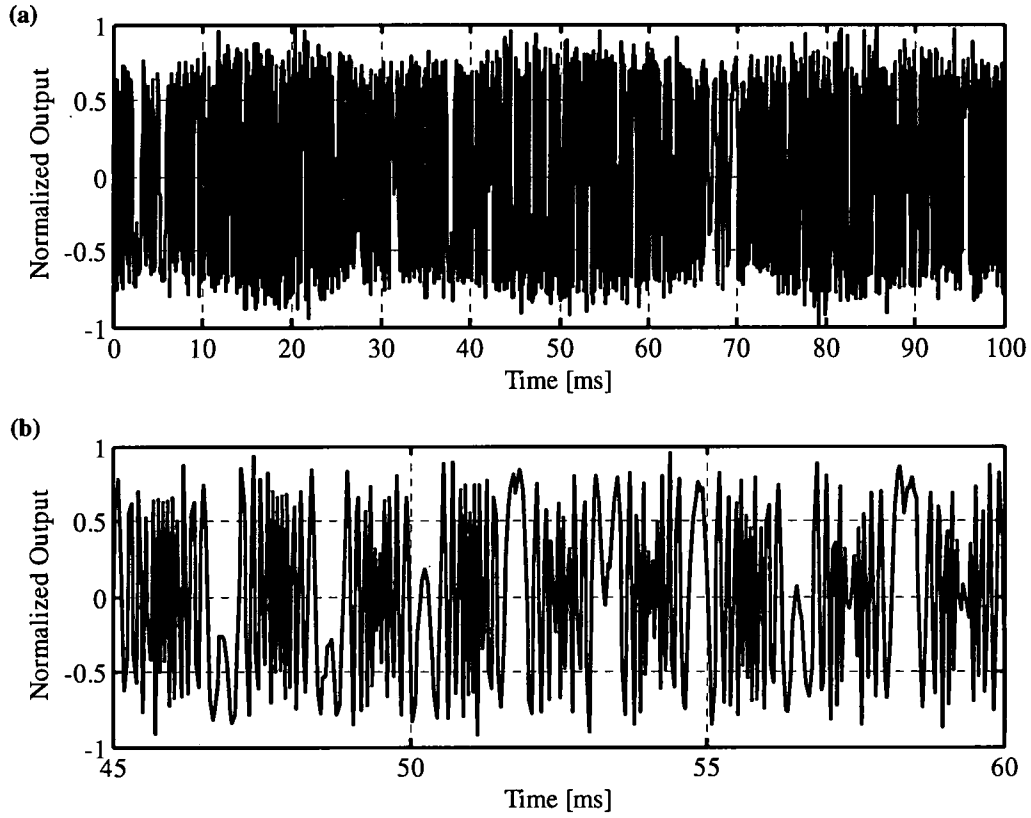


**Figure 56: Range slice of the phase history for the oscillating Doppler target (a) and expanded view (b) showing the phase wraps associated with the recovered motion using sub-code processing with  $N_c=1000$  and  $N_{codes}=20$ .**

### E. Filter bank Processing

If the velocity of a target or the differential velocity between targets is sufficiently high, reducing the Doppler sensitivity though sub-code processing is impractical. For a single translating target, the signal is

$$q(t) = A(x_n, y_n, z_n) \sigma_n \int_{-\infty}^{\infty} \exp\left(-j2\pi \frac{2v_o}{\lambda} \left(\tau - \frac{2R_{tgt}}{c}\right)\right) w\left(\tau - \frac{2R_{tgt}}{c}\right) w^*(\tau - t) d\tau \quad (96)$$

where  $v_o$  is the velocity of the target and  $R_{tgt}$  is the target range.

A Doppler correction of the form

$$\exp\left(j2\pi\frac{2v_{offset}}{\lambda}(\tau)\right) \quad (97)$$

is then applied to cancel the effect of large velocities where  $v_{offset}$  is an offset velocity.

Inserting the Doppler correction of Eq. (97) into the single target matched filter output of Eq.

(96), the Doppler corrected matched filter output can be written

$$\begin{aligned} q(t) &= A(x_n, y_n, z_n) \sigma_n \\ &\int_{-\infty}^{\infty} \exp\left(j2\pi\frac{2v_o}{\lambda}(\tau)\right) \exp\left(-j2\pi\frac{2v_o}{\lambda}\left(\tau - \frac{2R_{tgt}}{c}\right)\right) w\left(\tau - \frac{2R_{tgt}}{c}\right) w^*(\tau - t) d\tau \\ &= A(x_n, y_n, z_n) \sigma_n \int_{-\infty}^{\infty} \exp\left(-j2\pi\frac{2v_o}{\lambda}\left(\frac{2R_{tgt}}{c}\right)\right) w\left(\tau - \frac{2R_{tgt}}{c}\right) w^*(\tau - t) d\tau \end{aligned} \quad (98)$$

where the Doppler term is completely cancelled. This shows that the Doppler can be cancelled for a single target; however, if there are multiple targets, or a target with velocity changing with time, a single Doppler correction will not be effective on all targets.

The translation target used in this experiment is an example of the latter. Figure 57(a) shows one half cycle of the line of site velocity of this target as well as the remainder of the velocity divided by the velocity of the first Doppler null. Figure 57(b) shows the corresponding portion of the phase history which shows that the velocity varies over 8 times the Doppler null velocity. A single Doppler offset would not restore this phase history.

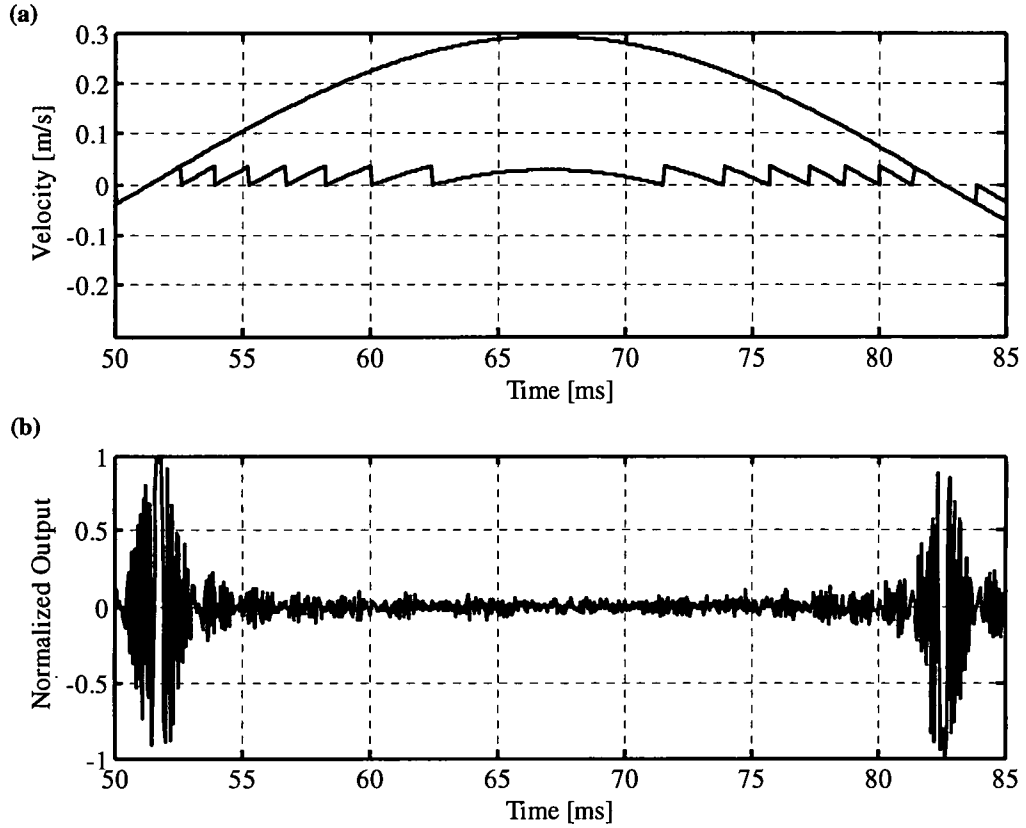


**Figure 57: Illustration of Doppler Tolerance nulls within translating target phase history (a), and measured output showing Doppler suppression (b).**

In this case, a filter bank is constructed as shown in Figure 58 using the Doppler correction given as

$$\exp(j\omega_n \tau) = \exp\left(j2\pi \frac{2v_n}{\lambda} \tau\right). \quad (99)$$

where  $v_n$  and  $\omega_n$  are the offset velocity and effective frequency of the  $n^{\text{th}}$  filter. Each matched filter operates on the same signal, but applies a different Doppler offset.

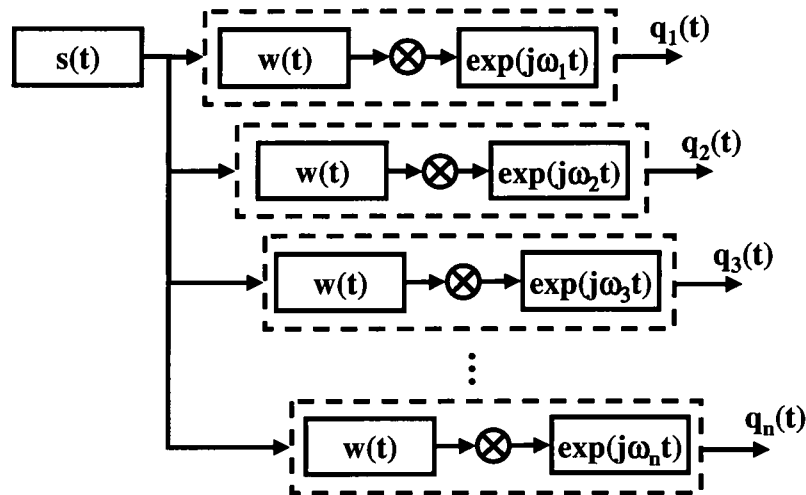


**Figure 58: Doppler filter bank processing block diagram with  $n$  offset frequencies.**

Figure 59 shows the Doppler filter outputs  $q_n(t)$  for the measured sinusoidal target. The velocity ranged from 5.62 cm/s to -11.62 cm/s in steps of 1.87 cm/s. The filter bank exploits the velocity variation and effectively localizes the target as a function of time (i.e., range) and frequency. As the offset velocity is varied as shown in Figure 59 (a) through (j) different regions of the velocity track are recovered. Note that the SAL target is suppressed in all outputs except Figure 59 (d) where  $v_{\text{offset}} = 0$ . This confirms that the LOS velocity of the SAL target is approximately zero. This also shows that a large platform line of sight velocity can be compensated for the SAL or micro-Doppler imaging modes.

In practice, both adaptive selection of code length as well as filter bank processing are utilized depending on the applications. The use of longer codes or sub-code segments increases the number of filters required to cover a given range of velocities. Since all of the filtering occurs after detection, the post processing can be tailored to optimize the imaging requirements.

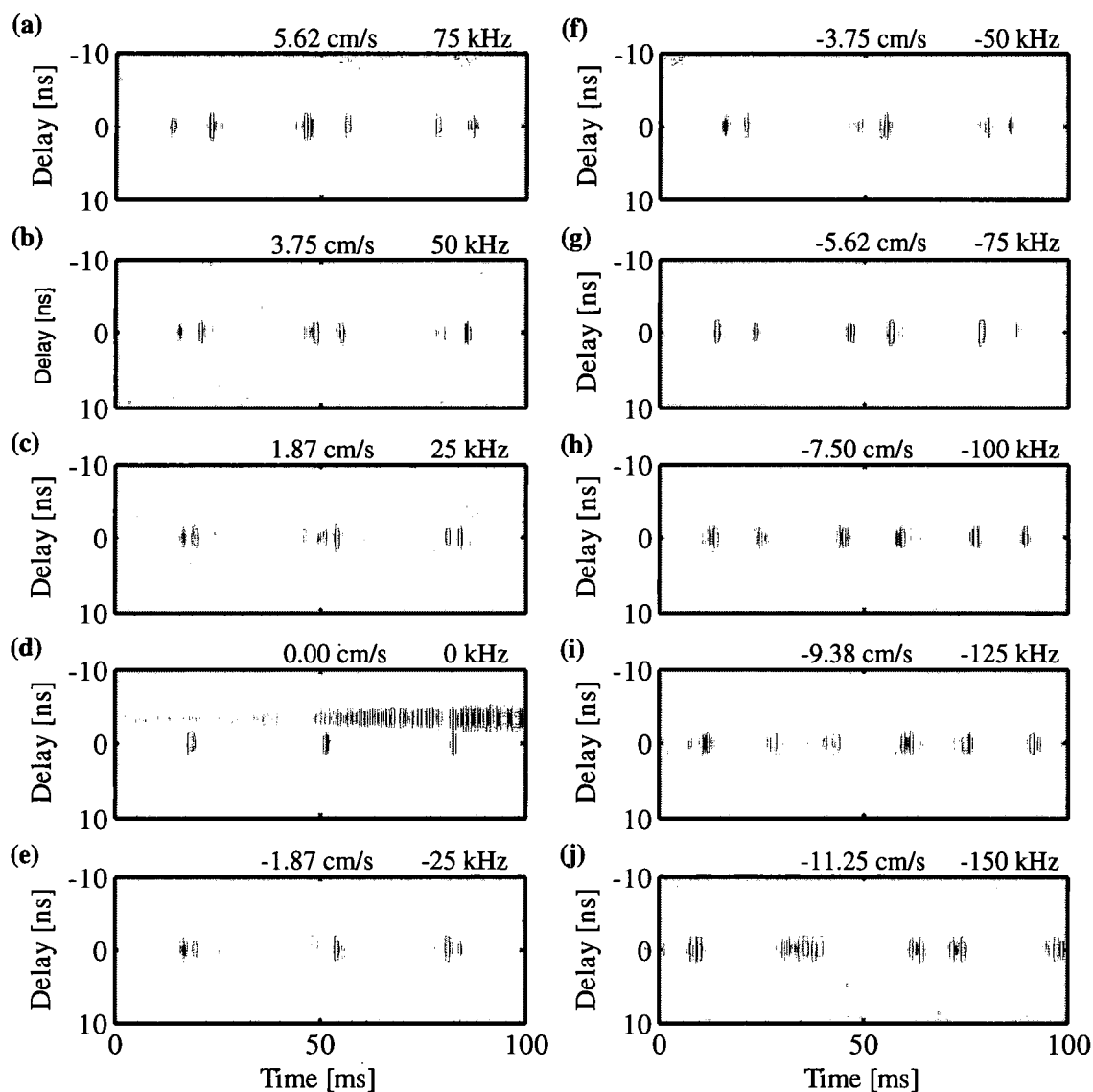


**Figure 59: Ten element Doppler filter bank output showing phase histories for velocities ranging from +5.52 cm/s (a) to -11.25 cm/s (j).**

## CHAPTER X

### SYNTHETIC APERTURE LADAR IMAGING

Synthetic aperture imaging localizes the individual scattering centers in two dimensions resulting in an intensity image as a function of range and cross-range. The most important factors governing the performance of range-Doppler imaging are the range resolution and sidelobe levels. In this chapter, synthetic aperture ladar images are simulated for using the PPN for both simple and complex targets. Finally, PPN waveform synthetic aperture imaging is experimentally demonstrated for a simple target.

#### A. Stripmap SAL Phase Variation

The motion induced range-dependent phase is the fundamental basis for all synthetic aperture imaging. For the stripmap SAL imaging geometry, the synthetic aperture phase of Equation (18) is calculated for a ladar moving along the x axis and three stationary targets. The three point targets were assumed to be at rest (i.e.,  $v_{no} = \mu_{no} = 0$  for all  $n$ ) and were assumed to be located at  $(x_1, y_1, z_1) = (0.0 \text{ m}, 20000.0 \text{ m}, 0.0 \text{ m})$ ,  $(x_2, y_2, z_2) = (0.2 \text{ m}, 20000.0 \text{ m}, 0.0 \text{ m})$  and  $(x_3, y_3, z_3) = (0.4 \text{ m}, 20000.0 \text{ m} + 5 \text{ waves}, 0.0 \text{ m})$ , respectively. The beam profile  $A(x_n, y_n, z_n)$  is assumed to be unity at the target range. Figure 60 relates the parabolic phase variation in three ways. First, the real component of the phase factor is shown for each of the three targets in Figure 60(a). This phase factor is the real component of the parabolic phase shown in Figure 60(b). This phase is the basis the of the cross-range matched filter. The

phase variations are similar for each target, but the spatial offsets between the phase patterns are proportional to the lateral location of the target. Finally, Figure 60(b) shows the spatial frequency variation as a function of platform location  $u$ . This demonstrates that in order to record more spatial frequency information, the baseline must be increased as indicated by Equation (24).

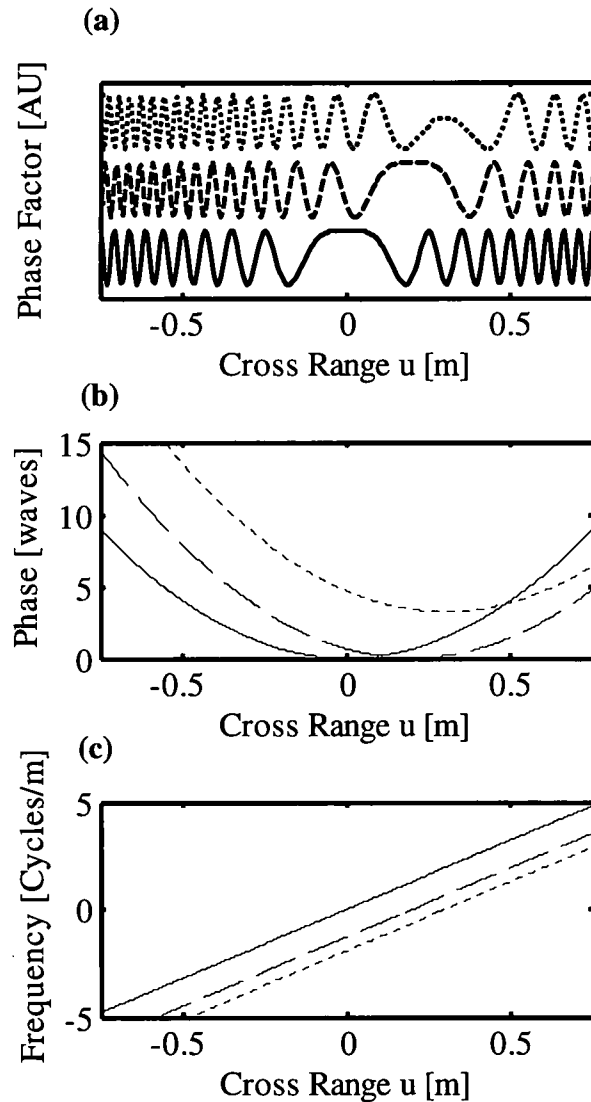


**Figure 60: SAL Phase migration for three targets is illustrated by the phase factor (top), quadratic phase (center) and frequency (bottom).**

The extent of this variation dictates how the SAL image formation is performed. Here, The Doppler beam sharpening and range-Doppler algorithms are utilized in the simulations and experimental validations as required

### **B. .Simulated PPN Synthetic Aperture Ladar Imaging**

The same 1000 chip PPN waveform, with  $T_c = 1$  ns, was then used to simulate synthetic aperture imaging for a collection of three point targets. We again assumed unity beam amplitudes and target cross sections for all targets. The resulting slow-time phase history and the fully compressed range, cross-range image are shown in Figure 61.

To create this figure the three point targets were assumed to be at rest (i.e.,  $v_{no} = \mu_{no} = 0$ , for all  $n$ ) and located at  $(x_1, y_1, z_1) = (-0.25$  m, 20000.25 m, 0.0 m),  $(x_2, y_2, z_2) = (0.0$  m, 20,000.0 m, 0.0 m) and  $(x_3, y_3, z_3) = (0.5$  m, 19999.5 m, 0.0 m), respectively. To create Figure 61.(a) we then plotted the real part of the fast-time matched filter output, described by Eq. (21), for a series of 300 sequentially transmitted waveforms (i.e., the PRF was assumed to be  $1/N_c T_c$ ) across an effective synthetic aperture of 17.2 cm. Similar to the range-Doppler case, these responses were then “vertically” aligned along the slow-time axis. Recall that in SAL imaging the real aperture is moved continuously as waveforms are periodically transmitted. The slow-time phase history is therefore a function of the cross-range real aperture location  $u$ . Notice that Figure 61(a) clearly shows the range dependent phase migration for each of our assumed point targets.

Final SAL image formation was accomplished by compressing the data along the slow time dimension using the Doppler beam sharpening algorithm [9]. In particular, the two dimensional matched filter output is simply the frequency scaled Fourier transform of the

range compressed phase history, with respect to the slow-time dimension. Figure 61(b) then shows the fully compressed SAL image demonstrating correct range and cross-range localization of the three assumed point targets.

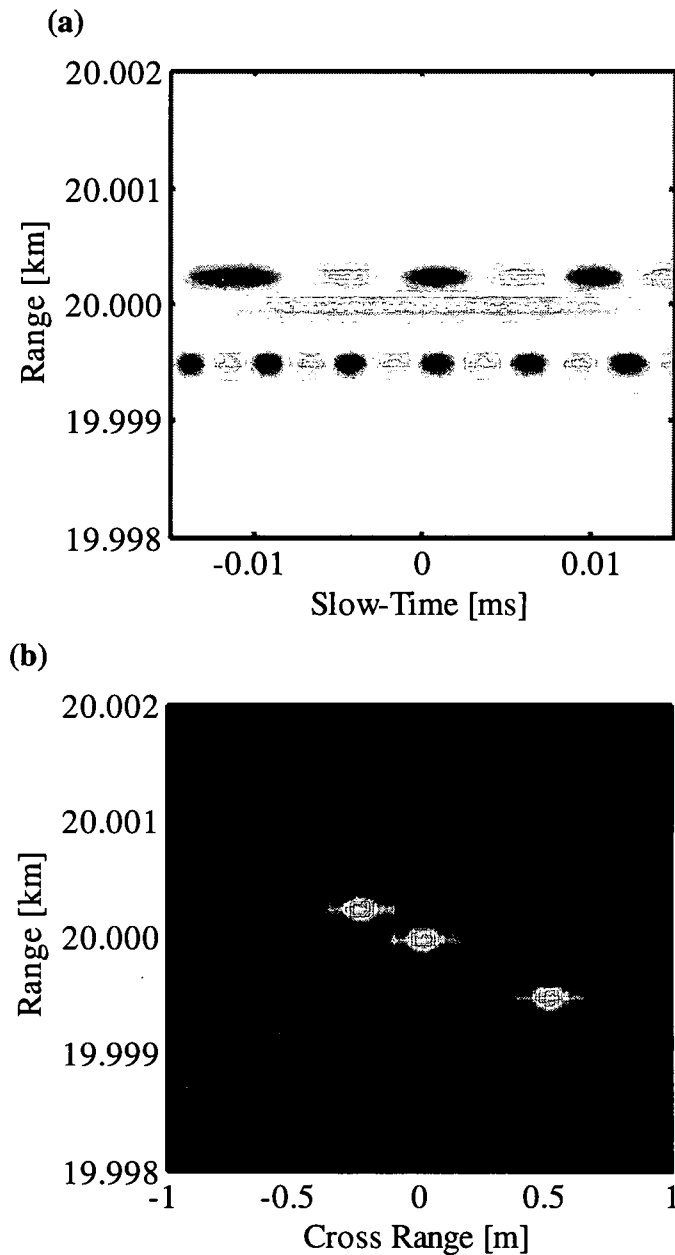


**Figure 61(a) A synthetic aperture phase history for the PPN waveform demonstrating the range dependent phase migration for each of three point targets. (b) The DBS fully compressed image demonstrating effective cross-range localization of each of the three targets.**

Moreover, the cross-range IPR for each of the waveforms can be examined by taking a slow-time cross section through any isolated target in the fully compressed SAL image. Examining point target two, for example, Figure 62 compares the cross-range imaging performance of various SAL waveforms by plotting the cross-range IPR for the PPN waveform (dashed line), and the previously defined LFM (solid line), and unmodulated Gaussian pulse (dotted line) waveforms. Notice that while the range IPR for each of the waveforms is significantly different as shown in Figure 44, the motion induced spatial bandwidth is the same for each waveform, therefore producing nearly identical cross-range IPRs as shown in Figure 62.

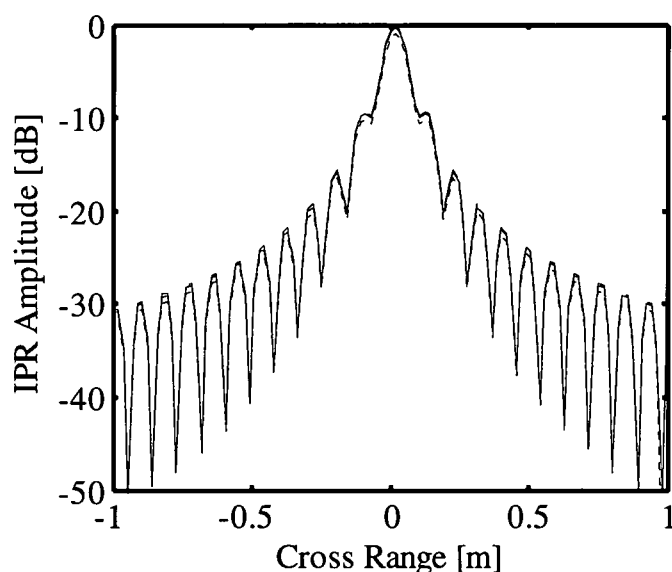


**Figure 62: Cross-range IPRs for the LFM, (solid line), PPN (dashed line) and 1 ns FWHM Gaussian pulse (dotted line) waveforms. The cross-range phase modulation is the same for each waveform, producing nearly identical results in cross-range compression.**

To illustrate the PPN waveform performance in a more realistic image a complex target consisting of a large number of unity cross-section targets is simulated. Figure 63

shows the phase history (top) and fully compressed image (bottom) of a more complex target, the University of Dayton Logo constructed as a distribution of 1500 point scatterers. The distribution of the targets in range can be inferred to some extent from the phase history directly; however, the target is completely unresolved in the cross-range dimension range distribution and little can be inferred about the target. The Doppler beam sharpening algorithm was applied to the range compressed phase history to produce the fully compressed image.

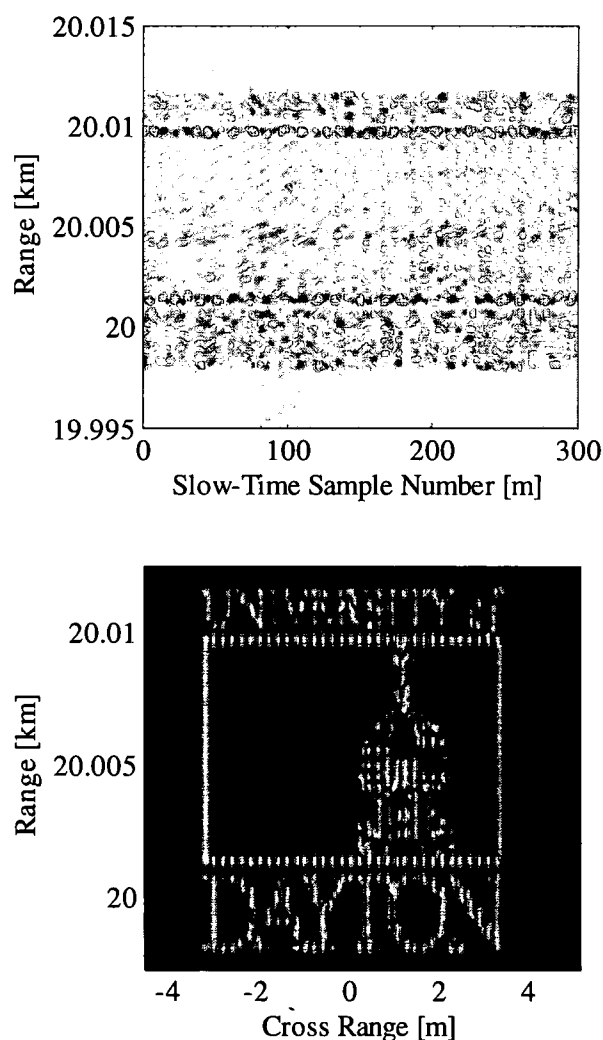


**Figure 63: Simulated PPN waveform synthetic aperture image of complex array of point targets, (University of Dayton Logo), demonstrating PPN synthetic aperture image quality.**

The logo successfully recovered from the single detector phase history with minimal impact from the slightly elevated sidelobes. This image demonstrates good localization even when multiple, closely spaced targets are present. The sidelobe performance of the PNN waveform provides excellent image quality with high contrast and minimal ghosting in the resulting image.

### **C. Experimental Block Diagram**

The configuration of the laboratory ladar used is shown in Figure 45. Since the operation is at short range, it uses only the signal channel omitting the monitor channel of the complete system as described in Chapter VI. Each transmitted waveform has 20 sub-codes with 1000 bi-phase code chips each 1-ns in duration. The composite 20  $\mu$ s waveform is generated and transmitted continuously. The transmitted power is monitored using the low energy leg of the 96/4 splitter and the power meter preceding the transmit/receive switch. The variable attenuator in the transmit leg is set for maximum transmission.

After the T/R switch, the energy is collimated using the off axis parabolic (OAP) mirror as shown in Figure 51 to allow for spatially distributed targets. The OAP focal length and diameter are 280 cm and diameter is 30 cm, respectively. The fiber coupled transmit energy is mode matched to the OAP by adjusting the focus of the mode matching optics to provide the desired beam divergence. The output beam is collimated by translating the mode matching optics with respect to the OAP.

#### D. PPN SAL Imaging Experimental Targets

Two moving corner cube targets are used in this experiment as shown in Figure 51. The targets are separated by 53 cm in range which corresponds to a time delay of 3.5 ns. The first target is designed to illustrate translation and has large line of sight velocity components. For experimental simplicity, it is a vibrating corner cube with a low oscillation frequency and large accelerations. The vibrating target has an oscillation frequency of  $\omega_1 = 2\pi(1000)$  Hz and a peak displacement on the order of a wavelength.

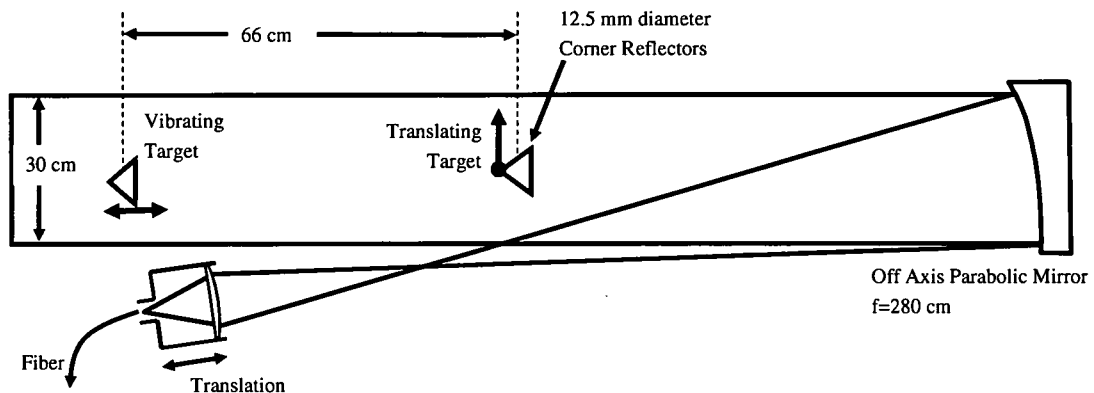


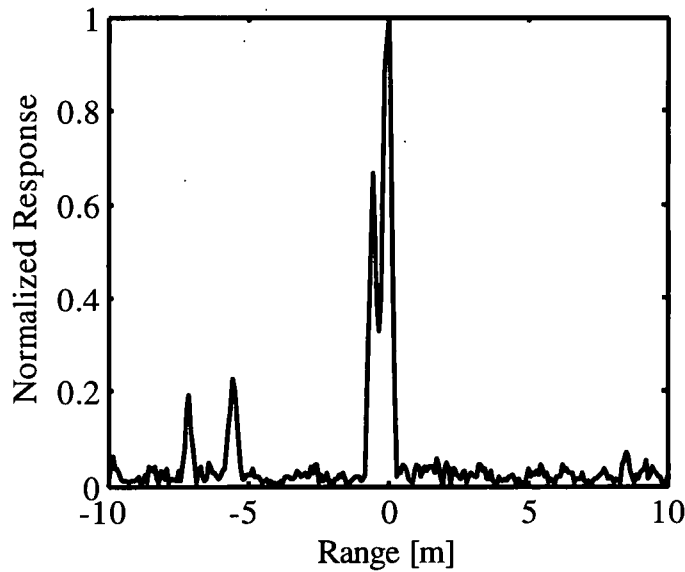
**Figure 64: SAL experiment target layout within 12 inch collimator.**

The SAL target in Figure 64 approximates the target's relative motion with respect to the ladar. Ideally, the cross-range velocity is constant with a zero line of sight component. The SAL motion is again approximated using the pendulum as shown in Figure 52. The pendulum creates the high velocity motion required over the beam footprint, but the motion is not ideal for two main reasons. First, the target is accelerating everywhere except where the arm is vertical. The accelerations are small around the vertical position, but still introduce undesired velocity variations. Second, there is a small vertical motion component

over the transmitted beam footprint due to the arc of the pendulum. Both the acceleration and vertical motion components are reduced as the length of pendulum is increased. Additional phase perturbations may also be introduced by non-ideal motions within the pendulum structure such as accelerations due to friction, target rotation, and structural vibrations. All of these non-ideal motions will limit the image formation performance within this experiment. They are however unimportant to this research since they are specific to the target simulation method, not relevant to the PPN ladar's ability to measure the phase signal. Many of these non-ideal motions can be mitigated with phase tracking algorithms, but are beyond the scope of this research.

## **E. Experimental Results**

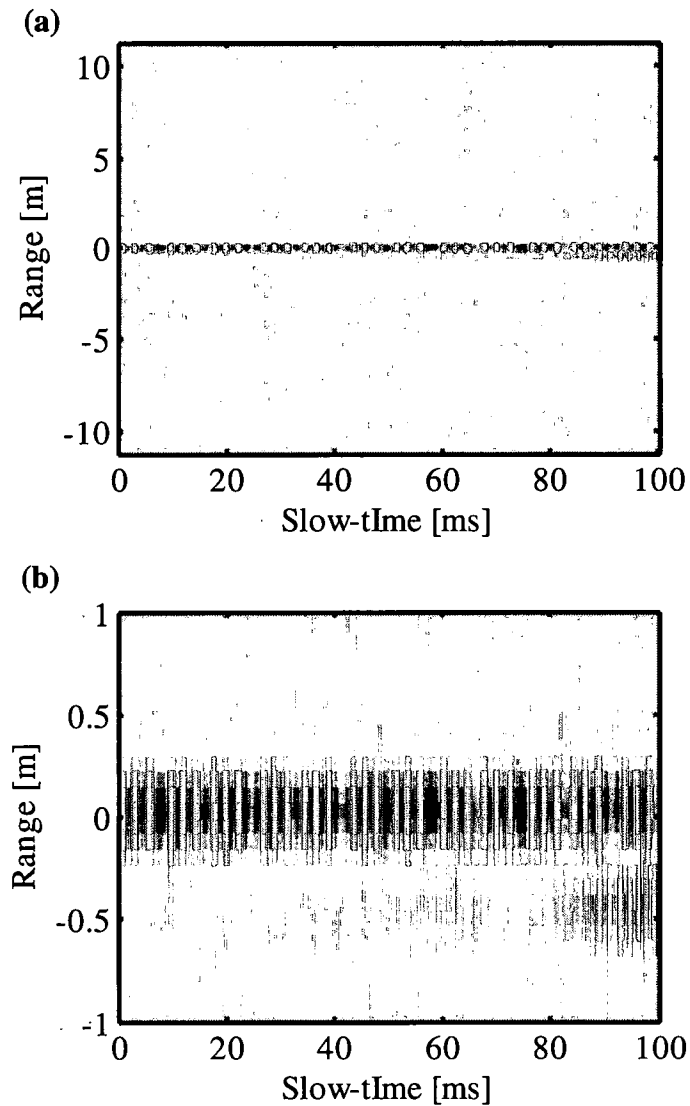
2500 PPN waveforms are transmitted using the experimental configuration of Figure 45 and targets shown in Figure 60. The return signals are recorded and range compressed via fast-time matched filter on each waveform record. Figure 65 shows an example of a range compressed return. The first two peaks are from optical back reflections within the ladar. The later two are due to the SAL and vibration targets, respectively. Note that the amplitude of the vibration is slightly larger than the SAL target.



**Figure 65: IPR for SAL and vibration targets at 0 m and -1 m respectively. The returns at -6 m and -8 m are due to back reflections in the telescope.**

The 300 sample section of the range compressed phase history shown in Figure 66(a). Here, the SAL target is moved continuously with respect to the ladar as the periodic waveforms are transmitted. The SAL target phase is a function of the cross-range distance  $u$  from the reference location for the matched filter. Here each column of the phase history is the length of one waveform  $N_c T_c$  and is separated from its neighbors by the same time temporal increment.

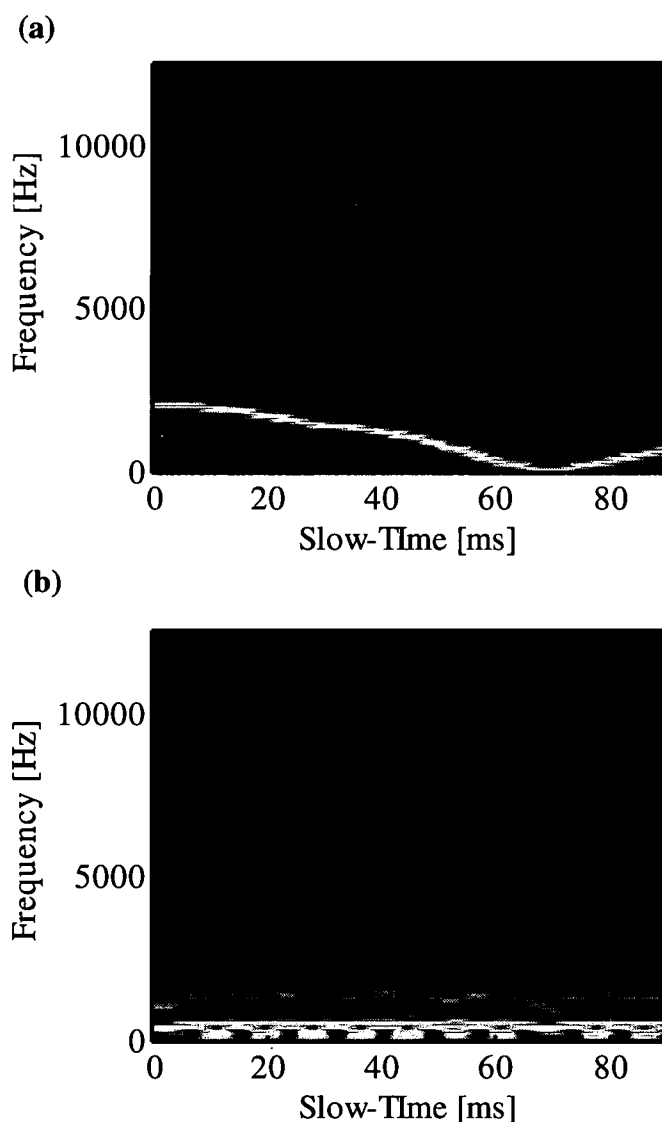
Figure 66(b) shows the region around the SAL and vibration targets clearly illustrating the phase associated with two motions. The SAL phase (upper target) has an approximately quadratic phase centered at the closest point of approach which is at approximately the 1900 record within the recorded phase history. The vibration phase (lower target) has the expected sinusoidal phase variation.



**Figure 66: SAL phase history for a SAL target and vibrating target (a). The expanded phase history (b) clearly show the difference between the phase of the two targets.**

As mentioned previously, the motion of the experimental SAL target is not ideal. To further quantify the motions, the spectrogram of the phase history cross sections associated with both targets were computed and are compared in Figure 67. The phase of the vibration target Figure 67(b) demonstrates a single tone associated with the oscillation frequency of the

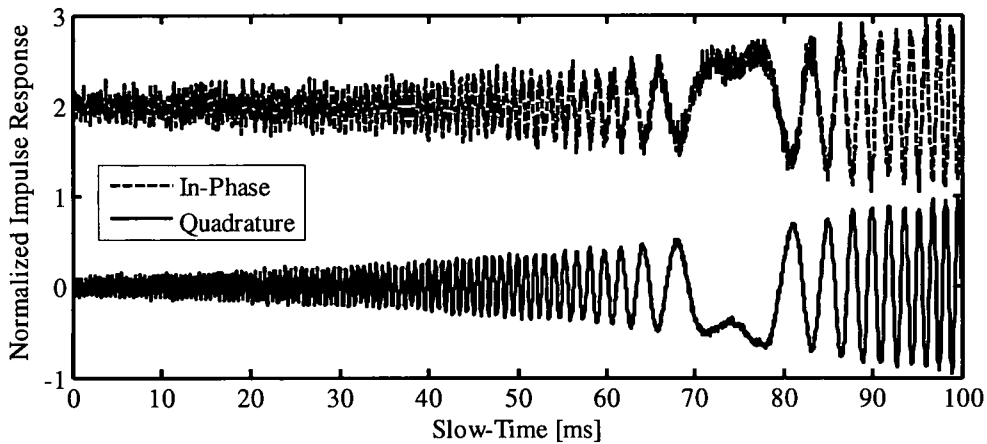
target as expected. The frequency due to the SAL motion should be linear for the stripmap SAL geometry. There are clear significant frequency deviations due to the non ideal motion of the pendulum. These deviations are primarily attributed to target acceleration due to the pendulum (departure from linear away from the center) and other non-ideal pendulum motion (corners within frequency migration).



**Figure 67: Spectrogram of the phase of the SAL target (a) and vibration target (b).**

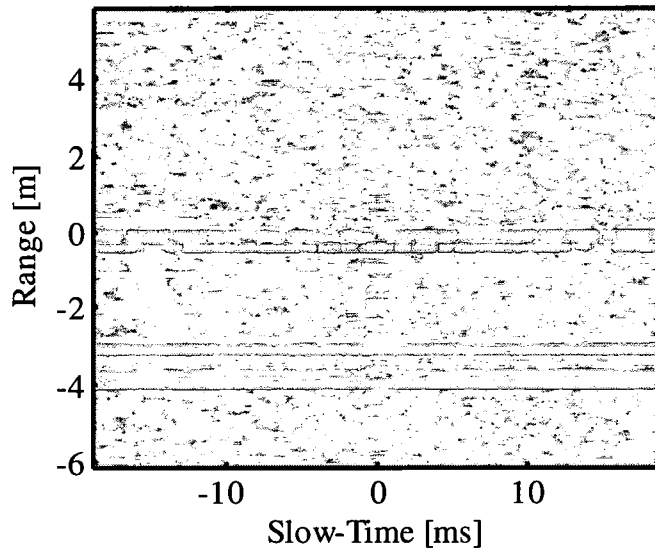
Phase tracking can be used to linearize the motion, but here the image is compressed in the slow-time dimension using a two dimensional matched filter similar to the range-Doppler image formation algorithm [9]. The matched filter consists of the transmitted waveform in the range dimension, and the phase associated with the non-deal motion in the cross-range dimension.

Figure 68 shows the in-phase and quadrature components of the cross-range matched filter which was extracted from the range compressed phase history.



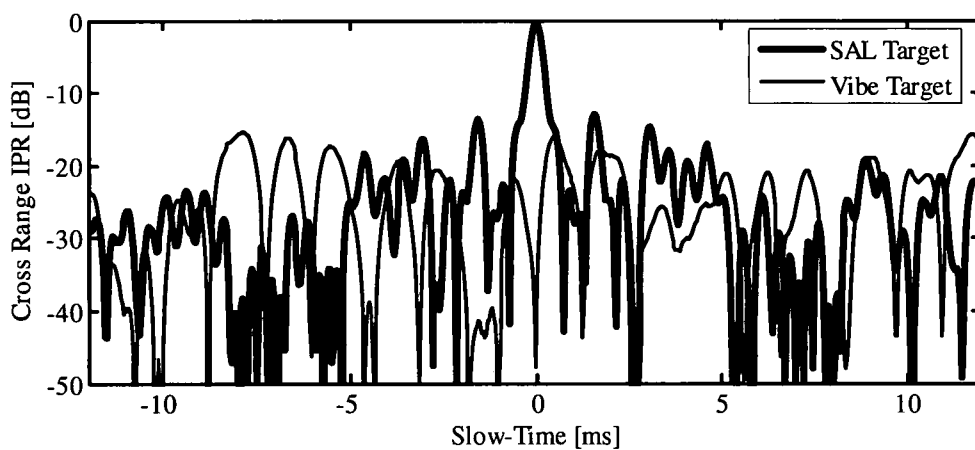
**Figure 68: In-phase and quadrature components of the cross-range matched filter kernel demonstrate quadrature phase offset and beam amplitude profile.**

Figure 69 shows the corresponding fully compressed SAL image obtained after applying the cross-range matched filter to the range compressed phase history. Each of the targets is correctly localized in range, but only the SAL target is localized in both dimensions. The returns due to the optical back reflections and the vibrating targets are visible, but have low amplitudes compared to the SAL target. Although the peak amplitudes these targets is comparable to the SAL target in the range compressed phase history, their cross-range phase



**Figure 69: Central portion of the fully focused SAL image of the SAL and vibration targets.**

variation is mis-matched with the motion induced matched history phase. This suppresses their responses in the fully compressed SAL image. The cross-range IPRs for the SAL and vibration targets are shown in Figure 70 and are produced by taking the slow-time cross section through each target in the fully compressed SAL image.



**Figure 70: Cross-range IPR for the SAL target and Vibe Target.**

Again, only the SAL target has the correct phase and is compressed. Although the range-compressed vibration signal is larger, it is suppressed in the range-compressed image with a peak less than the SAL target's sidelobes. Figure 71 compares the cross-range and range IPRs for the fully compressed SAL image.

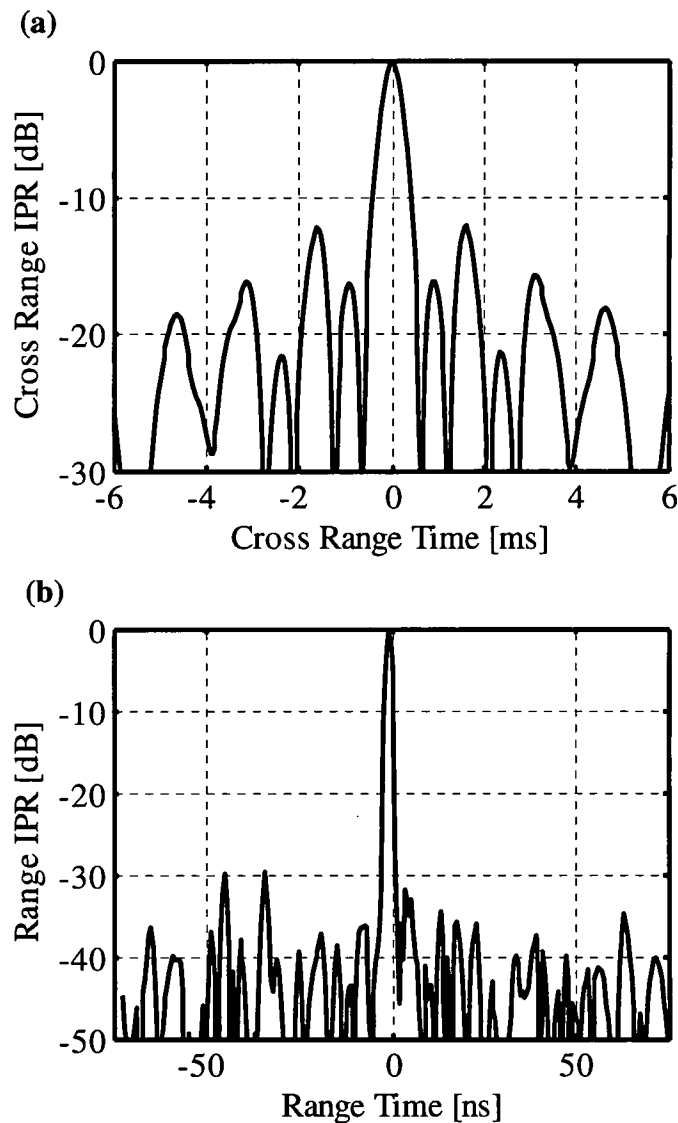


**Figure 71: Comparison of the cross-range IPR (a) and the range IPR (b).**

The IPRs were produced by taking both the slow-time and fast time cross sections through the peak response of the SAL target in the fully compressed SAL image. The range IPR, as expected, has random uniformly distributed sidelobes associated with the PPN waveform. The cross-range IPR (a) has sidelobes consistent with those associated with the quadratic SAL phase.

Figure 72 compares the measured cross-range IPR to the theoretical results for a ladar with perfect linear motion with respect to the target. The mainlobe width and peak sidelobe levels are in good agreement. The sidelobe structure is significantly different due to the non-ideal motion in the experimental data.

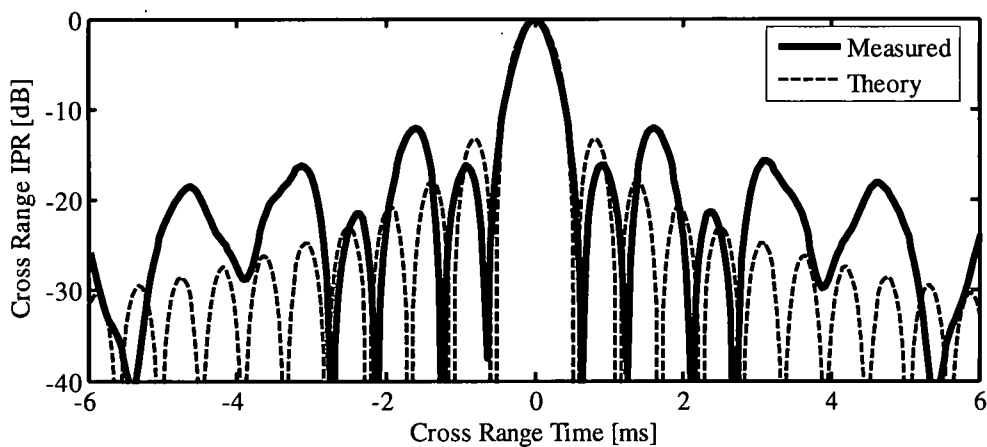


**Figure 72: Measured (solid) and theoretical (dashed) cross-range IPR.**

The use of the PPN waveform has been demonstrated for SAL imaging through simulation and experiment. The range and cross-range performance are in good agreement with theory and should produce high quality SAL images in an operational ladar.

## CHAPTER XI

### MICRO-DOPPLER IMAGING

Micro-Doppler imaging localizes the individual scattering centers of an object as a function of range and characterizes their micro-motions (i.e., vibrations). The output consists of a intensity profile proportional to the cross-section of the scattering centers at each range. In addition, a vibration spectra corresponding to each range describes the vibration of the scatterer. The most important factors governing the performance of range-Doppler imaging are the range resolution and sidelobe levels. In this chapter, micro-Doppler imaging is simulated using the PPN for both simple targets. PPN micro-Doppler imaging is experimentally demonstrated and characterized as a function of received single waveform CNR.

The range resolution of the PPN waveform is proportional to the chip length  $T_c$ , and is insufficient to detect the extremely small vibrational motions. Instead, the phase modulation associated with the motion is detected. Figure 73 demonstrates the nature of the micro-Doppler phase modulation applied to the PPN waveform using a simple sinusoidal signal. The transmit waveform strikes the target at a position shown by the solid target and returns toward the source. If the target has velocity  $v_{no}$ , it moves through a distance  $v_{no}N_cT_c$  during the waveform duration  $N_cT_c$ . The phase between the returns from the two surface locations is

$$\phi = \frac{2\pi}{\lambda} 2v_{no}N_cT_c, \quad (100)$$

where the factor of two comes from the round trip propagation over the change in range.

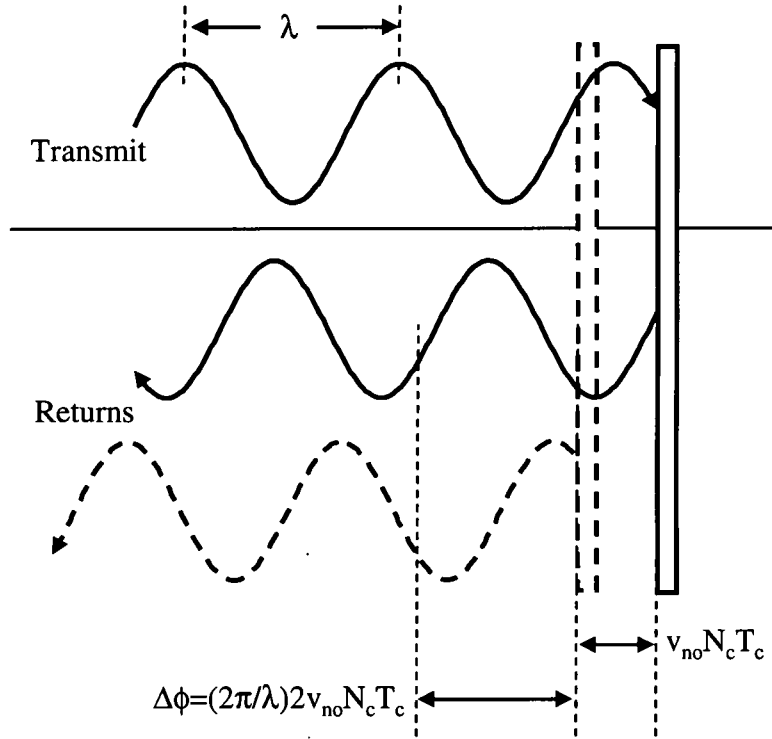


**Figure 73: Micro-Doppler phase signature.**

The phase is obtained from the matched filter output  $q_{\mu D}(t)$  of Equation (27) by computing the angle of the complex return. To measure the vibration of an object, the phase must be observed over time. Therefore, multiple waveforms are transmitted consecutively and a two-dimensional phase history constructed where the fast-time dimension is the matched filter output for each waveform. The slow-time dimension contains the phase history for each range sampled at the waveform duration  $N_c T_c$ .

The velocity at each range  $v_R$  is then

$$v_r = \frac{\lambda}{4\pi\Delta T_{CPI}} \Delta\phi_{CPI} \cdot \quad (101)$$

where  $\Delta T_{CPI}$  and  $\Delta \phi_{CPI}$  are the coherent processing interval and the phase difference over the coherent processing interval respectively. The temporal record of each velocity observation creates the velocity time history where the velocity amplitude, frequency, and phase are dictated from the surface motions of the target. Spectral analysis is then applied to the sequence for each velocity time series at each independent range location to produce spectral amplitude as a function of range.

### A. Simulated PPN Micro-Doppler Imaging

Finally, the same 1000 chip PPN waveform, with  $T_c = 1\text{ns}$  and  $T_w = N_c T_c = 1\mu\text{s}$ , was used to simulate micro-Doppler imaging. We again assumed unity beam amplitudes and target cross sections for all targets, and assumed a wavelength of  $1.5\mu\text{m}$ . As in the range-Doppler case, three point targets were assumed to be located at  $(x_1, y_1, z_1) = (-0.25\text{ m}, 20000.25\text{ m}, 0.0\text{ m})$ ,  $(x_2, y_2, z_2) = (0.0\text{ m}, 20,000.0\text{ m}, 0.0\text{ m})$  and  $(x_3, y_3, z_3) = (0.5\text{ m}, 19999.5\text{ m}, 0.0\text{ m})$ , respectively. In addition, the targets were assumed to have vibration frequencies  $\omega_1 = 2\pi \cdot 500$ ,  $\omega_2 = 2\pi \cdot 900$  and  $\omega_3 = 2\pi \cdot 2000\text{ rad/s}$ , as well as peak line-of-sight displacements  $\mu_n/\omega_n$  of 1500, 250 and 500 nm, respectively. All targets were assumed to be vibrating independently.

The range compressed micro-Doppler phase history of Figure 74 (a) was then formed by plotting the real part of the fast-time matched filter output described by Eq.(27) for a series of 1250 sequentially transmitted waveforms (i.e., the PRF was assumed to be  $1/N_c T_c$ ). As before, these responses were then “vertically” aligned along the slow-time axis. This phase history demonstrates that all three of the target points have been correctly located in range. The temporal phase history also shows the vibration induced phase migration

associated with each of the targets. In particular, notice that target 1 moves through a distance greater than  $\lambda/2$ . The resulting phase wrapping is manifest as a non-sinusoidal behavior target 1's phase history.

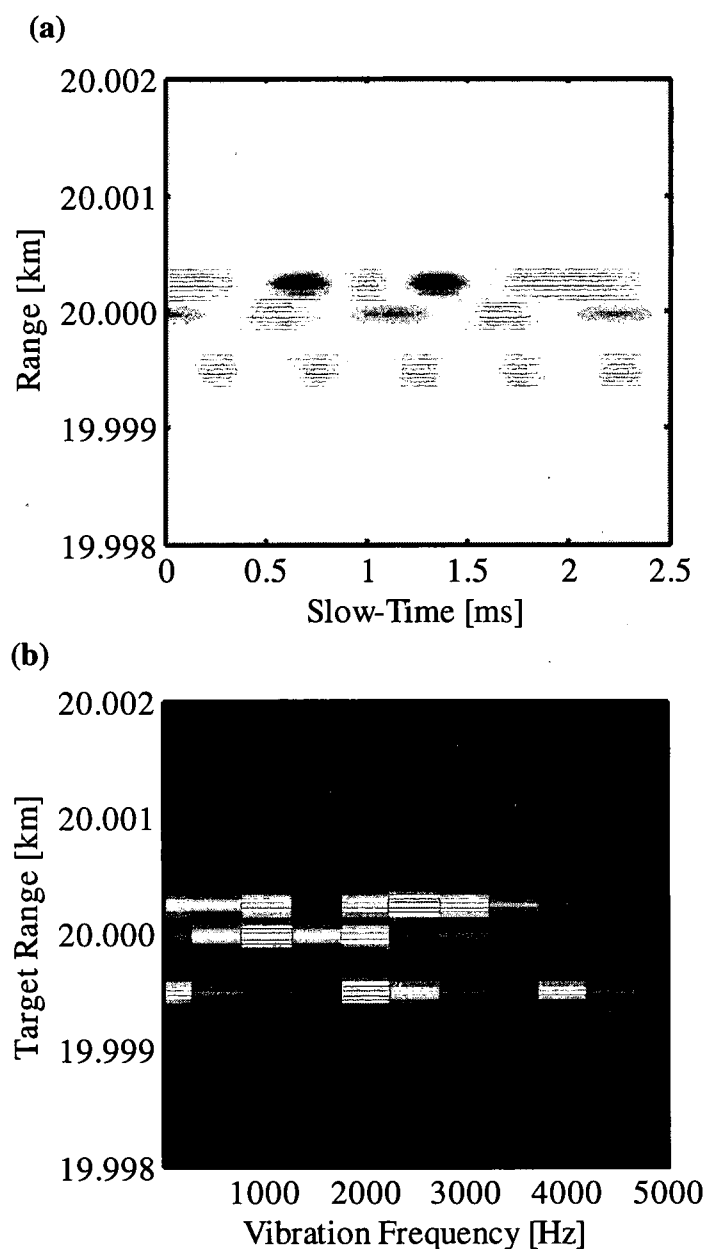


**Figure 74: The real component of the range compressed micro-Doppler phase history for three point targets illuminated by a  $T_c=1\text{ns}$  PPN waveform. (b) The micro-Doppler image of the point target array.**

The full micro-Doppler image, shown in Figure 74(b), is then found by performing the one dimensional Fourier transform operation on the phase history data, with respect to the slow-time dimension. The figure coordinates indicate range and vibration frequency, and the brightness indicates the vibration amplitude. As expected from the phase history, all of the targets remain correctly localized in range. The spectral amplitudes of targets 2 and 3 also show a single bright peak at the correct oscillation frequency; however, the phase wrapping due to the large vibrational amplitude of target 1 results in broadening of its resulting spectra. Phase unwrapping techniques can be used to mitigate this phenomenon, though processing shorter code sequences can also insure unambiguous micro-Doppler imaging.

## **B. Experimental Block Diagram**

The configuration of the laboratory ladar used is shown in Figure 75. Since the operation is at short range, it uses only the signal channel omitting the monitor channel of the complete system as described in Chapter VI. Each transmitted waveform has 20 sub-codes with 1000 bi-phase code chips each 1-ns in duration. The composite 20  $\mu$ s waveform is generated and transmitted continuously.

## **C. Micro-Doppler Target Description**

The experiment uses two similar experimental configurations. The first requires high single waveform CNR to measure the system vibration noise floor. To achieve high CNR, the variable attenuator in the transmit leg is set for maximum transmission and the mode matching on the OAP collimator was adjusted for reduced beam size. The second experiment examines the performance with reduced CNRs. In this case, the full beam size is

used and the transmitted power is varied using the variable attenuator and monitored using the low energy leg of the 96/4 splitter and the power meter preceding the transmit/receive switch.

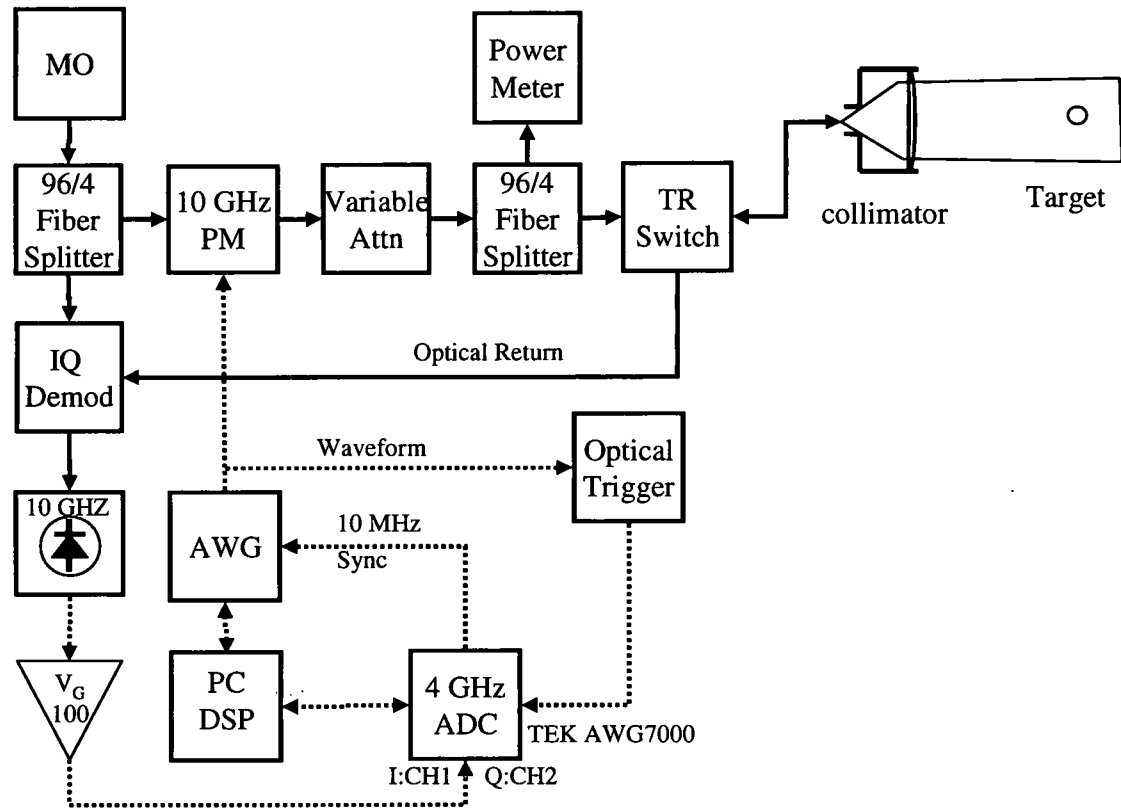


**Figure 75: Micro-Doppler Experimental block diagram.**

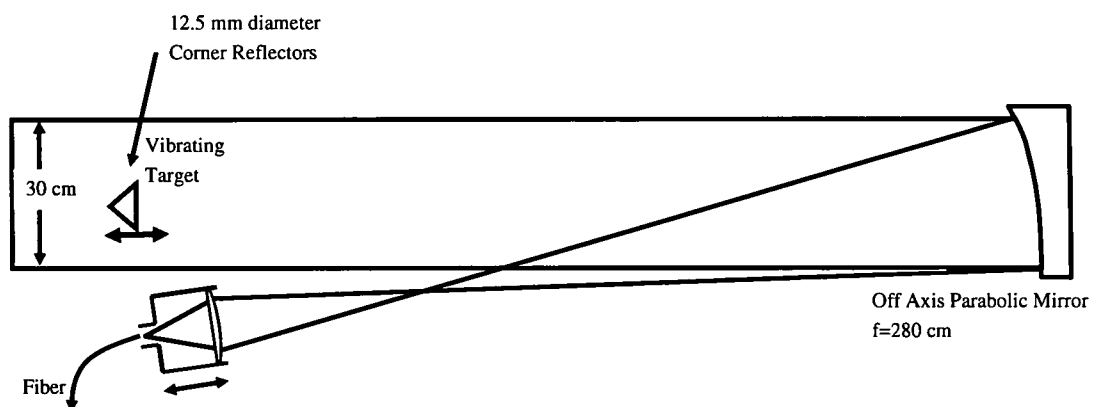


**Figure 76: Micro-Doppler target diagram with 12 inch collimator.**

The target in both cases is a vibration target adjusted to produce the lowest possible amplitude signal resulting in of 60 Hz slightly non-sinusoidal signal with an approximately 4  $\mu\text{m}$  maximum displacement.

#### D. Experimental Results

To demonstrate micro-Doppler imaging, 2,500 PPN waveforms are transmitted using the experimental configuration of Figure 75 and targets shown in Figure 76. The return signals are recorded and range compressed via fast-time matched filter on each waveform record. Figure 77 shows the real component of the two dimensional phase history. The single waveform CNR is greater than unity producing a waveform limited range IPR.

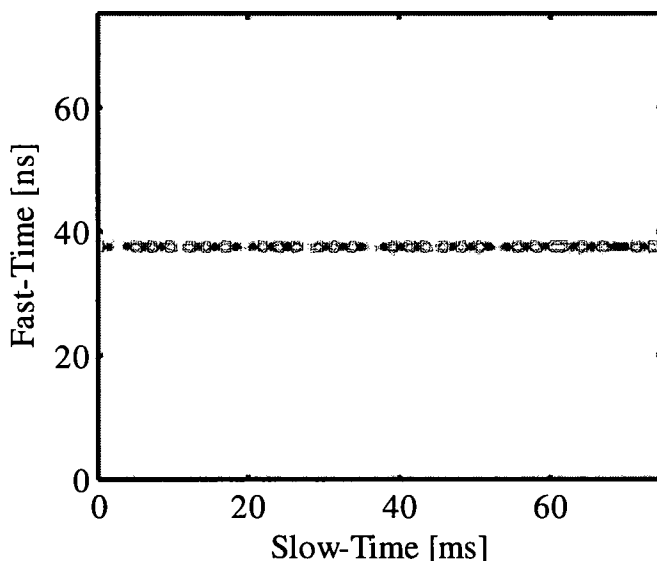


**Figure 77: Phase history of 30 Hz micro-Doppler Target.**

The slow-time cross section of the phase history at the target range is plotted in the complex plane Figure 78. Figure 78(a) shows this uncorrected vibration phase history which has a 1:3 in-phase to quadrature imbalance. This imbalance produces the elliptical pattern in the

complex plane as describe in Chapter III. Figure 78(b) show the corrected phase history after appropriate channel scaling.

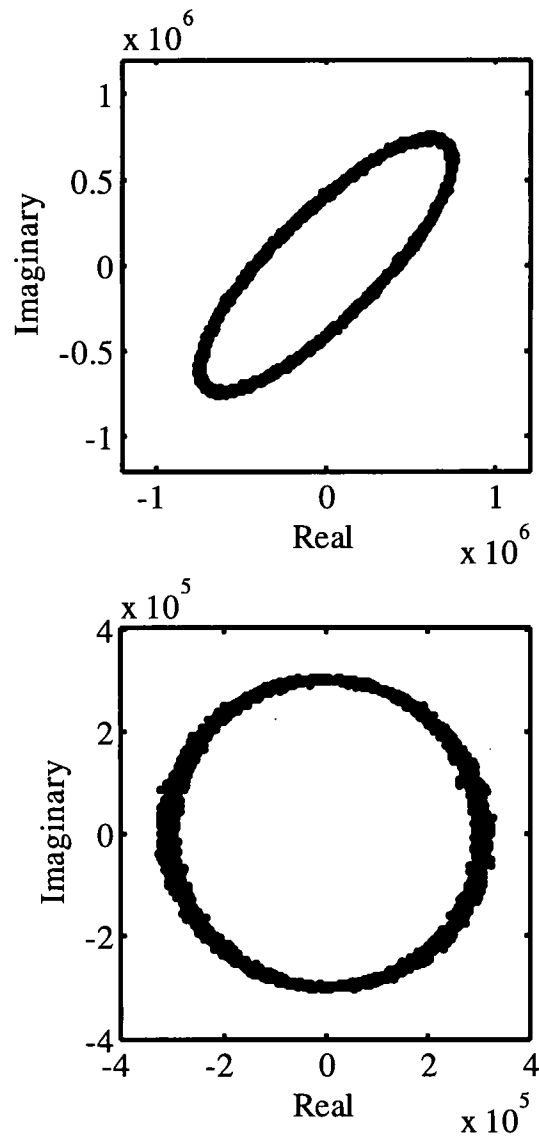


**Figure 78: Micro-Doppler phase hsiotry (a) and spectra (b).**

Scaling in post processing is possible, but it will result in increased noise in regions where radii of the measured signals are reduced. The measured phase in radians is shown in Figure 79(a). For vibration excursions larger than a wavelength, the phase is wrapped.

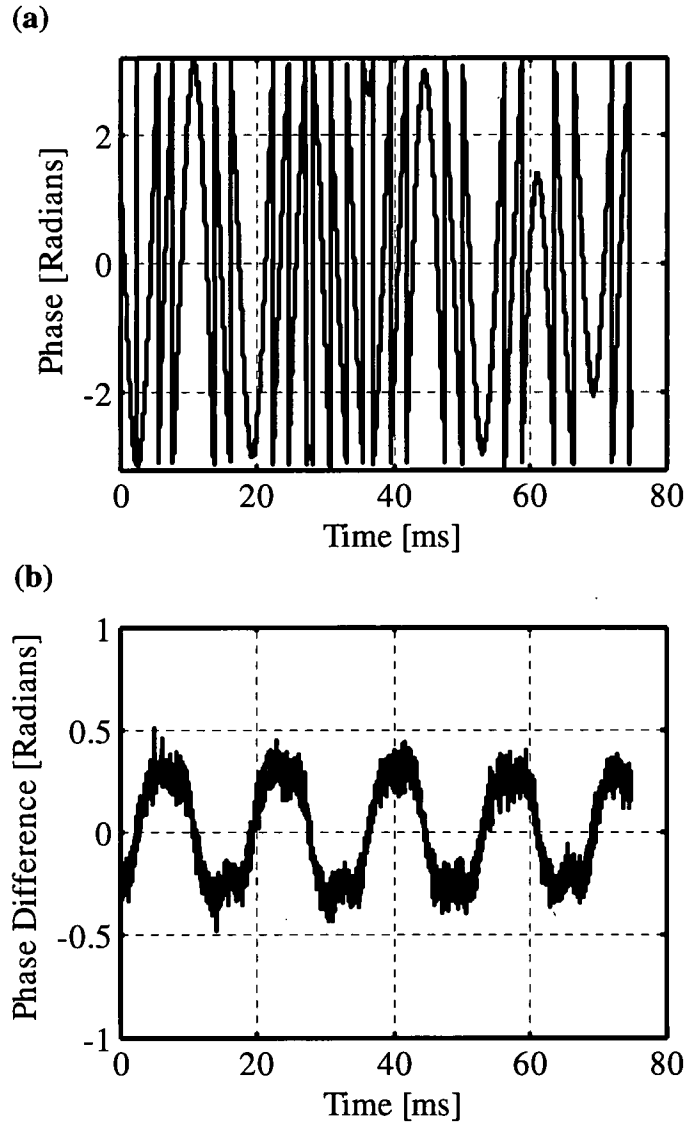


**Figure 79: Phase of 30 Hz micro-Doppler target (a) and the phase difference for a 5 PPN waveform (i.e., 100  $\mu$ s) coherent processing interval.**

Figure 79(b) shows the phase difference obtained by subtracting the measured phases separated by a fixed coherent processing interval. The velocity is related to the phase difference by Equation (101) and the velocity spectral amplitude can be found by spectral analysis. The vibration spectral amplitude shown in Figure 80, is produced by calculating the

power spectral density, taking the square root and applying the scaling to produce velocity [53]. The target frequency is correctly localized at 60 Hz.

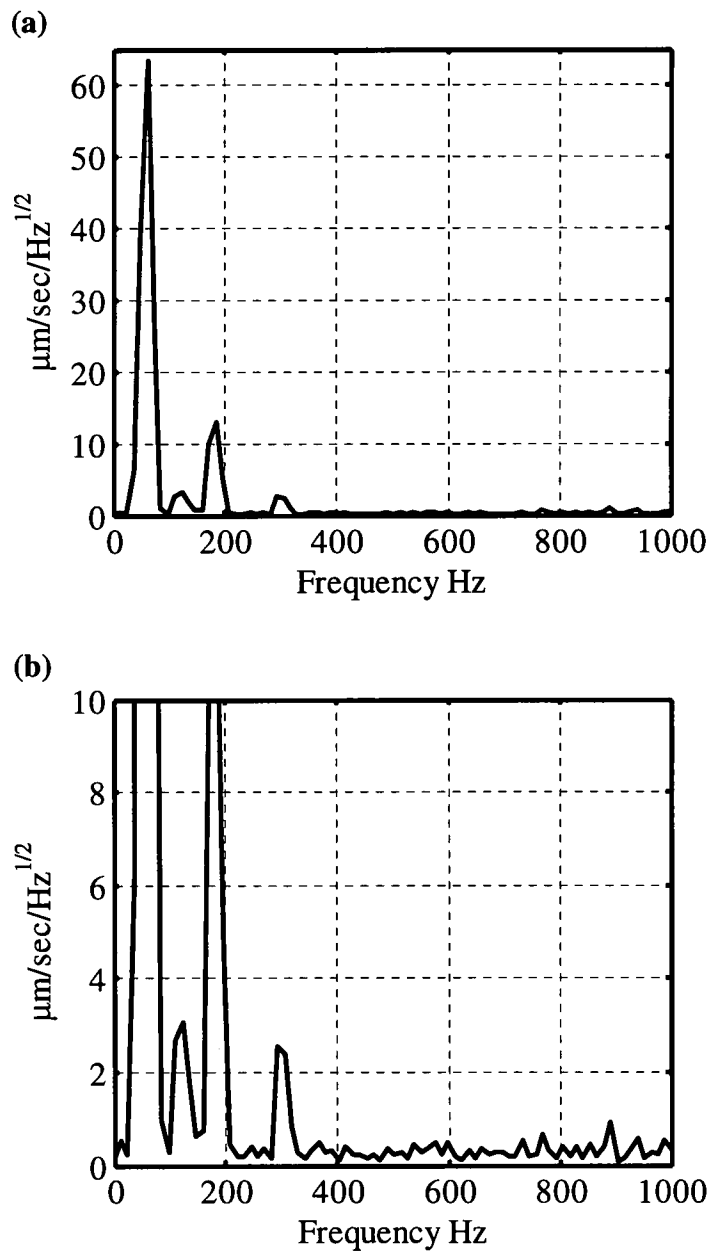
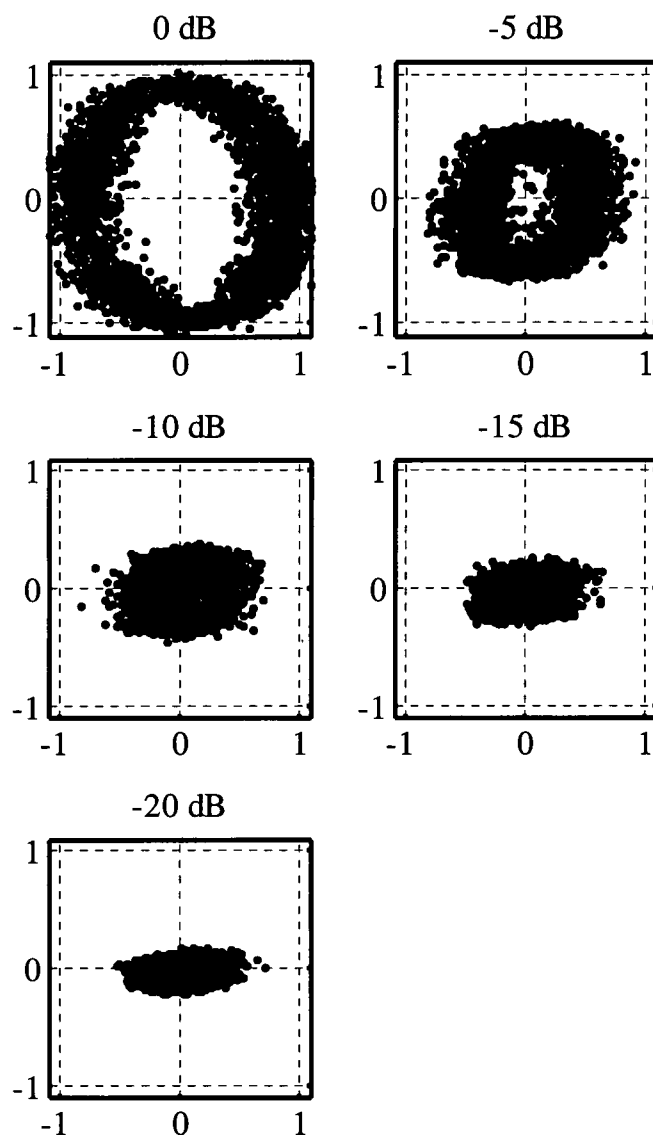


**Figure 80: Vibration velocity spectra (a) and an expanded view (b) showing the noise system noise floor.**

.Multiple harmonics are also present which are due to the deviation of the signal from ideal sinusoidal behavior as shown in Figure 79(b). Figure 80(b) shows an expanded view of the resulting spectra to highlight the measured noise floor.

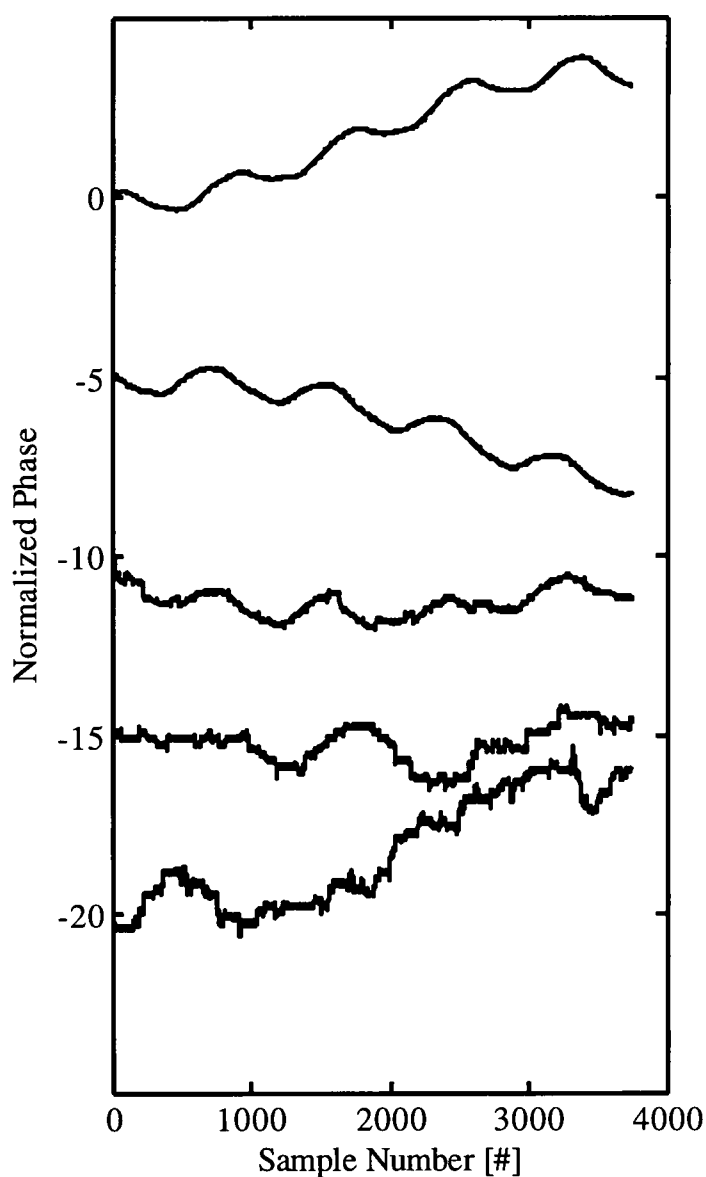
Figure 79 and Figure 80 demonstrate the best possible performance of the ladar. This performance is limited by noise within the system from a variety of sources including the master oscillator, modulator noise, mechanical instability and electronics. The performance will also be degraded by the CNR of the returned signal [54]. To illustrate the effect of reduced CNR, the OAP collimator the OAP mode matching was adjusted to produce a fully expanded beam and the variable attenuator in the transmit leg was used to reduce the transmit power in 5 dB increments. The single waveform CNR was approximately -20 dB.

Figure 81 shows the corresponding range compressed signals in the complex plane for 0 dB attenuation through 20 dB attenuation. Recalling that the distance from the origin is proportional to the CNR, it is clear that the phase measurement becomes noisier as the CNR is increased (i.e., the attenuation is increased). The phase is an angular measurement, so as the distance from the origin decreases, the relative uncertainty in the phase estimate grows.



**Figure 81: Matched filter complex output for a vibrating target as a function of transmit power attenuation.**

Figure 82 shows the unwrapped phase histories for the data shown in Figure 81. Each phase history is normalized to the 0 dB attenuation phase history. The 60 Hz signal is clearly visible for transmit attenuations up to 10 dB, but noise begins to dominate at high attenuations.



**Figure 82: Recovered phase as a function of transmit power attenuation.**

To further emphasize this, Figure 83 shows the normalized peak output within the range bin as a function of the transmit power attenuation. The peak of the measured IPR agrees well through 10 dB of attenuation, but then diverges from the nominal line.

For attenuations beyond 10 dB, the noise has a growing impact on measured peak of the IPR finally resulting in measurements that are completely dominated by noise.

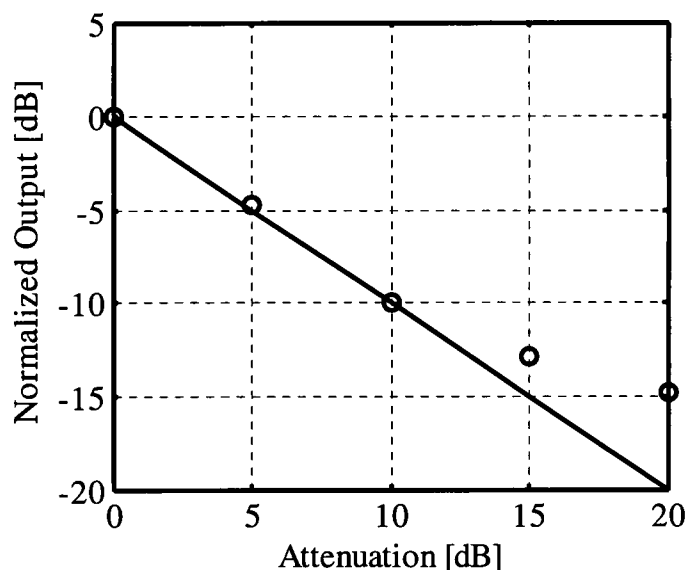


**Figure 83: Normalized output as a function of transmit power attenuation.**

A PPN waveform radar is shown to be capable of producing excellent micro-Doppler measurements. The measured system noise floor ( $\sim 1 \mu\text{m}/(\text{sec Hz}^{1/2})$ ) is more than sufficient for a wide variety of measurement applications. The use of the PPN waveform also allows a great deal of processing flexibility adapting the waveform duration, sampling frequency and coherent processing interval to the measurement requirements.

## CHAPTER XII

### MULTI-APERTURE INTERFEROMETRIC IMAGING

Remote sensing coherent ladar imaging has been demonstrated at ranges far beyond the useful range of a traditional diffraction limited imaging system. To overcome the diffraction limitations of a finite aperture, synthetic aperture ladar uses multiple spatial samples from a single small aperture in motion to synthesize a larger effective aperture. This results in higher spatial resolution, but only in the along-track dimension in which the samples were collected. Again, conventional SAL imaging was demonstrated in the laboratory as well as in flight, but is sensitive to undesired platform motions. A multiple-input, multiple-output (MIMO) ladar based on periodic pseudo noise waveforms and code division multiple access (CDMA) multiplexed transmission may be applied in the along-track dimension to implement differential SAL (DSAL). DSAL is substantially insensitive to platform motion [55]. In addition, apertures separated in the cross-track dimension are used to support interferometric SAL (IFSAL) to provide enhanced cross-track (i.e., height) estimation.

Interferometric synthetic aperture radar (IFSAR) is a commonly used radar technique developed to realize enhanced resolution in the cross-track, or vertical dimension. IFSAR utilizes the phase between each resolution cell of two synthetic aperture images collected from two closely spaced vertically offset apertures to make an estimate of the cross-track position, or height of an object [56,57]. Implementing IFSAR techniques at optical

wavelengths is extremely challenging and is impacted by phase variations from a variety of sources including variations between the two apertures, target and atmospheric decorrelation, and target motion [58].

Here, the focus is on a technique to measure the phase between the apertures using PNN waveforms in a CDMA architecture. The technique uses a multiple sub-code, pseudo-noise (PPN) waveform to phase two or more physical apertures and allows multi-input, multi-output (MIMO) operation. An optical delay introduces a one sub-code delay between the apertures so orthogonal sub-codes are transmitted and received from each of the apertures. This CDMA implementation allows each aperture to detect and process the codes from all of the transmitting apertures. Since a single transmit waveform and receiver are used, the relative phase between the apertures is measured and monitored. Differential SAL exploits the same PPN/CDMA transceiver construct, but with the apertures aligned in the along-track dimension. The two apertures moving along the same path are used to produce a SAL difference signal that is relatively insensitive to common aperture translation and vibration. This chapter develops expressions for the optically delayed CDMA signals for both interferometric and differential SAL. Finally, a laboratory PPN ladar system is used to demonstrate multi-code PPN waveforms and processing, MIMO operation via optically delayed CDMA, and multi aperture phase measurement.

#### **A. CDMA Multi-Aperture Ladar**

Applications such as interferometric or differential SAL require the use of multiple spatially separated apertures. In addition it is necessary to establish and monitor the phase

relationship between these apertures. Here, the PPN waveform is applied with code-division multiple access (CDMA) multiplexing to enable multi-input multiple-output (MIMO) ladar aperture. We describe an optical method to implement a two aperture system. The required signal processing is described and the application to interferometric and differential synthetic aperture ladar is discussed.

## B. Optical Delay CDMA/MIMO

Both the orthogonality and diversity of the PPN sub-codes are exploited to implement the multiple aperture system. As shown in Figure 84(a), the outgoing composite code is divided into two legs. The un-delayed leg is transmitted from the aperture denoted U. The second leg is delayed by one sub-code length via a fiber delay line. The length of the fiber  $l_{fiber}$  is

$$l_{fiber} = \frac{c N_c T_c}{n_{fiber}}, \quad (102)$$

where  $n_{fiber}$  is the index of refraction of the fiber,  $N_c$  is the number of chips in a sub-code and  $T_c$  is the chip width, and  $c$  is the speed of light.

In optical fiber where the index of the fiber  $n_{fiber}=1.5$ , the delay line length is 200 meters for a sub-code with 1000 chips, 1 nanosecond in duration. The delayed codes are transmitted through aperture D as shown in Figure 84(a). Both code sequences propagate to the target, but along slightly different paths due to the separation of the apertures. Upon reflection, both the undelayed signal from aperture U and the delayed signal from aperture D are collected by both apertures resulting in three copies of the signal as shown in the lower portion of Figure 84(b). In the first path denoted as UU, the code is transmitted and received from the

undelayed aperture and experiences no delay. In the second path denoted UD, the code is transmitted and received from either the delayed or undelayed aperture and experiences a 1 sub-code delay.

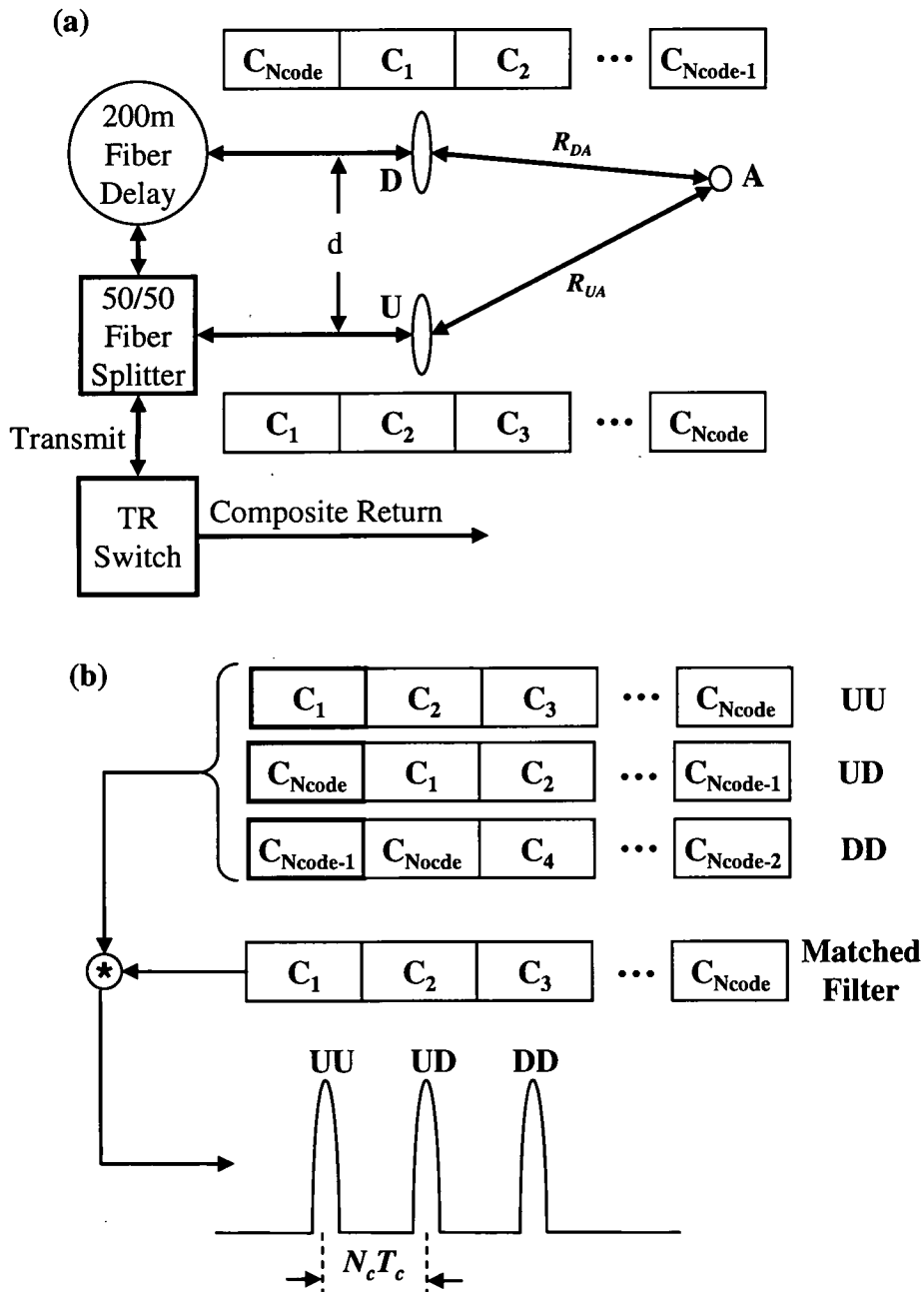


Figure 84: Two aperture MIMO fiber implementation block diagram.

Finally, in the third path denoted DD, the code is transmitted and received from the delayed aperture and experiences a 2 sub-code delay. All paths are recombined at the fiber combiner and processed as a single return with delayed components. Applying the matched filter for the undelayed composite code to the multi-aperture return results in three delayed signals notionally shown in Figure 84(b).

The UU and DD paths measure the round trip path from aperture U and D to the target denoted as  $2R_{UA}$  and  $2R_{DA}$  respectively. The third path is similar, whether beginning at the un-delayed or delayed aperture (UD or DU) and measures the sum of the path from the un-delayed aperture U to the target A and back to the delayed aperture D and is denoted as  $R_{UA} + R_{DA}$ . The phase relationships between each of the paths is monitored since the measurements are all derived from a single, common waveform and are processed in a single receiver. Although the range resolution  $\Delta R$  of the PPN waveform is proportional to the chip width, (i.g.,  $\Delta R = 0.166$  m with  $T_c = 1$ -nanosecond), the relative motion between the apertures and the target can be determined to a fraction of the optical wavelength since the relative phase between the apertures can now be measured.

In PPN CDMA, the matched filter output is consistent with Eq. (76), but is the superposition of delayed orthogonal sequences convolved with the composite waveform matched filter  $w^*[-n]$ . The mainlobe response at  $q[0]$  is due to the correlated signal components and remains unchanged. The sidelobes, however, are the summation of  $N-1$  cross correlations between the different PN codes resulting in an increase in sidelobe levels proportional to the number of code sequences.

### C. Cross-Track Interferometric SAL

Synthetic aperture imaging is a geometric imaging approach which localizes targets as a function of range and cross-range. Targets are localized in range utilizing high bandwidth waveforms, and in cross-range by exploiting the phase variation of the signal due to the controlled relative motion between the aperture phase center and the target as described by Eq. (18). Assuming the stripmap geometry of Figure 4, multiple target observations are collected where each temporal waveform record (i.e., fast-time record) is collected as a function of aperture location  $u$  (i.e., slow-time record). The fast-time records are then assembled into a two dimensional phase history  $s[k, u]$  written as

$$s[k, u] = \sum_{n=1}^{N_{gt}} \left\{ A(x_n, y_n, z_n) \sigma_n \exp\left(-j \frac{4\pi R_n(u)}{\lambda}\right) \frac{1}{\sqrt{N_c T_c}} \sum_{m=1}^{N_c} \phi_m \left[ k \frac{T_s}{T_c} - (m-1) - \frac{2R_n(u)}{T_c c} \right] \right\}, \quad (103)$$

where  $R(u)$  is the line-of-sight range between the ladar and at target at location  $u$ . In general, two dimensional matched filtering is used to produce the range, cross-range image; however, since the effective aperture is increased in the along-track dimension, the resolution of the resulting two dimensional image is only increased in the along-track dimension as well.

Interferometric synthetic aperture ladar (IFSAL) is one technique which may be used to provide improved localization of a target in the cross-track dimension. In IFSAL, the two cross-track apertures shown in Figure 85 have a vertical separation  $d$  and velocity  $v_p$  which provides three path measurements to the targets. The first phase measurement is the round trip from the un-delayed  $U$  aperture to the target  $A$  calculated as

$$\phi_{UA}(u) = 2 \frac{2\pi}{\lambda} \sqrt{(u - x_A)^2 + (y_U - y_A)^2 + (z_U - z_A)^2}, \quad (104)$$

where  $(u, y_u, z_u)$  is the location of the ladar, and  $(x_A, y_A, z_A)$  is the location of the target.

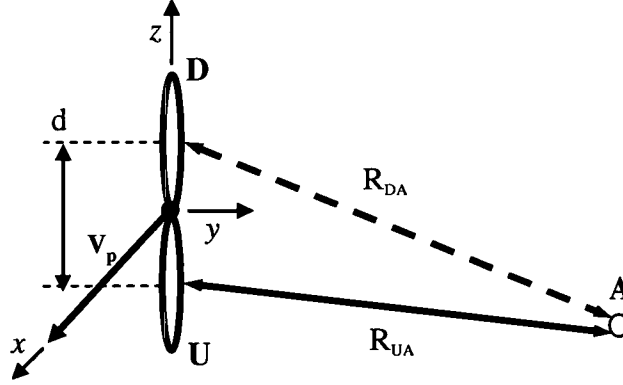


**Figure 85: Interferometric SAL measurement geometry with two apertures offset in the cross-track (i.e., vertical) direction.**

The second is the round trip phase from the delayed aperture  $D$  to the target  $A$  and is written as

$$\phi_{DA}(u) = 2 \frac{2\pi}{\lambda} \sqrt{(u - x_A)^2 + (y_U - y_A)^2 + (z_U + d - z_A)^2}, \quad (105)$$

where  $d$  is the aperture separation. The final path is from the un-delayed aperture  $U$  to the target  $A$  and back to the delayed aperture  $D$ , or visa-versa, and is written as

$$\begin{aligned} \phi_{DAU}(u) = & \frac{2\pi}{\lambda} \sqrt{(u - x_A)^2 + (y_U - y_A)^2 + (z_U + d - z_A)^2} \\ & + \frac{2\pi}{\lambda} \sqrt{(u - x_A)^2 + (y_U - y_A)^2 + (z_U - z_A)^2} \end{aligned} \quad (106)$$

which is simply the sum of the individual paths  $R_{UA} + R_{DA}$ . For example, the round trip quadratic phase for two ladar apertures operation at a wavelength of  $\lambda = 1.5 \mu\text{m}$  and separated

by 30 cm assuming a target 50 km away is shown in Figure 86. This shows that the phase is offset for the vertical distribution, but the phase centers remain unchanged.

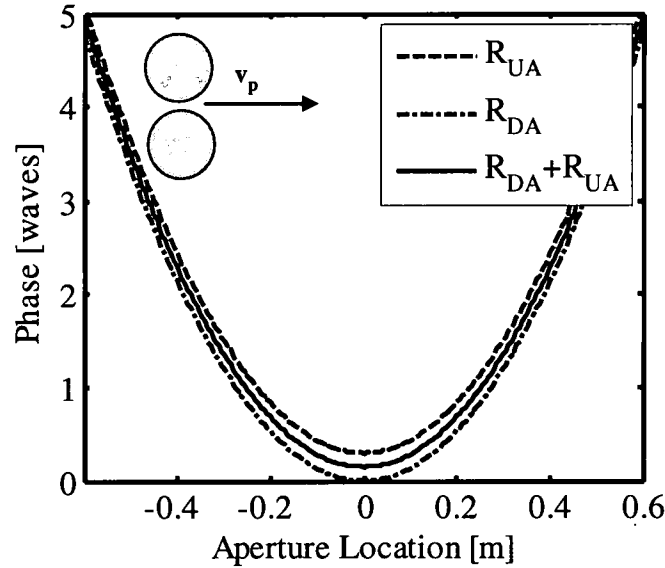


**Figure 86: Interferometric SAL phase variation as a function of platform location,  $u$ .**

Figure 87(a) shows the phase measured by each aperture as a function of target height. Here the ladar is stationary measured from the center of the beam. The phase from each path is quadratic, but offset by the aperture separation. Figure 87(b) also shows the phase difference for two target locations, one 0.3 meters above the center of the apertures and the other at -0.6 meters below, indicating the phase difference is unique with target height. To estimate the target height, the measured phase difference  $\Delta\phi$  between the two paths is written as

$$\Delta\phi = \frac{2\pi}{\lambda}(2R_{UA} - 2R_{DA}) = \frac{2\pi}{\lambda} \left( 2\sqrt{(z_A - d/2)^2 + y_A^2} - 2\sqrt{(z_A + d/2)^2 + y_A^2} \right). \quad (107)$$

The phase on the left side of Eq. (107) is in terms of the measured phase and those on the right are based upon the geometry of the target and apertures.

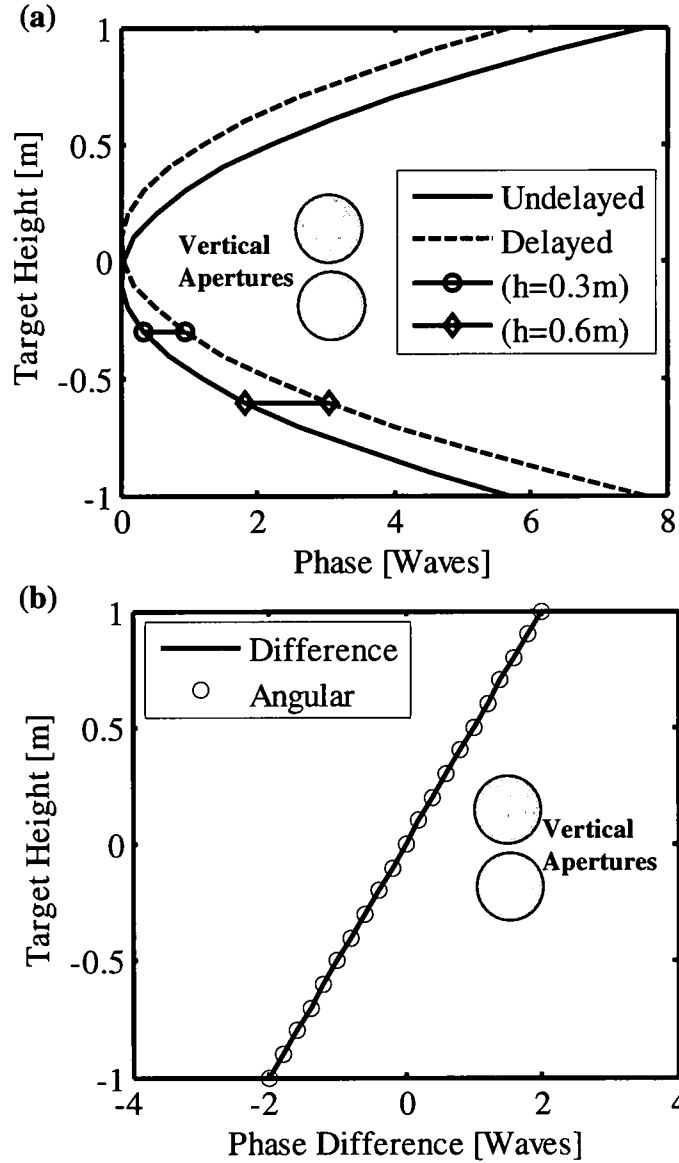


**Figure 87: Interferometric SAL phase (a) and phase difference (b).**

Moving the range, or  $y$  components, out of the radicals of Eq. (107) will allow them to be expanded using a Taylor series

$$\left( R_{UA} - \frac{2\pi}{\lambda} 2R_{DA} \right) = y_A \sqrt{1 + \left( \frac{z_A - d/2}{y_A} \right)^2} - y_A \sqrt{1 + \left( \frac{z_A + d/2}{y_A} \right)^2}. \quad (108)$$

Keeping only the first terms in the expansion, the phase difference becomes

$$(R_{UA} - R_{DA}) = y_A \left( 1 + \frac{1}{2} \left( \frac{z_A - d/2}{y_A} \right)^2 \right) - y_A \left( 1 + \frac{1}{2} \left( \frac{z_A + d/2}{y_A} \right)^2 \right). \quad (109)$$

Simplifying the series by combining terms yields

$$(R_{UA} - R_{DA}) = \frac{y_A}{2} \left( \left( \frac{z_A - d/2}{y_A} \right)^2 - \left( \frac{z_A + d/2}{y_A} \right)^2 \right). \quad (110)$$

Finally expanding the two quadratic terms and performing the subtraction, the phase is expressed as

$$(R_{UA} - R_{DA}) = -\frac{z_A d}{y_A} = \Delta\phi \frac{\lambda}{4\pi}, \quad (111)$$

which can then be solved to produce and estimate of the height  $z_A$ . Rearranging Eq. (111) to solve for the height  $z_A$  yields

$$z_A = \frac{\lambda y_A}{4\pi d} \Delta\phi, \quad (112)$$

where the estimate is a function of the wavelength, the distance to the target, the separation of the apertures and the phase between the signals. Assuming the wavelength and separation are fixed and known, then the height estimate depends only on the range to target and the relative phase. The height estimate will be ambiguous for phase differences  $\Delta\phi$  that are multiples of  $2\pi$ . Inserting  $2\pi$  of  $\Delta\phi$  in Eq. (112) into the previous equation yields the ambiguous height  $z_{amb}$  as

$$z_{amb} = \frac{\lambda y_A}{2d}. \quad (113)$$

The extent of the beam is limited by the diffraction limited beam width. The number of height ambiguities within a diffraction limited beam is given by the ratio of the beam diameter  $D_b$  and the ambiguity height  $z_{amb}$  and is written as

$$\frac{D_b}{z_{amb}} = \frac{2.44 \frac{\lambda}{D_o} R_n}{\frac{\lambda R_0}{2d}} = \frac{2 \cdot 2.44d}{D_o} \quad (114)$$

where  $D_o$  is the aperture diameter and  $d$  is the aperture separation. Since  $d$  must be greater than or equal to  $D_o$  for vertically separated physical apertures, there will be at least 4.88 ambiguity cycles within the beam footprint. The use of additional apertures or alternative aperture separations may be able to mitigate this ambiguity, but is beyond the scope of this work.

#### **D. Along Track Differential SAL**

Synthetic aperture lidar is sensitive to uncompensated motion due to the short wavelength of the transmit laser. Along-track Differential SAL (DSAL) has been proposed as a way to produce SAL images that are immune to both platform translation and vibration [59]. We show that a CDMA multi-aperture lidar can implement DSAL using a single transmit and receive channel and slightly modified image formation processing.

Figure 88 shows the DSAL geometry where 2 apertures of diameter  $D_o$  are separated by a distance  $d$  in the along track direction. The apertures are assumed to be adjacent in the along track dimension and  $D_o=d$ . The forward aperture is the CDMA un-delayed aperture U and the trailing aperture is the delayed aperture D.

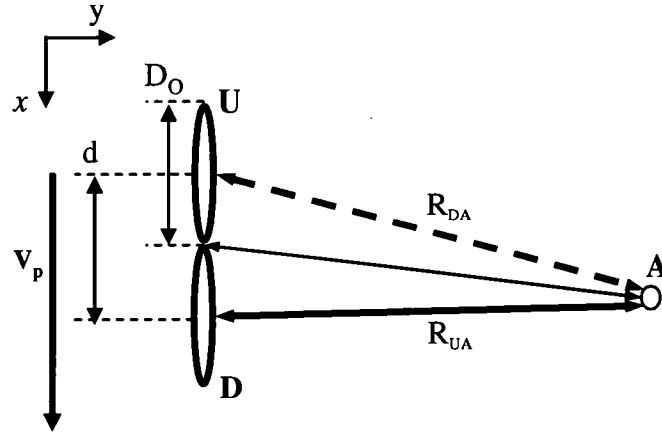


**Figure 88: Differential SAL Geometry with two apertures offset in the along-track (i.e., horizontal) direction.**

The range between each of the apertures  $R_{UA}$  and  $R_{DA}$ , and the target, now includes the along-track aperture offset and are written

$$R_{UA} = \sqrt{(u - x_n + d/2)^2 + (y - y_n)^2} = (y - y_n) \sqrt{1 + \frac{(u - x_n + d/2)^2}{(y - y_n)^2}} \quad (115)$$

$$R_{DA} = \sqrt{(u - x_n - d/2)^2 + (y - y_n)^2} = (y - y_n) \sqrt{1 + \frac{(u - x_n - d/2)^2}{(y - y_n)^2}}, \quad (116)$$

where it assumed that  $z_n=0$ . The ranges are approximated using the Taylor's series expansion and keeping only the first terms according to

$$R_{UA} = (y - y_n) \left[ 1 + \frac{1}{2} \left( \frac{(u - x_n + d/2)^2}{(y - y_n)^2} \right) \right] \quad (117)$$

$$R_{DA} = (y - y_n) \left[ 1 + \frac{1}{2} \left( \frac{(u - x_n - d/2)^2}{(y - y_n)^2} \right) \right] \quad (118)$$

Now taking the difference between the two phases yields the range difference  $\Delta R$

$$R_{UA} - R_{DA} = \frac{1}{2} \left( \frac{(u - x_n + d/2)^2}{(y - y_n)} - \frac{(u - x_n - d/2)^2}{(y - y_n)} \right) \quad (119)$$

which after simplification and multiplication by  $2\pi/\lambda$ , becomes the differential phase  $\Delta\phi$  written as

$$\Delta\phi = j \frac{2\pi}{\lambda} d \frac{(x_n - u)}{(y - y_n)} \quad (120)$$

Since  $\Delta\phi$  is differential, common mode disturbances will cancel resulting in a signal immune to radial motion.

Figure 89 shows the range migrations (solid lines) for a stripmap DSAL operation at a wavelength of  $\lambda = 1.5 \mu\text{m}$  where the center of the region of interest is at 50 km and centered at  $x=0$  m.

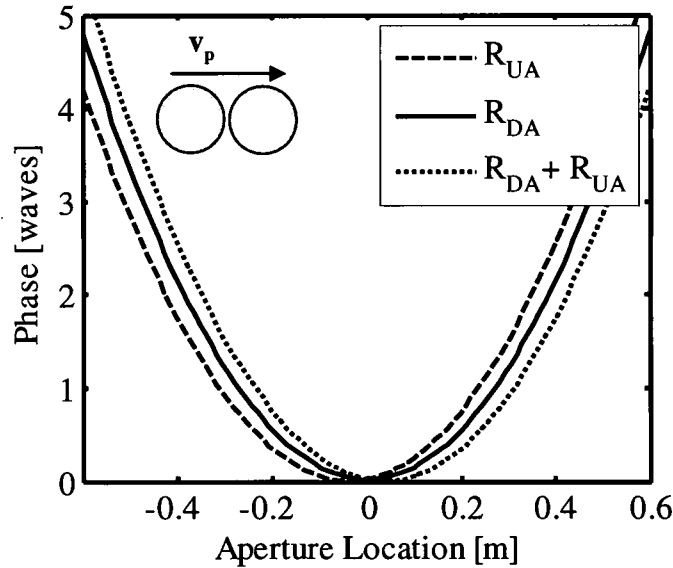


**Figure 89: Along track Differential SAL phase variation with aperture location.**

When uncompensated radial motion is added, the range histories of each aperture (dashed lines) are severely distorted compared to the apertures with no motion (solid lines).

To illustrate the impacts, a large translational velocity (i.e., 10 mm over the aperture) and vibration with 10 cycles per aperture time and a peak displacements of  $2\text{ }\mu\text{m}$  are added to the platform motion. In this example, the offset due to translation is initially 0, but then increases linearly across the phase history as shown in Figure 90. The micro-Doppler phase is visible throughout. Either of these severely degrades the response of the matched filter.

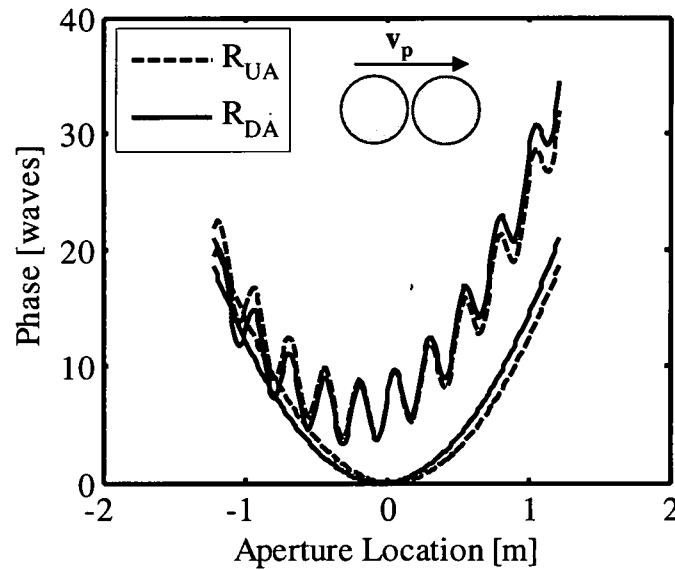


**Figure 90: DSAL phase for a stationary target (solid lines) and a target with translational and vibrational motion components (dashed lines).**

The differential signal between the apertures is shown in Figure 91 (circles) and is compared to the ideal differential signal with no motion (solid line). Both signals are in excellent agreement indicating that the differential approach is able to mitigate the effects of the residual motion. The differential signal is then processed using an approach similar to Doppler beam sharpening, but now the matched filter is based on the differential phase. Extending this technique to other imaging geometries should be possible, but is beyond the scope of this work.

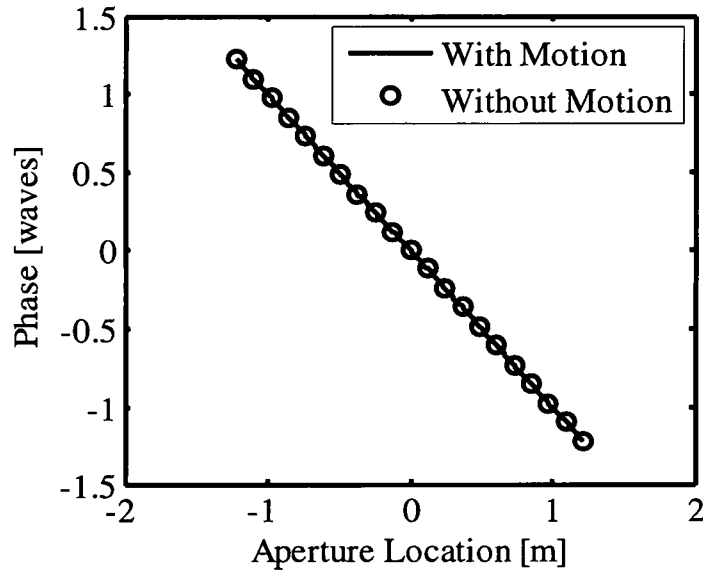


**Figure 91: DSAL phase for moving target (solid line) and stationary target (circles).**

#### **E. MIMO Experimental Ladar System**

The MIMO experiment is designed to demonstrate the key aspects of PPN waveforms in CMDA/MIMO ladar including PPN waveform generation, optically delayed transmission and reception, CDMA multi-code compression, and multi-aperture phase retrieval. The phase retrieval is demonstrated using a vibrating target rather than a moving aperture to simplify the experiment, but is directly transferable to IFSAL and DSAL experiments.

The laboratory ladar system shown in Figure 92 is designed to generate, transmit, detect and record long sequence PPN waveforms in a MIMO architecture using CMDA encoding. The system is fiber based operating at a wavelength  $1.5\ \mu\text{m}$ . The stable master oscillator (MO) is a continuous wave Koheras Adjustik laser with nominal spectral line width less than 1 kHz. The MO is isolated from the remainder of the system by an Optics for Research fiber isolator (OFR IOT-F-1550). The MO is split with a 96/4 fiber splitter.



first undelayed leg  $U$  is fiber coupled to a collimator and directed to the target. The second leg  $D$  is delayed by a sub-code length using a 200m polarization maintaining fiber, before fiber coupling to an identical collimator and directed to the target. The target is a 1.25 cm corner cube mounted on a Hardy vibration calibration stand. The fiber collimators each produced a 3.4 mm output beam and are co-aligned by contact mount on a v-block. The return light from the corner cube contains signals transmitted from both apertures and both signals are collected by both the un-delayed and delayed apertures creating the UU, DD, and UD paths described previously. The coupling is degraded due to the short range to target and finite beam size. The signals from the apertures are recombined and passed back through the return path of the T/R switch and mixed with the un-modulated fraction of the MO in a free space quadrature mixer. The resulting phase modulated signal is detected at baseband on two matched fiber coupled PicoSecondPulse Laboratory DC-10 GHz detectors. A Tektronix 7052 arbitrary waveform generator is used to generate the phased codes to drive the modulator. For this experiment 20 binary PPN sub-codes each with  $N_c=1000$  phase chips of width  $T_c = 1$  ns are generated and transmitted continuously from each aperture. Both the in-phase and quadrature outputs are digitized and stored on two channels of an Aqiris 582 digitizer at 4 GS/second. The resulting waveforms are transferred to a PC for post processing and analysis.

#### **F. Optically Delayed CDMA Multi-Aperture Waveforms and Pulse Compression**

To demonstrate multi-aperture operation, the multi sub-code PPN waveform is generated, optically delayed, and transmitted from two apertures via CDMA as described. The CNR of the return signal containing the superposition of the UU, DU and DU paths is

much less than unity due to the poor target coupling with the co-aligned apertures at short range. After applying a single matched filter to the composite return signal, however, the three IPRs shown in Figure 93 were generated.

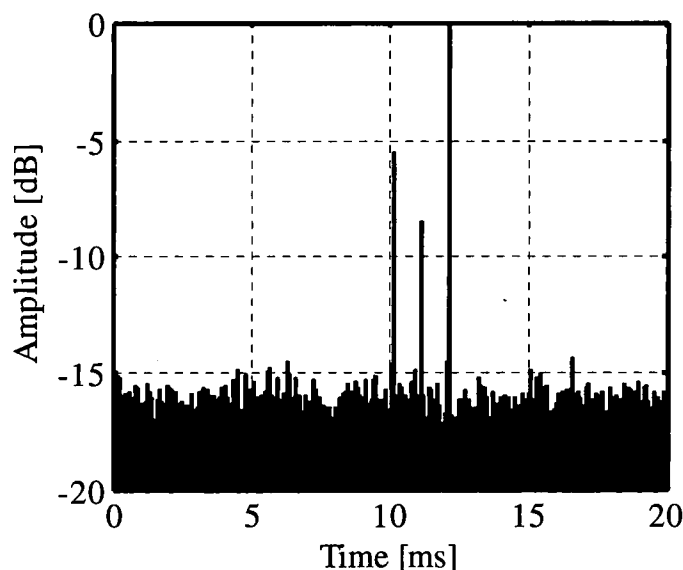


**Figure 93: Measured IPRs for the TDM/CDMA MIMO LADAR.**

Each demonstrated resolution consistent with the transmitted chip width. The side-lobe levels are elevated from the ideal levels due to the reduced CNR of the return signal. Inter-signal interference also contributed to the sidelobe increase, but with only two simultaneous codes being transmitted, the growth here is dominated by the CNR. The three returns are the UU, DD and DU paths measured from two separate apertures using a single receiver/processing path.

### **G. MIMO Phase Recovery**

Long segments of the data are used to demonstrate phase recovery between each of the apertures. Here we apply the same single matched filter to the entire signal record

containing 300 mega-samples resulting in a repetitive output signal containing the three IPR peaks with the phase associated with the vibrating target. The 30 Hz vibration undergoes multiple cycles during the measurement time. The complex data associate with each IPR peak is used to calculate the phase of each aperture path. A segment of the measured modulo  $2\pi$  phase is shown in Figure 94.

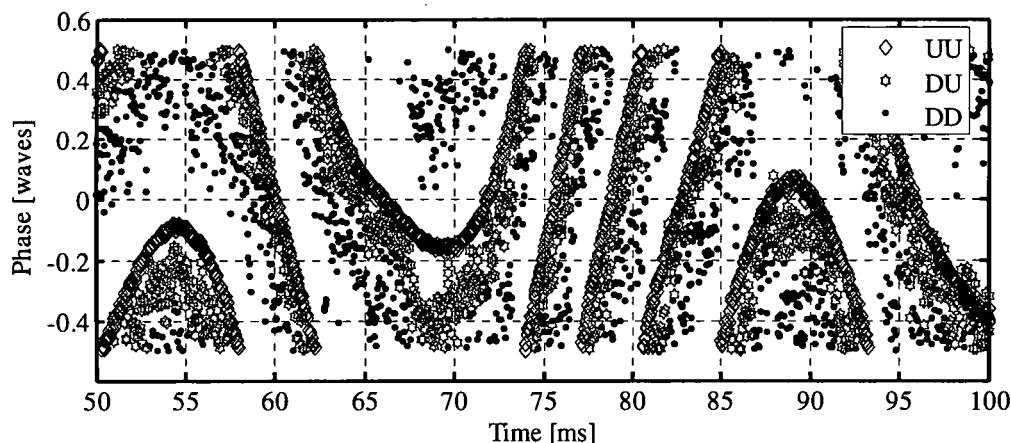
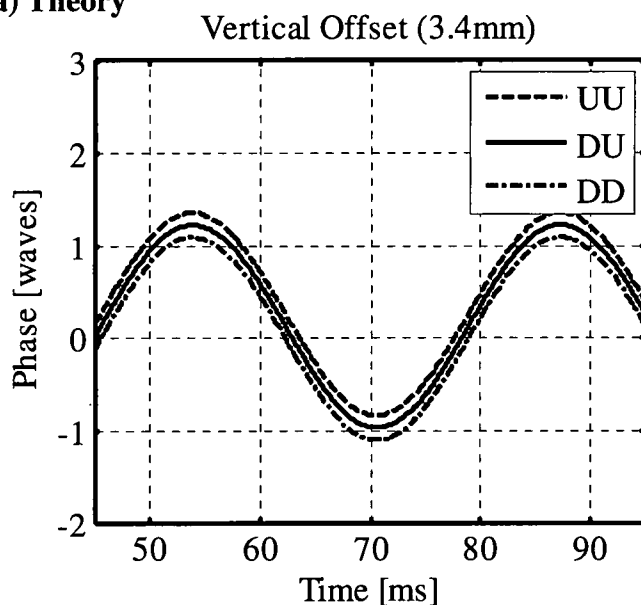


**Figure 94: Two aperture MIMO wrapped phase for UU, DD, and DU paths.**

The noise on the phase estimate is proportional to the CNR of each path. The disparity in CNR between channels is due to the sub-optimal coupling of the short range measurement and is not indicative of a systems performance at range. Multiple phase wraps are visible, but after unwrapping and digital lowpass filtering, the resulting phase histories shown in Figure 95 are in good agreement with the 30 Hz oscillation. In the measured data, the 30 Hz signal is superimposed on a low frequency trend more clearly visible in full sequence of data. This slow variation is real and is attributed to the non-ideal, low frequency behavior of the target system. As expected for the stationary aperture case the relative phase

of the UU, DD and DD signals is constant and is used to establish and monitor the relative phase between each of the aperture paths.

(a) Theory



(b) Measured

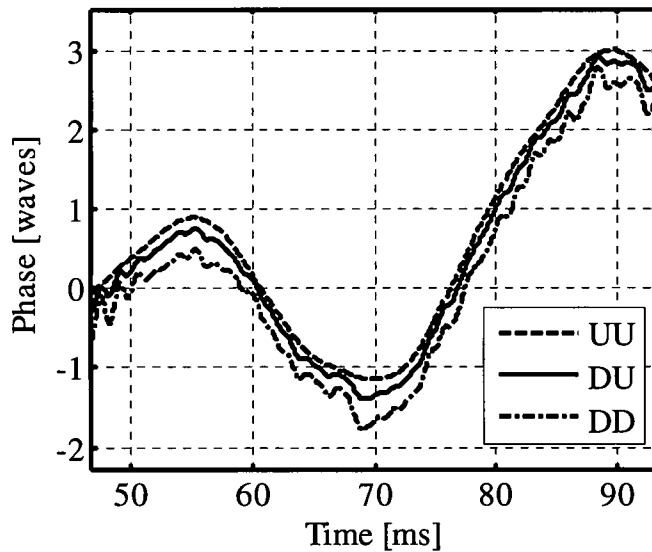


**Figure 95: Theoretical phase (a) and measured phase (b) for the two aperture MIMO configuration.**

## **H. Conclusions**

Periodic, pseudo noise sequences have been shown to provide the capability to make simultaneous high range resolution and high phase resolution measurements in a multifunction imaging ladar. Here we demonstrated a method to utilize PPN waveforms with optically delayed CDMA encoding to implement MIMO ladar. The signals from a two aperture system is measured and processed with a single receiver.

The application of this technique to IFSAL and DSAL were described. Although there are significant additional challenges for both, this technique provides the basic requirement of measuring phase referenced signals from separated sub-apertures. An experimental ladar was developed and demonstrated the essential features of the PPN waveform applied to multi-aperture ladar including multi-code signal, optical delay CDMA, composite waveform matched filter processing and phase recovery.

## CHAPTER XIII

### SYSTEM LEVEL MODELING

The previous chapters presented a coherent laser radar based on a periodic pseudo-noise waveform. Here, the performance of a PPN ladar is evaluated parametrically as a function of the system parameters, platform altitude, range to the target, and atmospheric conditions. Imaging requirements are somewhat independent of the observation platform, but depend directly upon the target to be imaged. For spatial sensors, the resolution is dictated by the size of the target and the degree of similarity of targets. For this analysis, the parameters shown in below will be assumed as a design point of a sensor with parameter variation about that point.

#### *1) Laser Radar Equation*

The laser radar equation (LRE) relates the performance of a ladar system to the characteristics of the ladar system, the propagation channel, the target, and the measurement geometry [16, 38, 60]. The LRE can be written in a variety of forms, but the return power  $P_r$  at the detector is written here as

$$P_r = P_T T_{ATM} \frac{A_{Tgt}}{A_{Tx}} R_{tgt} T_{ATM} \frac{A_{RA}}{A_{Rx}}, \quad (121)$$

where  $P_T$  is the transmit power,  $T_{ATM}$  is the atmospheric transmission,  $R_{tgt}$  is the reflectivity of the target,  $A_{Tgt}$  is the target area,  $A_{Tx}$  is the diameter of the transmit beam at the target,  $A_{RA}$

is the collection area of the receive optics and  $A_{Rx}$  is the diameter of the reflected beam at the receiver.

Parameter	Symbol	Value
<b>Platform</b>		
Range (Nominal)	R	75 km
Platform Altitude (Nominal)	$h_p$	40 kft
Platform Velocity	Vac	100 m/s
<b>Atmosphere</b>		
Transmission Model	MLS	FASCODE Mid-Latitude Summer 23 km Visibility
Turbulence Model	HV5/7	Hufnagel-Valley 5/7
<b>Ladar System</b>		
Wavelength	$\lambda$	1.5 $\mu\text{m}$
Real Aperture Diamter	$D_{RA}$	15 cm
Average Power	$P_t$	10 W
PPN Waveform	$N_{\text{code}}$ $N_c$ $T_c$	20 sub-codes 1000 chips/sub-code Chip duration 1 ns
<b>Performance</b>		
Spatial Resolution (Range & Cross-range)	$\Delta R, \Delta CR$	15 cm
Noise Equivalent Vibration Velocity	NEVV	30 $\mu\text{m}/(\text{sec } \sqrt{\text{Hz}})$
Frequency Range	$\Delta f$	10-3000 Hz
Frequency Resolution	$\Delta \Phi$	1 Hz

In Eq. (1) the transmit power is attenuated by the propagation through the atmosphere  $T_{ATM}$ . If the area of the target  $A_{Tgt}$  is less than the area of the transmit beam  $A_{Tx}$  then the return power is decreases as the ratio of the areas. If the area of the target is greater than the beam (i.e., the beam is completely captured by the target) this ratio is unity. Writing the areas in terms of the diameters the return power becomes

$$P_R = P_T \frac{D_{Tgt}^2}{D_{Tx}^2} T_{ATM}^2 R_{tgt} \frac{D_{RA}^2}{D_{Rx}^2} , \quad (122)$$

where  $D_{Tgt}$ ,  $D_{RA}$ ,  $D_{TX}$  and  $D_{RX}$  are, respectively, the diameter of the target, the real aperture of the system the transmit beam at the target at the diameter of the return beam at the ladar aperture. This version of the LRE is for an unresolved target where the diameter of the target  $D_{Tgt}$  is less than the diameter of the transmit beam  $D_{Tx}$ . To include both cases, the target interaction efficiency function  $\eta_D$  defined as

$$\eta_D = \begin{cases} 1 & D_{Tx} \leq D_{tgt} \\ \left( \frac{D_{tgt}}{D_{Tx}} \right)^2 & D_{Tx} > D_{tgt} \end{cases} \quad (123)$$

where  $\eta_D$  is unity if the transmit beam is smaller than the target (i.e., the resolved target) and  $\eta_D$  is the squared ratio of the target and beam diameters if the transmit beam is larger than the aperture (i.e., the unresolved case). Inserting this efficiency and assuming a Lambertian target, the LRE becomes

$$P_R = P_T T_{ATM}^2 R_{tgt} \frac{D_{RA}^2}{4R^2} \eta_D, \quad (124)$$

which is a function of  $1/R^2$  for resolved targets when  $\eta_D=1$  and  $1/R^4$  otherwise. Assuming matched filter processing, then the single waveform CNR may be calculated from the waveform energy as

$$CNR = \frac{P_R}{N} = \frac{E_T T_{ATM}^2 \sigma_{tgt} D_{RA}^2}{4h \frac{c}{\lambda} R^2} \eta_D \eta_O \eta_M \eta_T, \quad (125)$$

where  $h$  is Planck's constant,  $\lambda$  is the operating wavelength,  $\eta_O$  is the efficiency of the optical system, and  $\eta_M$  is the system coherent mixing efficiency under ideal conditions. The final efficiency factor incorporates the reduction in effective aperture due to atmospheric turbulence. The atmospheric coherence diameter at the aircraft is given by

$$r_0 = \left[ .4233 k = \left( \frac{2\pi}{\lambda} \right)^2 \int_0^R C_n^2 \left( h_p + \frac{z}{R} (h_t - h_p) \right) \left( \frac{z}{R} \right)^{5/3} dz \right]^{-3/5} \quad (126)$$

where  $h_p$  is the height of the platform,  $h_t$  is the height of the target, and  $z = R$  corresponds to the receiving aperture location [61]. The efficiency due to turbulence  $\eta_T$  is modeled here as

$$\eta_T = \begin{cases} 1 & r_0 \geq D_{RA} \\ \left( \frac{r_0}{D_{RA}} \right)^2 & r_0 < D_{RA} \end{cases}, \quad (127)$$

where  $r_0$  is the coherence diameter of the atmospheric path and  $D_{RA}$  is the effective diameter of the real aperture. Equation (127) then shows that the mixing efficiency has a strong dependence on the coherence diameter once it is less than the diameter of the real aperture. Although not immediately apparent from Eq. (123), the target interaction efficiency  $\eta_i$  is also impacted by turbulence. The diameter of transmit beam at the target  $D_{Tx}$  can grow beyond the diffraction limited beam size due to the atmospheric phase perturbation of the wave front. The transmit beam size  $D_{Tx}$  at the target is modeled as

$$D_{Tx} = 2 \sqrt{\left( \frac{D_{RA}}{2} \right)^2 \left( 1 - \frac{R}{r_f} \right) + R^2 \left( \frac{\lambda}{\pi} \right)^2 \left[ \left( \frac{2}{D_{RA}} \right)^2 + \left( \frac{1}{r_0} \right)^2 \right]}, \quad (128)$$

where the first term is the diameter due to focus, and the second term describes the growth due to diffraction limited by the smaller of the real aperture or the atmospheric coherence diameter  $r_0$  [62].

Turbulence will impact the efficiency of a coherent laser radar, but it can also limit the ability to form a synthetic aperture. The impact is described qualitatively using the three regions shown in Figure 96. The regions are defined in terms of the synthetic aperture fraction which is the ratio of the required baseline to the coherence diameter  $r_0/L$  is written as

$$A = \begin{cases} 1 & r_0 \geq L & \text{Region I} \\ r_0 / L & D_{RA} \leq r_0 < L & \text{Region II} \\ 0 & r_0 < D_{RA} & \text{Region III} \end{cases}, \quad (129)$$

where  $L$  is the required baseline for a given slant range,  $r_0$  is the coherence diameter, and  $D_{RA}$  is the real aperture of the ladar.

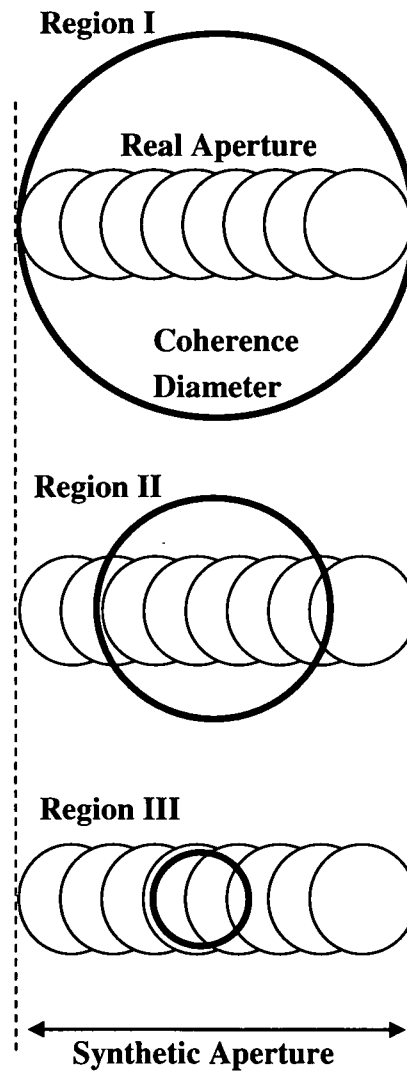


**Figure 96: Synthetic aperture fraction relating required baseline to the atmospheric coherence diameter.**

In Region I, both the real aperture of the ladar and entire synthetic aperture fit within atmospheric coherence diameter. In this case there is no effect on image formation or coherent mixing efficiency. In Region II, The coherence diameter is smaller than the synthetic aperture, but larger than the real aperture. In this case, each real aperture is coherent, so mixing efficiency is not effected; however, the coherence diameter is smaller than the synthetic aperture so the SA resolution may be limited without additional processing. As the aperture fraction decreases significantly below unity, the synthetic aperture will become harder to form since the number of apertures with related phase also becomes smaller. In Region III, the coherence diameter is smaller than both synthetic aperture and the real aperture. In this case, the mixing efficiency is reduced as the ratio of the coherence diameter to the real aperture squared, and the resolution of the real aperture is reduced. In region III, the synthetic aperture may be difficult or impossible to form.

Turbulence also has an impact on the selection of the ladar operating wavelength. Although the effect of turbulence is much less at longer wavelengths, the impact is relatively weak since the required based grows with wavelength as well. Taking the ratio of the coherence diameter, Eq. (128) to the required aperture size  $L$  for a fixed required resolution,  $\delta$ , yields

$$\frac{r_o}{L} \propto \frac{\lambda^{6/5}}{\frac{\lambda}{\delta}} \propto \lambda^{1/5} \quad (130)$$

which shows the actual dependence is fairly weak. The calculation of the atmospheric coherence diameter, additional sensing and imaging impacts, as well as other salient atmospheric quantities will be discussed further in the next sections.

(i) *Atmospheric Turbulence*

Atmospheric turbulence can have a significant impact on coherent laser radars that includes image blurring, inadequate target interactions due to beam growth, break up and wanderer, and most importantly, introduction of phase perturbations to the wavefront. The effective receiver diameter  $r_0$  is a measure of the wave front coherence which can have a significant effect on coherent systems.

For a target on the ground reflecting the energy transmitted from a ladar aperture on an aircraft, the coherence diameter at the aircraft is given by

$$r_0 = \left[ .4233 k = \left( \frac{2\pi}{\lambda} \right)^2 \int_0^R C_n^2 \left( h_p + \frac{z}{R} (h_t - h_p) \right) \left( \frac{z}{R} \right)^{5/3} dz \right]^{-3/5} \quad (131)$$

where  $h_p$  is the height of the platform,  $h_t$  is the height of the target, and  $z = R$  corresponds to the receiving aperture location [61]. The region near the aperture has the strongest effect on coherence diameter as indicated by the  $(z/R)^{5/3}$  factor in the integral from the target to the ladar. The coherence diameter has a strong  $\lambda^{6/5}$  dependence on wavelength as well as on the refractive index structure function  $C_n^2(h(z))$  of the atmosphere. The structure function describes variations in the index of refraction of the air due to uneven heating and turbulent mixing. It is a function of altitude which is in turn a function of the path along the line of sight,  $z$ . The  $C_n^2$  altitude profile is governed by a variety of factors including solar loading, surface type, and wind velocity. An infinite number of atmospheres are possible, and there are a variety of index structure profile models which attempt to capture representative atmospheric conditions for various regions and conditions. The Hufnagel-Valley model for  $C_n^2$  is a widely used model based on parametric fits of measure data and is given as

$$C_n^2 = .00594 \text{ sec}^2 \text{ m}^{-8/3} \left( \frac{V_p}{27} \right)^2 \left( 10^5 \frac{h}{\text{m}} \right)^{20} \exp\left( \frac{-h}{1000\text{m}} \right) + 2.7 \cdot 10^{-16} \text{ m}^{-2/3} \exp\left( \frac{-h}{1500\text{m}} \right) + C_{n0}^2 \exp\left( \frac{-h}{100\text{m}} \right), \quad (132)$$

where  $V_p$  is the wind velocity,  $h$  is the height of the surface and  $C_{n0}^2$  governs the turbulence near the surface [63]. This model can be used to predict the performance of both incoherent and coherent optical systems. With the windspeed set to  $V_p=21$  m/s and the an initial value for the index structure of  $C_{n0}^2=2 \times 10^{-14} \text{ m}^{-2/3}$ , the resulting index profile is denoted as HV 5/7 and is fairly representative of an average atmosphere. Multiplying the profile by .2 and 5 as shown in Figure 96, provides reasonable best and worst case turbulence profiles which are inclusive of a wide variety of locations and conditions.

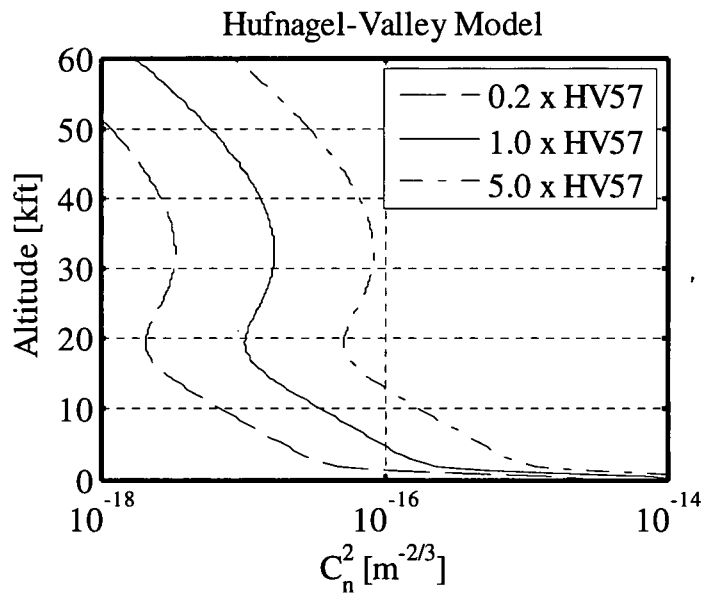


**Figure 97: Hufnagel-Valley HV 5/7 Index structure function altitude profiles.**

Figure 98 shows the iso-contours of the effective coherence diameter  $r_0$  calculated for standard HV 5/7 conditions. With the target at the origin, the coherence diameter at any

range-altitude combination may be read directly from the plot. As expected from observation of Figure 97, platforms at higher altitude have significantly larger coherence diameters. At low altitudes, the diameters are significantly smaller and on the order of the real aperture for much of the ranges of interest.

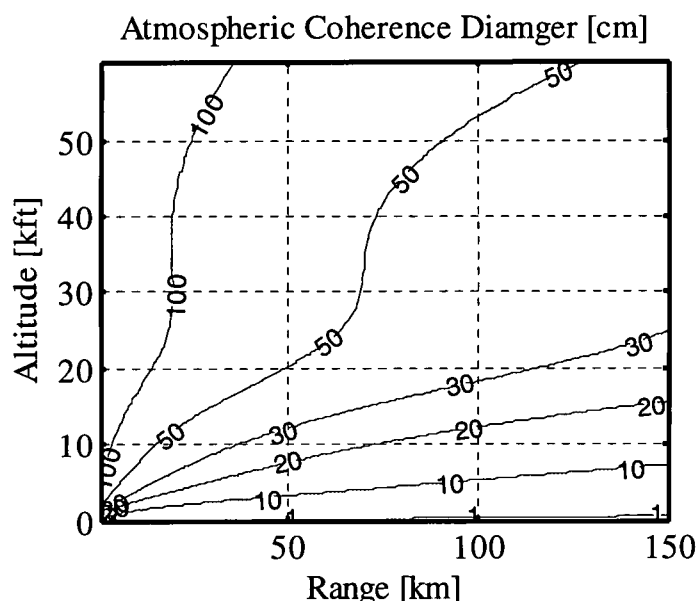


**Figure 98: Calculated coherence diameter isocontours for all platform range and altitude combinations with the target at the origin.**

The regions where the mixing efficiency is impacted, (i.e., where the coherence diameter is less than the diameter of the real aperture) is apparent in Figure 98; however, the effect on synthetic apertures is less obvious since the required baseline to achieve a desired resolution varies with range. To illustrate the effect on aperture synthesis, iso-contours of the aperture fraction as defined in Eq. (129) are calculated for both the nominal HV 5/7 and the 5x atmosphere and a 15 cm real aperture and are shown in Figure 96.

The standard HV 5/7 atmosphere produces unity aperture fractions over much of the point design region. The compression of the iso-contours at the lower altitudes indicates the coherence diameter is less than the real aperture where the coherent mixing efficiency will be

adversely affected and the poor phase relationship between samples makes aperture synthesis difficult. In the 5x atmosphere (bottom), the operational range is severely compressed toward both shorter ranges and higher altitudes. The low altitude region where the coherence diameter is less than the real aperture is significantly larger.

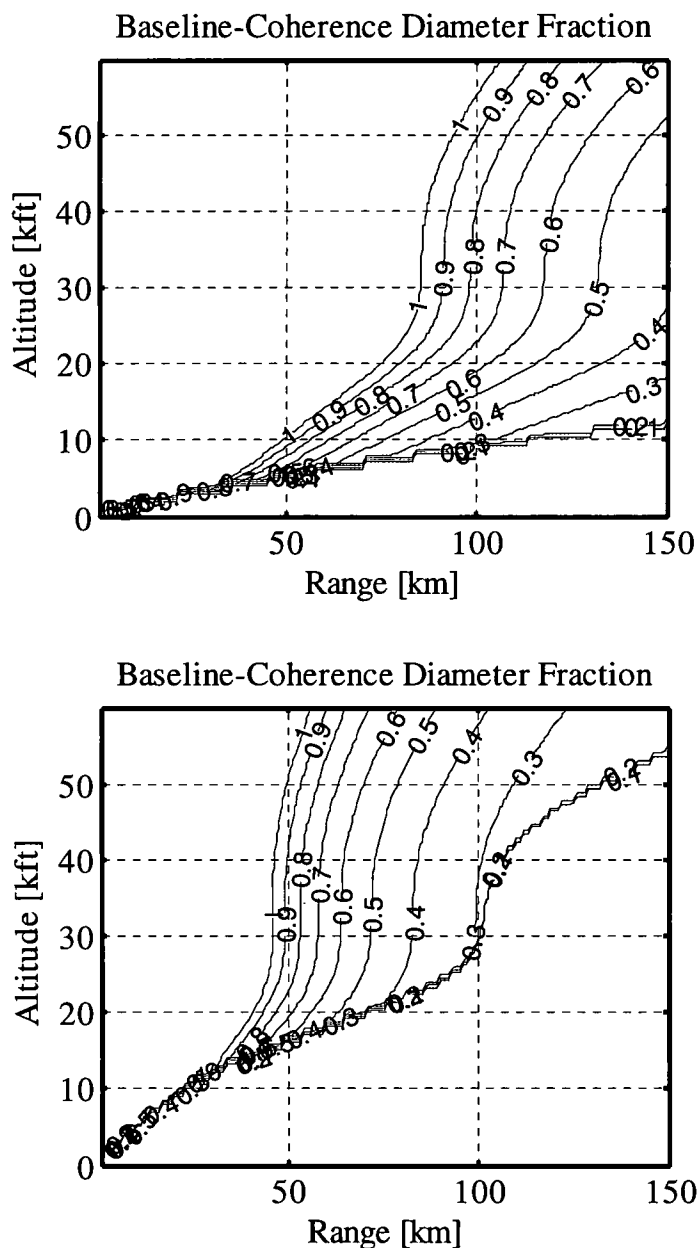


**Figure 99: Aperture fraction iso-contours for the standard HV 5/7 atmosphere (top) and the 5xHV 5/7 atmosphere (bottom).**

The atmospheric coherence time  $\tau_{urb}$  is the time for which the phase is correlated and can be written as

$$\tau_{urb} = 2 \left[ 291 \left( \frac{2\pi}{\lambda} \right)^2 \int_0^R C_n^2 \left( h_p + \frac{z}{R} (h_t - h_p) \right) \left| V_w - V_{ac} \left( 1 - \frac{z}{R} \right) \right|^{\frac{5}{3}} dz \right]^{-\frac{3}{5}} \quad (133)$$

where  $V_w$  is the wind velocity and  $V_{ac}$  is the aircraft velocity [64]. For a stationary ladar (i.e.,  $V_w = 0$ ) the coherence time it is dominated by the wind velocity. For a moving ladar in the spotlight mode, there is an apparent wind velocity that increases linearly from zero on the ground to  $V_{ac}$  at the aircraft.

#### (ii) *Atmospheric Transmission*

A great deal of research has been conducted on models for atmospheric transmission. This research will use a standard line transmission code called FASCODE - Fast Atmospheric Signature Code (Spectral Transmittance and Radiance) which was developed by the Air Force Geophysics Laboratory [65]. Here a layered atmosphere was assumed and FASCODE was used to calculate the transmission for a 10 km path at discrete altitudes ranging from 0 to 60 km for a variety of wavelengths, atmospheric models, and aerosol models. The transmission over any path can then be calculated by integration over the path using the layered atmosphere and Beer's law. The resulting two way transmission iso-contour plot for the Mid-Latitude Summer and 23 km visibility models is shown in Figure 100.

Like the turbulence, higher altitude offers better performance transmission performance. The low altitude attenuation is significant with the current models. In more challenging atmospheres low altitude operation would incur transmissions losses greater than an order of magnitude worse.

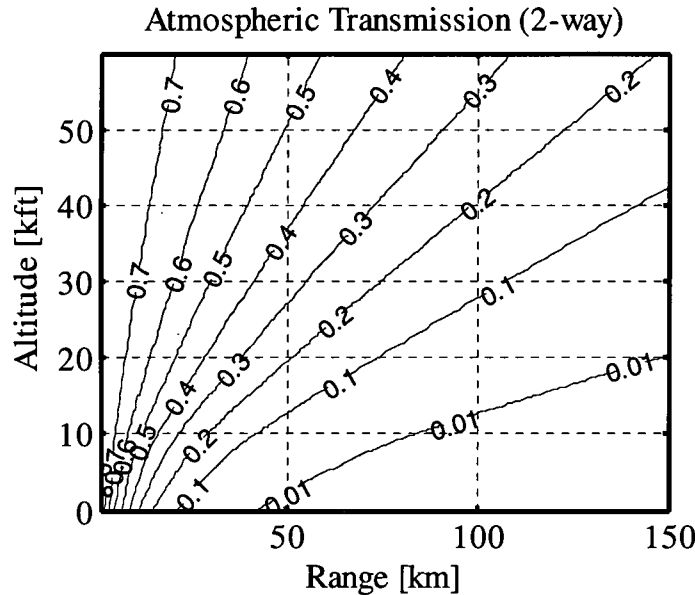


**Figure 100: Two way atmospheric transmission iso-contours calculated with FASCODE for a target at the origin to a platform at any range altitude combination.**

### (iii) Performance Predictions

Integrating the turbulence impacts and the FASCODE transmission calculations into the LRE, overall performance predictions for a PPN waveform system can be made. The power required  $P_{Req}$  to provide a single waveform CNR of 0 dB is found by solving LRE in Eq. (125) for the transmit power and is written

$$P_{Req}(R, h_p) = 10^{CNR_{Req}/10} 4 \frac{hc}{\lambda} \frac{B(R^2 + h_p^2)}{\eta_o \eta_M \eta_D \eta_T T^2 \rho_{Tgt}} \quad (134)$$

where the mixing efficiency  $\eta_M$ , target coupling efficiency  $\eta_D$ , and turbulence efficiency  $\eta_T$  are all implicit functions of the ground range  $R$  and platform altitude  $h_p$  as well as the atmospheric turbulence conditions. Figure 101 shows required transmit power iso-contours of a single beam PPN ladar.

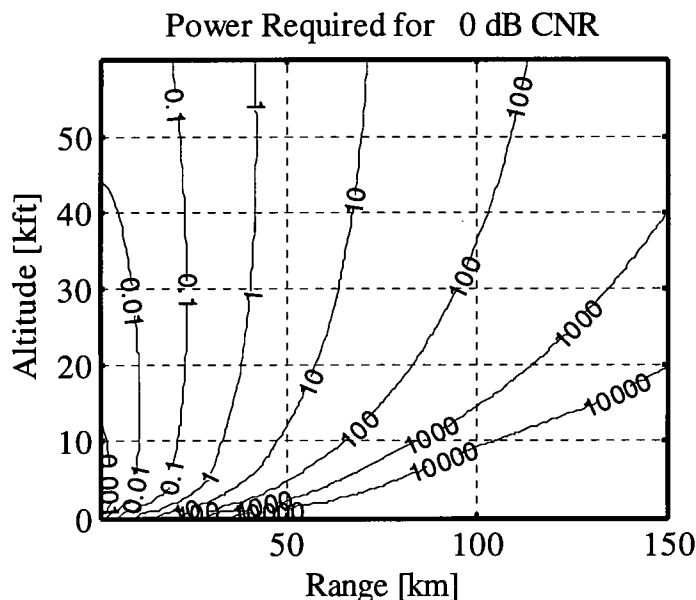


**Figure 101: CNR isocontours for a PPN coherent laser radar transmitting 10W of Average Power.**

The iso-contours were calculated for a ladar with a 30 cm real aperture using the HV 5/7 turbulence model and FASCODE with the Mid-Latitude Summer and 23 km Visibility aerosol models. The combined impact at low altitudes is sufficient to reduce the utility at long ranges for platform altitudes below 10,000 ft. The required power at the design point range of 75 km and altitudes above 20 kft is between 10 and 100 W. As shown during the discussion of the IPR, a PPN ladar can operate at CNRs significantly less than -20 dB which indicates that operation throughout the range should be possible with significant link budget margin. Further reduction in CNR from additional atmospheric losses or reduced target cross

section would reduce the image contrast. The measured resolution would eventually be affected as well, but only as the CNR reduction approached a large fraction of the signal processing gain associated with the PPN waveform. It should be noted that this is for a single beam. To form an image of an area larger than the diffraction limited beam width of a single beam such as the size of a vehicle, multiple beams are required which effectively increases the overall required transmit power by the number of beams.

The PPN waveform is a high average power, high duty cycle waveform which can be implemented with realizable components. It can make all the measurements necessary for multimode operations and can be implemented with efficient optical amplifiers in efficient, steady state operation.

## CHAPTER XIV

### SUMMARY AND RECOMMENDATIONS

#### A. Summary and Contributions

This work successfully expanded the knowledge base of multi-mode laser radar imaging. It combines the binary phase waveforms and waveform diversity techniques originally developed for radar with simultaneous waveform transmission architectures from optical communications to provide enhanced imaging from both single and multiple aperture systems. The research focused on the utilization of periodic pseudo noise waveforms with mode specific processing to implement range, Range-Doppler, synthetic aperture and micro-Doppler imaging.

This work extends the PPN waveform concept developed for radar by incorporating sub-code processing and waveform diversity into ladar imaging. Coherent processing of sub-codes provides the ability to tailor the Doppler sensitivity of the composite waveform as well as provide waveform limited IPR performance where the single waveform CNR is low. If orthogonal sub-codes are transmitted, coherent sub-code processing results in sidelobe performance corresponding to the equivalent full length composite waveform. Since the resolution primarily depends only on the phase chip duration, the energy used for a given measurement can be adapted by processing only the segments required to achieve the necessary CNR. A single sub-code, or sub-code fraction, can be used at short ranges for high

rate real aperture imaging. or longer code sequences can be used at long range where more energy per measurement is required.

Code division multiple access (CDMA) is a multiple channel transmission method common to radio frequency communications systems. Here CDMA was used to transmit multiple simultaneous PPN waveforms for ladar imaging. Using CDMA, multiple orthogonal waveforms can be transmitted from multiple apertures. Multiple input, multiple output (MIMO) apertures in this configuration collect the relative phase between the apertures necessary for height estimation via interferometric synthetic aperture ladar (SAL) and motion insensitive imaging via differential synthetic aperture ladar (DSAL).

A MIMO aperture configuration was developed with the ability to measure the relative phase between multiple apertures using a single transmit/receive channel. A single PPN waveform was divided, optically delayed by integer multiples of the sub-code duration, and transmitted from multiple apertures. Upon reception from the multiple apertures, the single CDMA composite return signal from each of the apertures was the coherent sum of waveforms from each path between the apertures. A single matched filter operation was used to generate the returns from each path including the relative phase between each path. The approach was experimentally demonstrated for two coherent apertures.

A genetic algorithm was applied to select PPN waveforms that produced reduced IPR sidelobes within a finite range region of interest. A cost function was developed to minimize the PSLR and ISLR with the region of interest and improvements of 6-10 dB were demonstrated at high single waveform CNR (i.e.,  $\text{CNR}=1$ ). The improvements were shown to increase performance over a wide range of CNRs relative to a randomly selected PPN code. The genetic algorithm was extended to optimize the IPR for MIMO apertures using

delayed PPN and CDMA. Codes were genetically selected with IPRs with multiple sidelobe suppression notches at integer multiples of the sub-code delay. Both the single notch code and multiple notch code were experimentally demonstrated.

Finally, an experimental ladar was developed and demonstrated the salient aspects of a PPN system including waveform generation, detection and processing; the four primary imaging modes, and multiple aperture operation via CDMA. This testbed will serve as the experimental foundation for a variety of future research efforts.

## **B. Directions for Future Research**

This research successfully developed and demonstrated a multi-mode imaging ladar concept based on binary phase PPN waveforms. The PPN system demonstrated range, range-Doppler, SAL, and micro-Doppler imaging from both a single and multiple apertures. There are four recommended areas for future research including ladar system development, alternate waveforms, processing algorithms, and MIMO aperture demonstrations.

A laboratory system was developed sufficient for operation within the laboratory or at ranges of a few kilometers with modest modifications. Demonstration of the system at long range will require development and integration of a variety of critical components including laser power amplifiers, low loss transmit/receive switches,

This research was focused on the binary phase PPN waveform. This waveform is relatively simple to generate, can easily be processed as sub-codes to adapt energy usage and Doppler sensitivity, can be used efficiently with CDMA, and provides resolution independent of the processed code length. Addition wave forms such as the poly-phase PPN codes

should also be investigate which could provide additional Doppler tolerance for long waveforms. Genetic selection of poly-phase waveforms should also be investigated.

The basic algorithms necessary for each imaging mode were developed; however, algorithm development is extremely important to the successful implementation of a full PNN ladar. The required algorithms are diverse ranging from parallel waveform processing, to adaptive sub-code processing, and platform motion detection and compensation. Much of this research was informed by developments in RF systems, but was be tailored or extended for application at optical wavelengths.

Finally, MIMO apertures based on the PPN waveform were demonstrated to have the ability to measure the relative phase between multiple apertures. The application of these apertures to IFSAL and DSAL was introduced, but the experimental application should be examined. In addition, the sensitivity and limitations of the technique to factors such as intra-aperture motion, atmospheric variations, mechanical alignment, and motion uncertainties should be examined.

### **C. Summary of Original Contributions**

- PPN waveforms applied to multi-mode coherent ladar (range, range-Doppler, SAL, and  $\mu$ -Doppler)
- Generation, transmission, detection and analysis of optical PPN waveform
- Discrete signal/matched filter models developed for each mode
- Use of orthogonal sub-codes in ladar for agile Doppler sensitivity
- Use of orthogonal sub-codes in ladar for IPR performance enhancement and energy management
- Genetically optimized IPR for single aperture multimode ladar
- Multiple PPN waveforms with CDMA multiplexing in coherent ladar
- CDMA applied to enable multiple input multiple output aperture ladar
- Approach to implement optically delayed PPN for CMDA
- Demonstrated multiple genetically optimized IPR regions for delayed PPN CDMA ladar operation.
- Multiple aperture IPR and phase recovery using single receiver
- Application of CDMA/MIMO apertures for IFSAL & DSAL

## REFERENCES

1. Polytec, "Single Point Vibrometers", [http://www.polytec.com/usa/158\\_421.asp](http://www.polytec.com/usa/158_421.asp).
2. R. R. Ebert and P. Lutzmann, "Vibration imagery of remote objects," Proc. SPIE **4821**, 1-10 (2002).
3. J. Czarske and O. Dölle, "Investigations on the frequency measuring error of laser Doppler velocimeters using the quadrature demodulation techniques", Optics for the Next Millennium Proc SPIE **3749** (1999).
4. B. Redman, W. Ruff, and K. Aliberti, "Direct Detection Laser Vibrometry with an Amplitude Modulated Ladar", Laser Radar Technology and Applications IX, Proc. SPIE **5412**, (2004).
5. T. Green, S. Marcus, B. Colella, "Synthetic-aperture-radar imaging with a solid-state laser", Appl. Opt. **34** 6941-6949 (1995).
6. W. Buell, N. Marechal, J. Buck, R. Dickinson, D. Kozlowski, T. Wright, and S. Beck, "Demonstrations of Synthetic Aperture Imaging Ladar", Laser Radar Technology and Applications X, Proc. SPIE **5791** (2005).
7. J. Ricklin, B. Schumm and P. Tomlinson, Synthetic Aperture Ladar for Tactical Imaging (SALTI) Flight Test Results and Path Forward", Presented at the Coherent Laser Radar Conference, Snowmass Colorado, 9-13 July, 2007.
8. J. Goodman, *Introduction to Fourier Optics*, (McGraw-Hill, 1968).
9. M. Richards, *Fundamentals for Radar Signal Processing*, (McGraw-Hill, 2005).
10. J. Johnson, "Analysis of image forming systems," in Image Intensifier Symposium, AD 220160 (Warfare Electrical Engineering Department, U.S. Army Research and Development Laboratories, Ft. Belvoir, VA, (1958), pp. 244-273.
11. N. Levanon and E. Mozeson, *Radar Signals*, (Wiley-Interscience, 2004).
12. M. Dierking, F. Heitkamp, L. Barnes, "High temporal resolution laser radar tomography for long range target identification", Presented at the IEEE/OSA Signal Synthesis & Reconstruction Conference, June 1998.
13. M. Skolnik, *Radar Handbook*, (McGraw-Hill, 1990)
14. M. Skolnik, *Introduction to Radar Systems*, (McGraw-Hill, 2005)

15. L. Cohen, *Time Frequency Analysis: Theory and Applications*, (Prentice Hall Signal Processing Series, 1995)
16. A.V. Jelalian, *Laser Radar Systems*, (Artech House, 1992).
17. A. Kachemyer, "Range Doppler Imaging: Waveforms and Receiver Design", SPIE **999**, Laser Radar III (1988)
18. Gatt; S. Henderson, W. Thomson, D. Bruns, "Micro-Doppler lidar signals and noise mechanisms: theory and experiment", Proc. SPIE **4035**, p. 422-435 (2000)
19. Jean-Pierre Cariou , Béatrice Augere, Matthieu Valla, "Laser source requirements for coherent lidars based on fiber technology", C. R. Physique **7**, 213–223 (2006)
20. R. Drever et al., "Laser phase and frequency stabilization using an optical resonator," Appl. Phys. B: Photophys. Laser Chem. **31**, 97–105 (1983).
21. C. Salomon et al., "Laser stabilization at the millihertz level", J. Opt. Soc. Am. B **5** (8), 1576 (1988)
22. Koheras Inc, "Adjustik System", Product Information Sheet, 2008
23. Frederico Tosco, *Fiber Optic Communications Handbook*, (McGraw Hill, 1990).
24. D. Hogenboom and C. DiMarzio, "Quadrature detection of a Doppler signal", Applied Optics, **37**, No. 13 (May 1998)
25. Ju-Yi Lee, Der-Chin Su, "Improved common-path optical heterodyne interferometer for measuring small optical rotation angle of chiral medium", Optics Communications **256** (2005), 337–341
26. J. Czarske and O. Dölle, "Investigations on the frequency measuring error of laser Doppler velocimeters using the quadrature demodulation technique ", Part of the 18th Congress of the International Commission for Optics: Optics for the Next Millennium, SPIE **3749**, 277-786 (1999)
27. L. Couch II, *Digital and Analog Communication Systems* (Prentice Hall, 2001).
28. P.J. Chidgey, "In-phase and quadrature detection using 90° optical hybrid receiver experiments and design considerations", Optics Communications **281**, (2008) 2735–2739.

29. T. Hodgkinson, R. Harmon, D. Smith, and P. Chidgey, "In-phase and quadrature detection using 90° optical hybrid receiver experiments and design considerations", *Optics Communications* 281 (2008) p. 2735–2739.
30. Dany-Sebastien Ly-Gagnon, Satoshi Tsukamoto, Kazuhiro Katoh, and Kazuro Kikuchi, "Coherent detection of optical quadrature phase-shift keying signals with carrier phase estimation", *Journal of Lightwave Technology* 24, No. 1, January 2006 p. 12-21.
31. A. Kachelmeyer, "Range Doppler Imaging: Waveforms and Receiver Design", *SPIE* 999, *Laser Radar III* (1988)
32. S. Fowler, G. Kamerman and G. Lawson, "Analysis of heterodyne efficiency for coherent laser radars", *SPIE* 1936 *Applied Laser Radar Technology* (1993)
33. A. Siegman, "Antenna Properties of Optical Heterodyne Receivers", *Proc. IEEE*: 54 pp. 1350-1356, (1966).
34. S. Henderson and P. Gatt, 'Coherent Laser Radar Tutorial', MSS Conference, Boulder CO, (August 2003)
35. B. Parvitte, V. Zéninari, C. Thiébeaux, A. Delahaigue and D. Courtois, "Infrared laser heterodyne systems", *Spectrochimica Acta Part A* 60 (2004) pp. 1193-1213
36. "Model 5866 10 GHz Linear Amplifier Product Specification", PicoSecondPulse Labs, Boulder, CO, SPEC-4040109, Revision 1, April 2008.
37. A. Jelalian, *Laser Radar Systems*, (Artech House, 1992).
38. M. John Yoder, "Comparison of BRDFs, missile cross-sections and airborne laser radar ranges at wavelength of 10.6, 1.06 and 0.6  $\mu\text{m}$ ", IRIS Specialty Group on Active Systems, Naval Postgraduate School, Monterey, CA, 24-26 February 1999.
39. N. Levanon, "Cross-correlation of long binary signals with longer mismatched filters", *IEE Proc.-Radar Sonar Navig.* (2005).
40. A. Dyka, "Chebyshev Minmax Deconvolution Filtering For a Pair of Discrete Pulses", *Compel: The International Journal for Computation and Mathematics in Electrical and Electronic Engineering* 9:2 (June, 1990)
41. European Space Agency ASAR CAL/VAL Team, "Quality measurements definition for ASAR Level 1 products", Technical Note, (14 March 2002)

42. K. Letscha and P. Berensb, "PSLR Estimation for SAR Systems with Consideration of Clutter Background", SAR Image Analysis, Modeling, and Techniques VII, edited by Francesco Posa, Proc. of SPIE **5980** (2005).
43. W. Huang and I. Andonovic, "Coherent Optical Pulse CDMA Systems Based on Coherent Correlation Detection", IEEE Transaction on Communications **47:2**, (IEEE, 1999).
44. S. U. Pillai, B. Himed, K. Y. Li, "Waveform Diversity for Space Based Radar", Proc. of Waveform Diversity and Design, Edinburgh, Scotland, Nov 8-10, 2004.
45. Arthur Breipohl, *Probabilistic Systems Analysis*, (John Wiley & Sons, 1970).
46. Sune R. J. Axelsson, "Noise Radar For Range/Doppler Processing and Digital Beamforming Using Low-Bit ADC", IEEE Transaction on Geoscience and Remote Sensing. **41:12**, (IEEE, 2003) pp. 2703-2721.
47. D. Garmatyuk and R. Narayanan, "SAR imaging using a coherent ultrawideband random noise radar, SPIE Conference on Radar Processing, Technology, and Applications IV, SPIE **3810** (July 1999).
48. Y. Li, A. Hoskins, F. Schlottau, K. Wagner, C. Embry, and W. Babbitt, "Ultrawideband coherent noise lidar range-Doppler imaging and signal processing by use of spatial-spectral holography in inhomogeneously broadened absorbers", Applied Optics, Vol. 45, No. 25 (September 2006).
49. Y. Cheng, Z. Bao, P. Zhao, and Z. Lin, "Doppler Compensation for Binary Phase-Coded Waveforms", IEEE Transactions on Aerospace and Electronic Systems **38:3** (July 2002).
50. M. Bell and S. Monroq, "Diversity waveform signal processing for delay-Doppler measurement and imaging", Digital Signal Processing **12**, 329-346 (2002)
51. Guey, J. -C. and Bell, M. R., Diversity Waveform sets for delay-Doppler imaging. IEEE Trans. Inform. Theory **44** (IEEE, 1998), 1504-1522.
52. T. Bucciarelli, A. Marone, M. Minorenti and R. Rarisi, "Genetic Algorithms and Radar Code Design", 8<sup>th</sup> International Conference on Signal Processing Applications and Technology, San Diego, CA pp. 1862-1866. (1997)
53. Welch, P.D, "The Use of Fast Fourier Transform for the Estimation of Power Spectra: A Method Based on Time Averaging Over Short, Modified Periodograms," IEEE Trans. Audio Electroacoustics, Vol. AU-15 (June 1967), pp. 70-73

R70 203 5585

54. P. Gatt, S. Henderson, J. Thomson and S. Hannon, "Noise Mechanisms Impacting Micro-Doppler Lidar Signals: Theory and Experiment", SPIE Aerorosense Conference, (April 2000)
55. E. Stappaerts, E. Scharlemann, Differential Synthetic Aperture Ladar", UCRL-JRNL-209959, February 25, (2005).
56. Christian D. Austin and Randolph L. Moses, "Interferometric Synthetic Aperture Radar Detection and Estimation Based 3D Image Reconstruction", SPIE Vol. 6237, Algorithms for synthetic aperture radar imagery. Conference No13, ETATS-UNIS (2006).
57. Austin, Christian D.; Moses, Randolph L., "Algorithms for Synthetic Aperture Radar Imagery XII. Edited by Zelnio, Edmund G.; Garber, Frederick D. Proceedings of the SPIE **5808** 1-14 (2005).
58. Curtis W. Chen and Scott Hensley, "Amplitude-based height-reconstruction techniques for synthetic aperture ladar systems," J. Opt. Soc. Am. A 22, 529-538 (2005)
59. E. Stappaerts, E. Scharlemann, Differential Synthetic Aperture Ladar, Lawrence Livermore National Laboratory Report, UCRL-JRNL-209959. February 25, 2005.
60. J. H. Shapiro, B. A. Capron, and R. C. Harney, "Imaging and target detection with a heterodyne-reception optical radar", Applied Optics. 20 (19), 1 October 1981, pp. 3292-3313.
61. R. Beland, *The Infrared & Electro-Optical Systems Handbook*, Vol. 2, Chpt. 2, (SPIE Press, 1993).
62. Fontanella, D. Roberts, and D. Shoup, 'Wavelength selection for long range laser vibration sensing", Proc. SPIE **3380** (1998) pp. 107-124
63. R. Beland, "Propagation Through Atmospheric Optical Turbulence," in *The Infrared and Electro-Optical Systems Handbook*, vol. 2, Chap. 2, F. G. Smith, Ed. Bellingham, WA: SPIE, 1993.
64. D. Park, J. Shapiro, "Performance analysis of optical synthetic aperture radars," SPIE **999** Laser Radar III, 1988.
65. H.J.P. Smith, D.J. Dube, M.E. Gardner, S.A. Clough, F.X. Kneizys, and L.S. Rothman, FASCODE- Fast Atmospheric Signature Code (Spectral Transmittance and Radiance), Air Force Geophysics Laboratory Technical Report AFGL-TR-78-0081, Hanscom AFB, MA, (1978).